

Investigations on ZnO based functional layers for enhanced photovoltaic performances in dye-sensitised solar cells

Thesis Submitted to AcSIR for the Award of the Degree of
DOCTOR OF PHILOSOPHY
in **CHEMICAL SCIENCES**



By

Swetha S.

Registration No: 10CC13J39009

Under the guidance of

Dr. U. S. Hareesh



**CSIR-NATIONAL INSTITUTE FOR INTERDISCIPLINARY
SCIENCE AND TECHNOLOGY (CSIR-NIIST)
THIRUVANANTHAPURAM-695019, KERALA, INDIA**

August, 2019

DECLARATION

I hereby declare that the Ph.D. thesis entitled “**Investigations on ZnO based functional layers for enhanced photovoltaic performances in dye-sensitised solar cells**” is an independent work carried out by me at the **Materials Science and Technology Division (MSTD), CSIR-National Institute for Interdisciplinary Science and Technology (CSIR-NIIST), Thiruvananthapuram** under the supervision of **Dr. U.S. Hareesh, Principal Scientist**, and it has not been submitted anywhere else for any other degree, diploma, or title.



Swetha S.

Thiruvananthapuram

August, 2019

CSIR-NATIONAL INSTITUTE FOR INTERDISCIPLINARY
SCIENCE AND TECHNOLOGY (CSIR-NIIST)
Council of Scientific and Industrial Research (CSIR)
GOVERNMENT OF INDIA
Thiruvananthapuram-695019, India



Dr. U. S. Hareesh
Principal Scientist

Functional Materials Section
Materials Science and Technology Division

CERTIFICATE

This is to certify that the work incorporated in this Ph.D. thesis entitled "*Investigations on ZnO based functional layers for enhanced photovoltaic performances in dye-sensitised solar cells*" submitted by *Ms. Swetha S.* to *Academy of Scientific and Innovative Research (AcSIR), New Delhi* in partial fulfilment of the requirements for the award of the *Degree of Doctor of Philosophy* in *Chemical Sciences* embodies original research work under my guidance. I further certify that this work has not been submitted to any other University or Institution in part or full for the award of any degree or diploma. Research materials obtained from other sources have been duly acknowledged in the thesis. Any text, illustrations and tables used in the thesis from other sources have also been duly cited and acknowledged.


Swetha S.


Dr. U. S. Hareesh
(Thesis Supervisor)

Thiruvananthapuram
August, 2019

Telephone: 0471 2535504 (office) 09446337222 (mobile) E-Mail: hareesh@niist.res.in

ACKNOWLEDGEMENT

It is my great pleasure to convey my deep sense of gratitude to my research supervisor Dr. U. S. Hareesh for suggesting the research problem and for his guidance, constant support, and encouragement that led to the successful completion of this work.

I am extremely thankful to Dr. Suraj Soman for the valuable collaboration throughout my research work, without which I could not achieve this goal. I am really indebted to him for providing device fabrication and related characterisation facilities, discussions and suggestions to complete my research work efficiently.

I would like to thank Dr. A. Ajayaghosh, present Director, and former Directors Dr. Suresh Das and Dr. Gangan Prathap of CSIR-NIIST, Thiruvananthapuram for allowing and providing the facilities and infrastructure of the institute for doing the research work.

I acknowledge Dr. S. Savitri, Dr. Harikrishna Bhatt, Dr. P. Prabhakar Rao, Dr. M. L. P. Reddy, Dr. M.T. Sebastian, present and former Head of Materials Sciences and Technology Division (MSTD), for allowing me to carry out my work as well as to access various characterisation facilities at MSTD.

I express my sincere thanks to Dr. Balagopal N. Nair, for the very effective scientific discussions, and critical comments which helped me a lot for the completion of my research work. I wish to thank Dr. Narayanan Unni K. N., Dr. G. S. Sailaja, Dr. K. G. K. Warriar, Prof. M. Padmanabhan and Dr. Satyajith Shukla for all the encouragement and support throughout my Ph.D. tenure.

I sincerely acknowledge my doctoral committee members Dr. S. Ananthakumar, Dr. E. Bhoje Gowd, Dr. Biswapriya Deb for their suggestions and constant support for my research work. I thank Dr. C. H. Suresh, Dr. R. Luxmi Varma, Dr. Mangalam S. Nair present and former AcSIR programme coordinators at CSIR-NIIST, for effective execution of course work, help and advice to complete the academic procedures of AcSIR.

I am immensely grateful to Mr. A. Peer Mohammed for helping me in doing several characterisations, constant support and encouragement. I would also like to thank Mr. Kiran and Mr. Robert Philip for doing TEM analysis, Mrs. Soumya, Mr. Hareesh, Mr. M. R. Chandran for SEM analysis, Mr. Prithviraj and Ms. Ajuthara for XRD analysis, Mrs. Hanna B. for DRS measurements, Mr. Rajeev for thickness measurement, Mr. Aswin Maheswar and Mr. Listo Vargheese for AFM analysis and Ms Anju for IR spectroscopic analysis.

I whole heartedly thank Mr. Sourava Chandra Pradhan and Mrs. Anooja Jagadeesh for the photovoltaic characterisations, fruitful discussions and memorable companionship throughout the research tenure.

I sincerely thank Dr. B. Krishna Kumar, Mrs. Jasmine Russel and Mr. Rothish for analysing the samples, support and suggestions regarding CSIR 800 project.

I would like to thank my M.Sc./M.Tec. project students Ms. Archana, Mr. Priyesh, Ms. Vidhu, Ms. Athira and Ms. Anju for their help in some of the experiments that have carried out.

With great pleasure, I thank my dear labmates Dr. Subha P. V., Ms. Shijina K. , Dr. Suyana P., Dr. Minju Thomas, Mr. Firoz Khan, Dr. Mega Joy, Dr. Smitha V. S., Dr. Sundar R., Mr. R. Unni Krishnan, Mr. Vishakh Vijayan, Mrs. Nimisha G., Ms. Vayshna Priya, Mrs. Surya S. Kuttan, Ms. Devika Surendran, Mr. Achu R., and Dr. Narasimman for the love, encouragement and all the help that they have extended to me.

I would like to thank my senior labmates Dr. Jaimy K. B., Dr. Jayasankar, Dr. Manjumol, Dr. Arun Kumar, Dr. Sree Remya S., Dr. Asha Krishnan and Dr. Sankar Sasidharan, for the motivation and immense support during initial stages of my research tenure. I extend my gratitude to former group members Mr. Midhun Mohan, Mrs. Sreeja Chandran, Ms. Jinu Joji Mr. Jintu Francis, and Mrs. Vidya K. for the friendship.

Dr. Manu Jose, Ms. Sumina N. B., Mr. Sriram, Dr. Harsha N., Mr. Lingamoorthy, Mr. Jayadev, Mr. Gokul, Mr. Sabu and Mr. Manuraj are acknowledged for various help and affection.

I thank my roommates Dr. Nisha N., Ms. Sharathna, Ms. Manasi Ingale, and Mrs. Sruthi Suresh for the friendship and encouragement throughout my stay at CSIR-NIIST research scholar's hostel. I would like to extend my gratitude to all my besties at hostel especially Ms. Anjali K. Sajeev, Ms. Sarikalekshmi, Ms. Amrutha, Ms. Roshima and Ms. Ranjana for the love and support.

I am extremely thankful to my family, for constant affection and being there with me at all the time, without I could not achieve this goal.

I thank all my teachers starting from my school days to those at CSIR-NIIST who motivated and blessed me.

I am grateful to UGC and CSIR, New Delhi for the financial assistance and providing the facilities for the completion of this work.

Swetha S.

Declaration	i
Certificate	ii
Acknowledgement	iii
Contents	v
List of figures and tables	xii
List of abbreviations	xx
Preface	xxi

CONTENTS

Chapter 1	Introduction to Dye-sensitised solar cells and photoanode materials	1-52
1.1	Introduction	3
1.1.1	Generations of solar cells	4
1.1.1.1	First generation Solar cell	4
1.1.1.2	Second generation Solar cell	4
1.1.1.3	Third generation Solar cell	5
1.2	Dye-sensitised solar cells (DSSCs)	6
1.2.1	Components of DSSC	6
1.2.2	Transparent conductive substrate	7
1.2.3	Semiconductor mesoporous film	7
1.2.3.1	TiO ₂ based DSSC	7
1.2.3.2	ZnO based DSSC	8
1.2.4	Dye-sensitiser	8
1.2.5	Electrolyte	9
1.2.5.1	Liquid electrolyte	10
1.2.5.2	Quasi-solid-state electrolytes	10
1.2.5.3	Solid state transport materials	10
1.2.6	Counter electrodes	10
1.3	Working principle of DSSC	11
1.4	Improvements in photoanodes of DSSC	12

1.4.1	Nanostructured semiconductor metal oxides	13		
1.4.2	Nanorods/wires	13		
1.4.3	Nanotubes	14		
1.4.4	Hierarchical structures	15		
1.4.5	Composites	16		
1.4.6	Doping	17		
1.4.7	Light scattering layer	18		
	1.4.7.1	Theories of light scattering	19	
1.4.8	Interfacial engineering	23		
	1.4.8.1	Pre-blocking layer	24	
	1.4.8.2	Post-blocking layer	25	
1.5	Indoor light Dye-sensitised solar cells	26		
1.6	Zinc Oxide	27		
1.6.1	Crystal structure of ZnO	28		
1.6.2	Synthesis of ZnO	31		
	1.6.2.1	Solution phase growth methods	32	
		1.6.2.1.1	Precipitation method	32
		1.6.2.1.2	Sol-gel method	32
		1.6.2.1.3	Solvothermal and	33
			Hydrothermal synthesis	
		1.6.2.1.4	Chemical bath	33
			deposition(CBD)	
	1.6.2.2	Vapour phase growth methods	34	
		1.6.2.2.1	Pulsed-Laser Deposition	34
			(PLD)	
		1.6.2.2.2	Chemical Vapour	34
			Deposition (CVD)	
		1.6.2.2.3	Thermal evaporation	35

1.7	Definition of the problem	35
1.8	Experimental and analytical techniques	36
1.8.1	Fabrication of DSSC	36
1.8.1.1	Fabrication of anode	36
1.8.1.2	Fabrication of cathode	38
1.8.1.3	Assembling of the device	38
1.9	Techniques used for interfacial charge transfer analysis	38
1.9.1	Electrochemical impedance spectroscopy (EIS)	38
1.9.2	Intensity modulated photovoltage spectroscopy (IMVS) and Intensity modulated photocurrent spectroscopy (IMPS)	40
1.9.3	Open circuit voltage decay (OCVD)	40
1.9.4	Charge extraction analysis	41
1.10	Photovoltaic parameters	41
1.10.1	Short circuit current density (J_{sc})	41
1.10.2	Open circuit voltage (V_{oc})	41
1.10.3	Fill factor (FF)	42
1.10.4	Power conversion efficiency (PCE)	42
	References	42
Chapter 2	Fugitive inclusions of ZnO micro flowers for enhanced light scattering and improved photovoltaic performance in TiO₂ based bifacial DSSCs	53-86
2.1	Introduction	55
2.2	Experimental Section	57

2.2.1	Synthesis of Zinc Oxide Microflower	57
2.2.2	ZnO Paste preparation	57
2.2.3	Etching of ZnO microflowers	57
2.2.4	Fabrication of DSSC	57
2.2.5	Material characterisation	59
2.2.6	Photovoltaic characterisation	59
2.3	Results and Discussion	60
2.3.1	Synthesis and characterization of ZnO microflowers	60
2.3.2	X-ray diffraction analysis	60
2.3.3	Morphology analysis	61
2.3.4	Surface area and pore size analysis	63
2.3.5	Characterisation of TiO ₂ paste	63
2.3.6	Characterisation of photoanode films	65
2.3.6.1	X-ray diffraction analysis	65
2.3.6.2	Scanning electron microscopy	66
2.3.6.3	Energy dispersive X-ray analysis and Elemental mapping	67
2.3.6.4	Diffuse reflectance spectroscopy	69
2.3.6.5	Atomic force microscopy	71
2.3.6.6	Dye loading studies	71
2.3.7	Photovoltaic Characterisations	72
2.3.7.1	Current voltage characteristics and IPCE measurements	72
2.3.7.2	Interfacial charge transfer analysis	75
2.3.8	Photovoltaic performance under indoor light	80
2.4	Conclusions	83
	References	84
Chapter 3	ZnO hierarchical structures as sacrificial inclusions for enhanced light scattering in TiO₂ photoanodes of dye- sensitised solar cell	87-131

3.1	Introduction	89
3.2	Experimental	91
	3.2.1 Synthesis of zinc oxide hierarchical structures	91
	3.2.2 ZnO paste preparation	91
	3.2.3 Etching of ZnO hierarchical structures	91
	3.2.4 Material characterisation	91
	3.2.5 Fabrication and characterisation of DSSC	92
3.3	Results and Discussion	94
	3.3.1 Synthesis of ZnO hierarchical structures	94
	3.3.2 X-ray diffraction analysis	95
	3.3.3 Thermogravimetric analysis	96
	3.3.4 Scanning electron microscopy	96
	3.3.5 Surface area and pore size analysis	98
	3.3.6 Infrared spectroscopy	99
	3.3.7 Transmission electron microscopy	100
3.4	Characterisation of photoanode films	101
	3.4.1 X-ray diffraction analysis	101
	3.4.2 Scanning electron microscopy	102
	3.4.3 Energy dispersive X-ray analysis	102
	3.4.4 X-ray photoelectron spectroscopy	105
	3.4.5 Diffuse reflectance spectroscopy	106
	3.4.6 Atomic force microscopy	107
	3.4.7 Dye loading studies	108
3.5	Photovoltaic Characterisations	109
	3.5.1 Current voltage characteristics and IPCE measurements	109
	3.5.2 Electrochemical impedance spectroscopy	112
	3.5.3 Intensity-modulated photovoltage spectroscopy and Intensity-modulated photocurrent spectroscopy	114
	3.5.4 Photovoltaic performance under indoor light	116

	conditions	
3.6	Conclusions	117
3.7	Macro porous titania scattering layers from TiO ₂ -ZnO mixed compositions	118
	3.7.1 Synthesis of TiO ₂ – ZnO Paste	118
3.8	Results and Discussion	119
	3.8.1 X-ray diffraction analysis	119
	3.8.2 Scanning electron microscopy and Energy dispersive X-ray analysis	119
	3.8.3 Diffuse reflectance spectroscopy	122
	3.8.4 Dye loading studies	124
3.9	Photovoltaic characterisation of dye-sensitised solar cells	125
	3.9.1 Current voltage characteristics and IPCE measurements	125
	3.9.2 Photovoltaic performance under indoor light	127
3.10	Conclusions	128
	Reference	128
Chapter 4	Fine tuning ZnO blocking layers for enhanced photovoltaic performance in ZnO based dye-sensitized solar cells	131-156
4.1	Introduction	133
4.2	Experimental	136
	4.2.1 Deposition of blocking layer	136
	4.2.2 ZnO paste preparation for porous active layer	137

4.2.3	ZnO characterisation	137
4.3	Fabrication and Characterisation of DSSC	137
4.4	Results and Discussion	139
4.4.1	Synthesis and characterisation of ZnO nanoparticles and films	139
4.4.2	X-ray diffraction analysis	139
4.4.3	Transmission electron microscopy	140
4.4.4	Bandgap analysis	140
4.4.5	Thermogravimetric analysis (TGA)	141
4.4.6	Scanning electron microscopy	142
4.4.7	BET surface area analysis	142
4.4.8	Atomic force microscopy	143
4.4.9	Photovoltaic characterisation of dye-sensitised solar cells	145
4.4.9.1	Current-voltage characteristics	145
4.4.9.2	IPCE measurements	147
4.4.9.3	EIS measurements	148
4.4.9.4	OCVD measurements	150
4.4.9.5	IMVS measurements	151
4.5	Conclusions	152
	References	153
Chapter 5	Summary and future projections	157-160
	List of publications	161
	List of conferences	162

LIST OF FIGURES

Chapter 1

1	Figure 1.1	Efficiency chart of photovoltaic cells (2019) by NREL, USA.	5
2	Figure 1.2	Schematic representations of main components of DSSC.	6
3	Figure 1.3	Structure of commonly used dyes in DSSC.	9
4	Figure 1.4	Schematic illustration of working principle of DSSC.	11
5	Figure 1.5	Double layer and mixture structure of light scattering materials used in DSSC.	20
6	Figure 1.6	(a) Mechanism of pre-blocking layer on FTO glass in DSSC (b) post-blocking layer on TiO ₂ particles in DSSC.	24
7	Figure 1.7	Emission spectra of LED and CFL.	27
8	Figure 1.8	ZnO crystal structures: Rock salt (cubic), Zinc blende (cubic) and Wurtzite (hexagonal). Gray and black spheres denote Zn and O atoms, respectively.	28
9	Figure 1.9	Schematic representation of steps involved in the fabrication of DSSC.	37
10	Figure 1.10	A typical (a) Nyquist plot and (b) bode plot of a dye-sensitised solar cell.	39
11	Figure 1.11	Equivalent circuit for impedance fitting.	40

Chapter 2

12	Figure 2.1	Design strategy illustrating the fabrication of DSSC utilising ZnO flowers as sacrificial layer to impart surface roughness over nanocrystalline TiO ₂ active layer photoelectrodes.	58
13	Figure 2.2	XRD patterns of as-synthesised ZnO at different reaction time.	61

14	Figure 2.3	SEM images of as-synthesised ZnO micro flowers at 30 min (a), 2 h(c)and 5 h (e) and corresponding TEM images b, d and f (SAED patterns are given in inset).	62
15	Figure 2.4	(a) N ₂ adsorption/desorption isotherms of as-synthesised ZnO micro flowers and (b) corresponding BJH pore size distribution curve.	63
16	Figure 2.5	(a) XRD pattern of annealed TiO ₂ film and (b) TEM image of the respective film (SAED pattern is given in inset).	64
17	Figure 2.6	(a) N ₂ adsorption/desorption isotherms of TiO ₂ film and (b) corresponding BJH pore size distribution curve.	64
18	Figure 2.7	TGA curve of TiO ₂ paste used for active layer.	65
19	Figure 2.8	XRD patterns of annealed photoanode films (a) TiCl ₄ treated TiO ₂ film (b) TiO ₂ -ZnO bilayer film (c) TiCl ₄ treated TiO ₂ -ZnO bilayer film.	66
20	Figure 2.9	SEM images of TiCl ₄ treated TiO ₂ film (a and b), TiO ₂ -ZnO flower film (c and d) and TiCl ₄ treated TiO ₂ -ZF film (e and f).	67
21	Figure 2.10	EDX of (a) TiCl ₄ treated TiO ₂ film, (b) TiO ₂ -ZnO flower film and (c) TiCl ₄ treated TiO ₂ -ZF film.	68
22	Figure 2.11	Elemental mapping of (a) TiCl ₄ treated TiO ₂ film, (b) TiO ₂ -ZnO film and (c) TiCl ₄ treated TiO ₂ -ZF film.	69
23	Figure 2.12	UV-vis diffuse reflectance spectra of TiCl ₄ treated bare TiO ₂ and TiO ₂ -ZF flower photoanodes before dyeloading (magnified portion of graph from 600 nm-700 nm wavelength is given in inset).	70
24	Figure 2.13	Photoanodes before TiCl ₄ treatment (a) bare TiO ₂ film (left) and TiO ₂ -ZnO film (right) and corresponding films after TiCl ₄ treatment (b).	70
25	Figure 2.14	AFM images of TiCl ₄ treated (a) bare TiO ₂ and (b) TiO ₂ -ZF photoanodes.	71

26	Figure 2.15	Absorption spectra of the desorbed dyes from the photoanodes.	72
27	Figure 2.16	(a) J - V characteristic with front illumination, (b) IPCE with front illumination, (c) J - V with back illumination and (d) IPCE with back illumination of TiO_2 and TiO_2 -ZF.	73
28	Figure 2.17	(a) Nyquist plot and (b) Bode plot from EIS.	76
29	Figure 2.18	Equivalent circuit for impedance fitting.	76
30	Figure 2.19	(a) Chemical capacitance and (b) Lifetime as a function of Fermi voltage (V_F).	77
31	Figure 2.20	Transport time as a function of Fermi voltage.	78
32	Figure 2.21	(a) Diffusion length (L_n) and (b) Charge collection efficiency (η_{cc}) as a function of Fermi voltage (V_F).	78
33	Figure 2.22	(a) Lifetime (τ_n) and (b) Transport time (τ_d) as a function of LED current.	79
34	Figure 2.23	Lifetime as a function of V_F derived from OCVD measurement.	80
35	Figure 2.24	Emission spectra of CFL.	81
36	Figure 2.25	Current density versus potential (J - V) characteristic for TiO_2 and TiO_2 -ZF under indoor light (1000 lux, CFL).	81
37	Figure 2.26	Current density versus potential (J - V) characteristic of different number of ZnO flower layer over TiO_2 layer in DSSC.	82

Chapter 3

38	Figure 3.1	Schematic illustration of the fabrication of DSSC utilising ZnO fibril aggregates and ZnO sheet aggregates structure as sacrificial layer to introduce surface roughness over nanocrystalline TiO_2 active layer photoanodes.	93
----	-------------------	--	----

39	Figure 3.2	XRD patterns of “as-synthesised” and respective samples annealed at 300°C.	95
40	Figure 3.3	TGA curves of LHZCs.	96
41	Figure 3.4	SEM images of LHZCs.	97
42	Figure 3.5	(a) N ₂ adsorption/desorption isotherms of ZnO derived by annealing LHZCs at 300 °C and (b) corresponding BJH pore size distribution curve.	98
43	Figure 3.6	IR spectra of LHZCs and corresponding annealed films; samples collected by scraping from the FTO glass.	99
44	Figure 3.7	TEM images of annealed Zfb film (a and b) and Zsh film (c and d).	100
45	Figure 3.8	XRD patterns of annealed photoanode films: (a) TiO ₂ , (b and c) TiO ₂ -ZnO (fibril and sheet), (d) TiO ₂ -Zfb and (e) TiO ₂ -Zsh.	101
46	Figure 3.9	SEM images of TiO ₂ (a and b), TiO ₂ -ZnO fibril bilayer film (c and d), TiO ₂ -ZnO sheet bilayer film (e and f), TiO ₂ -Zfb film (g) and TiO ₂ -Zsh film (h).	103
47	Figure 3.10	EDX of (a) TiO ₂ -ZnO fibril bilayer film, (b) TiO ₂ -ZnO sheet bilayer film, (c) TiO ₂ -Zfb film and (d) TiO ₂ -Zsh film.	104
48	Figure 3.11	XPS survey spectra of photoanode films: TiO ₂ -Zfb film and TiO ₂ -Zsh film.	105
49	Figure 3.12	UV-vis diffuse reflectance spectra of photoanode films before dyeloading.	106
50	Figure 3.13	Photoanodes before TiCl ₄ treatment (a) bare TiO ₂ film, (b) TiO ₂ -ZnO fb film, (c) TiO ₂ -ZnO sh film and corresponding films after TiCl ₄ treatment (d, e and f) respectively.	107
51	Figure 3.14	AFM spectra of (a) TiO ₂ and (b) TiO ₂ -Zfb and (c) TiO ₂ -Zsh photoanodes.	107

52	Figure 3.15	Absorption spectra of the desorbed dyes from the photoanodes.	108
53	Figure 3.16	(a) <i>J-V</i> characteristics under one sun condition and (b) IPCE spectra of the devices with front side illumination.	110
54	Figure 3.17	<i>J-V</i> characteristics under one sun conditions of the devices with back side illumination.	111
55	Figure 3.18	(a) Nyquist Plot and (b) Bode Plot obtained from EIS measurement.	113
56	Figure 3.19	(a) Capacitance plot and (b) Lifetime plot from EIS in dark.	114
57	Figure 3.20	(a) Life time plot and (b) Transport time plot obtained from IMVS and IMPS data respectively.	115
58	Figure 3.21	(a) Diffusion coefficient plot obtained from IMPS and (b) Charge collection efficiency plot obtained from IMPS and IMVS data.	115
59	Figure 3.22	<i>J-V</i> characteristics of the devices, when illuminated with 1000lux day-light CFL from (a) front side and (b) back side.	116
60	Figure 3.23	Schematic illustration of the fabrication of porous TiO ₂ scattering layer for DSSC utilising ZnO sheet aggregates structure as sacrificial inclusions.	118
61	Figure 3.24	XRD patterns of TiCl ₄ treated films.	119
62	Figure 3.25	SEM images of TiCl ₄ treated bilayer films: T Z10 (a and b), T Z20 (c and d) and T Z40 (e and f).	120
63	Figure 3.26	EDX of TiCl ₄ treated bilayer films: (a) T Z10, (b) T Z20 and (c) T Z40.	121
64	Figure 3.27	EDX of TiCl ₄ treated film cross section of the best device T Z20.	121

65	Figure 3.28	Photographs of photoanodes before and after TiCl ₄ treatment.	122
66	Figure 3.29	UV-vis diffuse reflectance spectra of TiCl ₄ treated photoanodes (a) without dye and (b) absorption spectra after dyeloading.	123
67	Figure 3.30	Photographs of substrates used to analyse absorbance spectra after dye loading.	124
68	Figure 3.31	Absorption spectra of the desorbed dyes from the photoanodes.	124
69	Figure 3.32	(a) <i>J-V</i> characteristics of the devices with front illumination and (b) IPCE of the devices with front illumination.	126
70	Figure 3.33	<i>J-V</i> characteristics of devices with front illumination under 1000 lux.	127

Chapter 4

71	Figure 4.1	Schematic representation of blocking layer effect.	136
72	Figure 4.2	(a) XRD pattern of as synthesised ZnO nanoparticle and (b) XRD of ZnO film annealed at 500°C.	139
73	Figure 4.3	TEM images of (a) as-synthesised ZnO nanoparticles and (b) its paste annealed at 500°C.	140
74	Figure 4.4	Band gap plot of as-synthesised ZnO nanoparticles.	141
75	Figure 4.5	TGA curve of ZnO paste used for active layer.	141
76	Figure 4.6	SEM image of ZnO active layer.	142
77	Figure 4.7	N ₂ adsorption/desorption isotherms (a and c) and BJH pore size distribution curve (b and d) for as-synthesised ZnO nanoparticles and ZnO nanoparticles scraped from the annealed active layer.	143
78	Figure 4.8	AFM images (a) BL1, (b) BL2, (c) BL3 (d) BL4 and (e) bare FTO coated glass.	144
79	Figure 4.9	(a) <i>J-V</i> and (b) IPCE characteristics without ZnO	145

		blocking layers and with blocking layers.	
80	Figure 4.10	Nyquist plots of ZnO DSSCs with various blocking layer thickness.	148
81	Figure 4.11	Randles circuit used for fitting the impedance data.	148
82	Figure 4.12	(a) The variation of recombination resistance as a function of applied potential and (b) variation of lifetime as a function of applied potential.	149
83	Figure 4.13	(a) The variation of lifetime as a function of applied potential obtained from OCVD measurements and (b) variation of lifetime as a function of light intensity obtained from IMVS measurement.	151

LIST OF TABLES

Chapter 1

1	Table 1.1	Efficiency improvements in DSSC by nanoarchitectures.	15
2	Table 1.2	Properties of ZnO.	29

Chapter 2

3	Table 2.1	Photovoltaic parameters for TiO ₂ and TiO ₂ -ZF from front side illumination and back side illumination under one sun conditions.	74
4	Table 2.2	<i>J-V</i> parameters for TiO ₂ and TiO ₂ -ZF under indoor light (1000 lux, CFL).	82
5	Table 2.3	<i>J-V</i> parameters for different number of ZnO flower layer over TiO ₂ layer in DSSC under one sun conditions.	83

Chapter 3

5	Table 3.1	Surface area and average pore size of the samples.	99
6	Table 3.2	Atomic% of elements present in photoanode layer.	105
7	Table 3.3	<i>J-V</i> parameters for TiO ₂ , TiO ₂ -Zfb and TiO ₂ -Zsh devices with front side illumination under one sun conditions.	111
8	Table 3.4	Photovoltaic parameters of the devices with back side illumination under one sun conditions.	112
9	Table 3.5	Photovoltaic parameters of the devices under 1000 lux illumination.	117
10	Table 3.6	Dye loading studies.	125
11	Table 3.7	Photovoltaic parameters of the devices with front side illumination under one sun conditions.	126
12	Table 3.8	Photovoltaic parameters of the devices with front side illumination under 1000 lux conditions.	128

Chapter 4

13	Table 4.1	Concentration of ZnO solution and thickness of the blocking layers deposited.	144
14	Table 4.2	Characteristic photovoltaic parameters obtained from DSSCs prepared with different ZnO compact blocking layers.	146

LIST OF ABBREVIATIONS

Atomic force microscopy	AFM
Barrett–Joyner–Halenda	BJH
Blocking layer	BL
Brunauer-Emmet-Teller	BET
Chenodeoxycholic acid	CDCA
Compact fluorescent lamp	CFL
Conduction band	CB
Diffuse reflectance spectroscopy	DRS
Dye-sensitised solar cell	DSSC
Dye-sensitised cell	DSC
Energy dispersive X-ray	EDX
Highest occupied molecular orbital	HOMO
Incident photon current conversion efficiency	IPCE
Intensity modulated Photocurrent Spectroscopy	IMPS
Intensity modulated Photovoltage spectroscopy	IMVS
Joint committee for powder diffraction standards	JCPDS
Light emitting diode	LED
Lowest occupied molecular orbital	LUMO
Open Circuit Voltage decay	OCVD
Power conversion efficiency	PCE
Scanning electron microscopy	SEM
Selected area electron diffraction	SAED
Thermo gravimetric analysis	TGA
Transmission electron microscopy	TEM
Ultra violet	UV
Valence band	VB
X-ray diffraction analysis	XRD
X-ray photoelectron spectroscopy	XPS

PREFACE

Dye-sensitised solar cells (DSSC/DSC) are promising technology solutions for sustainable energy production owing to its low fabrication cost and relatively high power conversion efficiencies (PCE) at indoor as well as outdoor light conditions. Recent reports highlight the phenomenal performance of DSSC/DSC under various indoor lighting sources such as fluorescent lamps and light-emitting diodes (LEDs) compared to the other solar cell technologies. This has enabled them to be capable of powering wireless sensors and consumer electronics. Titanium dioxide (TiO_2) is the most commonly used photoanode material in DSSC/DSCs owing to its larger band gap, high conduction band edge and high surface area for dye loading. To date the PCEs up to 14% are realised with such devices. Apart from TiO_2 , zinc oxide (ZnO) is also explored as a viable alternative due to its attributes like high bulk electron mobilities and ease of synthesising it in variety of morphologies. In the past few years, concerted efforts are pursued towards the improvement of power conversion efficiency in DSSC/DSCs by developing photoanode materials with superior features. The widely pursued strategies includes synthesising semiconductors with high surface area for high dye loading, employing 1D materials for fast electron transport, submicron sized particles for internal light scattering layer and deposition of blocking layer to reduce electron recombination etc.

The photo anode in DSSC/DSC comprises of an active layer, blocking layer and scattering layer. Tuning of these layers play a remarkable role in enhancing the PCE in DSSC/DSC. The present thesis addresses the fabrication of scattering and blocking layers of DSSC/DSC using ZnO nanostructures. Insertion of scattering and blocking layers increases the light harvesting characteristics and reduces electron-hole recombination respectively in the photoanode architecture, thereby improving efficiency of cells. Scattering layers generally make use of submicron particles and layers thus fabricated are found to be opaque. Herein, we demonstrate a methodology to create surface roughness on TiO_2 layer to impart light scattering in DSSC/DSC with ZnO hierarchical structures without much lose in transparency of the photoanode. Fine-tuned blocking layers generated through a wet chemical method is utilised as blocking layers. Dip

coating method was used to deposit blocking layers over FTO. The effect of blocking layer thickness on the photovoltaic properties of ZnO based DSSCs are investigated.

Chapter 1 provides a general introduction to dye-sensitised solar cells, their architecture and examines the role of blocking and scattering layers on the overall power conversion efficiencies. A comprehensive review of the structural, compositional and morphological modifications in TiO₂ and ZnO-based DSSCs is carried out to identify and define the problem.

In chapter 2, the efficiency of a DSSC/DSC solar cell is manipulated by engineering the surface texture of the photoanode for improved light scattering in the active titania layer. Herein, surface roughness was introduced in the TiO₂ layer by applying a sacrificial layer of ZnO micro flowers of 2-4 μm sizes during cell fabrication. The ZnO aggregates deposited on TiO₂ layers are selectively etched by the TiCl₄ treatment. The voids as well as the surface roughness created scattering centres, thereby improving the photocurrent generation. A PCE improvement of 12.9% in full sun and 84% in 100 lux compact fluorescent lamp (CFL) illumination was achieved by employing templated TiO₂ surface created by the etching of ZnO micro flowers. As the electrode offers transparency, it can possibly serve as a potential candidate for bifacial DSSC in building-integrated photovoltaic (BIPV) sector.

Chapter 3 deals with the surface roughness and pore engineering of the photoanode films to improve the light scattering inside the titania layer of DSSC/DSC by employing micron sized ZnO hierarchical structures (fibril and sheet aggregates) as fugitive inclusions. A bilayer photoanode was constructed with bare TiO₂ as bottom layer and TiO₂-ZnO mixture as top layer. The ZnO inclusions are etched selectively by TiCl₄ leaving behind its voids in the TiO₂ layer. Three different weight% of TiO₂-ZnO mixture paste was fabricated to study the effect of voids in light scattering and dye loading in DSSC. It was observed that, for the optimum composition of TiO₂-ZnO mixture, PCE values of 9.4% is obtained from the bilayer structured anode whereas monolayer TiO₂ offered 6.3% under one sun

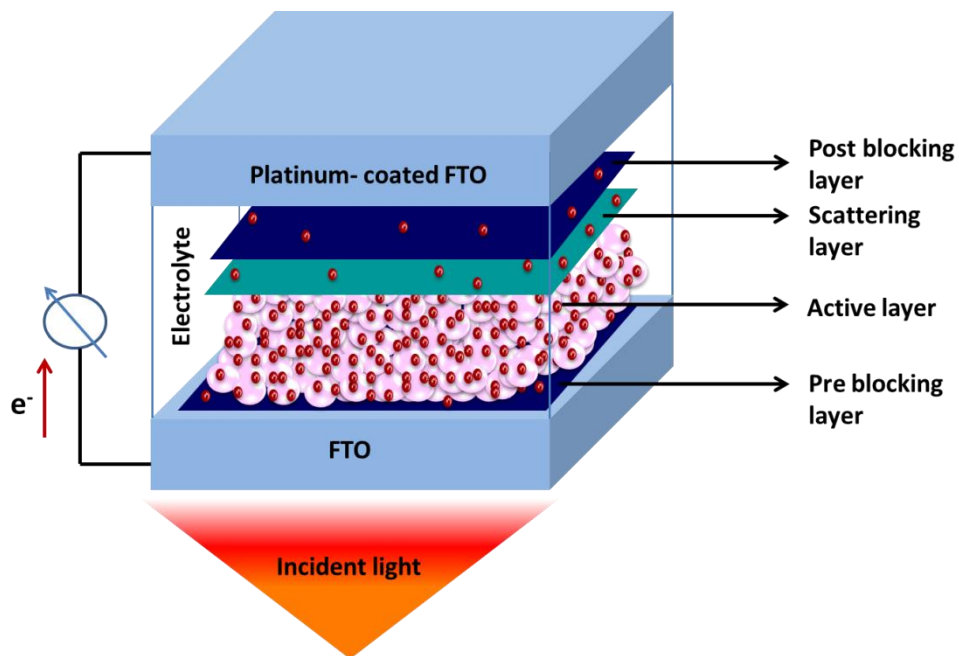
condition. The PCE efficiency values under ambient light condition (1000 lux) showed an improvement from 12.33% to 17.85%.

The effect of Zinc Oxide (ZnO) blocking layers (BLs) of different thickness, on the photovoltaic performance of ZnO based DSSC is investigated in chapter 4. The recombination of photo injected electrons is one of the major limiting parameters in the performance of DSSCs which occurs either through recombination from FTO with the oxidised dye molecules or with the electrolyte at the FTO/electrolyte interface. Devices with optimised ZnO blocking layer thickness (12 nm) lead to improved performance (2.57% PCE) in comparison to the devices fabricated using bare FTO (1.27% PCE) by suppressing interfacial recombination at the FTO/ZnO interface thereby enhancing the lifetime for better power conversion efficiencies.

Chapter 5 provides a summary of the whole work that has been carried out in establishing the role of ZnO functional layers on TiO₂ and ZnO based DSSCs.

Chapter 1

Introduction to Dye-sensitised solar cells and photoanode materials



Dye-sensitised solar cells (DSSCs) are recognised as efficient, renewable and economic photovoltaic devices with potential for mass energy production. Recent reports highlight the phenomenal performance of DSSC/DSCs, compared to other solar cell technologies, under various indoor lighting sources such as fluorescent lamps and light-emitting diodes (LEDs) enabling them to be capable of powering wireless sensors and consumer electronics.

1.1 Introduction

Energy is an essential requirement of human society and its consumption is rapidly increasing with the advancements in technologies. Non-renewable energy sources, such as fossil fuels comprising of oil, natural gas, and coal are currently dependent upon to meet our present day energy demand. However, the massive consumption of fossil fuels lead to its exhaustion and it is projected that the fossil fuels reserves of the world may last only 35 years for oil, 37 years for natural gas and 107 years for coal.¹ Moreover, consumption of such fossil fuels are also identified with serious environmental hazards, for instance CO₂ emission, global warming, and air pollution. Consequently there is an urgent need to reduce our dependence on non-renewable energy resources. Hydro, wind, solar, biomass, geothermal and nuclear are the various renewable energy sources that we are utilising today. Among these, solar energy is recognised to be the promising alternative for energy production as it is the most pure and abundant source of energy.² Annually sun provides about 1.5×10^{18} kW h of energy, whereas reserves of oil, coal, and gas are 1.75×10^{15} kW h, 1.4×10^{15} kW h, and 5.5×10^{15} kW h, respectively.³ Thus yearly sunlight can provide hundred times more energy than the world's entire known fossil fuel reserves. Enormous efforts are taken by researchers worldwide to enhance the exploitation of solar energy in an efficient and cost effective way. Photovoltaics is a viable option to directly convert sunlight into electricity. Even though sun provides copious, clean and green form of energy, harvesting it in an appropriate manner is challenging. Investigations and innovations are pursued by researchers to develop solar cells in a cost effective and highly efficient manner.

Solar cells are photovoltaic devices that convert sunlight to electricity. In 1839 French physicist Becquerel has demonstrated photoelectrochemical effect which is the basic working principle behind the solar cell.⁴ According to the emergence of the different types of solar cells they are named as first generation, second generation and third generation. An overview of different types of solar cells particularly dye-sensitised solar cells (DSSC) and materials used for its fabrication is detailed in the following section.

1.1.1 Generations of solar cells

1.1.1.1 First generation Solar cell

The first generation of solar cells include silicon solar cell, is first developed in 1954 at Bell laboratories Ltd. by Chaplin, Fuller and Pearson.⁵ They utilised p-n junction silicon strips to fabricate the solar cell and achieved a power conversion efficiencies (PCE) of 4%. The efficiency is further improved by bringing the p-n junction more close to the surface so that more photons can be utilised, and also by doping. Si solar cells make use of monocrystalline and polycrystalline silicon substrates. The highest efficiency reported for monocrystalline Si solar cell is 26.1% and for poly crystalline around 22.3% (**Figure 1.1**). The less efficiency of poly crystalline Si solar cell compared to mono crystalline Si solar cell is due to the crystal defects in poly crystalline Si, that are acting as recombination centers. The low energy band gap of ~1.1 eV for Si makes it a perfect candidate for solar cell applications.² They can absorb photons from both visible and IR region according to Planck's equation and this is the one of the major reasons for the high efficiency of Si solar cells.

$$E = \frac{hc}{\lambda} \quad (1)$$

Even though Si solar cells are capable of delivering high PCE, high cost of installations prompted the need for other. The large scale application of Si solar cells necessitates the need for huge amount of Si and the processing of it will increase the chemical hazards to the environment.

1.1.1.2 Second generation Solar cell

Second generation solar cells deals with thin film technologies. Thin film technologies employ small amount of materials which are grown deposited on substrates such as glass plastic etc. to thickness in micrometer regime. Semiconductor materials used for thin film technologies include cadmium telluride (CdTe),⁶ gallium arsenide (GaAs),⁷ copper indium/gallium selenide (CIS/CIGS)⁸ etc. Thin films have superior photophysical properties that can improve the performance of solar cell compared to bulk materials. The semiconductor material consumption is less in thin film solar cell and also the expense of production of second generation solar cell is lower than that of crystalline Si

solar cells. However CdTe possess serious disposal problems. It is a highly toxic poisonous heavy metal and is environmentally hazardous.⁶

1.1.1.3 Third generation Solar cell

Thereafter third generation solar cells emerged with the aim to process materials at the nanoscale and scale up the same up to macroscopic areas. This generation is very different from the previous ones due to the use of wide band gap semiconductors. The various types of solar cells falls under this category include Dye-sensitised solar cells (DSSCs),⁹ quantum dot-sensitised solar cells (QDSSCs),¹⁰ Perovskite solar cells,¹¹ Polymer solar cells¹² etc. The working mechanism and fabrication technology is extensively different from Si solar cells. The third generation solar cell offer remarkable cost effectiveness over first and second generation solar cells. Yet these entities have not touched the efficiency levels of Si solar cells still it opens up a new approach to perform well with the use of nanotechnology. The efficiency chart of photovoltaic cells (2019) from NREL is presented in **Figure 1.1**.¹³

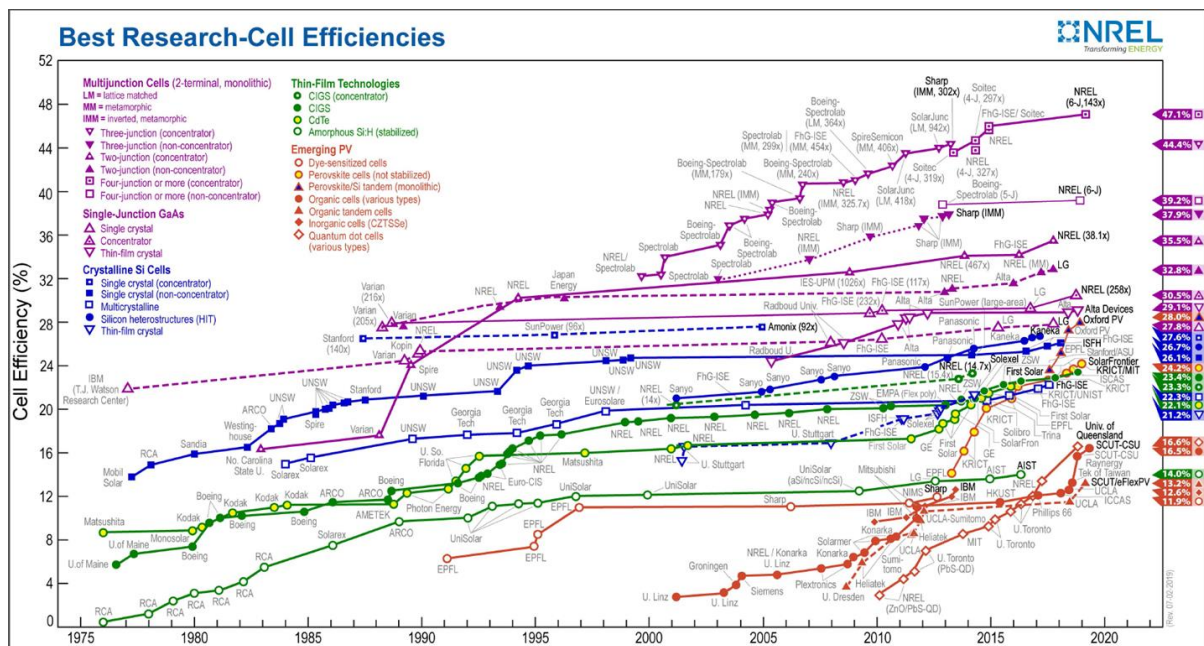


Figure 1.1 Efficiency chart of photovoltaic cells (2019) by NREL, USA.

(<https://www.nrel.gov/pv/cell-efficiency.html>)

1.2 Dye-sensitised solar cells (DSSCs)

DSSCs are photovoltaic devices developed by Brian O' Regan and Michael Gratzel in 1991.¹⁴ DSSC emerged from the concept of natural photosynthesis. In DSSC organic dye molecules is utilised as light absorbing material. Detailed device structure and working principle of DSSC is discussed in the following sections. DSSC, by virtue of its properties like transparency, multi-colour options, ease of integration into building facades, environmental friendliness and low production cost are considered advantageous compared to conventional silicon solar cell. Even though the power conversion efficiency of DSSC is lower than that of Si solar cells, under indoor light conditions DSSCs perform incredibly good. This unique property makes them best alternative power source to wired and battery energy sources.¹⁵

1.2.1 Components of DSSC

DSSC consists of five basic components (1) Transparent conductive substrate (2) mesoporous semiconductor layer (3) dye sensitizer adsorbed to the semiconductor (4) electrolyte and (5) counter electrode such as platinum or carbon (**Figure 1.2**).

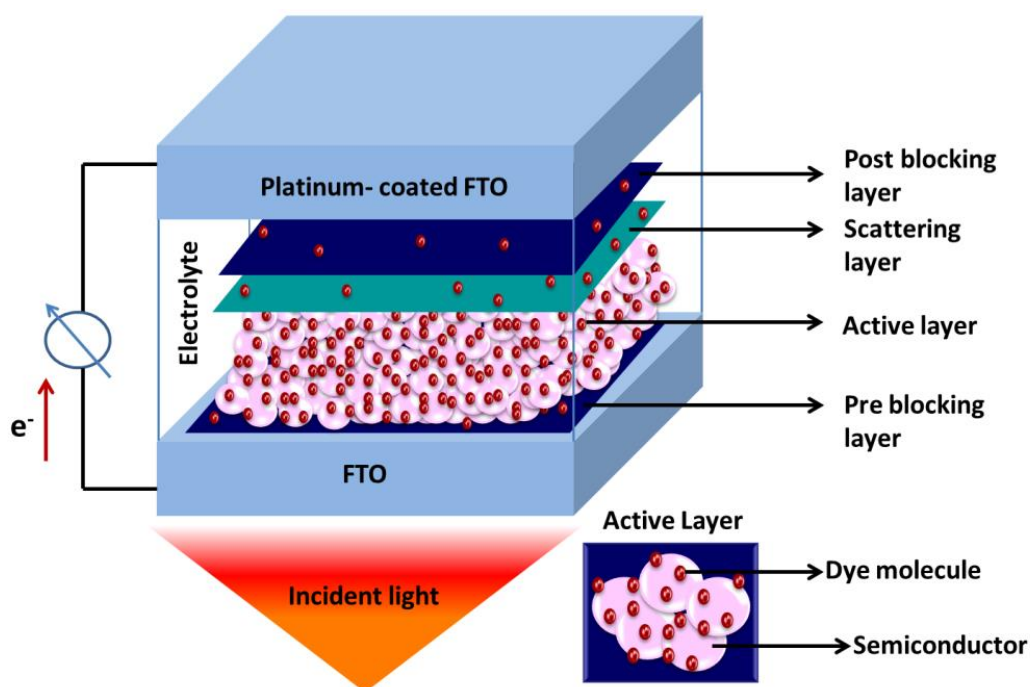


Figure 1.2 Schematic representations of main components of DSSC.

1.2.2 Transparent conductive substrate

Transparent conductive glass fluorine doped tin oxide (FTO) or indium doped tin oxide (ITO) is used as substrates for fabricating DSSC. The substrate is a crucial part of DSSC as it controls the amount of sunlight penetrates into the cell and also it carries electrons to the external load. The conductive glass should be highly transparent to the visible, infrared and far-infrared regions, stable at high temperatures ~ 500 °C and chemically inert to avoid reaction with the chemicals in DSSC.²

1.2.3 Semiconductor mesoporous film

Wide band gap semiconductor materials such as TiO_2 ,¹⁶ ZnO ,¹⁷ SnO_2 ,¹⁸ Nb_2O_5 ,¹⁹ can be employed for mesoporous film fabrication. Ternary oxides like SrTiO_3 ,²⁰ BaSnO_3 ,²¹ and Zn_2SnO_4 ²² are also been explored as photoanode materials for DSSC. These materials are made into a paste and then doctor bladed over the conductive glass substrate. TiO_2 is the most widely used semiconductor for DSSC and is reported to deliver highest PCE so far. Enormous efforts have been done to optimise the semiconductor properties in order to improve the charge transport, dye loading, light scattering etc. in the solar cell.

1.2.3.1 TiO_2 based DSSC

Titanium dioxide is the most widely used photoanode semiconductor material for DSSC due to the superior features such as wide band gap, high chemical stability, high surface area, mesoporosity, higher conduction band (CB) edge and less toxicity. TiO_2 exists in three crystalline forms, termed as anatase, brookite and rutile. Out of these anatase and rutile are in tetragonal crystal structure whereas brookite belongs to orthorhombic crystal structure. Rutile phase is the most thermodynamically stable form. Anatase TiO_2 is an indirect band gap semiconductor where rutile and brookite are direct band gap semiconductors. Owing to the indirect band gap nature, direct transition of photogenerated electrons from the conduction band (CB) to valence band (VB) is not possible. As a result the life time of the photogenerated electron is higher in anatase compared to the other two forms. Apart from these the average effective mass of the photogenerated electrons of anatase phase is less than the other polymorphs. This will help in faster transport of the electrons and therefore less recombination rate.²³⁻²⁵ The maximum efficiency reported for anatase TiO_2 based DSSC is 14%.²⁶

1.2.3.2 ZnO based DSSC

Zinc oxide (ZnO) is explored as a viable alternative to titania due to its attributes like high electron mobilities (2-3 orders of magnitude higher than TiO_2), wide band gap (3.3 eV), high exciton binding energy (60 meV) and the ease of synthesising it in a variety of nanostructures^{17, 27} (ie; nanosheets,²⁸ nanowires,²⁹ nanotrees,³⁰ nanotubes,³¹ nanotetrapods,³² nanorods,³³ hierarchical aggregates³⁴ etc.) compared to TiO_2 .¹⁷ However the maximum PCE reported for ZnO-based DSSC is 8% and is significantly lower than the highest efficiency reported for TiO_2 .³⁵ The main drawback associated with ZnO based DSSCs is the formation of dye- Zn^{2+} aggregates under acidic conditions which prevents efficient injection of electrons. The low injection leads to the relaxation of the excited dye molecule to the ground state affecting the efficiency of cells. ZnO possess very low surface area due to which poor dye loading, results in less light harvesting, and efficiency of device.¹⁷

1.2.4 Dye-sensitiser

Dye is one of the most vital part of DSSC. The dye molecules should satisfy the following essential characteristics^{2, 25}

- i) It should be able to absorb the whole of visible region and a part of near IR region (panchromatic absorption) in the electromagnetic spectrum.
- ii) Dye molecule should possess anchoring groups such as $-\text{COOH}$, $-\text{H}_2\text{PO}_4$, $-\text{SO}_3\text{H}$ etc. in order to have strong bonding with the semiconductor for the efficient electron injection into the CB of semiconductor.
- iii) The lowest unoccupied molecular orbital (LUMO) of the dye molecule should be in high energy level than the CB edge of the semiconductor to offer efficient electron transfer process from the excited dye to the conduction band of the semiconductor.
- iv) The oxidised state of the dye must have more positive potential than the redox potential of the electrolyte.
- v) Dye molecules should be photo stable as well as electrochemically and thermally stable. Various types of dye molecules are employed so far, which

includes metal complexes, porphyrins, phthalocyanines, metal free organic dyes etc. Metal complexes especially ruthenium Ru (II) complexes are widely utilised for DSSC due to their broad absorption spectra. N719, N3, black dyes are commonly used ones (**Figure 1.3**)

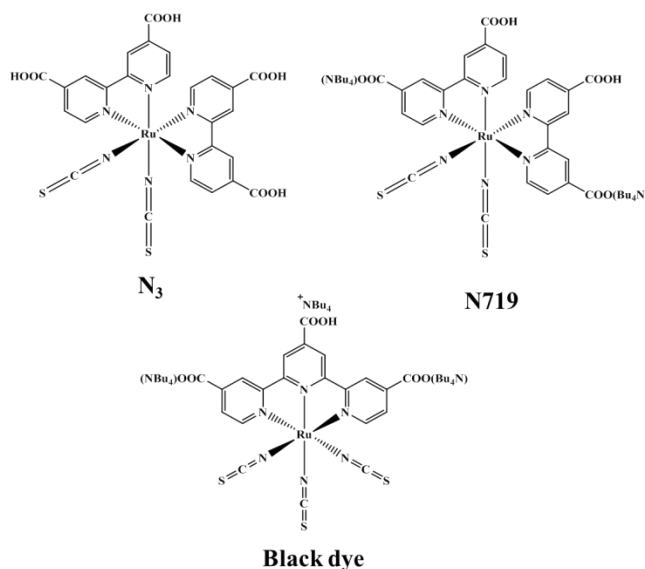


Figure 1.3 Structure of commonly used dyes in DSSC.

1.2.5 Electrolyte

Electrolyte is meant to control the charge carrier transport between the electrodes and regeneration of dye molecules in DSSC. Majorly three types of electrolytes are used in DSSC, liquid electrolyte, quasi-solid-state electrolyte and solid-state transport materials. Iodide/triiodide (I^-/I_3^-) redox couple is well exploited in the liquid electrolyte category. Electrolyte has pronounced effect on the photovoltaic parameters such as current density (J_{sc}), photovoltage (V_{oc}), fill factor (FF) etc. V_{oc} is extremely affected by the redox potential of the electrolyte. Similarly J_{sc} is affected by the transport of the redox couple constituents in the electrolyte. Diffusion of charge carrier in electrolyte and the charge transfer resistance on the electrolyte-electrode interface was found to influence the FF of DSSC. Electrolytes must ensure fast diffusion of charge carriers and shall also be able to create better interfacial contacts with the semiconductor layer and counter electrode. They should possess high chemical, thermal and optical stability. As the electrolyte are coloured, they will absorb a part of visible light which in turn reduce the visible light available for the dye. Based on the physical state, composition and formation mechanism

electrolyte are classified into three different types liquid electrolyte, solid-state transport materials and quasi-solid-state electrolyte.³⁶

1.2.5.1 Liquid electrolyte

Iodide/triiodide redox couple is the most widely used liquid electrolyte for DSSC. A suitable solvent with high dielectric constants, low viscosity and high volatility is used. For iodide/triiodide organic solvents like acetonitrile, propionitrile, methoxy acetonitrile etc. are used. Li^+ ions are added to the liquid electrolyte to accord better performance. As the size of Li^+ ion is small it can diffuse it into the dye loaded TiO_2 mesoporous film and form Li^+e^- ambipolar species in the CB of TiO_2 which increases the transport speed of the electrons. This will improve the J_{sc} of the DSSC.^{25, 36}

1.2.5.2 Quasi-solid-state electrolytes

Quasi-solid-state is a particular state of a material between solid and liquid state, they can display both cohesive and diffusion properties. They possess long term stability than liquid electrolyte and shows high ionic conductivity and interfacial contact property. Thermosetting polymer electrolytes, thermoplastic polymer electrolytes, composite polymer electrolytes and ionic liquid electrolytes belong to this category.³⁷⁻³⁹

1.2.5.3 Solid state transport materials

Quasi-solid-state electrolytes also possess certain stability issues as the electrolytes contain solvents which upon storage or air exposure solvent exudation occurs. In this context, solid state transport materials offer additional advantage over the other two categories, especially for large scale applications. Solid state transport materials includes ionic conductors, inorganic hole-transporting materials (HTM) (eg. CuI ,⁴⁰ CuSCN ,⁴¹ CsSnI_3 ⁴²) and organic HTMs (eg. poly(3-hexylthiophene) (P3HT),⁴³ poly(3-octylthiophene) (P3OT),⁴⁴ P3HT/PCBM (phenyl-C 61-butyricacid methyl ester (PCBM)),⁴⁵ poly(3,4-ethylenedioxythiophene) polystyrene sulfonate (PEDOT:PSS),⁴⁶ SpiroMeOTAD⁴⁷).

1.2.6 Counter electrodes

The function of counter electrode is to collect electrons from the external load and to reduce the redox electrolyte, it can also perform collection of holes from HTM in the case of Solid-state DSSC. Counter electrodes are generally constructed by depositing a conducting film of metal such as platinum over FTO glass. As platinum is highly

expensive, cheap organic materials such as carbon,⁴⁸ graphene,⁴⁹ PEDOT,⁵⁰ and inorganic materials like NiO,⁵¹ ZnO⁵² etc. are considered as commercial alternatives.

1.3 Working principle of DSSC

A schematic representation of working principle of DSSC is given in **Figure 1.4** The most vital part of DSSC is the dye adsorbed mesoporous metal oxide semiconductor layer. The working of DSSC commences by the photoexcitation of dye molecules, followed by the electron injection into the conduction band of the metal oxide semiconductor. Regeneration of the dye molecule is performed by the redox electrolyte, which in turn gets regenerated at the counter electrode. The maximum voltage that can be drawn is V_{oc} . It is the potential difference produced by the cell and is the measure of energy difference between the electrolyte chemical potential and the Fermi level of the semiconductor. Recombination reactions are common during the working of DSSC and therefore the recombination loss need to be subtracted from the potential difference obtained.

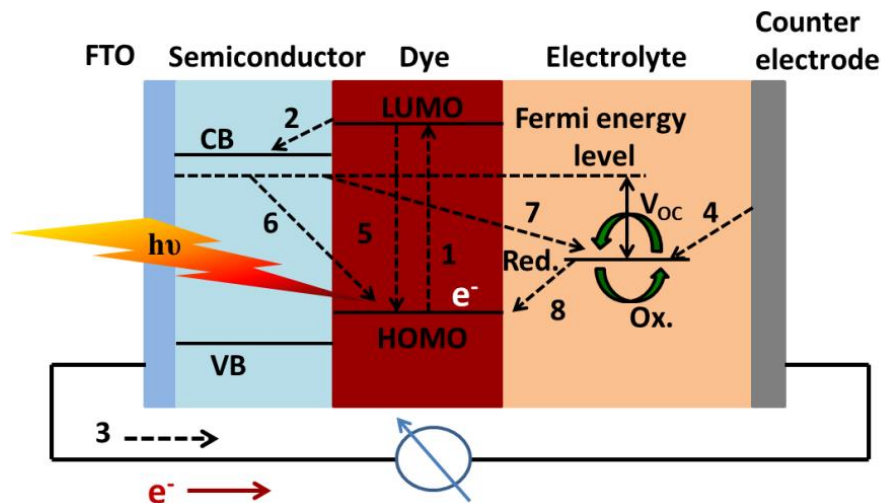


Figure 1.4 Schematic illustration of working principle of DSSC.

The different events in the photoelectrochemical processes in DSSC are described as follows^{2, 9, 25}

- i) Optical excitation of dye molecule (process 1)

Dye molecules will absorb photon of energy equal to or more than its energy gap to excite an electron from its HOMO to the LUMO.

- ii) Electron injection to the CB of the semiconductor (process 2)

The electrons in the LUMO which are loosely bound to the dye molecules will get injected to the conduction band of the semiconductor metal oxide through interfacial electron transfer. The holes generated by the optical excitation remains in the HOMO of the dye molecule. The collected electrons are then transported to the FTO or ITO glass to the counter electrode (process 3).

iii) Reduction of electrolyte at the counter electrode (process 4)

Triiodide is produced as a result of the oxidation of dye molecule. The triiodide then get reduced at the counter electrode to produce iodide and the circuit is completed by collecting the electron through external load.

iv) Regeneration of dye by electrolytic reduction (process 8)

The oxidised dye molecules after the electron injection into the CB of TiO₂ is regenerated by the electron donor in the electrolyte. The regeneration efficiency of the dye molecule is defined as the probability of an oxidised dye regenerated by an electron donor in the electrolyte, by the recombination with an electron in the semiconductor.

Electron recombination processes are commonly seen in DSSC and leads to the deterioration of the device performance. Process 5 indicates the recombination of excited photoelectron with the oxidised dye. Processes 6 and 7 show the recombination of the electrons in conduction band of the semiconductor with oxidised dyes and ions in the electrolyte respectively. Recombination electrons (back electron transfer) from the exposed surface of conductive glass to the electrolyte is also usually seen in DSSC, which will also affects the device performance adversely.

1.4 Improvements in photoanodes of DSSC

Enormous methods have been implemented to boost the performance of DSSCs by designing different types of dye molecules, semiconductors film, electrolyte and counter electrodes. As the thesis work focuses on the modification of semiconductor layer for DSSC, the following section will focus on the different approaches explored so far for the same. Major strategies to improve photoanodes of DSSC include utilisation of a variety of nano/micro structured semiconductors, composite materials, doping of semiconductors, inclusion of blocking layers, inclusion of scattering layers etc.

1.4.1 Nanostructured semiconductor metal oxides

Tailoring of nanomaterials is essential to enhance its photophysical properties which can increase the PCE in DSSC. Typical DSSC uses ~ 20 nm particle with high surface for the fabrication of photoanode. However, in nanoparticles the electron transfer progress in a random manner and encountering several defects, surface states and grain boundaries in the film.^{9, 53} This will lead to electron recombination decreasing the PCE of device. Therefore, one dimensional (1D) nanomaterials are widely exploited in DSSC due to their fast charge transport and reduced charge recombination processes. Different types of nanostructures used in DSSC are detailed in the following section. Nanostructured TiO₂ and ZnO used in DSSC are summarised in the **table 1.1**.

1.4.2 Nanorods/wires

Nanorods and nanowires are extensively used 1-D nano materials for DSSC. Rods and wires like structures possess high electrical conductivity due to their longer electron diffusion length than the nanoparticles. However, possess very less surface area, due to which the dye loading and thus the light harvesting efficiency are reduced. This has prompted researchers to improve the performance of DSSC by tuning the aspect ratio of 1D nanostructures.

Meclare *et al.* have synthesised monodisperse anatase nanorods with 13-17 nm length via a surfactant free solvothermal method. The DSSC fabricated with such nanorods has displayed a PCE of 7.5% whereas standard cell fabricated with TiO₂ P25 has shown only 5.585%.⁵⁴ Jiu *et al.* fabricated single crystalline anatase TiO₂ nanorods with lengths of 100-300 nm and 20-30 nm diameter by hydrothermal method using cetyltrimethylammonium bromide (CTAB) as surfactant. They were able to achieve a PCE of 7.29% in DSSC.⁵⁵ Wu *et al.* fabricated vertically aligned multilayer anatase nanowires of length 15-55 μm on FTO glass. DSSC fabricated with ~ 47 μm long multi layered anatase TiO₂ nanowire arrays offered a PCE of 9.4% which is very high when compared to TiO₂ P25 nanoparticles (PCE of 7.33%). These nanowire arrays possess high internal surface area and promote light scattering.⁵³ In another work, the same group has synthesised long TiO₂ nanowire trunk with numerous short TiO₂ nanorod branches on FTO glass via hydrothermal method and utilised as photoanode in DSSC. The photoelectrodes fabricated from this hierarchical architecture array of 18 μm length

showed a PCE of 7.34% owing its better specific surface area for dye loading and enhanced light scattering ability.⁵⁶ Xu *et al.* developed a synthesis for multilayer assemblies of ZnO nanowire arrays. A PCE of 7% was obtained using four layers of ZnO nanowire arrays with a total thickness of 40 μm .⁵⁷

1.4.3 Nanotubes

Nanotube arrays are intensively used in DSSCs owing to its unique morphology. Vertically grown nanotubes can adsorb dyes on its outer walls as well as inner walls and hence can provide high surface area than any other 1D nanomaterial. The first TiO_2 nanotube based DSSC was fabricated in 2005 by Schmuki *et al.* but the efficiency was found to be very poor (0.036%), which is lower than that of nanoparticle based DSSC.⁵⁸ Chen *et al.* reported synthesis of double-wall TiO_2 nanotubes (DWTNTs) by two-step anodization method. DSSC fabricated with DWTNTs on the flexible Ti substrate offered a PCE of 6.90%, where single-wall TiO_2 nanotubes (SWTNTs) showed a PCE of 4.66% by back side illumination. This increment for DWTNTs was attributed to the increase in the J_{sc} caused by the higher surface area for dye adsorption.⁵⁹ Elzarka *et al.* grown anodic TiO_2 nanotube layer with average diameter of 550 nm and length $\sim 12 \mu\text{m}$. They have decorated the tubes with TiO_2 nanoparticles to form hierarchical structures in order to increase the surface area. Thin insulating layers of SiO_2 and Al_2O_3 were used as blocking layers. The blocking layers are meant to reduce the recombination between the photogenerated electrons and oxidised species in the electrolyte. The fabricated DSSC under back side illumination has shown a PCE of 2.7% for the bare tubes, 5.8% for the hierarchical structures, 6.3% and 6.7% for blocking layer deposited ones.⁶⁰ As TiO_2 nanotubes are usually grown on Ti metal substrates, due to the opacity of the substrate, the efficiency measurements are done by back side illumination (counter electrode side). To tackle this issue researchers have developed a method to deposit the TiO_2 nanotubes on FTO glass with the aid of TiO_2 nanoparticles. Lamberti *et al.* have attempted a similar method and obtained a PCE of 6.26 % which is further increased to 7.56% by TiCl_4 treatment with front side illumination.⁶¹ Wang *et al.* have also fabricated DSSC with TiO_2 nanotube arrays of 33 μm length utilising a similar deposition strategy. They were able to realize a PCE of 9.02%. The arrays were treated with TiO_2 sol to deposit TiO_2 nanoparticles with ~ 20 nm size and the PCE was found to be increased to 9.86%.^{62, 63}

1.4.4 Hierarchical structures

Hierarchical structures have gained much attention in the field of photovoltaics due to their superior properties like high surface area, higher diffusion of electrolyte, light scattering effect etc. Hierarchical spheres, beads and aggregates of TiO₂ and ZnO are utilised in the fabrication of photoanodes in DSSC as these materials are porous in nature with high surface area. Sauvage *et al.* synthesised TiO₂ mesoporous beads and applied as photoanode in DSSC. The synthesised beads possess surface area of 89 m²/g and an average pore size of 23 nm due to which the dye absorption as well as light scattering properties were enhanced compared to P25 particles. A PCE of 10.6% was achieved in TiO₂ bead based DSSC whereas, P25 delivered only 8.5%.⁶⁴ Zhang *et al.* synthesised ZnO hierarchical spheres with diameters of 100 and 500 nm (which are aggregates of ZnO nano particles having ~ 15 nm) sizes to act as effective light scattering points. The maximum PCE obtained was 5.4% and was much more than that obtained for ZnO nano particles (2.4%).⁶⁵ Hollow spheres with single and multi-shells were developed for DSSC by Hwang *et al.*. These materials provided high surface area, easy electron transport and better light scattering as the incident light get reflected by the shells present in the material. For optimised multi shelled TiO₂ hollow nano particle based DSSC, a PCE of 9.4% was obtained. On the other hand single shell counterpart offered only 8%.⁶⁶ Attafi *et al.* reported hierarchically structured TiO₂ aggregates via one step solvothermal method. The synthesised structures were of 700 nm and 300 nm in diameter and was composed of 8.5 and 105 nm TiO₂ crystals, with surface area of 138 and 106 m²/g respectively. Due to the larger sizes they imparted good light scattering effects. The device fabricated with these structures delivered a PCE of 9.1% and 8.2% compared to the standard cell efficiency of 7.4%.⁶⁷

Table 1.1 Efficiency improvements in DSSC by nanoarchitectures

Control sample	Material used for improvement	η of control sample (%)	η of modified sample (%)	Reference
TiO ₂ nanoparticles	TiO ₂ nanotubes & nanoparticles	3.84	8.80	68

TiO ₂ nanoparticles	TiO ₂ nanotubes	3.66	5.61	69
TiO ₂ nanotubes	TiO ₂ nanotubes with TiO ₂ nanoparticles	4.76	9.86	63
P25	TiO ₂ nanorods	6.59	7.91	70
P25	TiO ₂ nanowires	7.23	9.40	53
-	ZnO caterpillar-like nanowires	-	5.20	71
Short ZnO nanowires	Long ZnO nanowires	2.1	7.0	57
ZnO nanoparticles	ZnO hierarchical film	6.58	7.5	34
P25	TiO ₂ hierarchical beads	7.1	10.6	64
P25	TiO ₂ hierarchical spheres	6.49	10.57	72
TiO ₂ nanoparticles	Hierarchical TiO ₂ nanofibers	4.98	7.86	73

1.4.5 Composites

In order to improve the features of the photoanode, the semiconductors are mixed with second phase inclusions like graphene, carbon nanotubes, metals like Au and Ag, metal oxide like SnO₂ etc.⁹ Carbon based materials like carbon nanotubes and graphene are generally used in DSSC owing to their excellent attributes like electron mobility, high surface area and mechanical properties.

Graphene can reduce the charge recombination and resistance at electrolyte-photoanode interface and can also improve the electron transport through the semi conducting film to FTO substrate. Graphene is found to be a better candidate than carbon nanotubes in DSSC because of its 2D structure. TiO₂ can be easily anchored to the 2D bridge of

graphene and photogenerated electrons can be transported by graphene. In the case of 1D carbon nanotube composites, the intermolecular forces are less so that the contact between TiO₂ and the carbon nanotube results in large barrier for electron transfer leading to recombinations.⁷⁴ The quantity of the graphene and carbon nanotubes incorporated in the photoanode film should be carefully tuned as higher amounts of such inclusions will reduce the visible light required for the dye absorption. The number of photogenerated electrons are reduced and hence the device performance will also be lowered.⁹

Au and Ag are used in photoanodes of DSSC due to their property of plasmon resonance effect.^{75, 76} Plasmon resonance can improve the spectral absorption and therefore mixing/decorating TiO₂ with Au or Ag in DSSC will increase the photocurrent of the device. Additionally, Au and Ag can improve the charge transfer processes in DSSCs, and reduce the electron recombination by increasing the energy levels of TiO₂. Li *et al.* decorated TiO₂ with 2 nm-sized Au nanoparticles and utilised as photoanode for DSSC. The local-field optical enhancement at the TiO₂ surface triggered by plasma resonance of Au nanoparticles increased the dye absorption and hence the photocurrent of the device was increased. A PCE of 10.1% was achieved which is very high, compared to device with pure TiO₂ photoanode (5.5%)⁷⁷

Inclusion of other metal oxides into TiO₂ or ZnO is another strategy to enhance the device performance. Generally metal oxides with low dimensional structures are used so as to provide straight electron transfer to reduce the recombination.⁷⁸ For example, ZnO nanowires were grown within TiO₂ nanoparticle film, to increase the light scattering and reduce the resistance of the photoanode.⁷⁹ TiO₂ nanofibers were incorporated within ZnO film by Li *et al.*, the J_{sc} of the device was found to increase than that of pure ZnO based device.⁸⁰ Bilayer photoanode with SnO₂ nanoparticle bottom layer and ZnO nanorod as overlayer were fabricated by Huu *et al.* and achieved considerable enhancement of electron transport and lifetime of the device compared to those with bare SnO₂ film.⁸¹

1.4.6 Doping

Doping is done in a semiconductor oxide of photoanodes in DSSC in order to improve the device performance. Oxygen deficiency present in the semiconductor can generate

electron hole pair in DSSC. It can react with dye molecules resulting in the destruction of the dye or it can be surrounded by the ions present in the electrolyte which in turn decrease the life time of the device.⁸² Nitrogen doping is a widely pursued method in which nitrogen atom can replace the oxygen deficiency in the TiO₂ and convert it into visible light active TiO₂.⁸³ Guo *et al.* doped nitrogen in TiO₂ by using different nitrogen precursors such as ammonia, urea and triethyl amine through wet chemical method. The N doped electrodes offered a PCE of 8.3% where as standard P25 offered 5.76% and pure anatase TiO₂ gave 7.14%. They have also suggested that nitrogen doped from ammonia is the most efficient one than the other two precursors. An improved photocurrent of ~ 36% is observed for N doped systems due to the combined effects high dye loading and better electron transport.⁸⁴ Mahamood *et al.* fabricated up right standing boron doped ZnO porous nanosheets and applied as photoanode in DSSC. The incident to photon current conversion efficiency (IPCE) values of boron doped zinc oxide showed remarkable improvement in light harvesting particularly in the visible region. The highest PCE of 6.75% is achieved by using the vertically grown boron doped zinc oxide nanosheets.⁸⁵

Metals are also recognised to be effective candidate for doping. Transition metals and rare earth metals are used for this purpose. Transition metals used in DSSC include Cr,⁸⁶ Mg,⁸⁷ W,⁸⁸ Nb,⁸⁹ Sn,^{90, 91} Ta,⁹² Zn⁹³, Ni⁹⁴ and that of rare earth metals include Y, Eu, Tm and Yb.⁹ Durrant *et al.* synthesised mixed oxides by doping Zr in TiO₂ by thermal hydrolysis method. The band gap of the mixed oxide was found to be increased by 0.2 eV and the shift in the CB band resulted in high V_{oc} . Undoped TiO₂ offered a PCE of 7% where as the best device with doped TiO₂ showed a PCE of 8.1%.⁹⁵ Duan *et al.* studied the effect of Sn doping in TiO₂ film for DSSC. The highest PCE displayed was 8.3% with 0.5 mol% Sn doped TiO₂. The V_{oc} and J_{sc} of the device is improved due to the negative shift in the flat band and fast electron transport respectively.⁹⁰

1.4.7 Light scattering layer

Inclusion of light scattering layer is a widely accepted method in DSSC to enhance light scattering inside the device. Owing to the transparency of the nanoparticles in the photoanode most of the incident light will pass through it reducing the amount of

photons for the dye molecule for absorption. In order to tackle this issue, scattering layers employing submicron particles are used in DSSC. These particles scatter the incident light and reflect back into the active layer so that the average path length of light is increased, enhancing the probability of it being absorbed by the dye molecules and increasing the performance of the device.^{96, 97}

1.4.7.1 Theories of light scattering

When light is incident on an object, it can propagate either in forward direction or in backward direction. Propagation of light in forward direction is termed as refraction and absorption, and in backward direction is called as reflection. But when the size of the object is comparable to the wavelength of incident light, the incident light can reflect in all directions and this phenomenon is called as light scattering. The two major theories proposed for light scattering for spherical particles are Rayleigh scattering theory and Mie scattering theory. These theories rely upon the size of the scatters and the wavelength of the incident light. Rayleigh scattering theory is applied to non-absorbing spherical particles with small size. The condition for Rayleigh scattering are $\alpha \ll 1$ and $|m| \alpha \ll 1$, Where $\alpha = 2\pi r/\lambda$, r is the radius of the particle, λ is the wavelength of the incident light, m is the refractive index of the particle. According to this condition Rayleigh theory is applicable for the particle which possess dimensions smaller than the incident wavelength.

The other type of scattering is Mie scattering and it can be applied to the spherical particles that are absorbing or non-absorbing. The effective scattering occurs when the size of the particle are comparable to the wavelength of the incident light. Mie scattering efficiency is calculated by the expression

$$Q_{scat,Mie} = \frac{\sigma_{scat,Mie}}{\pi r^2} \quad (2)$$

Where σ_{scat} is the cross section of Mie scattering. With the above mentioned equation one can calculate the efficiency of Mie scattering from the particle size and incident wavelength. For example, a particle with size 200 nm can scatter the incident light in 400-650 nm wavelength range. This fact gives a rough idea regarding the particle size

need to be used for the fabrication of effective light scattering layer aimed to enhance the optical absorption in DSSC. It should be noted that in DSSC, due to the presence of electrolyte, change in refractive index with respect to air is expected resulting in a shift for the effective range of the particle sizes.^{96, 97}

Generally in DSSC light scattering is achieved by two methods: fabricating a double layer/bilayer structured photoanode and mixture structured photoanode (**Figure 1.5**). The double layer structured photoanode consists of a top layer made up of submicron sized particles to offer light scattering over a layer of nanocrystalline particle. Mixture structure photoanode comprises of a single layer with larger particles as well as nanoparticles mixed together. Nanoparticles used in both cases are of size ~ 20 nm to offer sufficient dye loading and larger particles are of sizes ranging from 200-500 nm to impart light scattering. Both designs possess certain drawbacks. The larger particles incorporated in both structure will reduce the internal surface area of the photoanode thereby reducing the dye adsorption. This will adversely affect the optical absorption and thus the current density of the device. In the case of double layer structured photoanode, the internal resistance of the device is increased which obstructs the charge transport of the device.

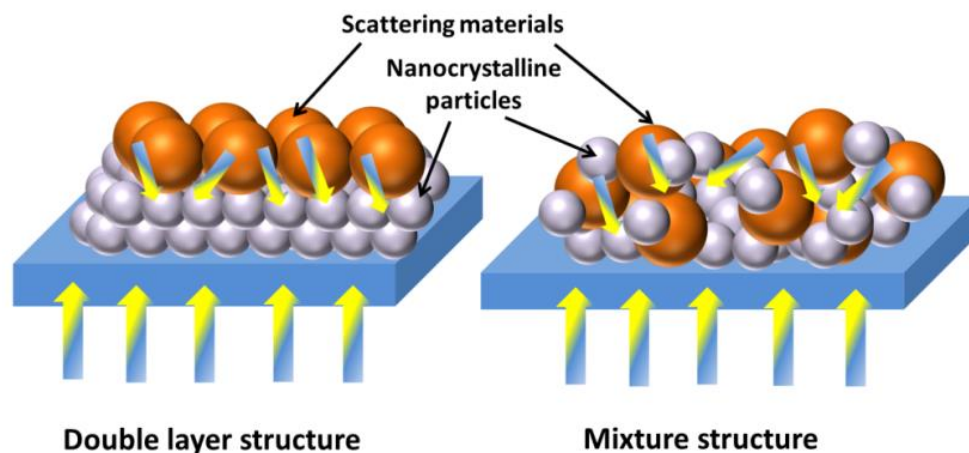


Figure 1.5 Double layer and mixture structure of light scattering materials used in DSSC.

It is inferred that the surface roughness can also induce the light scattering effects. In a study done by Yang *et al.* rough TiO₂ spheres with ~275 nm diameter had shown more diffuse reflectance than a film with smooth TiO₂ spheres. Nevertheless, the effect of rough surface on light scattering still remains unclear. Theoretical studies showed that light scattering due to surface roughness depends upon multiple factors like, particle size, particle surface structure, wavelength of incident light etc. Besides the improvement in light scattering, an added advantage is that rougher surface can enhance the dye loading compared to smoother surface.^{98,99}

Theoretical works done for the optimisation of DSSC structure with light scattering layers are also available. Ferber *et al.* investigated the size and concentration of the particles required for the effective light scattering in DSSC through computer simulations.¹⁰⁰ Akira usami *et al.* theoretically studied about the multilayer scattering happening in DSSC by Monte carlo simulations.¹⁰¹

Several morphologies have been investigated to encourage light scattering in DSSC. It includes nanorods, submicroprisms, nanospindles, nanoplates, nanofibres, nano belt, spheres etc.⁹⁷ Huang *et al.* synthesised ~830 nm mesoporous TiO₂ beads and employed as scattering layer on the top of the nanocrystalline TiO₂ film. Here, the mesoporous TiO₂ beads provided high surface area ~ 89 m²/g for good dye loading and also sufficient light scattering. A PCE of 8.84% was achieved with this structure compared to PCE of 7.87% in the device with scattering layer of 400 nm particle.¹⁰² Wang *et al.* studied the effect of light scattering in different categories of photoanodes (monolayer, bilayer and multilayer) by utilising various size of TiO₂ nanoparticles (23, 50 and 100 nm). When 23 nm sized particle was mixed with 100 nm TiO₂ particle a PCE of 8.4% was obtained while the photoanode prepared with ~ 23 nm particles yielded a PCE of 7.6%.¹⁰³ Guo *et al.* synthesised 1D hierarchical TiO₂ sub micron rods and mixed with P25 nanoparticles. The composite photoanode offered a PCE of 8.09% whereas the standard P25 nanoparticle based DSSC delivered only 5.37%. The increment in PCE is ascribed to the multifunctions imparted by TiO₂ sub micron rods; such as high specific surface area, high light scattering and improved electron transport.¹⁰⁴ Mahmood *et al.* fabricated a double layered boron doped ZnO (DL-BZO) light scattering layer, the top layer is made up of

submicrometer-sized boron-doped ZnO (BZO) sphere arrays and the DSSC thus fabricated exhibited a PCE of 7.2%. The top layer was able to provide fast electron transport as well as light scattering effects. This PCE was much higher than the double layered undoped ZnO (4.1%) and was found to be even better than 2.1% obtained for the monolayer BZO films.¹⁰⁵

Hybrid composites of ZnO nanoparticles and submicron sized SiO₂ nano spheres were employed in DSSC by Banik *et al.* They varied the SiO₂ content with respect to ZnO nanoparticles. 1 wt.% composite of silica yielded high PCE (3.08%) compared to pure ZnO nanoparticle based photoanode (2.53%). SiO₂ nanospheres helped to reduce the back electron transfer at photoanode/electrolyte interface, improving the efficiency of the device.¹⁰⁶

Core shell particles are also used to improve the light scattering in DSSC. Son *et al.* synthesised SiO₂/TiO₂ core shell nanoparticles with different diameters (110, 240 and 530 nm) to study the effect of size, refractive index and light scattering in DSSC. It was observed that SiO₂/TiO₂ core shell delivered the highest PCE compared to that employing SiO₂ (6.8%) or TiO₂ (7.4%). The highest PCE obtained for core/shell particles is 7.9%.¹⁰⁷

Inclusion of spherical voids/rough surface in photoanode is also identified to be good light scatters. Pu *et al.* treated TiO₂ photoanodes with laser to introduce pore and cracks over the film. After the laser treatment, the photoanodes become less transparent indicating the high light scattering owing to the rougher surface. The PCE is increased by 4.49% to 5.59% for cells with and without laser irradiation respectively.¹⁰⁸ In another paper, the same group has also investigated the effect of laser power density on the phase transition of TiO₂ photoanode. As the laser power density increases the anatase TiO₂ is transformed to rutile TiO₂ after the laser treatment and it is also noticed that the quantity of rutile phase increases with laser power density. The photovoltaic performance for the devices is also detailed and suggested that the enhancement in efficiency of the device is mainly due to the increase in the short circuit current density.¹⁰⁹

Yang *et al.* prepared photoanodes from composites of TiO₂ and carbon spheres with different sizes. The voids left after annealing act as light scatters in the photoanode. The device with photoanode fabricated from the composite of 500 nm carbon spheres (15 wt. % of TiO₂ nanoparticles) showcased the best performance of 7.2% while DSSCs fabricated with pure TiO₂ is observed to be 5.5%.¹¹⁰ Hore *et al.* documented the incorporation of spherical voids as scattering centres in TiO₂ film by employing carboxyl stabilised polystyrene spheres anchored onto the TiO₂ surface. These scattering voids increased the current density as well as fill factor, leading to an overall improvement in PCE by 25% under one sun condition.¹¹¹

Quasi-inverse opal (QIO) layers with imperfect periodicity of voids were investigated as scattering layers in DSSC by Han *et al.*. Anatase nanocrystals synthesised via sol gel method were mixed with aqueous solution containing monodisperse carboxylated polystyrene (PS) particles (420 nm and 970 nm) for the fabrication of QIO layer. These highly porous layers exhibited superior dye loading and effective light scattering. It was observed that the photocurrent of DSSC based on the 420 nm-QIO layer was significantly improved, offering a PCE of 5.7%.¹¹²

1.4.8 Interfacial engineering

Back electron (electron recombination) reactions in DSSC play significant role in reducing the PCE of DSSCs. These reactions occur primarily at the FTO/electrolyte interface and the mesoporous semiconductor/electrolyte interface. This in turn reduces the open circuit voltage and current density of DSSC. Interfacial engineering at FTO/mesoporous semiconductor layer is therefore a widely accepted method to tackle this issue. This is usually achieved by depositing a thin compact layer of TiO₂/ZnO over the FTO glass substrate which is termed as pre-blocking layer (**figure 1.6a**). Pre-blocking layer helps to reduce the exposure of bare FTO surface which is uncovered by mesoporous semiconductor layer, and minimizes the contact of electrolyte with the surface of FTO.^{113, 114} Post-blocking layer deposition is another strategy to passivate the recombination at mesoporous semiconductor/electrolyte interface (**figure 1.6b**). Here, an extra thin layer of TiO₂ is deposited by soaking it into moderate concentration (~ 40

mM) of TiCl_4 solution at $70\text{ }^\circ\text{C}$ which is then subjected to annealing to obtain the TiO_2 deposited mesoporous semiconductor film. Many reasons are suggested to explain the effect of post TiCl_4 treatment which includes, increased charge transport, improved surface area of the mesoporous film and increased light scattering effects.^{9, 115, 116} Therefore the enhancement of efficiency of DSSC due to TiCl_4 treatment is still under discussion. Apart from these, coatings of insulating materials like Al_2O_3 ,¹¹⁷ ZrO_2 ,¹¹⁸ Ga_2O_3 ,¹¹⁹ SiO_2 ¹²⁰ over semiconductor are also attempted to create a barrier for electron recombination.¹²¹

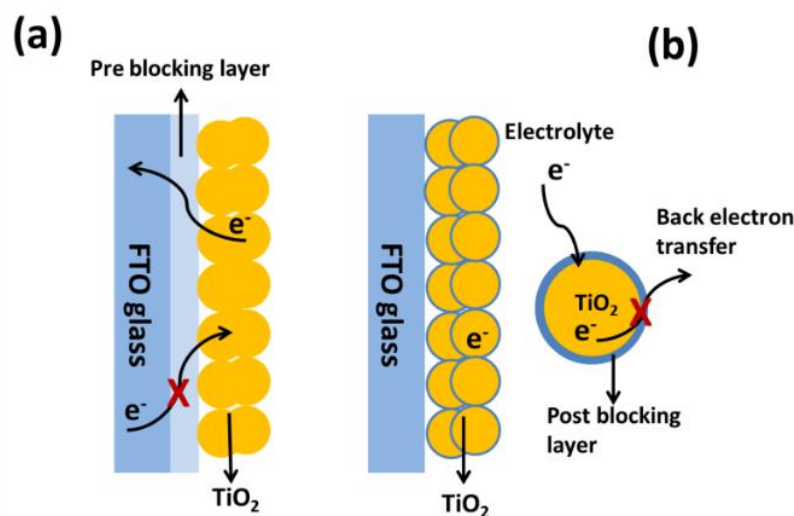


Figure 1.6 (a) Mechanism of pre-blocking layer on FTO glass in DSSC (b) post-blocking layer on TiO_2 particles in DSSC.

1.4.8.1 Pre-blocking layer

Several methods are attempted to fabricate compact TiO_2/ZnO blocking layers, which include spray pyrolysis,¹²² spin coating,¹²³ sputtering,¹²⁴ atomic layer deposition (ALD),¹²⁵ electrochemical deposition,¹²⁶ sol-gel method¹²⁷ etc. Kavan *et al.* fabricated compact TiO_2 layers on FTO by thermal oxidation, electrochemical deposition, spray pyrolysis and atomic layer deposition. All these methods allowed the fabrication of <0.1% pin hole free blocking layers with better blocking effect. The methods of ALD and electro deposition are found to be good for the fabrication of the compact TiO_2 layer, but the blocking effect is decreased after annealing at $500\text{ }^\circ\text{C}$ and hence these methods are

suggested only for the photoanodes where post calcination is not required. Even though blocking behavior of spray pyrolysed films were found to be less good, they were less sensitive towards calcination. The thermally oxidised Ti displayed good blocking effect as well as good stability towards calcination. But these films are not transparent and therefore cannot be utilised in DSSC where optical transparency of cathode is required.¹²⁶ Goes *et al.* studied the effect of dense TiO₂ layer between FTO and mesoporous TiO₂ layer. Approximately 25% improvement in PCE is obtained with respect to standard cell devoid of these layers. This is due to decrease in electron-hole recombination at FTO/electrolyte interface and improvements in electronic contact between mesoporous TiO₂ and FTO.¹²⁸ Gurupreet sikh *et al.* investigated the photovoltaic properties of DSSCs as a function of the thickness of BL in two morphologically diverse ZnO active layers of hierarchically self-assembled nanoparticles and microcubes. The BLs were deposited through spray pyrolysis method. The studies suggested that regardless of the morphology of the active layer, deposition of the BL leads to significant increase in the current density. They were able to fabricate solar cells with PCE of 5.6%, incorporating a BL thickness of 800 nm in ZnO nanoparticle based DSSC. A PCE of 2.6% was found for such devices without BL. In the case of ZnO microcube based DSSC the efficiency was found to be increased from 2.7% to 3.8% with the deposition of BL.¹²⁹ Yeoh *et al.* had investigated the effect of ZnO and TiO₂ blocking layers in TiO₂ based DSSCs. ZnO and TiO₂ were synthesised via sol gel method and deposited by spin coating technique over the FTO glass. By the deposition of 120 nm thick ZnO blocking layer, the PCE was found to be improved from 3.86% to 4.34% which was even enhanced to 4.36% by the replacement of ZnO with TiO₂ blocking layers.¹²³

1.4.8.2 Post-blocking layer

Sang *et al.* studied the effect of TiCl₄ treatment on TiO₂ film with concentration ranging from 5 to 500 mM on the film topology, charge carrier dynamics and photovoltaic performance in DSSC. The surface area of the TiO₂ film is observed to increase when the concentration of TiCl₄ solution is in the range of 15 to 50 mM, resulting in improved light harvesting and PCE. At higher TiO₂ concentrations (500mM) the light scattering is increased but the pore size of the film is decreased resulting in slower electron transport

as well as reduced device performance.¹¹⁶ Sommeling *et al.* studied the effect of post TiCl_4 treatment on TiO_2 films in DSSC. Their results suggested that the increased photo current in DSSC is due to the downward shift in the band edge of TiO_2 which consequently leads to large quantum efficiency of electron injection.¹¹⁵

1.5 Indoor light Dye-sensitised solar cells

The capability of DSSC to harvest energy in low light/diffused light is well known since it was invented. An efficiency of 12% in diffused light condition was already demonstrated by Gratzel *et al.* in a seminal report.¹⁴ Researchers didn't find any interest to explore the low light capabilities of DSSC, for want of enough applications. In recent years energy harvesting under indoor conditions or diffused light conditions has attracted substantial attention due to the unique requirements of the Internet of Things (IoT). Focusing on indoor light harvesting Hagfeldt *et al.* judiciously designed sensitizers D35 and XY1 with Cu redox shuttle and achieved remarkable efficiency of 28.9% at 1000 lux under warm white florescent tube. In the study they compared DSSC with GaAs solar cells and DSSC outperformed GaAs in indoor light conditions.¹⁵ The same year Chen-Yu Yeh *et al.* reported an efficiency of 28.56% at 6000 lux (under CFL) using TY6 dye along with Iodine electrolyte.¹³⁰ In yet another breakthrough, Gratzel *et al.* reported the record efficiency of 32% under fluorescent tube at 1000 lux utilising mesoporous TiO_2 electrode and the poly(3,4- ethylenedioxythiophene)(PEDOT) counter electrode were directly sandwiched without any spacer.¹³¹

Light emitting diodes (LED), compact fluorescence lights (CFL) are commonly used light sources to study the performance of DSSC under indoor light conditions. Change in the source light means, change in intensity of light as well as the spectra of the incident light. The emission spectrum of LED and CFL lies within 400 to 800 nm wavelength region where as AM 1.5G lies at 400 nm to 2000 nm.¹³² **Figure 1.7** shows the emission spectra of LED and CFL. Efficient light harvesting occurs when absorption spectra of solar cell matches with the emission spectra of the light source. The efficiencies of dye-sensitised cells (DSC, as it does not involves sun light intensity) under indoor light sources are recongnised to be very high when compared to one Sun conditions. The reason behind is still not known clearly. One of the suggested reasons for this is the spectral over lap of the absorption spectra of dyes with the emission spectra of the CFL/LED lamps as the

absorption of dye molecule lies between 400 nm to 700 nm. This superior spectral overlap is believed to afford a good light-harvesting property and enhanced device performance under low light environments.¹³⁰

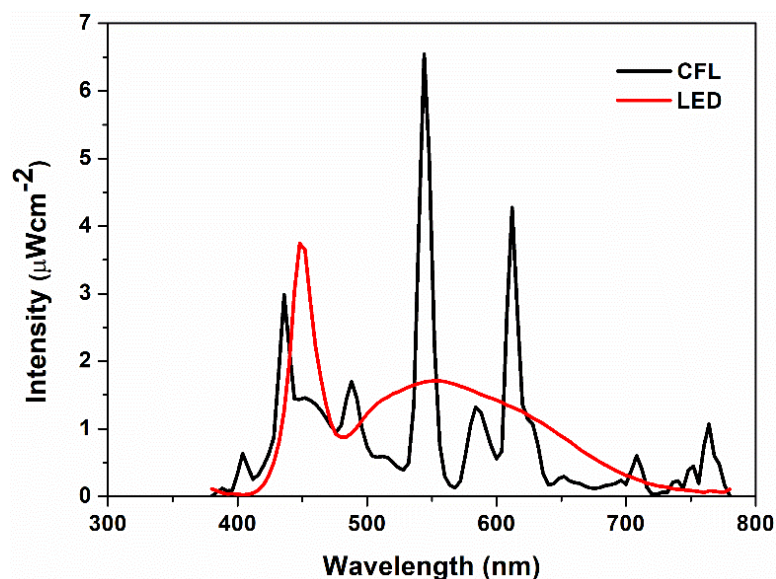


Figure 1.7 Emission spectra of LED and CFL

1.6 Zinc Oxide

Zinc oxide (ZnO) is a well-recognised material with enormous applications because of its unique physical and chemical properties. ZnO is categorised as a group II-VI semiconductor whose ionicity lies between the covalent and the ionic semiconductor.¹³⁴ It has a wide band gap of 3.3 eV, high exciton binding energy of 60 meV and possess high thermal and mechanical stability.^{27, 135} Even though ZnO is extensively studied for a variety of applications, it still continues to receive a great deal of interest in many fields like optoelectronics (photodetectors,¹³⁶ solar cells,¹⁷ light emitting diode¹³⁷), sensors,^{138, 139} catalysis¹⁴⁰ and biomedical fields.¹⁴¹ ZnO is also considered as a versatile material due to the ease of synthesis of nano/micro structures having diverse morphologies and sizes. 1D structures of rods, wires, tubes, needles, helices, ribbon, rings etc., 2D structures of plates, sheets, pellets etc. and 3D structures like flowers, urchins, snowflakes, dandelions etc.¹³⁵

1.6.1 Crystal structure of ZnO

ZnO crystallises in three forms, Wurtzite (hexagonal), Zinc blende (cubic) and Rock salt (cubic) as shown in **Figure 1.8**. Out of these the ambient and thermodynamically stable form is wurtzite. Wurtzite structure possess hexagonal unit cell with lattice Parameters

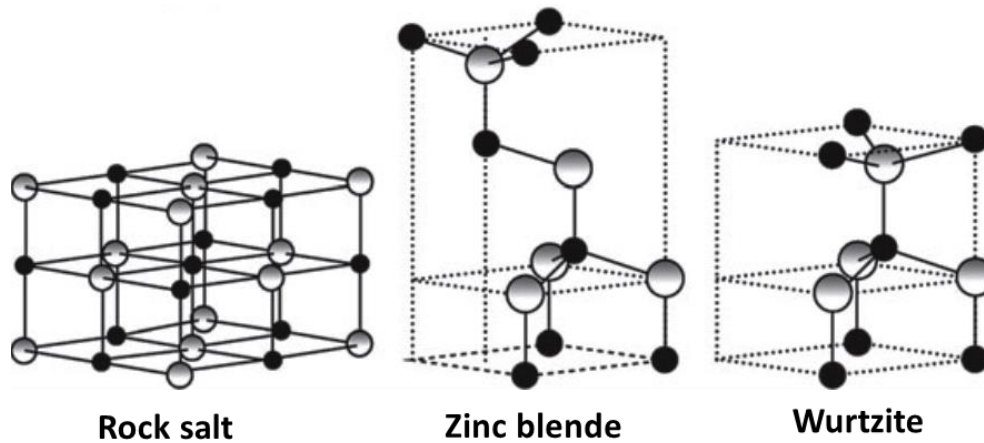


Figure 1.8 ZnO crystal structures: Rock salt (cubic), Zinc blende (cubic) and Wurtzite (hexagonal). Gray and black spheres denote Zn and O atoms, respectively.¹³⁴

of $a=0.325$ nm and $c= 0.521$ nm. The structure consists of alternating planes with tetrahedrally coordinated O^{2-} and Zn^{2+} ions packed alternatively along c axis resulting in a non centrosymmetric structure. Another significant characteristic of ZnO is its polar surfaces. The most common polar surface is the basal plane (0001) and this plane is responsible for the 1D growth of ZnO along [0001] direction.

The positively charged Zn (0001) and negatively charged oxygen (000 $\bar{1}$) surface results in a dipole moment and spontaneous polarization along the c axis. The versatility of ZnO in generating wide range of exotic structures with fascinating properties is ascribed to its growth along the directions (0001), (0 $\bar{1}$ 10) and (2 $\bar{1}$ 10) along with polar surfaces (0001). Among these the most common and fastest growth direction is [0001].^{134, 142}

Physical properties of ZnO are summarised in the **table1.2** given below.

Table 1.2 Properties of ZnO

Chemical formula	ZnO
Molar mass	81.38 g/mol
Density	5.1 g/cm ³
Stable phase at 300 K	Wurtzite (Hexagonal)
Lattice parameter	a = 0.325 nm, c = 0.521nm
Space group	P6 ₃ mc or C _{6v} ⁴
Density	5.1 g/cm ³
Band gap	3.3 eV (direct)
Refractive index	2.013, 2.029
Exciton binding energy	60 meV
Static dielectric constant	8.656
Thermal conductivity	0.6, 1-1.2 Wm ⁻¹ K ⁻¹
Heat capacity, Cp	9.6 cal mol ⁻¹ K ⁻¹

The properties of ZnO and some of the related applications is discussed in the following sections

i) Wide and direct band gap material

Being a wide band gap (3.3 eV) material ZnO exhibits UV light absorption in the wavelength region of 200-350 nm and emission in UV and visible region from 500-600 nm.²⁷ This qualifies it as a suitable material of optoelectronic devices like light emitting diode (LED), photodetector, laser light etc.¹⁴³ ZnO is also used as a potential candidate in

solar cells due its favourable band gap and conduction band edge position. Doping is done usually to tune the band gap of ZnO and this has helped to improve the performance of ZnO in various fields like photocatalysis, solar cells etc.^{17, 140} It possess high bulk electron mobility, one order magnitude greater than anatase TiO₂ due to which it is widely employed for solar cell applications.

ii) Electrical properties

ZnO is an intrinsic n-type semiconductor due to the presence of native defects such as O vacancies and Zn interstitials.¹⁴⁴ It possess high bulk electron mobility, one order magnitude greater than anatase TiO₂ due to which it is widely employed for solar cell applications.¹⁷

iii) Richest in morphologies

ZnO offers a wide variety of morphologies which can be generated through simple synthetic strategies due to its polar surfaces and anisotropic crystal structure. By careful tuning of synthesis parameters various kinds of morphology ranging from macron to nano size can be produced. This includes 1D, 2D and 3D materials. 1D materials receive special attention due to its unique electrical property than the bulk counterparts.²⁷

iv) Piezoelectric and pyroelectric property

The lack of centre of symmetry and anisotropic crystalline nature of wurtzite ZnO contributes to the piezo and pyro-electricity properties. With the application of mechanical stress or temperature, the tetrahedral structure gets deformed leading to the separation of positive and negative charges inducing a dipole moment. And this property can be utilised for device applications such as transducers and sensors.^{27, 145, 146}

v) Photoluminescence property

The photoluminescence property of ZnO is attributed to the crystallite size, defects in the crystal, and temperature.¹⁴⁷ The Zn vacancies present in the crystal act as acceptors and leads to n-type conductivity. ZnO thus finds use in field emission display (FED).¹⁴⁸It

shows strong luminescence in green-white region of the electromagnetic spectrum and are hence used for phosphor applications.¹⁴⁹

vi) Photo catalytic property

ZnO is recognised as a UV active photocatalyst. Upon irradiation of light, electron-hole pairs are generated and which reacts with atmospheric moisture to produce strong reactive oxygen species like peroxide, superoxide and hydroxyl free radicals. These radicals are strong enough to degrade the organic pollutants present in the waste water. Even though ZnO is not found as efficient as TiO₂, its photocatalytic activity can be improved by making it visible light active through the incorporation of other components.¹⁴⁰

vii) Biomedical applications

Owing to the ability of ZnO to absorb UV radiation, it is used in sun creams. It is used in several medicines due to its disinfecting as well as antibacterial property.^{135, 141}

viii) Thermal conductivity

Thermal conductivity is an important property of a semiconductor when it comes to high temperature application. ZnO has very high thermal conductivity and is therefore used as a filler in rubber to improve the thermal conductivity. Even the addition of a small amount of nano filler can impart high thermal conductivity.¹⁵⁰

1.6.2 Synthesis of ZnO

Various strategies are attempted to synthesis diverse variety of ZnO structures. The synthesis techniques used for ZnO can be categorised into two; solution phase growth process and vapor phase growth process. Solution phase growth process includes precipitation method, hydrothermal synthesis, sol gel synthesis etc. and vapour phase growth process includes chemical vapour deposition, thermal evaporation, pulse laser deposition etc.

1.6.2.1 Solution phase growth methods

1.6.2.1.1 Precipitation method

Precipitation is a commonly used method to synthesise ZnO, which involves reduction of zinc salt by a reducing agent followed by thermal treatment. The morphology and size of the particles is controlled by parameters such as concentration of the precursor, pH, temperature and reaction time. During the reaction, the product get supersaturated, the nucleation starts and the particles grows into various structures depending upon reaction conditions. Li *et al.* synthesised micron sized ZnO of different morphologies (nuts, rods and rice grains) using $\text{Zn}(\text{NO}_3)_2 \cdot 6\text{H}_2\text{O}$, NaOH in sodium dodecyl sulfate and triethanolamine as surfactant.¹⁵¹ Lanje *et al.* precipitated ZnO of size ~40 nm using $\text{Zn}(\text{NO}_3)_2 \cdot 6\text{H}_2\text{O}$ and NaOH as precursors. This simple cost effective method yielded good amount of product and hence can hence be used for large scale production of ZnO.¹⁵² Wang *et al.* synthesised ~50 nm sized particles from zinc chloride and ammonium carbonate solution using CTAB as surfactant. The products formed were crystalline wurtzite ZnO.¹⁵³

1.6.2.1.2 Sol-gel method

Sol-gel method is a very simple and cost effective method to generate products with high crystallinity and uniform size. The sol-gel process involves the conversion of a precursor solution into an inorganic solid by hydrolysis followed by condensation reaction. The colloidal suspension that obtained by hydrolysis is termed as sol, which is then condensed to form gel which is particles are aggregated. The calcination of gel will give the final product. This method offer particles with nano size. Benhebal *et al.* synthesised ZnO by sol-gel method from zinc acetate dehydrate and oxalic acid in ethanol medium. The synthesised product has a hexagonal wurtzite structure with spherical morphology and surface area of $10 \text{ m}^2/\text{g}$.¹⁵⁴ Ristić *et al.* reported sol-gel synthesis of ZnO nanoparticles by adding tetramethylammonium hydroxide to zinc 2-ethylhexanoate in propanol which results in the formation of particles with 20-50 nm size.¹⁵⁵

1.6.2.1.3 Solvothermal and Hydrothermal synthesis

As the name says, hydrothermal synthesis indicates the reaction done using water as solvent under temperature. The reaction is run usually in an autoclave where the reaction mixture is heated to a temperature range of 100-300 °C. Due to heating and cooling crystal nuclei are generated which grow into nanoparticle. By this method one can achieve narrow particle size distributions. Here, wide range of chemical compositions can be tried with the expense of lower energy for a shorter time through a single step process. One can attain variety of morphologies by this method by careful tuning of the reaction compositions, temperature and pressure. The products obtained are observed to be highly crystalline and phase pure. Solvothermal synthesis makes use of solvents other than water.

Chen *et al.* demonstrated the synthesis of aligned ZnO micro or nano tube arrays on zinc foil by simple hydrothermal method. These micro or nanotubes possessed diameters in the range of 100–700 nm. Using zinc acetate and equal amount of hexamethylenetetramine (HMT) in water as precursors and ammonia was added into the above solution. When zinc acetate was used as precursor flower-like ZnO as formed on the zinc foil. Each flower had the diameter of around 1 µm and was composed of numerous small ZnO nanowires.¹⁵⁶ Ying Zhou *et al.* synthesised ZnO nano rod arrays on glass substrates coated with ZnO seed layer via hydrothermal technique in the presence of polyethylene imine (PEI). The zinc nitrate hexahydrate and HMTA was used to grow nanorods.¹⁵⁶

1.6.2.1.4 Chemical bath deposition(CBD)

Chemical bath deposition (CBD) is a synthesis method that can be employed for the fabrication of one- dimensional ZnO nanostructures. The main advantage of CBD method is the low growth temperature which provides the possibility of using cheap substrates such as glass. Generally in chemical bath deposition method thin films and nano-materials can be simply deposited on a substrate. This method involves the nucleation and growth steps based on the formation of a solid phase from a solution. During this two-step process many parameters can affect the structure and morphology of the

products. Lin *et al.* have grown ZnO nanosheets by depositing layered hydroxide zinc carbonate on FTO glass followed by pyrolysis at 300 °C. Zinc nitrate and urea were used as the precursors. The ZnO sheet like structures obtained was composed of ZnO nanoparticles of 5-20 nm.²⁸

1.6.2.2 Vapour phase growth methods

In vapour phase methods the crystals are grown by depositing vapour or gaseous phase of materials. The different types of vapour phase growth methods like pulsed-laser deposition (PLD), chemical vapour deposition (CVD) and thermal evaporation are defined below.

1.6.2.2.1 Pulsed-Laser Deposition (PLD)

Pulsed-Laser Deposition is a technique where the target material is vapourised by using pulse lasers inside a vacuum chamber. The vapourised material is then deposited as a thin film on the substrate which is placed opposite to the target. The method is carried out under ultrahigh vacuum condition or in the presence of oxygen gas, which is generally employed for depositing oxides to completely oxygenate the film. High quality ZnO films were deposited by PLD in the temperature range of 200-800 °C. Wei *et al.* synthesised a thin film of ZnO by pulse vapour deposition from two different sources; ZnO powder and ceramic ZnO under 1.3 pa pressure and oxygen atmosphere. ZnO film from ZnO powder is obtained at 700 °C and from ceramic ZnO at 400 °C.¹⁵⁷ Matsubra *et al.* deposited Al, B and Ga doped ZnO by plus laser deposition technique, on glass substrate at 200 °C and used then for solar cell applications.¹⁵⁸

1.6.2.2.2 Chemical Vapour Deposition (CVD)

Chemical vapour deposition employs vacuum deposition of solid films with high quality and can be used for large scale fabrication. Here, the reactants are vapourised at high temperatures and transported with carrier gas (eg; nitrogen) where it react with the substrate surface to produce thin films. If metal-organics or alkoxides are used as precursors then the method is termed as metal-organic chemical vapour deposition method (MOCVD). Wang *et al.* grown ZnO on silicon by MOCVD by using diethylzinc and

oxygen as precursor. Nitrogen is used as the carrier gas. The ZnO films formed found to be c-oriented.¹⁵⁹ Wan *et al.* grown ZnO nano wires over Si substrate using pure Zn and also a mixture of graphite powder and ZnO. In the case of Zn powder, the growth on the Si substrate was self-catalysed, whereas in ZnO-graphite mixture the formation of ZnO nanowires is controlled by using gold particles as catalyst.¹⁶⁰

1.6.2.2.3 Thermal evaporation

In thermal evaporation solid material is heated at high temperature inside a vacuum chamber. The evaporated material get deposited over the substrate as film. Usually the source materials are heated upto the melting point and it is kept at the bottom of the chamber. The vapour rises above from the source and gets deposited over the substrate which is fixed inverted at the top of the chamber. Lee *et al.* synthesised ZnO with different morphology (nanobelts, nanorods and nanowires) at various substrate temperatures by the evaporation of ball milled ZnO at 1380 °C. By changing the substrate temperature the width/diameter of the products are found to be changed.¹⁶¹ Zheng *et al.* synthesised flowers like ZnO nanorods by thermal evaporation of ZnO/graphite on Si substrate. The products formed were highly crystalline and pure.¹⁶²

1.7 Definition of the problem

The photoanode in DSSC comprises of the three layers of blocking layer, active layer and scattering layer. Tuning the microstructural features of these layers play a remarkable role in enhancing the power conversion efficiency in DSSC. Light scattering layers are meant to increase the light harvesting characteristics of the device whereas blocking layers are incorporated to reduce the electron-hole recombination at FTO electrolyte interface of the device.

Light scattering effect in photoanodes of DSSCs is usually achieved by fabricating bilayer structured or mixture structured films. However, in the case of bilayer structured photoanode, the internal resistance of the solar cell is increased impeding the charge transport and in mixture structured film, submicron sized particles often reduce the active surface area for dye loading in the film resulting in low optical absorption.

Moreover, owing to the larger size of scattering particles, the fabricated photoanodes are opaque in nature and hence cannot be utilised for building integrated photovoltaic (BIPV) applications. The present work attempts to address the above issues through the use of fugitive ZnO hierarchical structures to impart surface roughness/voids in TiO₂ active layer. This method allows improved light scattering, creating a photoanode without sacrificing its surface area and transparency.

The power conversion efficiency of ZnO based DSSC is observed to be lesser than that of TiO₂ based DSSC and efforts have been made in ZnO based DSSC for the development of photoelectrodes to improve the performance of the device. Deposition of pre-Blocking layers (BL) are one of the methods employed to reduce the electron recombination at the FTO electrolyte interface. These are usually generated via atomic layer deposition (ALD), spray pyrolysis, sputtering, sol-gel methods etc. Some of these methods are very expensive and cannot be suggested for large scale applications. In the present thesis work ZnO nanoparticles are generated through a simple solution processed method and fine-tuned ZnO BLs of few nanometers thickness were deposited by dip coating method over FTO glass. The effect of blocking layer thickness on the photovoltaic properties of ZnO based DSSCs are investigated in detail.

1.8 Experimental and analytical techniques

1.8.1 Fabrication of DSSC

Fabrication of DSSC includes three major steps say, fabrication of anode, cathode and assembling of the device. The fabrication of DSSC that have done for the thesis work is discussed in this section. A schematic representation of the steps involved is provided in **Figure 1.9**.

1.8.1.1 Fabrication of anode

The anode as well as cathode is constructed over the conductive glass like FTO or ITO. The fabrication commences with the cleaning of FTO substrates. Cleaning is done by systematically sonicating the substrates in soap solution, deionised water, acetone and isopropanol. It is subjected to annealing at 500 °C in a furnace in order to remove trace of

organic substances present if any. The substrates are then subjected for pre-blocking layer deposition. This is achieved by immersing the substrates in aqueous 40 mM TiCl_4 solution for 30 minutes at 70 °C over a hot plate. Substrates are thoroughly washed with deionised water and ethanol and annealed at 500 °C. A very thin layer of TiO_2 is formed over FTO and is termed as preblocking layer. Next step is the deposition of the TiO_2 paste by doctor blade method in a specific area by employing a mask and further annealing it up to 500 °C. After annealing, the organic binders are burned out resulting in a mesoporous TiO_2 film. This film is then subjected to TiCl_4 treatment and annealed as aforementioned, during which a thin layer of TiO_2 is coated over the mesoporous film (which is termed as post-blocking layer). The substrates are then immersed in dye solution for 10-15 hours for proper dye adsorption by TiO_2 film. Finally, the dye soaked anodes are cleaned with solvent that is used for preparing the dye solution and dried.

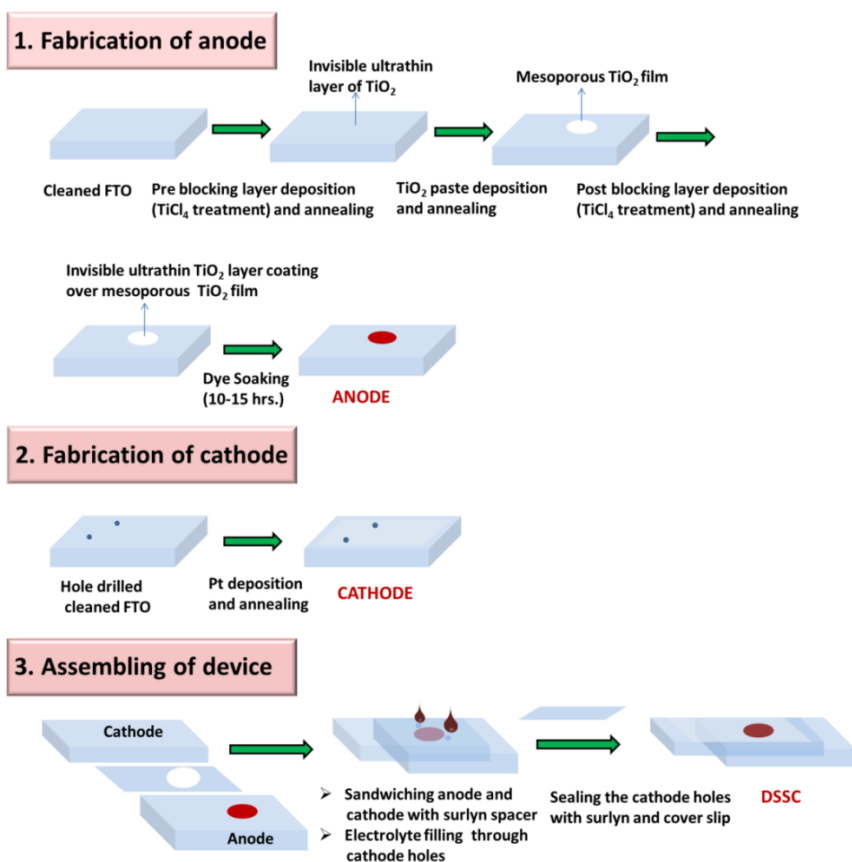


Figure 1.9 Schematic representation of steps involved in the fabrication of DSSC.

1.8.1.2 Fabrication of cathode

FTO substrates are cleaned in similar way that done for anodes. But prior to cleaning of the substrates, two tiny holes are drilled in that, in order to inject the electrolyte during the assembling of the device. The cleaned FTO substrates are coated with platinum sol with a brush and annealed at 380 °C for 20 minutes.

1.8.1.3 Assembling of the device

The anodes and cathodes are sandwiched by ~ 25 µm surlyn spacer by placing it over a hot plate. The electrolyte is infiltrated into the device through the holes of the cathode. Soon after, the holes are properly sealed with a cover slide and surlyn to avoid the evaporation/leakage of electrolyte. The devices are safely kept overnight to attain stability and after that photovoltaic measurements can be carried out.

1.9 Techniques used for interfacial charge transfer analysis

1.9.1 Electrochemical Impedance Spectroscopy (EIS)

EIS is a nondestructive small perturbation technique. It is one of the most used characterisation technique for interfacial analysis in DSSC. For accurate measurement one has to ensure linearity, that is the output signal is giving linear response to the input signal. For EIS measurement a small perturbation of amplitude 10 mV is given to the device and the response of the device is measured. From the input signal and the output signal impedance of the device is calculated.

$$\text{Input signal } V(\omega t) = V_0 \sin(\omega t) \quad (3)$$

$$\text{Output signal } I(\omega t) = I_0 \sin(\omega t - \phi) \quad (4)$$

where ϕ is the phase difference between $V(\omega, t)$ and $I(\omega, t)$

The impedance is calculated as

$$Z(\omega t) = \frac{V(\omega t)}{I(\omega t)} = \frac{V_0 \sin(\omega t)}{I_0 \sin(\omega t - \phi)} \quad (5)$$

This is again simplified to $Z(\omega) = Z'(\omega) + iZ''(\omega)$

$Z'(\omega)$ is the real part of impedance and $Z''(\omega)$

The real and imaginary parts of the impedance are related to the phase angle ϕ as

$$\phi = \tan^{-1}(Z''/Z') \quad (6)$$

For EIS analysis generally two plots are used, Nyquist plot and Bode plot

In Nyquist plot X axis is real part of impedance and Y axis imaginary part of impedance. Nyquist plot of DSSC consists of three semicircles (**Figure 1.10a**). The first semicircle corresponds to the Pt/electrolyte interface, second semicircle corresponds to the dye/semiconductor/electrolyte interface and third semicircle corresponds to the diffusion of ions in electrolyte. For Bode plot X axis is frequency and Y axis is phase angle. These plots are fitted with equivalent electrical circuit for further analysis (**Figure 1.10a**). **Figure 1.11** shows the equivalent circuit used for fitting impedance response. Resistance generally describes electron transfer events, while capacitances describe the electronic carrier accumulation and distribution across an interface.

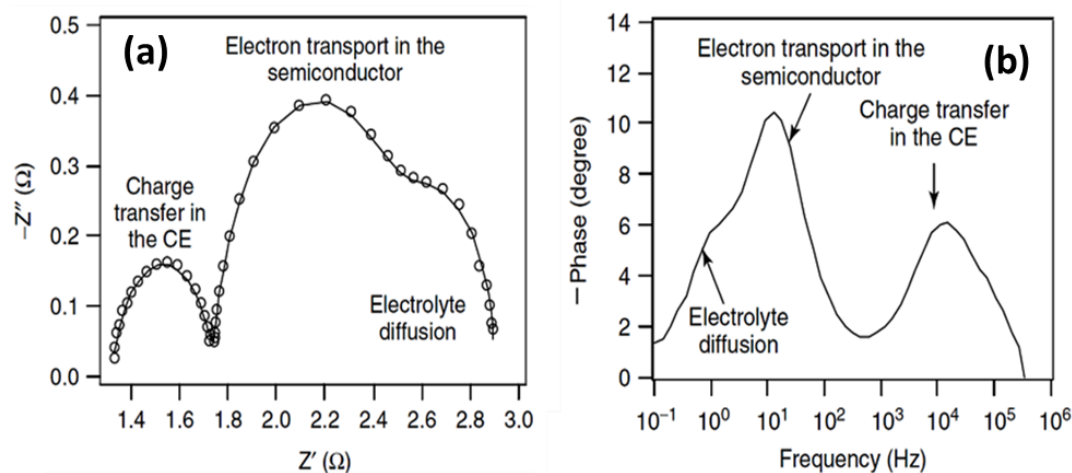


Figure 1.10 A typical (a) Nyquist plot and (b) bode plot of a dye-sensitized solar cell.¹³³

The equivalent-circuit model consists of R_s (resistance due to the FTO and contact resistance), R_{Pt} , C_{Pt} (resistance and capacitance at Pt/electrolyte interface), C_{TCO} (capacitance at FTO/electrolyte interface) and $B2$ (transmission line model used to

explain charge transfer at dye/TiO₂/electrolyte interface). B2 includes R_t (transport resistance for TiO₂), R_{rec} (recombination resistance at dye/TiO₂/electrolyte interface) and C_μ (Chemical capacitance of TiO₂ in contact with electrolyte)

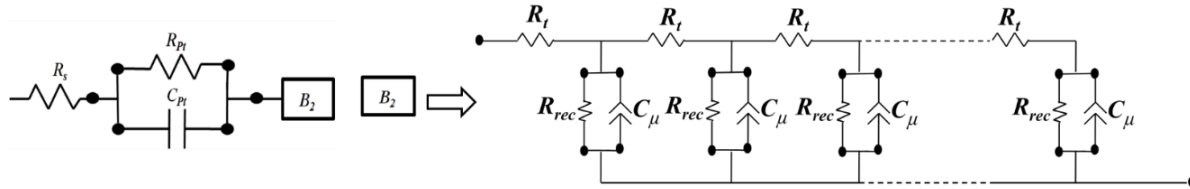


Figure 1.11 Equivalent circuit for impedance fitting.

1.9.2 Intensity modulated photovoltage spectroscopy (IMVS) and Intensity modulated photocurrent spectroscopy (IMPS)

IMPS and IMVS are also small perturbation techniques. Here, light perturbation is applied across the device and the corresponding response is measured while maintaining the linearity. For IMVS, cell is kept in open circuit condition and is illuminated with light, similarly in IMPS measurement cell is kept in short circuit and light is illuminated. Generally, the light perturbation is 10% of the steady state illumination. For both the IMPS and IMVS, the characteristics plots are Nyquist plot and Bode plot. In Nyquist plot X axis is real part of transfer function and Y axis is imaginary part of transfer function. Trans function is nothing but output signal or response of the device divided by input signal to the device. For Bode Plot X axis is frequency and Y axis is imaginary part of transfer function. Electron lifetime (τ_n) is calculated from IMVS and electron transport time (τ_d) is calculated from IMPS. τ_n is calculated from Bode plot of IMVS using the relation ' $\tau_n=1/2\pi f_m$ ' where f_m is the frequency corresponding to the highest value in imaginary part of transfer function (-H). τ_d is calculated from Bode plot from IMPS using the relation ' $\tau_d=1/2\pi f_m$ ' where f_m is the frequency corresponding to the highest value in imaginary part of impedance (-H').

1.9.3 Open circuit voltage decay (OCVD)

Open circuit voltage decay is a large perturbation technique used for charge transfer analysis at Dye/TiO₂/electrolyte interface. Light is illuminated with zero current across

device so that all the electrons accumulates at TiO_2 and its reaches to its V_{oc} condition. Then light is switched off and V_{oc} decays as the electrons recombine with electrolyte. From the voltage decay electron lifetime is calculated using the equation,

$$\tau_n = -\frac{k_B T}{e} \left(\frac{dV_{oc}}{dt} \right)^{-1} \quad (7)$$

Where K_B is Boltzmann constant, T room temperature and e is charge of electron.

1.9.4 Charge extraction analysis

Charge Extraction measurement is used to locate the position of conduction band of semiconductor and also to study the distribution of energy state in band gap of semiconductor. It involves switching on the illumination under different applied bias followed by switching off the light and then extraction of the charge by short circuiting the device.

1.10 Photovoltaic parameters

The performance of DSSC is evaluated through current-voltage (J - V) characteristics. From a typical J - V curve one can determine short circuit current density (J_{sc}), open circuit voltage (V_{oc}) and fill factor of the device.

1.10.1 Short circuit current density (J_{sc})

Short circuit current density (J_{sc}) is the maximum current obtained from the solar cell when the voltage across the device is zero ie; when it is short circuited. J_{sc} depends upon the photogenerated electrons and the recombination of electrons and holes. It is usually expressed in terms of current density

$$J_{sc} = \frac{I_{sc}}{A} \quad (8)$$

Where I_{sc} is short circuit current and A is the active area of the solar cell.

1.10.2 Open circuit voltage (V_{oc})

Open circuit voltage is the voltage obtained from the solar cell when the current across

the device is zero ie; open circuited condition. It is the maximum voltage that can be drawn from the solar cell. In DSSC, V_{oc} is the difference between the redox potential of the electrolyte and fermi level of the electrons in metal oxide semiconductor. V_{oc} significantly depends upon the recombination of the electrons.

1.10.3 Fill factor (FF)

Fill factor is defined as the ratio of maximum power of the solar cell per unit area to the product of J_{sc} and V_{oc} .

$$FF = \frac{J_{max}V_{max}}{J_{sc}V_{oc}} \quad (9)$$

1.10.4 Power conversion efficiency (PCE)

The most significant parameter assessing the device performance is the power conversion efficiency (η). It is calculated by using the equation given below

$$\eta = \frac{J_{sc}V_{oc}}{P_{in}} \times 100 \quad (10)$$

where P_{in} is the intensity of the incident light. Generally device performance is measured under 1 Sun condition (100 mW/cm² with air mass (AM) 1.5 G spectrum).

References

1. S. Shafiee and E. Topal, *Energy Policy*, 2009, **37**, 181-189.
2. K. G. Reddy, T. G. Deepak, G. S. Anjusree, S. Thomas, S. Vadukumpully, K. R. V. Subramanian, S. V. Nair and A. S. Nair, *Phys. Chem. Chem. Phys.*, 2014, **16**, 6838-6858.
3. Tze Chien Sum, Nripan Mathews, *Energy Environ. Sci.*, 2014, **7**, 2518.
4. A. Becquerel, *CR Acad. Sci. Paris*, 1839, **9**, 14.
5. D. M. Chapin, C. Fuller and G. Pearson, *J. Appl. Phys.*, 1954, **25**, 676-677.
6. V. Fthenakis, *Renew. Sust. Energ. Rev.*, 2009, **13**, 2746-2750.
7. J. J. Liou and W. W. Wong, *Sol. Energy Mater. Sol. Cells*, 1992, **28**, 9-28.

8. J. Ramanujam and U. P. Singh, *Energy Environ. Sci.*, 2017, **10**, 1306-1319.
9. K. Fan, J. Yu and W. Ho, *Mater. Horizons*, 2017, **4**, 319-344.
10. P. V. Kamat, *J. Phys. Chem. Lett.*, 2013, **4**, 908-918.
11. A. K. Jena, A. Kulkarni and T. Miyasaka, *Chem. Rev.*, 2019, **119**, 3036-3103.
12. L. Lu, T. Zheng, Q. Wu, A. M. Schneider, D. Zhao and L. Yu, *Chem. Rev.*, 2015, **115**, 12666-12731.
13. <https://www.nrel.gov/pv/cell-efficiency.html>
14. B. O'regan and M. Grätzel, *Nature*, 1991, **353**, 737-739.
15. M. Freitag, J. Teuscher, Y. Saygili, X. Zhang, F. Giordano, P. Liska, J. Hua, S. M. Zakeeruddin, J.-E. Moser, M. Grätzel and A. Hagfeldt, *Nat. Photonics*, 2017, **11**, 372-380.
16. M. Shakeel Ahmad, A. K. Pandey and N. Abd Rahim, *Renew.Sust.Energ. Rev.*, 2017, **77**, 89-108.
17. J. A. Anta, E. Guillén and R. Tena-Zaera, *J. Phys. Chem. C*, 2012, **116**, 11413-11425.
18. A. Birkel, Y.-G. Lee, D. Koll, X. V. Meerbeek, S. Frank, M. J. Choi, Y. S. Kang, K. Char and W. Tremel, *Energy Environ. Sci.*, 2012, **5**, 5392-5400.
19. A. Le Viet, R. Jose, M. V. Reddy, B. V. R. Chowdari and S. Ramakrishna, *J. Phys. Chem. C*, 2010, **114**, 21795-21800.
20. S. Burnside, J.E. Moser, K. Brooks, M. Grätzel and D. Cahen, *J. Phys. Chem. B*, 1999, **103**, 9328-9332.
21. S. S. Shin, J. S. Kim, J. H. Suk, K. D. Lee, D. W. Kim, J. H. Park, I. S. Cho, K. S. Hong and J. Y. Kim, *ACS Nano*, 2013, **7**, 1027-1035.
22. B. Tan, E. Toman, Y. Li and Y. Wu, *J. Am. Chem. Soc.*, 2007, **129**, 4162-4163.
23. J. Zhang, P. Zhou, J. Liu and J. Yu, *Phys. Chem. Chem. Phys.*, 2014, **16**, 20382-20386.
24. M.E. Yeoh and K.-Y. Chan, *Int. J. Energy Res.*, 2017, **41**, 2446-2467.
25. A. Hagfeldt, G. Boschloo, L. Sun, L. Kloo and H. Pettersson, *Chem. Rev.*, 2010, **110**, 6595-6663.
26. K. Kakiage, Y. Aoyama, T. Yano, K. Oya, J.-i. Fujisawa and M. Hanaya, *Chem. Comm.*, 2015, **51**, 15894-15897.
27. M. Laurenti, S. Stassi, G. Canavese and V. Cauda, *Adv. Mater. Interfaces*, 2017, **4**, 1600758.

28. C.-Y. Lin, Y.-H. Lai, H.-W. Chen, J.-G. Chen, C.-W. Kung, R. Vittal and K.-C. Ho, *Energy Environ. Sci.*, 2011, **4**, 3448-3455.
29. D. Barpuzary, A. S. Patra, J. V. Vaghasiya, B. G. Solanki, S. S. Soni and M. Qureshi, *ACS Appl. Mater. Interfaces*, 2014, **6**, 12629-12639.
30. S. H. Ko, D. Lee, H. W. Kang, K. H. Nam, J. Y. Yeo, S. J. Hong, C. P. Grigoropoulos and H. J. Sung, *Nano Lett.*, 2011, **11**, 666-671.
31. Y. Sun, D. J. Riley and M. N. R. Ashfold, *J. Phys. Chem. B*, 2006, **110**, 15186-15192.
32. Y. K. Mishra, G. Modi, V. Cretu, V. Postica, O. Lupan, T. Reimer, I. Paulowicz, V. Hrkac, W. Benecke, L. Kienle and R. Adelung, *ACS Appl. Mater. Interfaces*, 2015, **7**, 14303-14316.
33. S. Yun, J. Lee, J. Chung and S. Lim, *J. Phys. Chem. Solids*, 2010, **71**, 1724-1731.
34. N. Memarian, I. Concina, A. Braga, S. M. Rozati, A. Vomiero and G. Sberveglieri, *Angew. Chem.*, 2011, **50**, 12321-12325.
35. Y. He, J. Hu and Y. Xie, *Chem. Commun.*, 2015, **51**, 16229-16232.
36. J. Wu, Z. Lan, J. Lin, M. Huang, Y. Huang, L. Fan and G. Luo, *Chem. Rev.*, 2015, **115**, 2136-2173.
37. J. Wu, Z. Lan, S. Hao, P. Li, J. Lin, M. Huang, L. Fang and Y. Huang, *Pure Appl. Chem.*, 2008, **80**, 2241-2258.
38. A. Nogueira, C. Longo and M.A. De Paoli, *Coord. Chem. Rev*, 2004, **248**, 1455-1468.
39. J. N. de Freitas, A. F. Nogueira and M.-A. De Paoli, *J. Mater. Chem.*, 2009, **19**, 5279-5294.
40. C. Lie-Hang, X. Bo-Fei, L. Xi-Zhe, L. Ke-Xin, L. Yan-Hong, M. Qing-Bo, W. Rui-Lin and C. Li-Quan, *Chin. Phys. Lett.*, 2007, **24**, 555.
41. G. Kumara, A. Konno, G. Senadeera, P. Jayaweera, D. De Silva and K. Tennakone, *Sol. Energy Mater. Sol. Cells*, 2001, **69**, 195-199.
42. N. Chander, P. S. Chandrasekhar and V. K. Komarala, *RSC Adv.*, 2014, **4**, 55658-55665.
43. H. Wang, G. Liu, X. Li, P. Xiang, Z. Ku, Y. Rong, M. Xu, L. Liu, M. Hu, Y. Yang and H. Han, *Energy Environ. Sci.*, 2011, **4**, 2025-2029.
44. E. Lancelle-Beltran, P. Prené, C. Boscher, P. Belleville, P. Buvat, S. Lambert, F. Guillet, C. Marcel and C. Sanchez, *Eur. J. Inorg. Chem.*, 2008, **2008**, 903-910.

45. G. Yue, J. Wu, Y. Xiao, H. Ye, J. Lin and M. Huang, *Sci. Bull.*, 2011, **56**, 325-330.
46. J. C. Kim, M. M. Rahman, M. J. Ju and J.-J. Lee, *RSC Adv.*, 2018, **8**, 19058-19066.
47. C.-Y. Hsu, Y.-C. Chen, R. Y.-Y. Lin, K.-C. Ho and J. T. Lin, *Phys. Chem. Chem. Phys.*, 2012, **14**, 14099-14109.
48. S. Ito and A. K. Baranwal, *Counter Electrodes for Dye-sensitized and Perovskite Solar Cells*, 2018, **2**, 457-485.
49. H. Wang and Y. H. Hu, *Energy Environ. Sci.*, 2012, **5**, 8182-8188.
50. W. Wei, H. Wang and Y. H. Hu, *Int. J. Energy Res.*, 2014, **38**, 1099-1111.
51. H. Wang, W. Wei and Y. H. Hu, *Top. Catal.*, 2014, **57**, 607-611.
52. H. Wang, W. Wei and Y. H. Hu, *J. Mater. Chem. A*, 2013, **1**, 6622-6628.
53. W.Q. Wu, Y.-F. Xu, C.-Y. Su and D.-B. Kuang, *Energy Environ. Sci.*, 2014, **7**, 644-649.
54. G. Melcarne, L. De Marco, E. Carlino, F. Martina, M. Manca, R. Cingolani, G. Gigli and G. Ciccarella, *J. Mater. Chem.*, 2010, **20**, 7248-7254.
55. J. Jiu, S. Isoda, F. Wang and M. Adachi, *J. Phys. Chem. B*, 2006, **110**, 2087-2092.
56. W.Q. Wu, B.-X. Lei, H.-S. Rao, Y.-F. Xu, Y.-F. Wang, C.-Y. Su and D.-B. Kuang, *Sci. Rep.*, 2013, **3**, 1352.
57. C. Xu, J. Wu, U. V. Desai and D. Gao, *J. Am. Chem. Soc.*, 2011, **133**, 8122-8125.
58. J. M. Macák, H. Tsuchiya, A. Ghicov and P. Schmuki, *Electrochem. commun.*, 2005, **7**, 1133-1137.
59. W.-C. Chen, M.-H. Yeh, L.-Y. Lin, R. Vittal and K.-C. Ho, *ACS Sustain. Chem. Eng.*, 2018, **6**, 3907-3915.
60. A. Elzarka, N. Liu, I. Hwang, M. Kamal and P. Schmuki, *Chem.: Eur. J.*, 2017, **23**, 12995-12999.
61. A. Lamberti, A. Sacco, S. Bianco, D. Manfredi, F. Cappelluti, S. Hernandez, M. Quaglio and C. F. Pirri, *Phys. Chem. Chem. Phys.*, 2013, **15**, 2596-2602.
62. J. Zhang, S. Li, H. Ding, Q. Li, B. Wang, X. Wang and H. Wang, *J. Power Sources*, 2014, **247**, 807-812.
63. J. Zhang, Q. Li, S. Li, Y. Wang, C. Ye, P. Ruterana and H. Wang, *J. Power Sources*, 2014, **268**, 941-949.
64. F. Sauvage, D. Chen, P. Comte, F. Huang, L.-P. Heiniger, Y.-B. Cheng, R. A. Caruso and M. Graetzel, *ACS Nano*, 2010, **4**, 4420-4425.

65. Q. Zhang, T. P. Chou, B. Russo, S. A. Jenekhe and G. Cao, *Angew. Chem.*, 2008, **47**, 2402-2406.
66. S. H. Hwang, J. Yun and J. Jang, *Adv. Funct. Mater.*, 2014, **24**, 7619-7626.
67. K. Al-Attafi, A. Nattestad, Y. Yamauchi, S. X. Dou and J. H. Kim, *Sci. Rep.*, 2017, **7**, 10341.
68. Q. Zheng, H. Kang, J. Yun, J. Lee, J. H. Park and S. Baik, *ACS nano*, 2011, **5**, 5088-5093.
69. C. T. Yip, H. Huang, L. Zhou, K. Xie, Y. Wang, T. Feng, J. Li and W. Y. Tam, *Adv. Mater.*, 2011, **23**, 5624-5628.
70. M. Lv, D. Zheng, M. Ye, J. Xiao, W. Guo, Y. Lai, L. Sun, C. Lin and J. Zuo, *Energy Environ. Sci.*, 2013, **6**, 1615-1622.
71. M. McCune, W. Zhang and Y. Deng, *Nano Lett.*, 2012, **12**, 3656-3662.
72. D. Hwang, H. Lee, S.-Y. Jang, S. M. Jo, D. Kim, Y. Seo and D. Y. Kim, *ACS Appl. Mater. Interfaces*, 2011, **3**, 2719-2725.
73. Y. P. Lin, S. Y. Lin, Y. C. Lee and Y. W. Chen-Yang, *J. Mater. Chem. A*, 2013, **1**, 9875-9884.
74. N. Yang, J. Zhai, D. Wang, Y. Chen and L. Jiang, *ACS nano*, 2010, **4**, 887-894.
75. S. P. Lim, A. Pandikumar, N. M. Huang and H. N. Lim, *RSC Advances*, 2015, **5**, 44398-44407.
76. S. H. Hwang, H. Song, J. Lee and J. Jang, *Chem.: Eur. J.*, 2014, **20**, 12974-12981.
77. Y. Li, H. Wang, Q. Feng, G. Zhou and Z.-S. Wang, *Energy Environ. Sci.*, 2013, **6**, 2156-2165.
78. M. Yang, B. Dong, X. Yang, W. Xiang, Z. Ye, E. Wang, L. Wan, L. Zhao and S. Wang, *RSC Adv.*, 2017, **7**, 41738-41744.
79. Y. Bai, H. Yu, Z. Li, R. Amal, G. Q. Lu and L. Wang, *Adv. Mater.*, 2012, **24**, 5850-5856.
80. F. Li, G. Wang, Y. Jiao, J. Li and S. Xie, *J. Alloys Compd.*, 2014, **611**, 19-23.
81. N. K. Huu, D.-Y. Son, I.-H. Jang, C.-R. Lee and N.-G. Park, *ACS Appl. Mater. Interfaces*, 2013, **5**, 1038-1043.
82. M. Mrowetz, W. Balcerski, A. Colussi and M. R. Hoffmann, *J. Phys. Chem. B*, 2004, **108**, 17269-17273.

83. R. Asahi, T. Morikawa, T. Ohwaki, K. Aoki and Y. Taga, *Science*, 2001, **293**, 269-271.
84. W. Guo, Y. Shen, G. Boschloo, A. Hagfeldt and T. Ma, *Electrochim. Acta*, 2011, **56**, 4611-4617.
85. K. Mahmood and S. B. Park, *J. Mater. Chem. A*, 2013, **1**, 4826-4835.
86. M. Momeni, *Rare Metals*, 2017, **36**, 865-871.
87. K. Kakiage, T. Tokutome, S. Iwamoto, T. Kyomen and M. Hanaya, *Chem. Commun.*, 2013, **49**, 179-180.
88. P. Archana, A. Gupta, M. M. Yusoff and R. Jose, *Phys. Chem. Chem. Phys.*, 2014, **16**, 7448-7454.
89. M. Yang, D. Kim, H. Jha, K. Lee, J. Paul and P. Schmuki, *Chem. Commun.*, 2011, **47**, 2032-2034.
90. Y. Duan, N. Fu, Q. Liu, Y. Fang, X. Zhou, J. Zhang and Y. Lin, *J. Phys. Chem. C*, 2012, **116**, 8888-8893.
91. S. Ameen, M. S. Akhtar, H.-K. Seo, Y. S. Kim and H. S. Shin, *Chem. Eng. J.*, 2012, **187**, 351-356.
92. K. Lee and P. Schmuki, *Electrochem. Commun.*, 2012, **25**, 11-14.
93. X. Dou, D. Sabba, N. Mathews, L. H. Wong, Y. M. Lam and S. Mhaisalkar, *Chem. Mater.*, 2011, **23**, 3938-3945.
94. P. S. Archana, E. Naveen Kumar, C. Vijila, S. Ramakrishna, M. M. Yusoff and R. Jose, *Dalton Trans.*, 2013, **42**, 1024-1032.
95. M. Dürr, S. Rosselli, A. Yasuda and G. Nelles, *J. Phys. Chem. B*, 2006, **110**, 21899-21902.
96. Q. Zhang, D. Myers, J. Lan, S. A. Jenekhe and G. Cao, *Phys. Chem. Chem. Phys.*, 2012, **14**, 14982-14998.
97. T. G. Deepak, G. S. Anjusree, S. Thomas, T. A. Arun, S. V. Nair and A. Sreekumaran Nair, *RSC Adv.*, 2014, **4**, 17615-17638.
98. C. Li, G. W. Kattawar and P. Yang, *J. Quant. Spectrosc. Radiat. Transf.*, 2004, **89**, 123-131.
99. T. Nousiainen and K. Muinonen, *J. Quant. Spectrosc. Radiat. Transf.*, 2007, **106**, 389-397.

100. J. Ferber and J. Luther, *Sol. Energy Mater. Sol. Cells*, 1998, **54**, 265-275.
101. A. Usami, *Chem. Phys. Lett.*, 1997, **277**, 105-108.
102. F. Huang, D. Chen, X. L. Zhang, R. A. Caruso and Y. B. Cheng, *Adv. Funct. Mater.*, 2010, **20**, 1301-1305.
103. Z.-S. Wang, H. Kawauchi, T. Kashima and H. Arakawa, *Coord. Chem. Rev.*, 2004, **248**, 1381-1389.
104. D. Guo, S. Xiao, K. Fan and J. Yu, *ACS Sustain. Chem. Eng.*, 2017, **5**, 1315-1321.
105. K. Mahmood and H. J. Sung, *J. Mater. Chem. A*, 2014, **2**, 5408-5417.
106. A. Banik, M. S. Ansari, T. K. Sahu and M. Qureshi, *Phys. Chem. Chem. Phys.*, 2016, **18**, 27818-27828.
107. S. Son, S. H. Hwang, C. Kim, J. Y. Yun and J. Jang, *ACS Appl. Mater. Interfaces*, 2013, **5**, 4815-4820.
108. M.-Y. Pu and J. Z. Chen, *Mater. Lett.*, 2012, **66**, 162-164.
109. M.-Y. Pu, J.-Z. Chen and I. C. Cheng, *Ceram. Int.*, 2013, **39**, 6183-6188.
110. G. Yang, J. Zhang, P. Wang, Q. Sun, J. Zheng and Y. Zhu, *Curr. Appl. Phys.*, 2011, **11**, 376-381.
111. S. Hore, P. Nitz, C. Vetter, C. Prahl, M. Niggemann and R. Kern, *Chem. Commun.*, 2005, 2011-2013.
112. S.-H. Han, S. Lee, H. Shin and H. Suk Jung, *Adv. Energy Mater.*, 2011, **1**, 546-550.
113. H. Choi, C. Nahm, J. Kim, J. Moon, S. Nam, D.-R. Jung and B. Park, *Curr. Appl. Phys.*, 2012, **12**, 737-741.
114. Q. Yi, S. Cong, H. Wang, Y. Wang, X. Dai, J. Zhao, Y. Sun, Y. Lou and G. Zou, *Appl Surf Sci.*, 2015, **356**, 587-592.
115. P. Sommeling, B. O'regan, R. Haswell, H. Smit, N. Bakker, J. Smits, J. Kroon and J. Van Roosmalen, *J. Phys. Chem. B*, 2006, **110**, 19191-19197.
116. S.-W. Lee, K.-S. Ahn, K. Zhu, N. R. Neale and A. J. Frank, *J. Phys. Chem. C*, 2012, **116**, 21285-21290.
117. C. Prasittichai and J. T. Hupp, *J. Phys. Chem. Lett.*, 2010, **1**, 1611-1615.
118. T. C. Li, M. S. Góes, F. Fabregat-Santiago, J. Bisquert, P. R. Bueno, C. Prasittichai, J. T. Hupp and T. J. Marks, *J. Phys. Chem. C*, 2009, **113**, 18385-18390.
119. A. K. Chandiran, N. Tetreault, R. Humphry-Baker, F. Kessler, E. Baranoff, C. Yi, M. K.

- Nazeeruddin and M. Grätzel, *Nano Lett.*, 2012, **12**, 3941-3947.
120. H.J. Son, X. Wang, C. Prasittichai, N. C. Jeong, T. Aaltonen, R. G. Gordon and J. T. Hupp, *J. Am. Chem. Soc.*, 2012, **134**, 9537-9540.
121. A. K. Chandiran, M. K. Nazeeruddin and M. Grätzel, *Adv. Funct. Mater.*, 2014, **24**, 1615-1623.
122. P. J. Cameron and L. M. Peter, *J. Phys. Chem. B*, 2003, **107**, 14394-14400.
123. M.E. Yeoh and K.-Y. Chan, *J. Electron. Mater.*, 2019, 1-9.
124. A. Alberti, G. Pellegrino, G. Condorelli, C. Bongiorno, S. Morita, A. La Magna and T. Miyasaka, *J. Phys. Chem. C*, 2014, **118**, 6576-6585.
125. J. Ding, Y. Li, H. Hu, L. Bai, S. Zhang and N. Yuan, *Nanoscale Res. Lett.*, 2013, **8**, 9.
126. L. Kavan, N. Tétreault, T. Moehl and M. Grätzel, *J. Phys. Chem. C*, 2014, **118**, 16408-16418.
127. J. Guan, J. Zhang, T. Yu, G. Xue, X. Yu, Z. Tang, Y. Wei, J. Yang, Z. Li and Z. Zou, *RSC Adv.*, 2012, **2**, 7708-7713.
128. M. r. S. Góes, E. Joanni, E. C. Muniz, R. Savu, T. R. Habeck, P. R. Bueno and F. Fabregat- Santiago, *J. Phys. Chem. C*, 2012, **116**, 12415-12421.
129. G. S. Selopal, N. Memarian, R. Milan, I. Concina, G. Sberveglieri and A. Vomiero, *ACS Appl. Mater. Interfaces*, 2014, **6**, 11236-11244.
130. Y. S. Tingare, N. S. n. Vinh, H.-H. Chou, Y.-C. Liu, Y.S. Long, T.-C. Wu, T.C. Wei and C.-Y. Yeh, *Adv. Energy Mater.*, 2017, **7**, 1700032.
131. Y. Cao, Y. Liu, S. M. Zakeeruddin, A. Hagfeldt and M. Grätzel, *Joule*, 2018, **2**, 1108-1117.
132. C. L. Cutting, M. Bag and D. Venkataraman, *J. Mater. Chem. C*, 2016, **4**, 10367-10370.
133. L. Andrade, H. A. Ribeiro and A. Mendes, *Encyclopedia of Inorganic and Bioinorganic Chemistry*, 2011.
134. D. Sahu, C. P. Liu, R. C. Wang, C. L. Kuo and J. L. Huang, *Int. J. Appl. Ceram. Technol.*, 2013, **10**, 814-838.
135. A. Kołodziejczak-Radzimska and T. Jesionowski, *Materials*, 2014, **7**, 2833-2881.
136. M. Purica, E. Budianu and E. Rusu, *Thin Solid Films*, 2001, **383**, 284-286.
137. J. Jayabharathi, A. Prabhakaran, V. Thanikachalam and M. Sundharesan, *J.*

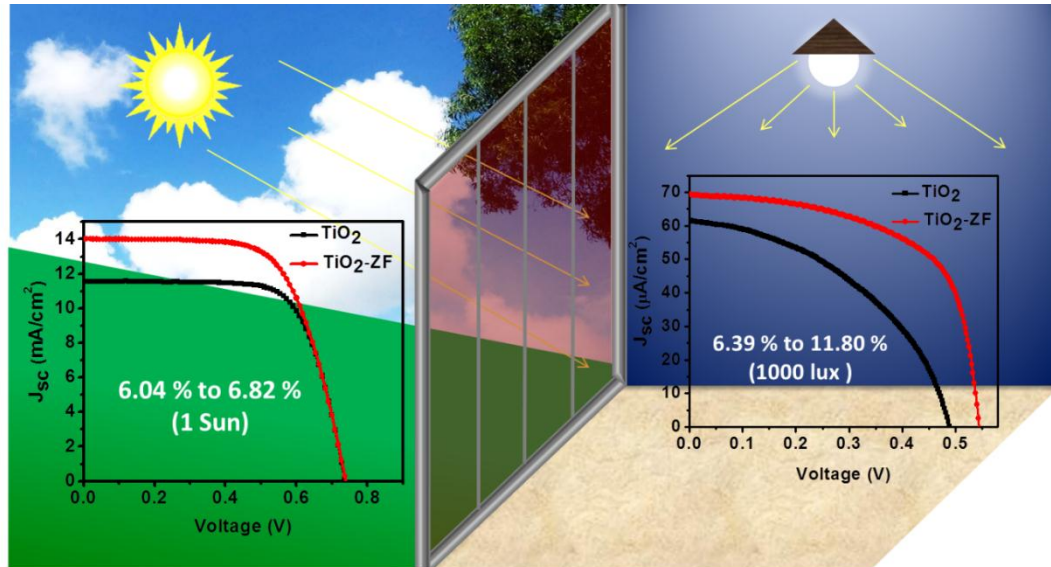
- Photochem. Photobiol. A*, 2016, **325**, 88-96.
138. P. Mitra, A. P. Chatterjee and H. S. Maiti, *Mater. Lett.*, 1998, **35**, 33-38.
139. X. Cheng, H. Zhao, L. Huo, S. Gao and J. Zhao, *Sens. Actuator B-Chem.*, 2004, **102**, 248-252.
140. C. B. Ong, L. Y. Ng and A. W. Mohammad, *Renew. Sust. Energ. Rev.*, 2018, **81**, 536-551.
141. S. Rajeshkumar, T. Lakshmi and P. Naik, in *Green Synthesis, Characterization and Applications of Nanoparticles*, eds., A. K. Shukla and S. Iravani, Elsevier, 2019, 445-457.
142. S. Cho, S.-H. Jung and K.-H. Lee, *J. Phys. Chem. C*, 2008, **112**, 12769-12776.
143. Ü. Özgür, Y. I. Alivov, C. Liu, A. Teke, M. Reshchikov, S. Doğan, V. Avrutin, S.-J. Cho and H. Morkoç, *J. Appl. Phys.*, 2005, **98**, 11.
144. C. Klingshirn, *ChemPhysChem*, 2007, **8**, 782-803.
145. J. Molarius, J. Kaitila, T. Pensala and M. Ylilammi, *J. Mater. Sci.: Mater. Electron.*, 2003, **14**, 431-435.
146. T. Shiosaki and A. Kawabata, *Appl. Phys. Lett.*, 1974, **25**, 10-11.
147. S. Lima, F. Sigoli, M. Jafelicci Jr and M. R. Davolos, *Int. J. Inorg. Mater.*, 2001, **3**, 749-754.
148. J. W. Soares, J. E. Whitten, D. W. Oblas and D. M. Steeves, *Langmuir*, 2008, **24**, 371-374.
149. S. Shionoya, W. M. Yen and H. Yamamoto, *Phosphor handbook*, CRC press, 2018.
150. A. Das, D.-Y. Wang, A. Leuteritz, K. Subramaniam, H. C. Greenwell, U. Wagenknecht and G. Heinrich, *J. Mater. Chem.*, 2011, **21**, 7194-7200.
151. P. Li, Y. Wei, H. Liu and X.-k. Wang, *J. Solid State Chem.*, 2005, **178**, 855-860.
152. A. S. Lanje, S. J. Sharma, R. S. Ningthoujam, J.-S. Ahn and R. B. Pode, *Adv. Powder. Technol.*, 2013, **24**, 331-335.
153. C.-l. Ma and X.-d. Sun, *Inorg. Chem. Commun.*, 2002, **5**, 751-755.
154. H. Benhebal, M. Chaib, T. Salmon, J. Geens, A. Leonard, S. D. Lambert, M. Crine and B. Heinrichs, *Inorg. Chem. Commun.*, 2013, **52**, 517-523.
155. M. Ristić, S. Musić, M. Ivanda and S. Popović, *J. Alloys Compd.*, 2005, **397**, L1-L4.
156. H. Chen, X. Wu, L. Gong, C. Ye, F. Qu and G. Shen, *Nanoscale Res. Lett.*, 2010, **5**, 570.

157. X. Wei, Z. Zhang, Y. Yu and B. Man, *Opt.Laser Technol.*, 2009, **41**, 530-534.
158. K. Matsubara, P. Fons, K. Iwata, A. Yamada, K. Sakurai, H. Tampo and S. Niki, *Thin Solid Films*, 2003, **431**, 369-372.
159. X. Wang, S. Yang, X. Yang, D. Liu, Y. Zhang, J. Wang, J. Yin, D. Liu, H. Ong and G. Du, *J. Cryst. Growth*, 2002, **243**, 13-18.
160. H. Wan and H. E. Ruda, *J. Mater. Sci.: Mater. Electron.*, 2010, **21**, 1014-1019.
161. J.S. Lee, K. Park, M.-I. Kang, I.W. Park, S.-W. Kim, W. K. Cho, H. S. Han and S. Kim, *J. Cryst. Growth*, 2003, **254**, 423-431.
162. J. Zheng, Q. Jiang and J. Lian, *Appl. Surf. Sci.*, 2011, **257**, 5083-5087.

Chapter 2

Fugitive inclusions of ZnO micro flowers for enhanced light scattering and improved photovoltaic performance in TiO₂ based bifacial DSSCs

Abstract



The efficiency of a DSSC can be tuned by engineering the surface texture of the photoanode for enhanced light scattering in the active TiO₂ layer without much loss in transparency. Herein, surface roughness/voids are introduced in the TiO₂ layer by applying a sacrificial layer of ZnO micro flowers that are selectively etched by TiCl₄ treatment. The voids as well as the surface roughness thus created act as scattering centers improving the light absorption by dyes, thereby improving the photocurrent generation. Under one sun illumination, an improvement in power conversion efficiency of 12.9% with front illumination and 17.5% from back illumination was obtained. With the surface engineered DSC an enhancement in power converting efficiency up to 84.7% was achieved in ambient light (1000 lux, CFL) conditions. It is expected that the photoanode designed with ZnO microflowers as a sacrificial layer will be an alternative approach to improve the performance of DSSCs under one sun and ambient light conditions for bifacial building integrated photovoltaic (BIPV) applications.

2.1 Introduction

Dye-sensitised solar cells (DSSCs) have been vigorously pursued for the last two decades as promising alternatives to conventional silicon and thin film technologies owing to its low production cost, ease of fabrication and relatively high power conversion efficiency (PCE ~14%).¹ More recently, dye sensitised cells (DSCs) are identified to be a better practical option for power generation under indoor light conditions, with efficiency reaching up to 32% under 1000 lux illumination.² This exceptional quality makes DSCs perfect substituent to wired and battery energy sources.³ Multiple strategies are being attempted to enhance the DSSC/DSC performance by developing efficient photoanodes. Fabricating semiconductor materials with high surface area in order to achieve superior dye loading and high porosity for electrolyte diffusion are the most pursued strategies to develop photoanodes with improved properties.⁴ Alternative approaches include the use of 1D structures for fast electron transport,⁵ and surface modification on conductive glass as well as semiconductor active layer with nanometer sized particles to reduce the electron recombination in DSSC.⁶⁻⁹

Apart from these approaches, insertion of scattering layer is a conventional strategy that has been long employed in DSSCs for optical absorption enhancements. According to Mie theory, particles with sizes comparable to the wavelength of incident light can effectively scatter incident light. Utilisation of such kind of particles in DSSC is aimed to reflect back the incident light to the active layer so that the average path length of light is extended, enhancing the probability of it being absorbed by the dye molecules.^{10, 11} In a typical DSSC/DSC, the photoanode is composed of nanoparticles with ~20 nm size with appreciably high surface area for effectively adsorbing dye molecules for efficient light harvesting. However, the nanoparticles thus employed are poor in light scattering and a large amount of incident light is lost by transparency of the photoanode, reducing the availability of incident photons for the dye. Generally light scattering is achieved in three different ways in DSSC 1) Incorporation of larger particles as light scattering centres into the nanocrystalline film^{12, 13} 2) depositing a layer comprising of submicron sized particles over nanocrystalline layer (bilayer structure)^{14, 15} 3) developing single layer photoanode with 3D hierarchical nanostructures which can provide effective light

scattering, direct charge transport and better dye adsorption.^{16, 17} A few reports discussed the effect of voids in active layer as scattering centres to enhance the performance of DSSC. Hore *et al.* reported inclusion of spherical voids as scattering centres in TiO₂ film through the incorporation of carboxyl stabilised polystyrene spheres anchored onto the TiO₂ surface. These hollow scattering voids increased the current density as well as fill factor, leading to an overall improvement in device efficiency by 25% under one sun conditions.¹⁸ Quasi-inverse opal (QIO) layers with imperfect periodicity of voids were demonstrated as scattering layers in DSSC by Han *et al.* They have synthesised highly crystalline anatase nanocrystals via sol gel method and mixed with an aqueous solution containing monodisperse carboxylated polystyrene (PS) particles (420 nm and 970 nm) for the fabrication of QIO layer. These porous layers exhibited high dye loading and effective light scattering over the wavelength range of 600–750 nm. It was observed that the photocurrent of DSSC based on the 420 nm QIO layer is significantly higher, consequently achieving a power-conversion efficiency of 5.7%.¹⁹ Laser treatment on TiO₂ photoanode was done by Pu *et al.* to introduce pores and cracks over it. After treatment, films become less transparent indicating the high light scattering due to the rougher surface. The PCE is increased by 4.49% to 5.59% for cells with and without laser irradiation respectively.²⁰

Commercially available scattering layer pastes of TiO₂ make use of 400 nm sized particles to fabricate scattering layer of ~ 4 μm thickness. Such layers are opaque in nature and therefore are not suitable for bifacial building integrated photovoltaic (BIPV) applications. Herein, a facile methodology is reported to generate surface roughness over TiO₂ photoanodes for enhanced light scattering in the active layer without much reduction in transparency of photoanodes is discussed (**Figure 2.1**). ZnO micro flowers are deposited to function as a sacrificial layer over TiO₂ active layer to create surface roughness. Owing to its three dimensional structure, ease of synthesis and fast etching rates, ZnO serves as an ideal choice for the aforesaid purpose. Photovoltaic performances of DSSCs with and without surface modification at one sun intensity (100 mW/cm²) and low light conditions (1000 lux) are studied, which showed prominent improvements in photovoltaic performance in both outdoor/indoor lighting conditions. This type of

surface modification of the photoanode to enhance light scattering is a first of its kind approach, to the best of our knowledge. It is believed that similar device engineering approaches would certainly aid in realising appreciable device efficiencies and the future requirements of BIPV industry.

2.2 Experimental Section

2.2.1 Synthesis of Zinc Oxide Microflower

ZnO micro flowers were synthesised through a hydrothermal process. For a typical synthesis, 3.7186 g of zinc nitrate hexahydrate ($\text{Zn}(\text{NO}_3)_2 \cdot 6\text{H}_2\text{O}$, Merck), dissolved in 100 ml distilled water, is added to 400 ml of distilled water containing 0.1752 g of hexamethylenetetramine (HMTA, Merck), 1.456 g of polyethyleneimine (PEI, 50 wt% solution in water, M_w 1300, Sigma aldrich) and 11.391 g of ammonia solution (25%, Merck). The reaction mixture is then placed in an autoclave at 90 °C for 5 h. Finally, the obtained products were washed with distilled water and dried at 60 °C in oven.

2.2.2 ZnO Paste preparation

About 0.0521 g of ethylcellulose (TCI) was made into a viscous liquid in terpineol (TCI) by heating. This was then blended with 0.1833 g of ZnO microflowers in a mortar to obtain the paste for doctor blading.

2.2.3 Etching of ZnO microflowers

Etching of the ZnO microflowers deposited on the TiO_2 film was done by immersing the annealed photoanodes in aqueous 40 mM TiCl_4 solution for 30 minutes at 70 °C. It was subsequently subjected to a programmed annealing processes upto 500 °C.

2.2.4 Fabrication of DSSC

The FTO substrates were systematically cleaned using detergent solution, distilled water, acetone, and isopropanol. The cleaned substrates were then annealed in furnace up to 500 °C. Pre-blocking layers were deposited by immersing cleaned FTO substrates in aqueous 40 mM TiCl_4 solution for 30 minutes at 70 °C. The deposited films were

subjected to a programmed heating at 325 °C for 15 min, 375 °C for 15 min, 450 °C for 15 min, and 500 °C for 30 min and cooled down to room temperature. This is followed by the deposition of active TiO₂ (Dyesol) layer and ZnO microflower layer by doctor blading process. The films were then annealed under the same conditions and heating schedule as mentioned above. For the deposition of post-blocking layer, annealed electrodes were immersed in aqueous 40 mM TiCl₄ (sigma aldrich) solution for 30 minutes at 70 °C and further heat treated at 500 °C. Electrodes were then immersed into N719 dye (Dyesol) solutions (0.3 mM) with chenodeoxycholic acid (CDCA) as co adsorbent (10 mM) and kept at room temperature for 15 h.

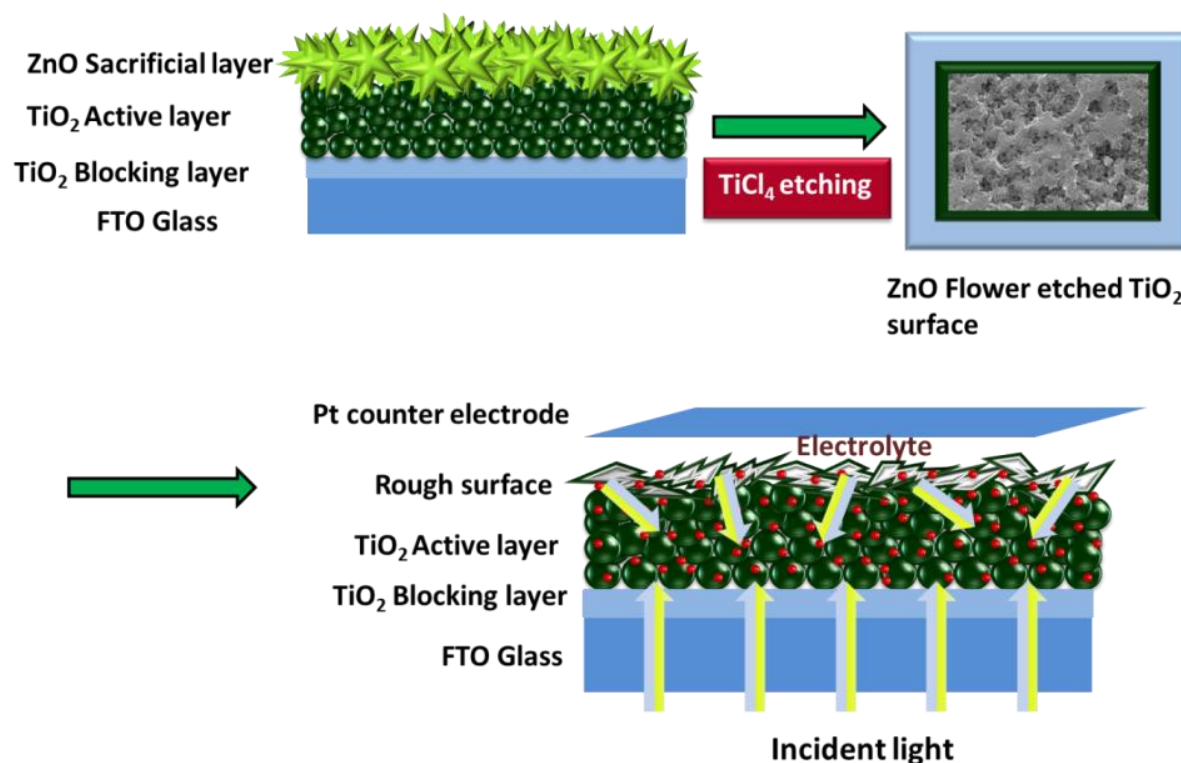


Figure 2.1 Design strategy illustrating the fabrication of DSSC utilising ZnO flowers as sacrificial layer to impart surface roughness over nanocrystalline TiO₂ active layer photoelectrodes.

Counter electrodes were prepared by coating Platinum sol (Dyesol) on FTO plates having pre-drilled holes and annealing at 380 °C for 20 min. The electrodes were then assembled with hot press using 25 µm surlyn spacer (Dyesol). The space in between

both the electrodes were filled with liquid I^-/I_3^- electrolyte composed of the standard compositions of 1-butyl-3-methylimidazolium iodide, lithium iodide, iodine, guanidinium thiocyanate and 4-*tert*-butyl pyridine in acetonitrile. The drilled holes were sealed with microscopic cover slide and surlyn to avoid electrolyte leakage. The scheme provided in **Figure 2.1** depicts the strategy employed to fabricate the DSSC.

2.2.5 Material characterisation

X-ray diffraction (XRD) analysis was performed to confirm the crystallinity and phase purity of fabricated ZnO hierarchical structures as well as the films (PANalytical X'Pert PRO operated with Cu $K\alpha$ radiation (X-ray wavelength $\lambda = 1.5406 \text{ \AA}$)). The morphology and the size of the materials synthesised were confirmed by SEM and TEM analysis. SEM analysis and energy dispersive spectroscopy (EDS) was done in scanning electron microscope (SEM) Carl Zeiss, Germany. TEM analysis was carried out in transmission electron microscope (HRTEM, FEI Tecnai 30 G2S-TWIN) operated at an accelerating voltage of 300 kV. Atomic force microscopy (AFM) images (Tapping-mode) were recorded by using Bruker multimode 8-AFM. The thickness of photoanode was measured using a Bruker Dektak XT profilometer. Diffuse reflectance spectra (DRS) of the photoanode films were recorded in UV/VIS/NIR spectrometer (Perkin Elmer Lambda 950).

2.2.6 Photovoltaic characterisation

Photocurrent density-voltage ($J-V$) characterisation of the fabricated cells were carried out under one sun conditions (100 mW/cm^2 , AM 1.5G) using a source meter (Keithley 2440) along with a class AAA solar simulator (Oriel 3A, Model PVIV- 94043A, Newport). Certified reference silicon solar cell (Newport) coupled with power meter was used to calibrate the light intensity. A circular mask with an area of 0.1256 cm^2 was used for measuring $J-V$ parameters (un-masked active area of the devices were 0.317 cm^2). The thickness of the photoanodes were measured to be $6\text{-}7\text{ }\mu\text{m}$. The incident photon-to-current conversion efficiency (*IPCE*) measurements of devices were performed under DC mode using a 250 W Xenon lamp coupled with a monochromator setup (Newport). $J-V$ measurement for indoor light conditions was carried using custom made set up with

fluorescent tube (CFL) as a light source. The irradiance of the CFL was measured with highly sensitive photodetector coupled with a measuring unit. The electrochemical impedance spectroscopy (EIS), intensity modulated photovoltage spectroscopy (IMVS), intensity modulated photocurrent spectroscopy (IMPS), the open-circuit voltage (V_{oc}) decay were performed using the electrochemical workstation, Autolab-PGSTAT 302N (Metrohm). For EIS, IMPS and IMVS studies frequency response analyser (FRA32M) was coupled with the workstation. The impedance plots were recorded in dark, at applied forward bias from 0.65 V to 0.75 V, with a perturbation of amplitude 10 mV with frequency ranging from 100 mHz to 100 kHz, increasing logarithmically. The obtained impedance plots were fitted with equivalent circuit containing transmission line model using NOVA 1.11 software. For IMVS and IMPS measurements Autolab was equipped with an LED driver to drive the white LED source, in addition to the FRA. In IMVS and IMPS measurements, light perturbation was 10% of the steady state light with frequency ranging from 1 Hz to 10 kHz. The open-circuit voltage decay (OCVD) measurements were done using LED as illumination source. The output current density of devices was matched with the current density as obtained under one sun condition.

2.3 Results and Discussion

2.3.1 Synthesis and characterisation of ZnO microflowers

The reaction mixture utilised for ZnO microflower synthesis composed of zinc nitrate hexahydrate ($Zn(NO_3)_2 \cdot 6H_2O$), hexamethylenetetramine (HMTA), polyethyleneimine (PEI) and ammonia solution. Zn^{2+} ions generated by the $Zn(NO_3)_2 \cdot 6H_2O$ and OH^- ions produced by HMTA, NH_4OH system reacted rapidly generating tetrahedral $Zn(OH)_4^{2-}$ and $Zn(NH_3)_4^{2-}$ complexes. Such complexes act as the growth units of ZnO crystal which preferentially grow along the c-axis [0001] direction. PEI in reaction mixture helps to reduce the width of the rods (petals) through its non polar lateral surface interaction resulting in the formation of flower shaped ZnO crystals.²¹

2.3.2 X-ray diffraction analysis

In order to study the morphology evolution of ZnO flowers, synthesis were carried out in

different reaction time (30 min, 2 h, and 5 h). The XRD patterns of the as-synthesised samples are presented in **Figure 2.2** and the planes (100), (002) and (101) at 2θ values between 30° and 40° confirmed the presence of hexagonal wurtzite phase of ZnO crystal matching with the Joint Committee on Powder Diffraction standards (JCPDS) file no. 76-0704.

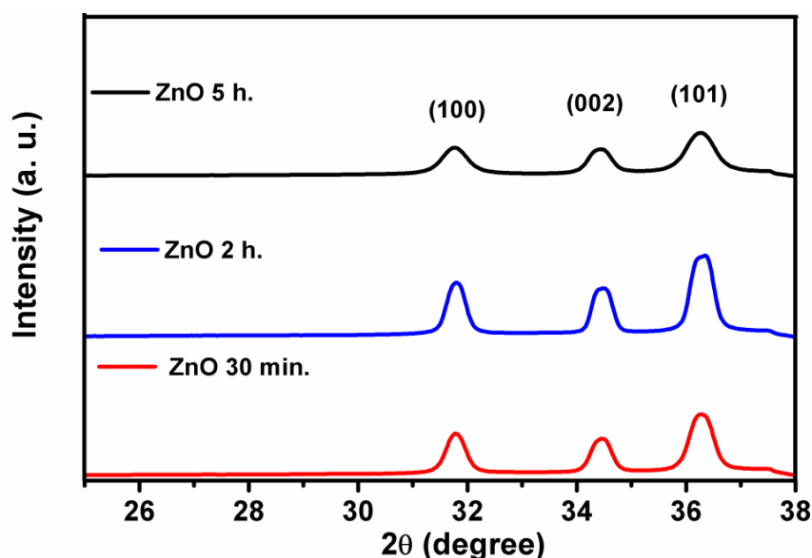


Figure 2.2 XRD patterns of as-synthesised ZnO at different reaction time.

2.3.3 Morphology analysis

SEM and TEM images of the as-synthesised samples under different reaction times are shown in the **Figure 2.3**. From the SEM images it is clear that after 30 min reaction the products obtained are micro rods (**Figure 2.2 a and b**). The rods so formed are of 1.6–2.8 μm in length and 0.12–0.25 μm in width, indicating an aspect ratio in the range of 11–13. It was observed that when the reaction time is extended to 2 hours, a mixture of rods and sheet like structures are formed (**Figure 2.3 c and d**). Further increase in the reaction time for 5 hours resulted in the formation of flowers with 2–4 μm size (**Figure 2.3 e and f**).

TEM images of the samples presented in **Figure 2.2 (b, d and f)** also confirmed the respective morphology and the selected area diffraction (SAED) pattern given in inset suggested high crystallinity of the ZnO formed at each time period.

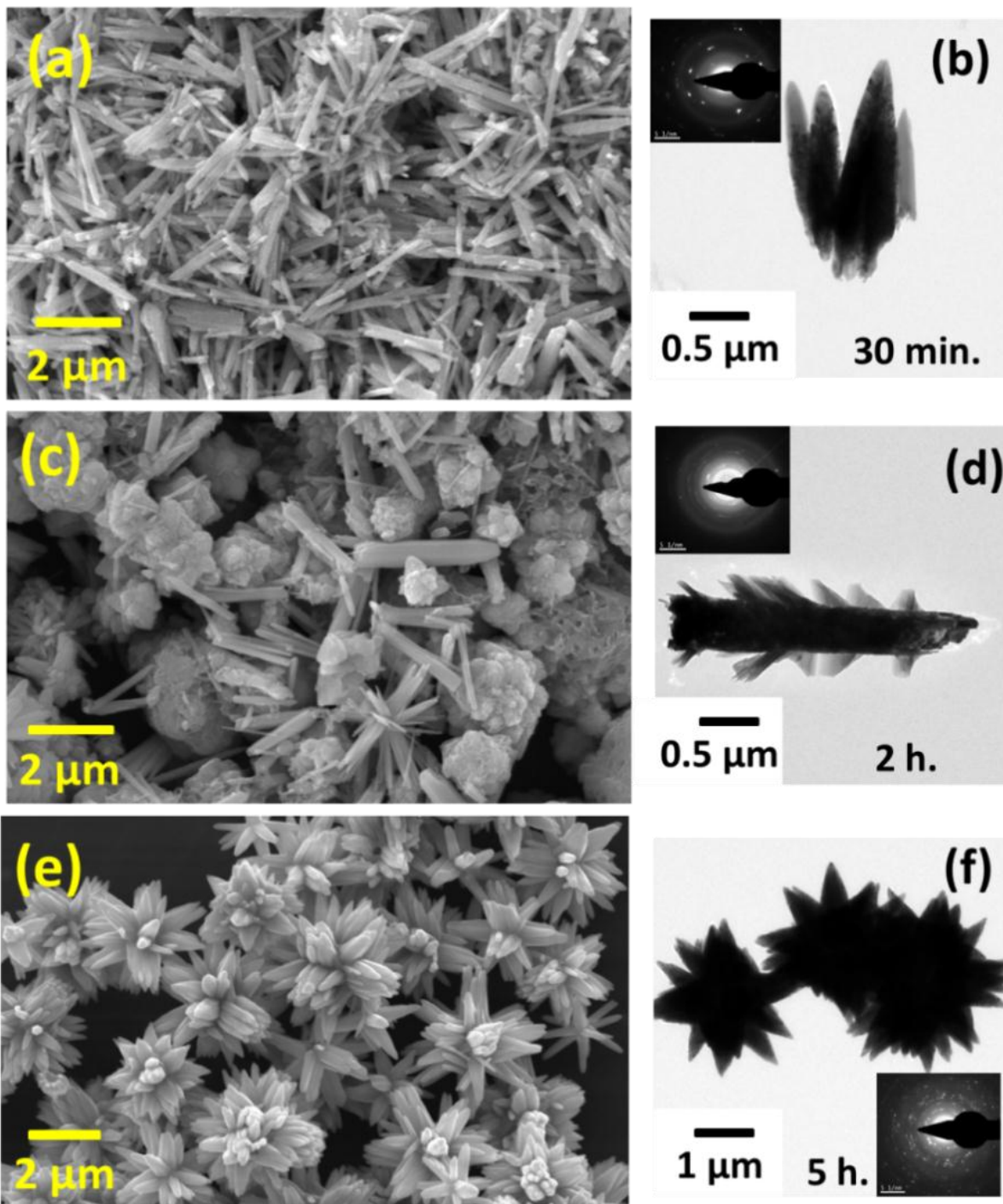


Figure 2.3 SEM images of as-synthesised ZnO micro flowers at 30 min (a), 2 h (c) and 5 h (e) and corresponding TEM images b, d and f (SAED patterns are given in inset).

2.3.4 Surface area and pore size analysis

Specific surface area and pore size distribution of the as-synthesised ZnO flower was measured using N₂ adsorption/desorption analysis. ZnO microflowers showed Type IIb isotherm with H3 hysteresis loop, shown in **Figure 2.4a**, which suggests that the particles are aggregates with slit shaped pores. The Brunauer-Emmet-Teller (BET) surface area is measured to be 2 m²/g. The lower surface area is due to the larger size of the rods which the flowers are composed off. The Barrett-Joyner-Halenda (BJH) pore size distribution of aforementioned powder is provided in **Figure 2.4b**. This plot indicates that the ZnO microflowers possess both meso and macro pores. It has a larger portion of macro pores with size ranges from 100 nm to 225 nm.

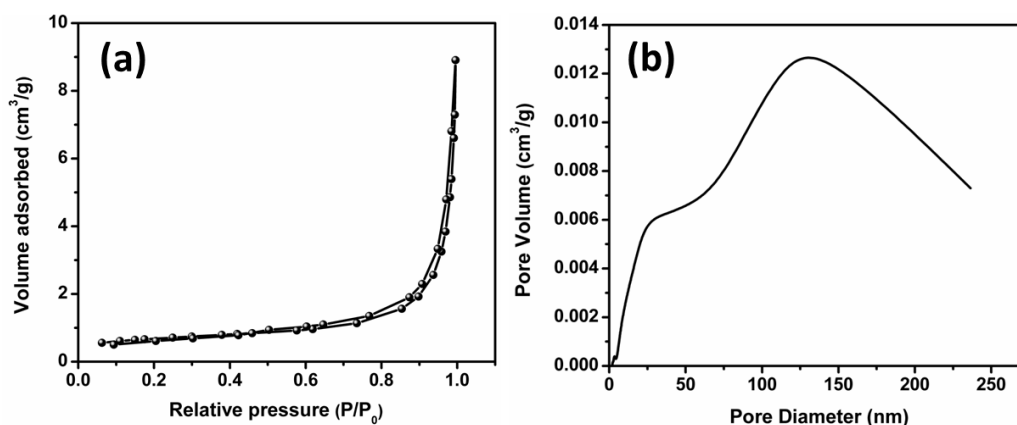


Figure 2.4 (a) N₂ adsorption/desorption isotherms of as-synthesised ZnO micro flowers and (b) corresponding BJH pore size distribution curve.

2.3.5 Characterisation of TiO₂ paste

Commercially available TiO₂ paste (Dyesol) is used for the fabrication of photoanodes and the basic characterisations carried out for the same is discussed in this section. **Figure 2.5a** shows the powder XRD patterns of the annealed film cast from TiO₂ paste. The peaks are assigned to the anatase phase of TiO₂, matches with the JCPDS file no. 01-075-1537. TEM analysis of the annealed TiO₂ film is presented in **Figure 2.5b** which reveals that the film is composed of elongated particles with size ranges from 10-40 nm. The SAED pattern given in inset suggests the crystalline nature of the sample.

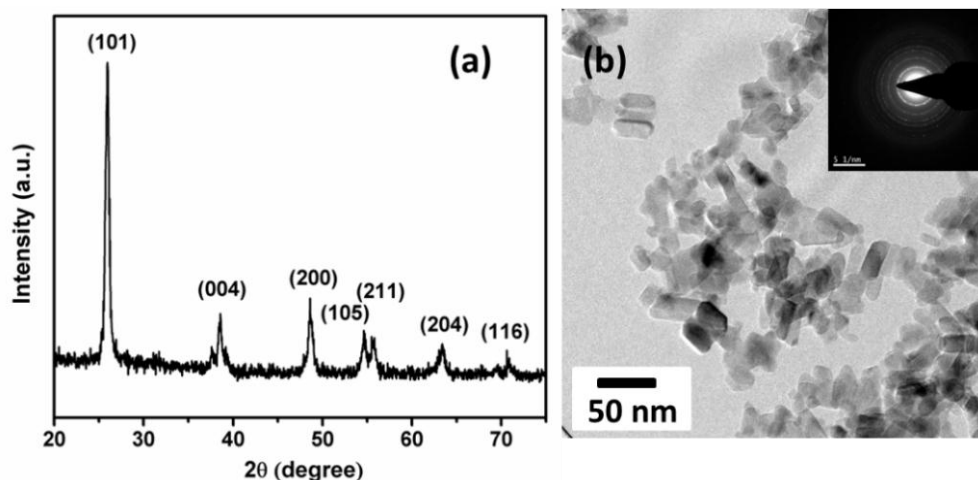


Figure 2.5 (a) XRD pattern of annealed TiO₂ film and (b) TEM image of the respective film (SAED pattern is given in inset).

The BET surface area and BJH pore size analysis are investigated using N₂ adsorption/desorption analysis. **Figure 2.6a** represents the N₂ adsorption/desorption isotherm of TiO₂ film scraped from the FTO glass. The plot displays type IIb isotherm with H3 hysteresis loop indicating the presence of slit shaped pores. The BET surface area is observed to be 54 m²/g. The BJH pore size distribution curve suggested that the mesoporous TiO₂ particles within the range of 10-70 nm, with an average pore size of 37 nm (**Figure 2.6b**).

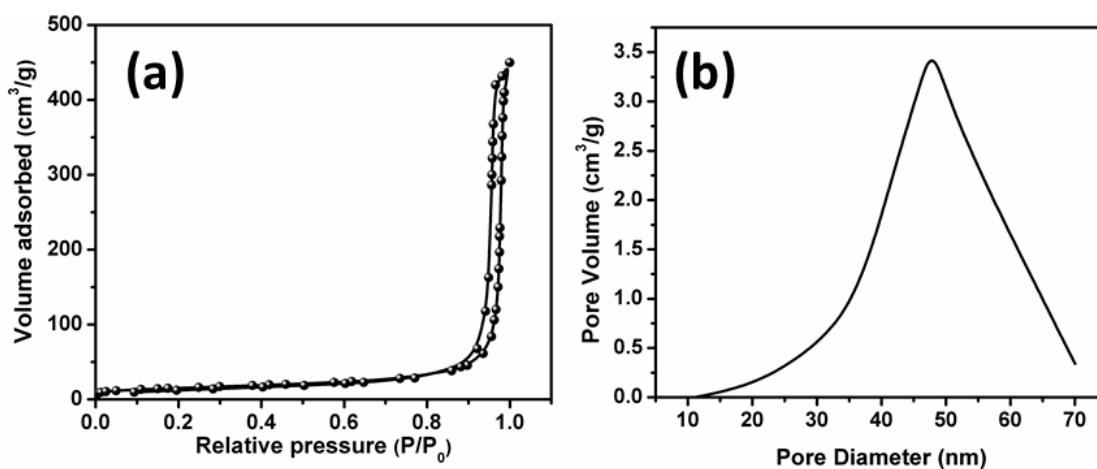


Figure 2.6 (a) N₂ adsorption/desorption isotherms of TiO₂ film and (b) corresponding BJH pore size distribution curve.

The thermal decomposition profile of the TiO₂ paste is presented in **Figure 2.7**. On heating upto 800 °C, about 62% of TiO₂ is obtained from the paste utilised for fabrication of photoanode films. The data showed a three stage weight loss for the paste with an initial weight loss of solvents in the temperature range of 94-235 °C. The second weight loss of ~35% at 235-350 °C is attributed to the combustion of ethyl cellulose to CO₂ (g) and H₂O (g) and the final weight loss ~8% at 350–500 °C is due to the combustion of residual carbonaceous material from ethyl cellulose.

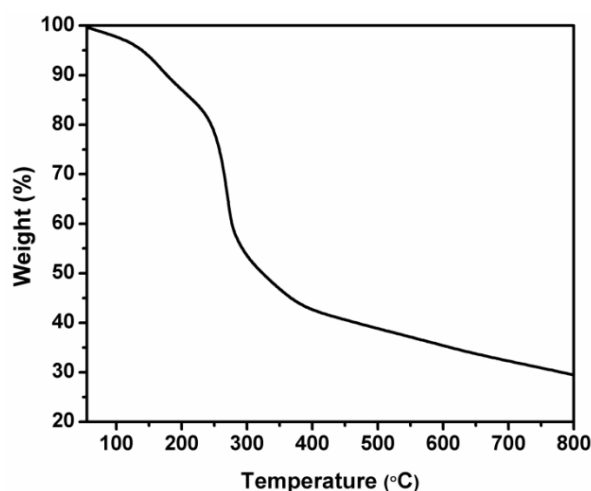


Figure 2.7 TGA curve of TiO₂ paste used for active layer.

2.3.6 Characterisation of photoanode films

2.3.6.1 X-ray diffraction analysis

The phase purity of the photoanode films utilised for the solar cell fabrication is discussed in this section. The XRD patterns of the annealed photoanode films scraped from the FTO glass, TiCl₄ treated TiO₂ film (TiO₂), TiO₂-ZnO bilayer film without TiCl₄ treatment and with TiCl₄ treatment (TiO₂-ZF) are shown in **Figure 2.8 a, b and c** respectively. The peaks of patterns in **Figure 2.8 a and c** are indexed to phase pure anatase TiO₂ crystal referring to the JCPDS file no 01-075-1537. The XRD pattern in **Figure 2.8c** is completely devoid of ZnO peaks confirming the complete etching of ZnO particles after TiCl₄ treatment. The untreated TiO₂-ZnO bilayer film indicated peaks of both anatase TiO₂ and wurtzite ZnO (**Figure 2.8b**).

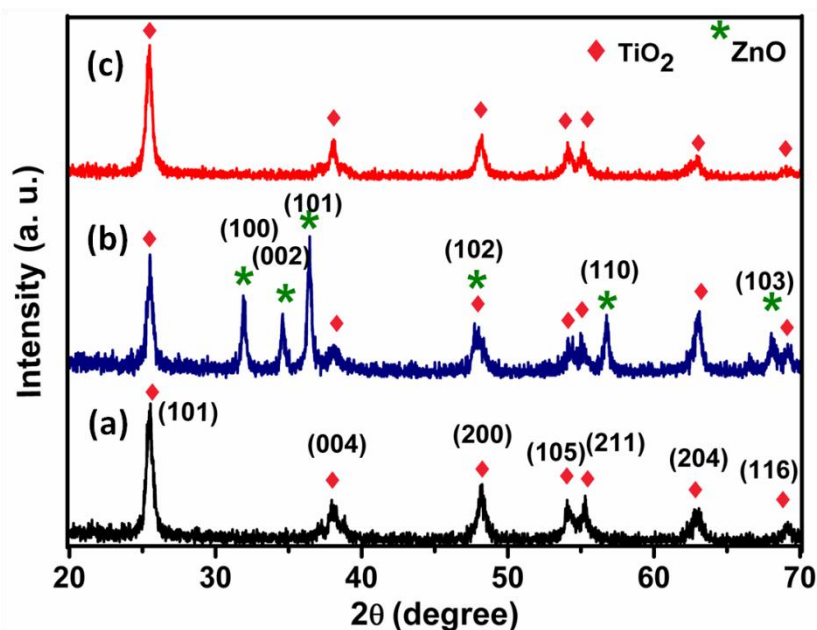


Figure 2.8 XRD patterns of annealed photoanode films (a) TiCl_4 treated TiO_2 film (b) TiO_2 -ZnO bilayer film and (c) TiCl_4 treated TiO_2 -ZnO bilayer film.

2.3.6.2 Scanning electron microscopy

The morphology and microstructural features of the doctor bladed photoanode films were analysed using SEM. **Figures 2.9 (a-f)** depict SEM images of TiCl_4 treated TiO_2 (**a** and **b**), TiO_2 -ZnO without TiCl_4 treatment (**c** and **d**) and TiCl_4 treated TiO_2 -ZnO (**e** and **f**) annealed films utilised for the cell fabrication. It is clearly seen that the TiCl_4 treated TiO_2 film is homogenous in nature and is composed of nanoparticles less than 50 nm in size (**Figure 2.9b**). SEM images of the TiO_2 -ZnO flower film (**Figure 2.9 c and d**) convey that the ZnO flowers covered the TiO_2 film and retained its morphology even after annealing at 500 °C. As the sacrificial layer containing ZnO was doctor bladed over the transparent TiO_2 paste, prior to annealing, protruding petals of the ZnO flowers get partly immersed into the TiO_2 layer. This surface structure is retained even after the annealing at 500 °C. The annealed electrodes were then subjected to TiCl_4 treatment. SEM **Figure 2.9 (e and f)** clearly depicted that the ZnO flowers are etched off due to the instability of basic ZnO in acidic TiCl_4 solution leaving behind isotopographical voids on the surface of TiO_2 film making it rough.²²

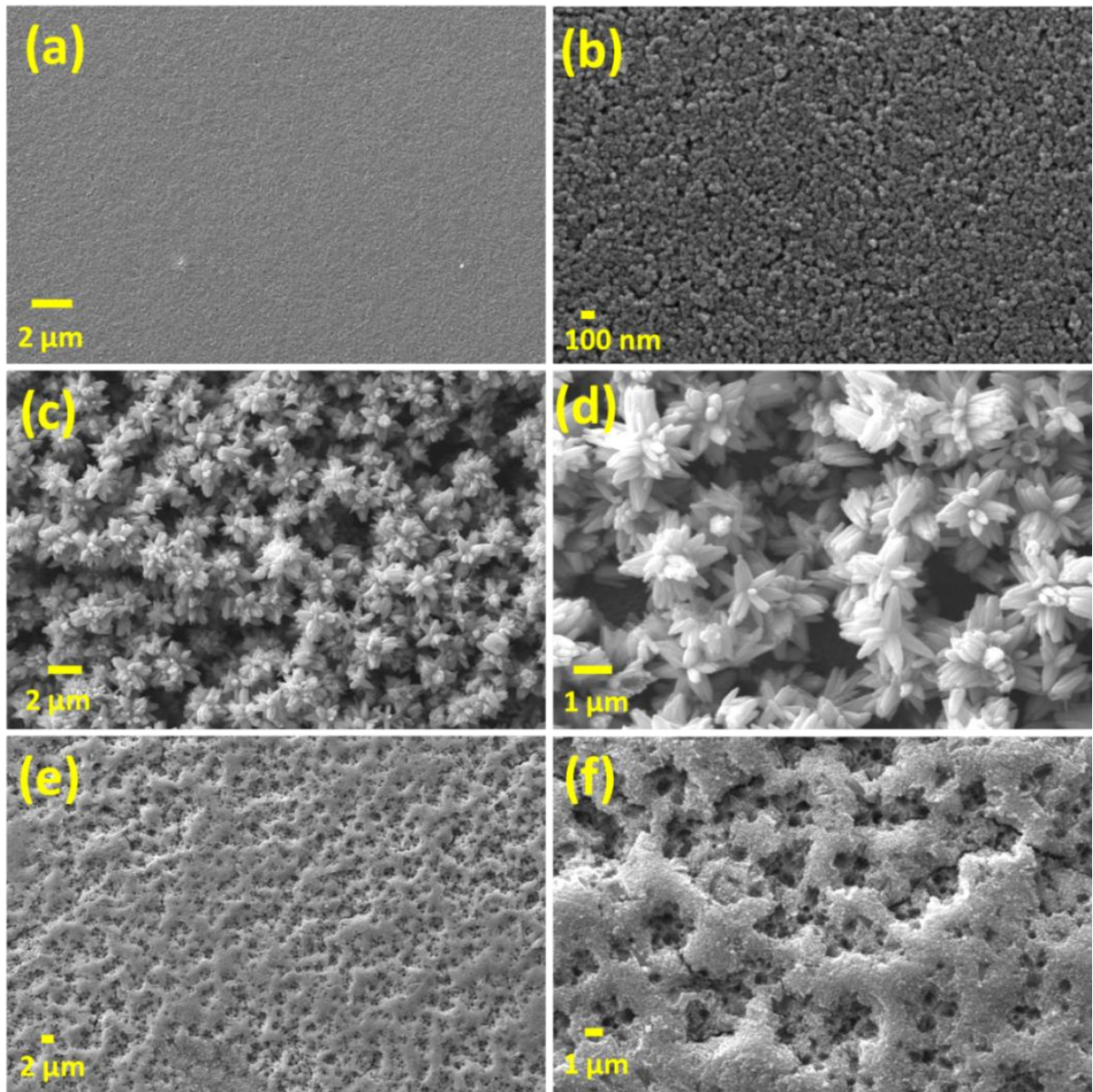


Figure 2.9 SEM images of TiCl₄ treated TiO₂ film (a and b), TiO₂-ZnO flower film (c and d) and TiCl₄ treated TiO₂-ZF film (e and f).

It is inferred that this method create surface roughness all over the film as the impressions of the flowers are clearly seen from the high resolution SEM image provided in the **Figure 2.9f**.

2.3.6.3 Energy dispersive X-ray analysis and Elemental mapping

In order to confirm the distribution of elements present in each film, we have carried out

energy dispersive X-ray (EDX) analysis (**Figure 2.10**). **Figures 10 a, b and c** correspond to the films TiCl_4 treated TiO_2 film, TiO_2 -ZnO bilayer film without TiCl_4 treatment and with TiCl_4 treatment respectively.

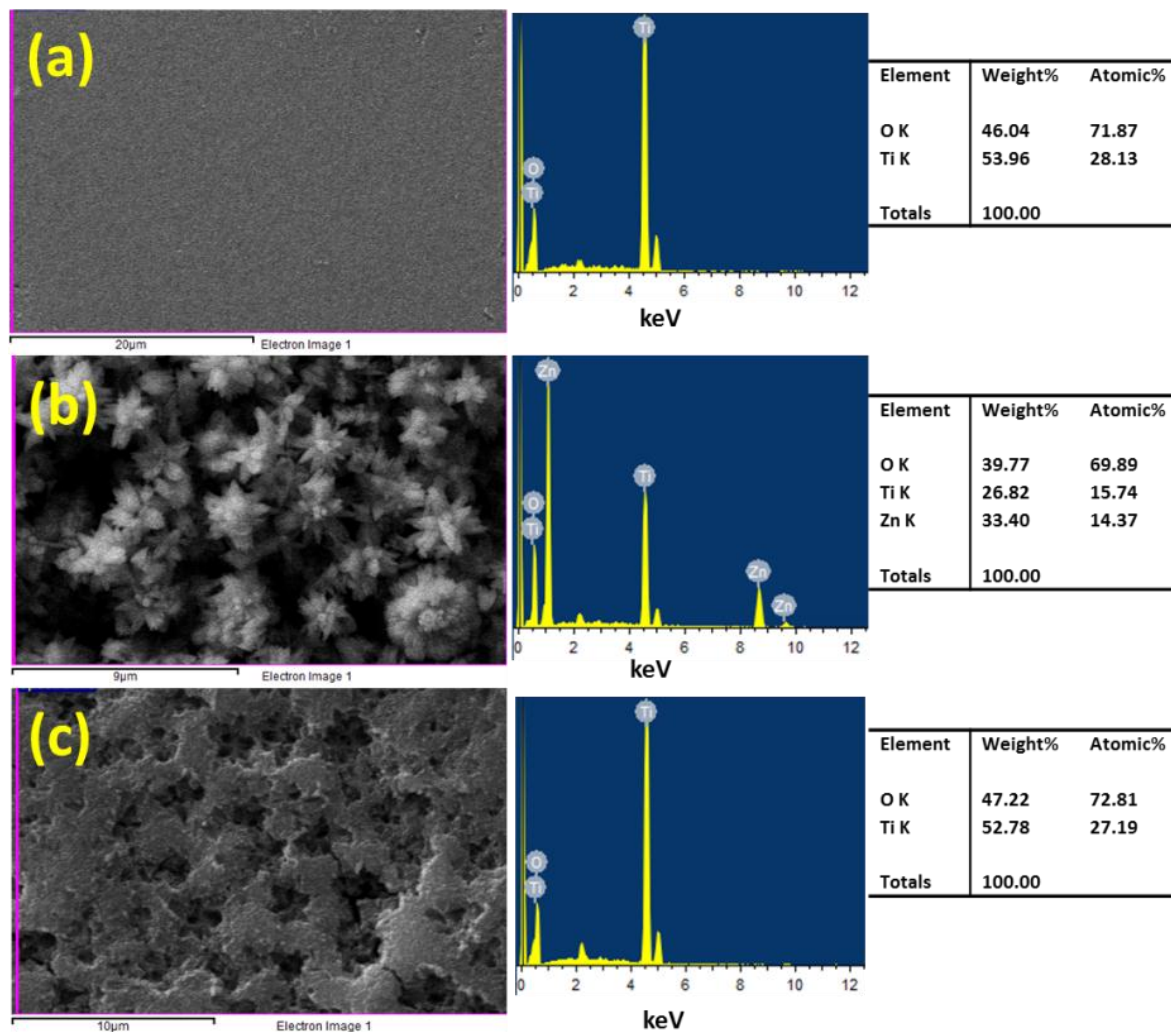


Figure 2.10 EDX of (a) TiCl_4 treated TiO_2 film, (b) TiO_2 -ZnO flower film and (c) TiCl_4 treated TiO_2 -ZF film.

The relative percentage of the elements present in each film is provided in **Figure 2.10**. No trace of Zn in TiCl_4 treated TiO_2 -ZF film confirmed the complete removal of ZnO after TiCl_4 treatment. The distribution of the elements (Ti, O and Zn) in the films TiCl_4 treated TiO_2 , TiO_2 -ZF and TiCl_4 treated TiO_2 -ZF are also analysed through elemental mapping and is presented in **Figure 2.11 a, b and c**

respectively. Distribution of Zn, Ti and O is clearly seen in TiO₂-ZF film without TiCl₄ treatment (**Figure 2.11b**).

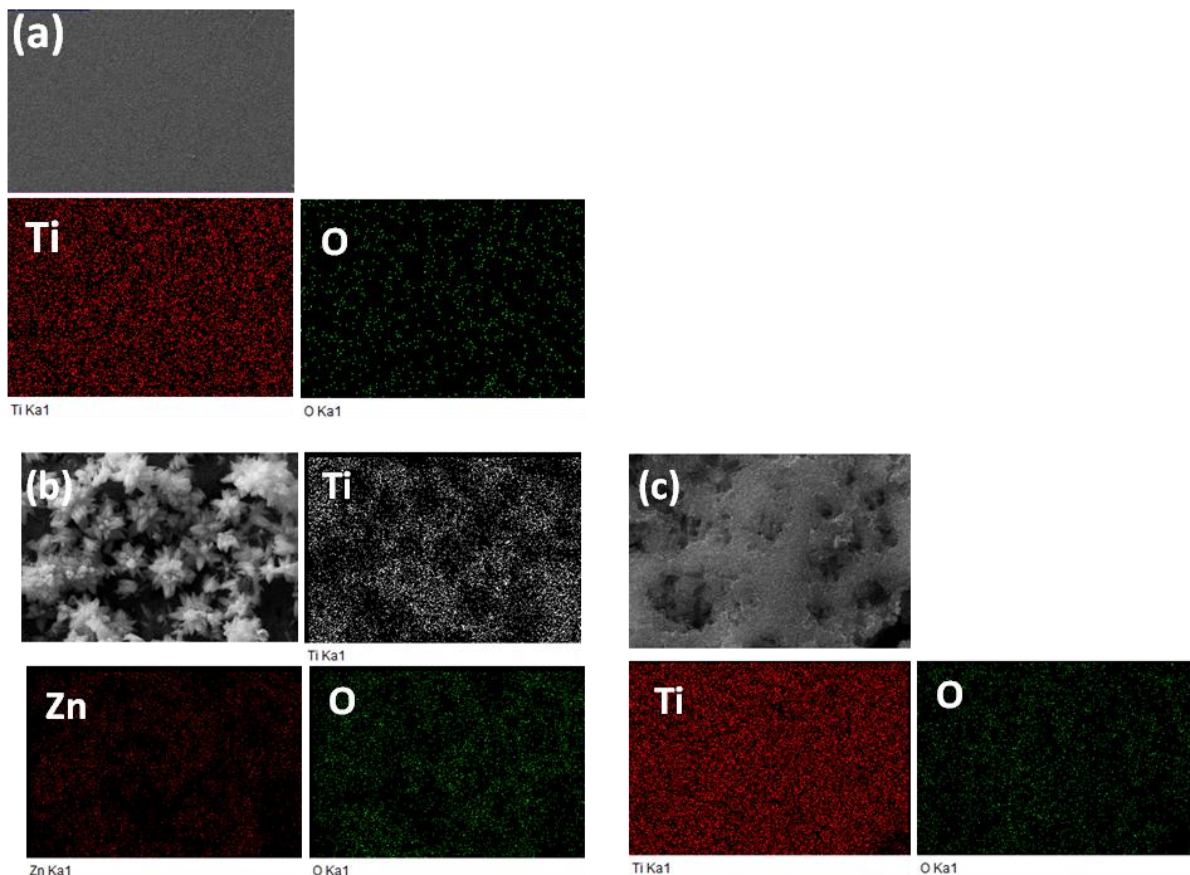


Figure 2.11 Elemental mapping of (a) TiCl₄ treated TiO₂ film, (b) TiO₂-ZnO film and (c) TiCl₄ treated TiO₂-ZF film.

2.3.6.4 Diffuse reflectance spectroscopy

Optical reflectance properties were analysed to verify the light scattering effect in TiCl₄ treated photoanodic films with bare TiO₂ and TiO₂-ZF film (**Figure 2.12**). The light reflection of surface modified and etched photoanode is about 6 to 0.5% higher than that of bare TiO₂ film in the wavelength range of 400-680 nm. The voids/surface roughness created over the surface of the TiO₂ film acted as light scattering centres enhancing the average path length of the incident light in the photoanode.

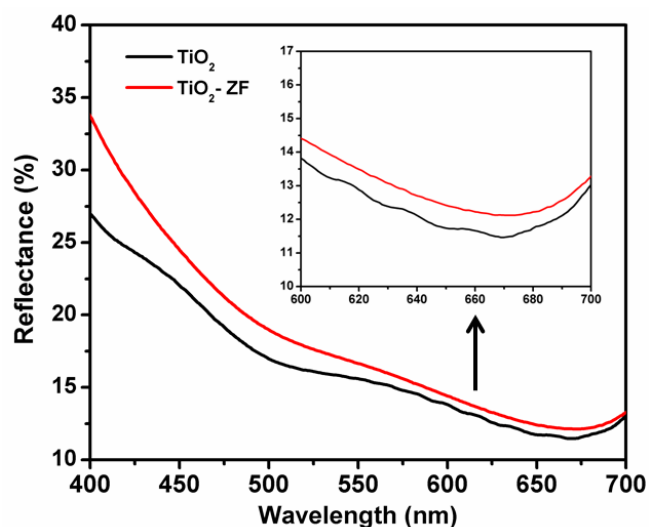


Figure 2.12 UV-vis diffuse reflectance spectra of TiCl_4 treated bare TiO_2 and TiO_2 -ZF flower photoanodes before dye loading (magnified portion of graph from 600 nm-700 nm wavelength is given in inset).

The photographs of the anodes before and after TiCl_4 treatment is presented in **Figure 2.13**. The bare TiO_2 films before and after TiCl_4 treatment is observed to be transparent whereas TiO_2 -ZnO film before TiCl_4 treatment is opaque owing to the micron size of ZnO flowers. After TiCl_4 treatment, the ZnO flowers were completely etched off creating voids of similar dimensions and topography. The transparency is slightly reduced when compared with TiCl_4 treated bare TiO_2 films.

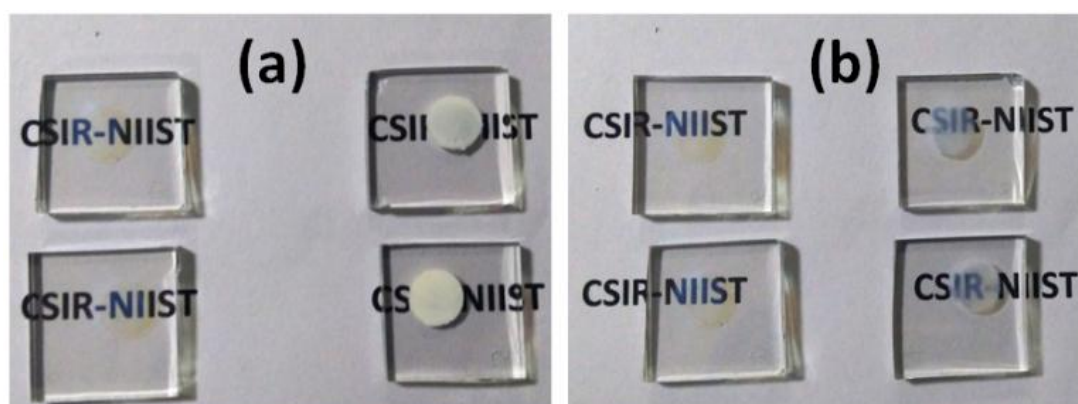


Figure 2.13 Photoanodes before TiCl_4 treatment (a) bare TiO_2 film (left) and TiO_2 -ZnO film (right) and corresponding films after TiCl_4 treatment (b).

2.3.6.5 Atomic force microscopy

Surface roughness of the photoanode films were investigated by AFM analysis (**Figure 2.14**). Bare TiO₂ film (**Figure 2.14a**) possessed a Rq (root mean square roughness) value of 18 nm and Rz value (maximum roughness) of 169 nm whereas the TiCl₄ treated TiO₂-ZF film (**Figure 2.14b**) showed a high Rq value of 244 nm and Rz value of 1566 nm. The presence of surface voids over the TiCl₄ treated TiO₂-ZF film has increased the surface roughness by around 10 times than that of the TiCl₄ treated TiO₂ film. This advantage of our approach over conventional scattering layer deposition method implies that the photovoltaic performance can be improved without the incorporation of an extra scattering layer thereby reducing the thickness of the photoanode and retaining the transparency of the active layer.

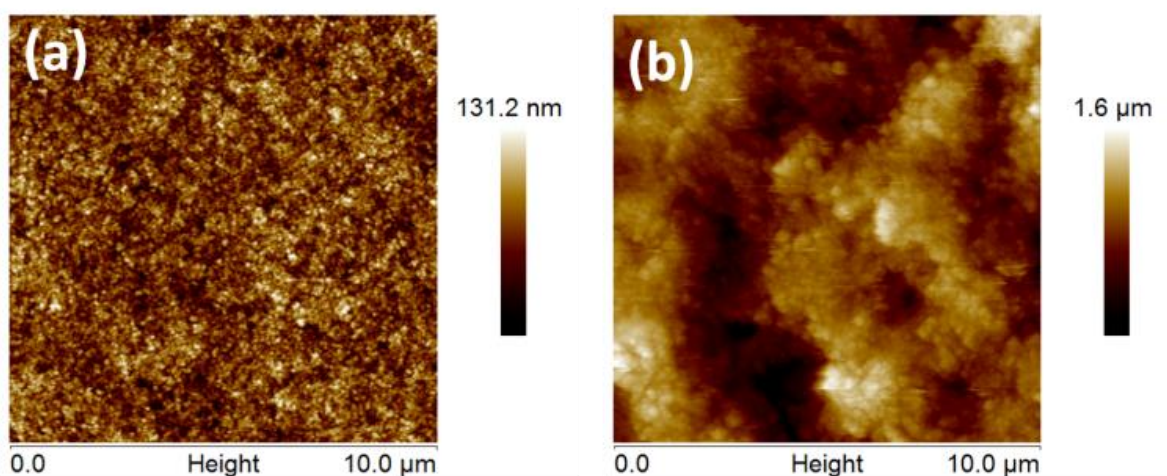


Figure 2.14 AFM images of TiCl₄ treated (a) bare TiO₂ and (b) TiO₂-ZF photoanodes.

2.3.6.6 Dye loading studies

The quantity of dye adsorbed on to the photoanodes was examined by using dye adsorption-desorption procedure. Desorption of the adsorbed dye is done by soaking the electrodes in 0.1 N NaOH solution in water. After the complete desorption of dye, the absorbance spectra of the desorbed dye was recorded (**Figure 2.15**). The concentration of the dye is calculated using the equation provided below.

$$\text{Dye loading} = AV/\epsilon Sb \quad (1)$$

Where A is the absorbance of the dye, V is the volume of NaOH used to desorb the dye (5 ml), ϵ is the molar extinction coefficient of the dye N719 ($13500 \text{ mol}^{-1} \text{ cm}^{-1}$), S is the area of the electrode (0.317 cm^2) and b is the path length (1 cm). Bare TiO_2 have shown a dye loading of $5.75 \times 10^{-8} \text{ mol cm}^{-2}$ and $\text{TiO}_2\text{-ZF}$ has also displayed almost similar dye loading of $5.64 \times 10^{-8} \text{ mol cm}^{-2}$. Hence it can be concluded that the roughness created over the TiO_2 layer by ZnO flower etching does not offer any improvement in dye loading.

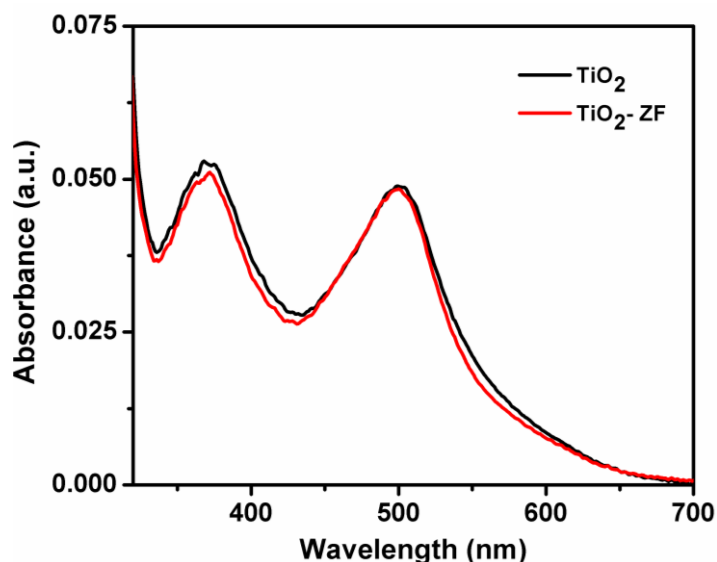


Figure 2.15 Absorption spectra of the desorbed dyes from the photoanodes.

2.3.7 Photovoltaic Characterisations

2.3.7.1 Current voltage characteristics and IPCE measurements

The current density and voltage characteristics (J - V) were determined through measurements under simulated one sun illumination using class AAA solar simulator. **Figure 2.16** shows the J - V and IPCE of TiO_2 and $\text{TiO}_2\text{-ZF}$ DSCs on front side (**Figure 2.16 a** and **b**) and back side illuminations (**Figure 2.16 c** and **d**). The corresponding parameters are summarised in **Table 2.1**. Illumination from the front side (active layer side) showed a V_{oc} of 737 ± 18 mV, J_{sc} of $11.56 \pm 0.80 \text{ mAcm}^{-2}$ with FF $70.88 \pm 6.60\%$ yielding a PCE upto $6.04 \pm 0.99\%$. Similarly $\text{TiO}_2\text{-ZF}$ showed a V_{oc} of 738 ± 29 mV, J_{sc} of $14.00 \pm 1.23 \text{ mAcm}^{-2}$ with FF $66.03 \pm 3.59\%$ resulting in a PCE upto $6.82 \pm 1.01\%$. There is

an increase of 21.1% in J_{sc} using TiO_2 -ZF compared to TiO_2 photoanode resulting in an improvement of 12.9% in PCE. V_{oc} of TiO_2 and TiO_2 -ZF were identical with a reduced FF in TiO_2 -ZF than TiO_2 . The slightly reduced FF indicate the possibility of increased recombination at P_{max} using TiO_2 -ZF. The detailed recombination dynamics is discussed further in the following sections. With illumination from back side (from counter electrode side) TiO_2 showcased a V_{oc} of 719 ± 15 mV, J_{sc} of 7.67 ± 1.01 mAcm⁻² with FF $72.75 \pm 3.34\%$ resulting in a PCE of $4.01 \pm 0.75\%$, concurrently TiO_2 -ZF showed V_{oc} of 720 ± 14 mV, J_{sc} of 9.48 ± 1.14 mAcm⁻² with FF $69.01 \pm 2.02\%$ yielding a PCE upto $4.71 \pm 0.74\%$.

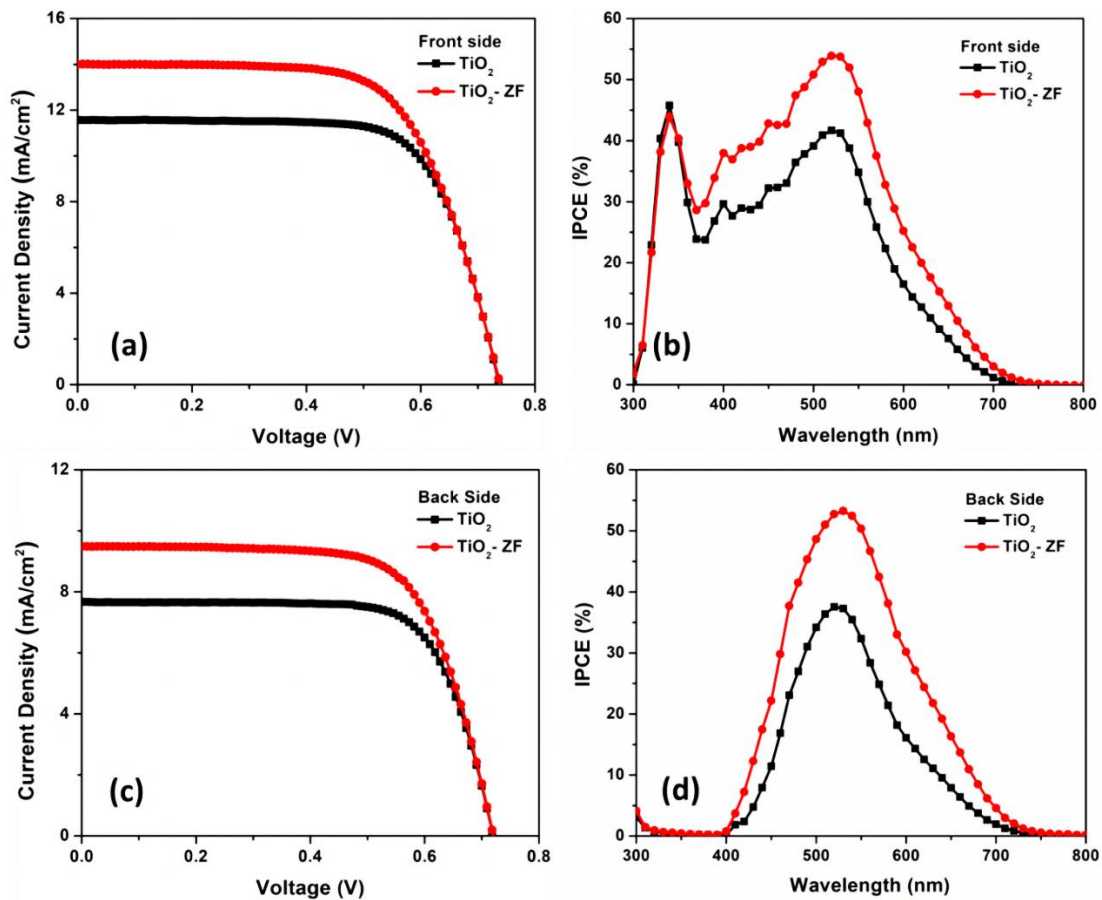


Figure 2.16 (a) J - V characteristic with front illumination, (b) IPCE with front illumination, (c) J - V with back illumination and (d) IPCE with back illumination of TiO_2 and TiO_2 -ZF.

With illumination from the back side, an enhancement of 23.5% in J_{sc} leading to 17.5% improvement in PCE was realised in TiO₂-ZF DSCs. It is to be taken into account that, for back side illumination, light pass through the I⁻/I₃⁻ electrolyte, due to which a certain portion of the light is absorbed by the electrolyte before it reaches the photoanode. Additional light absorption by electrolyte resulted in reduced J_{sc} and V_{oc} , resulting in relatively lower PCE with back side illumination compared to front illumination. Incident photon current conversion efficiency (IPCE) with illumination from both the photoanode and counter electrode sides were carried out and was in accordance with J - V results. IPCE of DSC on front illumination showed two distinguished peaks at wavelength 330 nm and 530 nm respectively (**Figure 2.16b**), while on back illumination, the resultant IPCE showed only one peak at 530 nm (**Figure 2.16d**). During back illumination light enters through surlyn (ie; back sealing cover used with cover glass) and light with wavelength upto 400 nm is cut off.

Table 2.1 Photovoltaic parameters for TiO₂ and TiO₂-ZF from front side illumination and back side illumination under one sun conditions.

Device	V_{oc} (mV)	J_{sc} (mAcm ⁻²)	FF (%)	η (%)	IPCE at 530 nm (%)
TiO₂ Front side	737 ± 18	11.56 ± 0.80	70.88 ± 6.60	6.04 ± 0.99	41.72
TiO₂-ZF Front side	739 ± 29	14.00 ± 1.23	6.03 ± 3.59	6.82 ± 1.01	53.84
TiO₂ Back side	719 ± 15	7.67 ± 1.01	72.75 ± 3.34	4.01 ± 0.75	37.52
TiO₂-ZF Back side	720 ± 14	9.48 ± 1.14	69.01 ± 2.02	4.71 ± 0.74	52.76

2.3.7.2 Interfacial charge transfer analysis

Substantial loss of energy due to the recombination of charges at the dye/TiO₂/electrolyte interface is always seen in DSCs and is reflected in the photovoltaic parameters such as V_{oc} , J_{sc} and FF . In the present context, as a means to gain higher photocurrent, roughness was introduced over TiO₂ film. To evaluate the induced change in forward and backward electron transfer, when TiO₂ comes in contact with electrolyte at modified surface, we carried out electrochemical impedance spectroscopy (EIS) in dark. The characteristic response of EIS is the Nyquist plot and Bode plot, as given in **Figure 2.17**. Nyquist plot showcased two distinct semicircles. The semicircle at higher frequency corresponds to the charge transfer at Pt/electrolyte interface and the semicircle at lower frequency is the response of charge transfer at dye/TiO₂/electrolyte interface. The Nyquist plot was fitted with equivalent circuit as given in **Figure 2.18**. The equivalent-circuit model consists of R_s (resistance due to the FTO and contact resistance), R_{Pt} , C_{Pt} (resistance and capacitance at Pt/electrolyte interface), C_{TCO} (capacitance at FTO/electrolyte interface) and $B2$ (transmission line model used to explain charge transfer at dye/TiO₂/electrolyte interface). $B2$ includes R_t (transport resistance for TiO₂), R_{rec} (recombination resistance at dye/TiO₂/electrolyte interface) and C_{μ} (Chemical capacitance of TiO₂ in contact with electrolyte). Electron lifetime is often calculated from Bode plot using the relation ' $\tau_n=1/2\pi f_m$ ' where f_m is the frequency corresponding to the highest phase (ϕ) value in the Bode plot. Chemical capacitance (C_{μ}) is used to locate the position of conduction band (CB) of TiO₂. **Figure 2.19a** shows C_{μ} as a function of Fermi voltage (V_F). V_F is given by the following equation^{23, 24}

$$V_F = V_{app} - V_{series} \quad (2)$$

$$V_{series} = I \times R_{series} \quad (3)$$

$$R_{series} = R_S + R_{Pt} + R_d \quad (4)$$

Where V_{app} is the applied DC voltage and V_{series} is the voltage drop due to the series resistance. I is the DC current derived from EIS. R_{series} is the total series resistance and R_d is the diffusion resistance of electrolyte. From C_{μ} vs V_F plot, a 10 mV shift in CB of TiO₂

towards negative potential in TiO₂-ZF with respect to TiO₂ was observed. Negative shift in CB of TiO₂ increases the driving force for recombination resulting in lower lifetime. In addition to this, negative shift in CB increases the driving force for electron injection promoting higher J_{sc} .

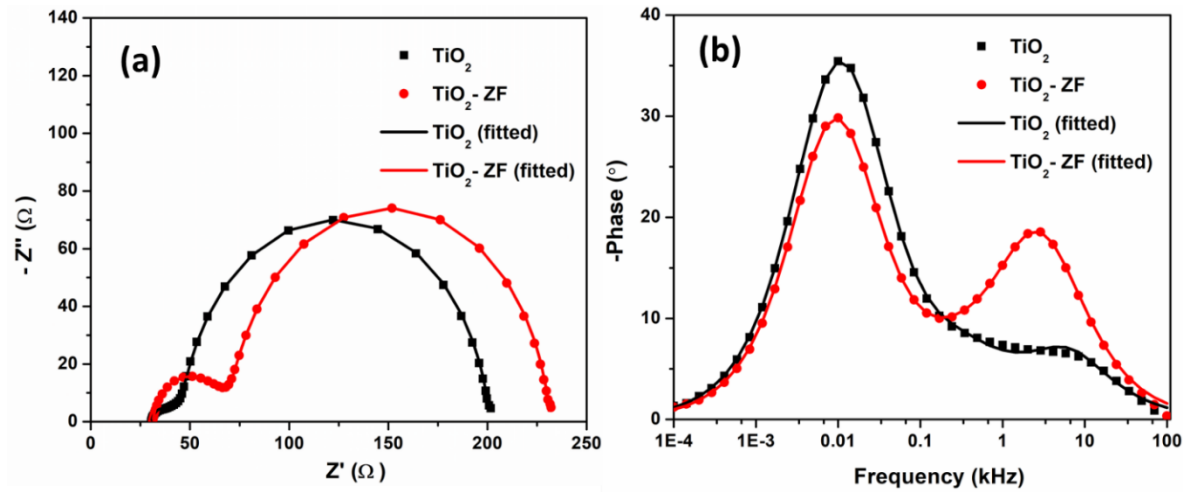


Figure 2.17 (a) Nyquist plot and (b) Bode plot from EIS.

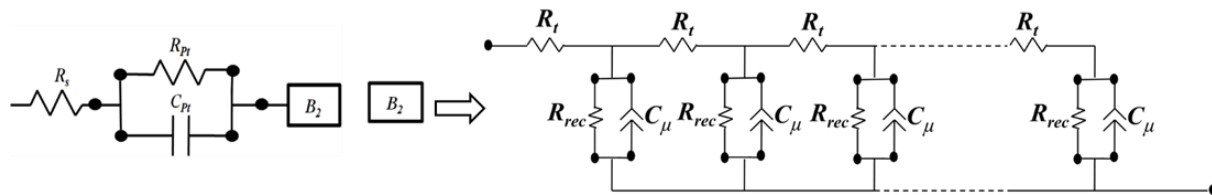


Figure 2.18 Equivalent circuit for impedance fitting.

Recombination at TiO₂/electrolyte interface is the most influential loss process in DSSC/DSC. Quantification of recombination process is a pre-requisite to formulate new methods to minimize such impediments to efficiency. Lifetime (τ_n) investigation contribute to analyse the recombination in dye solar devices. **Figure 2.19b** shows τ_n as a function of V_F . Lower lifetime i.e. higher recombination in TiO₂-ZF compared to TiO₂ was observed. Lifetime can decrease under two conditions (i) if the oxidised redox species in electrolyte approach semiconductor (ii) if the CB of semiconductor shifts more negatively creating higher driving force for recombination. Since the blocking layer is same in both devices (TiO₂ and TiO₂-ZF), the first condition is not valid here. The second condition

looks appropriate where a negative shift in conduction band in TiO₂-ZF compared to TiO₂ (**Figure 2.19a**) resulted in lower lifetime for TiO₂-ZF. Interestingly the V_{oc} of devices fabricated with TiO₂ and TiO₂-ZF were found to be identical which implies that the voltage loss in TiO₂-ZF as a result of increased recombination was compensated by the voltage gain due to the negative shift in CB. A close analysis of the lifetime plot revealed that the lifetime of TiO₂-ZF decreased with V_F at relatively higher rates compared to TiO₂.

The electron transport in TiO₂ in DSSC is governed by the diffusion phenomena. The minimum time required for the injected electrons to be collected at the working electrode accounts for the transport time (τ_d). **Figure 2.20** shows the transport time (τ_d) as a function of V_F . As apparent, TiO₂-ZF is endowed with short transport time compared to TiO₂. TiO₂ is a mesoporous material with large number of trap states present over the band gap. The electron transport in TiO₂ is always followed by multiple trapping and detrapping of electrons.^{25, 26} Very often, passivation of surface trap states yields shorter transport time. In the present study, ZnO is used as a sacrificial layer and no trace of ZnO is found over TiO₂. However, the nature of the parabola were identical for TiO₂ and TiO₂-ZF, excluding the possibility of any passivation of traps using ZnO sacrificial layer. Faster τ_d was realised in TiO₂-ZF compared to bare TiO₂ due to reduced R_t in TiO₂-ZF compared to bare TiO₂.

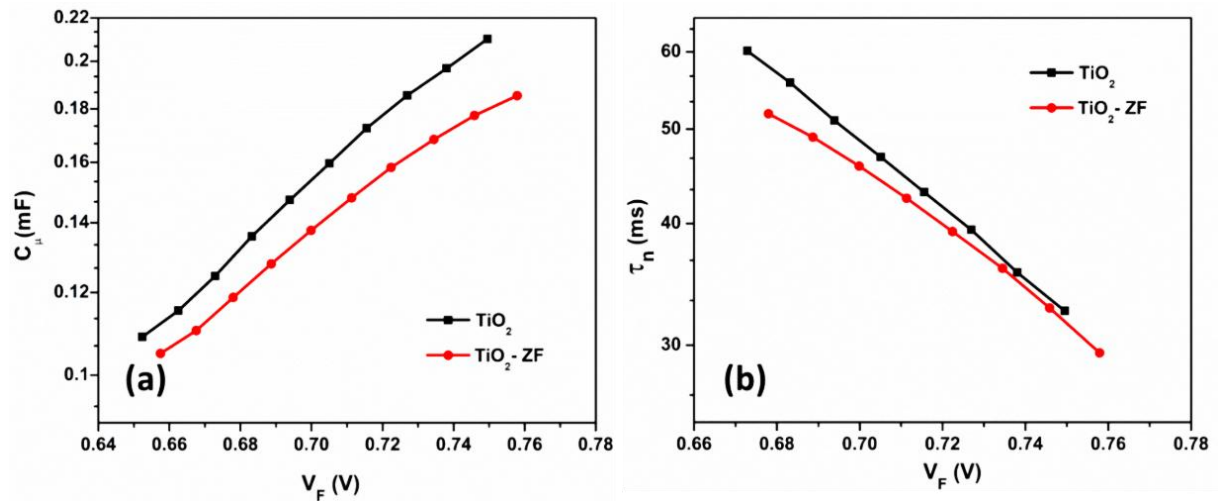


Figure 2.19 (a) Chemical capacitance and (b) Lifetime as a function of Fermi voltage (V_F).

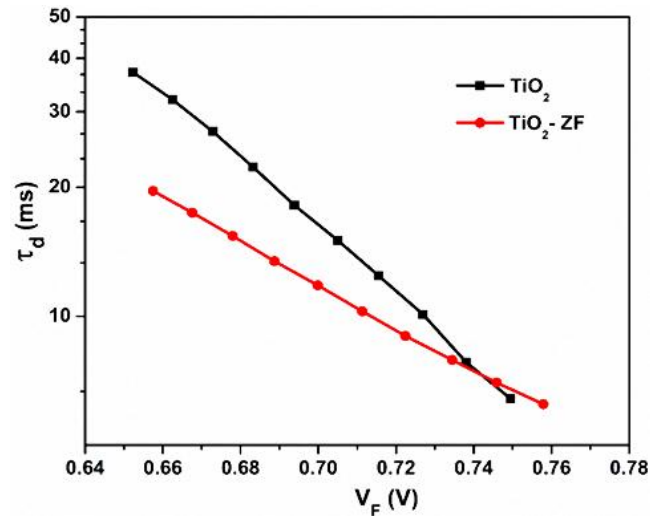


Figure 2.20 Transport time as a function of Fermi voltage.

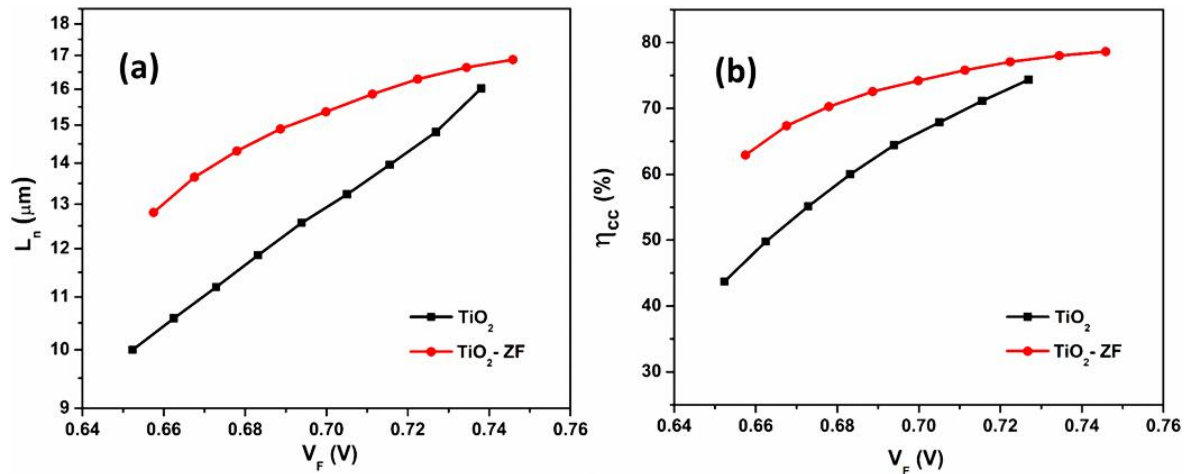


Figure 2.21 (a) Diffusion length (L_n) and (b) Charge collection efficiency (η_{cc}) as a function of Fermi voltage (V_F).

Once electrons are injected to the CB of TiO_2 , they diffuse towards the working electrode. Electron transport over TiO_2 is always coupled with recombination with oxidised species of electrolyte. For efficient charge collection, transport time must be smaller than the recombination time. Diffusion length (L_n) is one of the commonly used parameters that quantitatively influences charge collection. The minimum distance that an injected electron travels, before it recombines gives the diffusion length (L_n) which is given by the relation,²⁷

$$L_n = \sqrt{D_n \times \tau_n} \quad (5)$$

where D_n is diffusion coefficient and τ_n is the lifetime. For efficient charge collection L_n must be many times longer than the thickness of TiO_2 .²⁸ Charge collection efficiency (η_{cc}) is given by the relation,²⁹

$$\eta_{cc} = \left(1 - \frac{\tau_d}{\tau_n}\right) \times 100 \quad (6)$$

In the present case, TiO_2 -ZF showed a better L_n (**Figure 2.21a**) which resulted in improved charge collection efficiency (**Figure 2.21b**) compared to bare TiO_2 electrodes.

We also carried out a comprehensive study with light perturbation techniques involving Intensity Modulated Photovoltage spectroscopy (IMVS), Intensity Modulated Photocurrent Spectroscopy (IMPS). The electron lifetime (τ_n) was calculated from Bode plot of IMVS using the relation ' $\tau_n = 1/2\pi f_m$ ' where

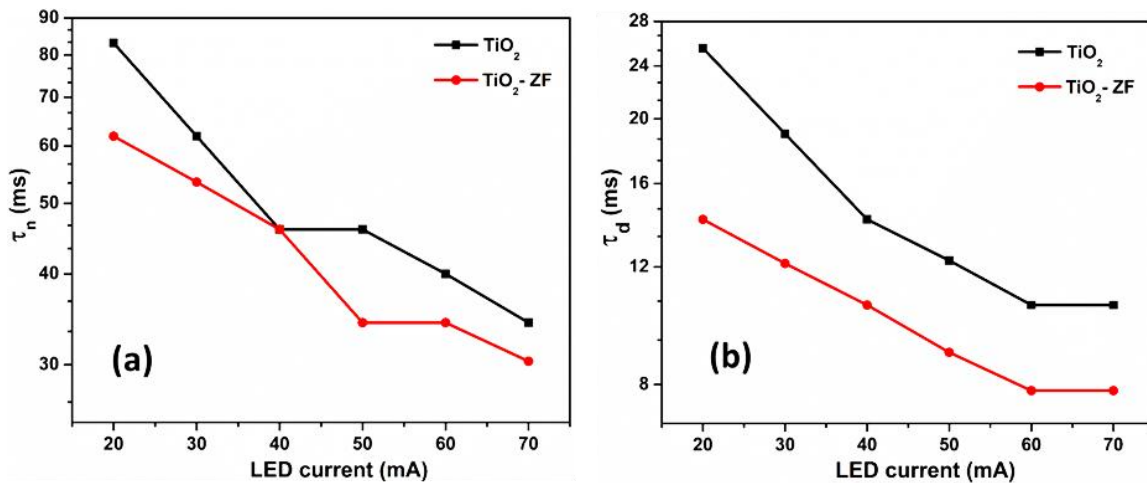


Figure 2.22 (a) Lifetime (τ_n) and (b) Transport time (τ_d) as a function of LED current.

f_m is the frequency corresponding to the highest value in imaginary part of transfer function ($-H'$).^{30, 31} τ_n as a function of light intensity is given in **Figure 2.22a**. TiO_2 -ZF showcased shorter lifetime than TiO_2 . The electron transport time (τ_d) was calculated from Bode plot, estimated from IMPS, using the relation ' $\tau_d = 1/2\pi f_m$ ' where f_m is the frequency corresponding to the highest value in imaginary part of transfer function ($-H'$).

As apparent in **Figure 2.22b** TiO₂-ZF showcased shorter transport time than TiO₂ which was in accordance with the transport time results obtained from EIS .

In addition to this, lifetime determined using OCVD also followed the same trend as obtained from both EIS and IMVS. The tail of the life time plot presented in **Figure 2.23** from OCVD measurements were parabolic for both TiO₂ and TiO₂-ZF indicating the influence of recombination from surface states.³²

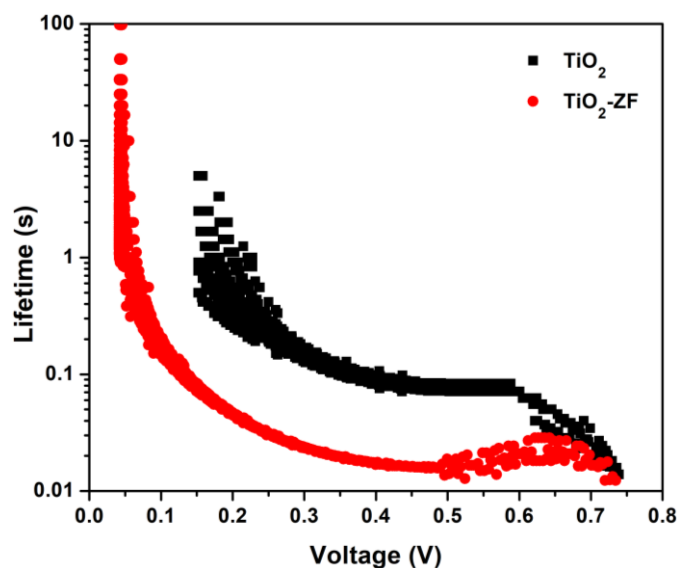


Figure 2.23 Lifetime as a function of V_F derived from OCVD measurement.

2.3.8 Photovoltaic performance under indoor light

More recently, DSC has emerged as the most promising photovoltaic technology to harness indoor light. The emission spectra of LED and CFL lies within the visible region (i.e. 400nm to 750nm) which matches with the absorption spectra of most of the dyes that are commonly used in DSC. Again the added advantage of DSC to retain voltage in such low intensities (1000 lux) makes it the best photovoltaic technology for indoor light harvesting application. The J - V data under indoor light conditions was carried out using a custom made set up coupled with a day light CFL as the source of illumination. The emission spectra of the CFL used for the efficiency measurements of the solar cells is provided in **Figure 2.24**. The J - V plot of TiO₂ and TiO₂-ZF under light of 1000 lux is given in **Figure 2.25** and the photovoltaic parameters are summarised in **Table 2.2**. Bare TiO₂

devices showed a V_{oc} of 489 ± 12 mV, J_{sc} of 61.81 ± 6.09 μAcm^{-2} with FF 44.4%, yielding a power conversion efficiency of $6.39 \pm 0.27\%$.

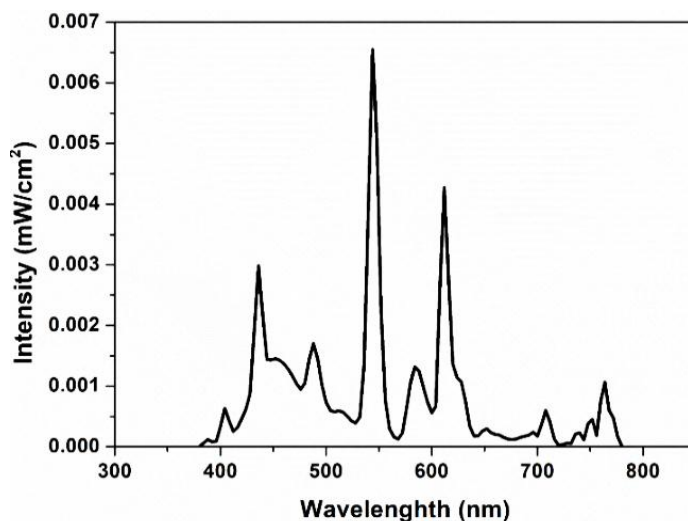


Figure 2.24 Emission spectra of CFL.

TiO_2 -ZF showed a V_{oc} of 545 ± 16 mV, J_{sc} of 68.86 ± 1.76 μAcm^{-2} and of FF $70.33 \pm 9.37\%$, giving a PCE of $11.80 \pm 1.35\%$. An improvement of 84.7% in overall PCE was achieved, employing TiO_2 -ZF devices compared to bare TiO_2 devices under indoor light conditions.

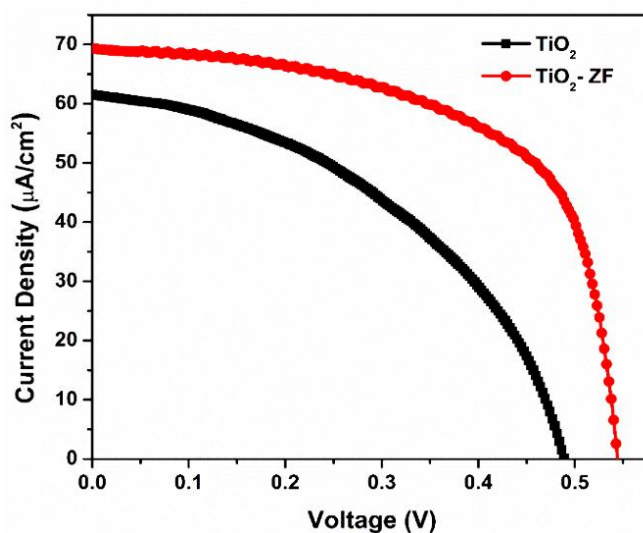


Figure 2.25 Current density versus potential (J - V) characteristic for TiO_2 and TiO_2 -ZF under indoor light (1000 lux, CFL).

Table 2.2 J - V parameters for TiO_2 and TiO_2 -ZF under indoor light (1000 lux, CFL).

Device	V_{oc} (mV)	J_{sc} (μAcm^{-2})	FF (%)	η (%)
TiO_2	489 ± 12	61.81 ± 6.09	44.40 ± 2.78	6.39 ± 0.27
TiO_2 -ZF	545 ± 16	68.86 ± 1.76	70.33 ± 9.37	11.80 ± 1.35

The effect of increasing the number of ZnO flower layers over TiO_2 layer in DSSC is also studied. 1-4 layers of ZnO flower is coated over TiO_2 layer (designated as TiO_2 -ZF1, TiO_2 -ZF2, TiO_2 -ZF3 and TiO_2 -ZF4) and the photovoltaic parameters are investigated under one sun conditions. It was found that increase in the number of ZnO flower layer has no effect in photovoltaic performance of the device (**Table 2.3**). Therefore it is concluded that one layer of ZnO flower is sufficient to bring the improvement in the power conversion efficiency of the device.

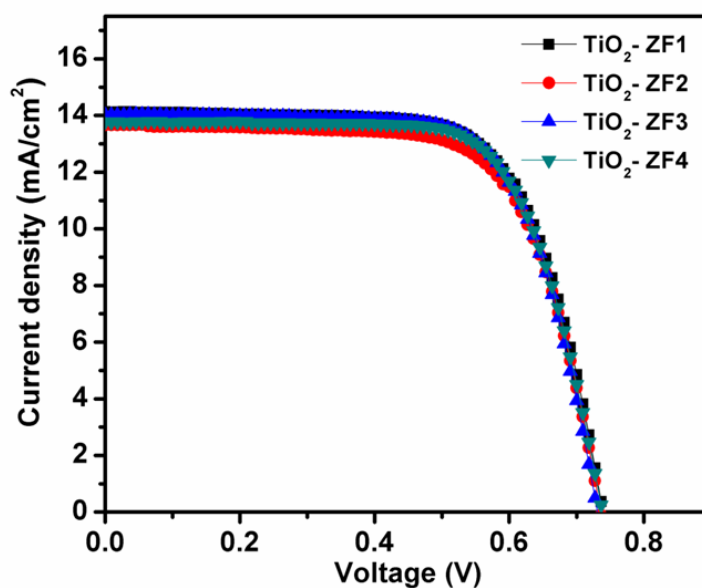
**Figure 2.26** Current density versus potential (J - V) characteristic of different number of ZnO flower layer over TiO_2 layer in DSSC.

Table 2.3. *J-V* parameters for different number of ZnO flower layer over TiO₂ layer in DSSC under one sun conditions.

Sample	V_{oc} (mV)	J_{sc} (mAcm⁻²)	FF (%)	η (%)
TiO ₂ -ZF1	740	14.12	69.32	7.24
TiO ₂ -ZF2	730	13.65	69.64	6.94
TiO ₂ -ZF3	730	14.04	70.48	7.22
TiO ₂ -ZF4	740	13.77	70.64	7.20

2.4 Conclusions

A new device design strategy is successfully showcased for DSSCs/DSCs through structural engineering of the semiconductor layer, achieving improved light scattering properties and higher power conversion efficiency. An improvement of 12.9% in full sun and 84% in 1000 lux CFL illumination was achieved by employing templated TiO₂ surface created by etching of fugitive inclusions of ZnO micro flowers. Even though the architectural change to TiO₂ resulted in higher recombination as evident from the perturbation results, the negative shift in conduction band along with shorter transport time and longer diffusion length helped TiO₂-ZF device to achieve better charge collection efficiency. Moreover, the modified electrode layers enable improved scattering through both front and back side illumination enabling the process to serve as a potential methodology for bifacial DSC in BIPV sector.

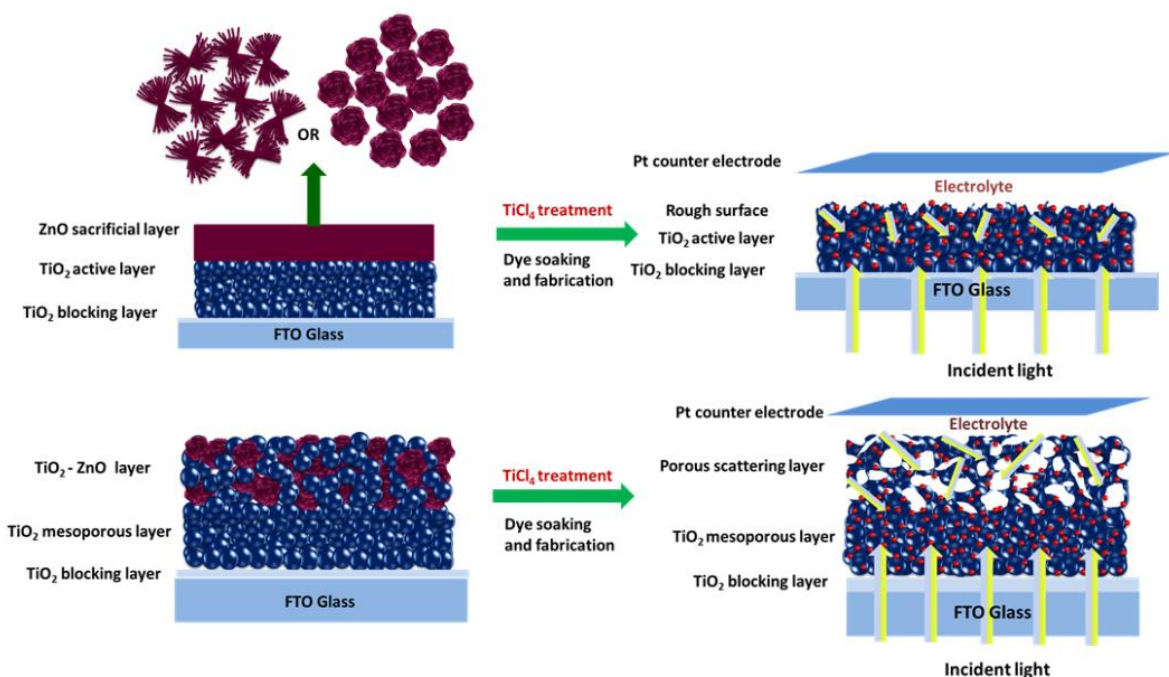
References

1. K. Kakiage, Y. Aoyama, T. Yano, K. Oya, J.-i. Fujisawa and M. Hanaya, *Chem. Comm.*, 2015, **51**, 15894-15897.
2. Y. Cao, Y. Liu, S. M. Zakeeruddin, A. Hagfeldt and M. Grätzel, *Joule*, 2018, **2**, 1108-1117.
3. M. Freitag, J. Teuscher, Y. Saygili, X. Zhang, F. Giordano, P. Liska, J. Hua, S. M. Zakeeruddin, J.-E. Moser, M. Grätzel and A. Hagfeldt, *Nat. Photon*, 2017, **11**, 372-378.
4. D. Yong, Z. Li, M. Li'e, J. Ling, H. Linhua, L. Zhaoqian, C. Shuanghong and D. Songyuan, *Adv. Funct. Mater.*, 2015, **25**, 5946-5953.
5. B. Liu and E. S. Aydil, *J. Am. Chem. Soc.*, 2009, **131**, 3985-3990.
6. S. Sasidharan, S. Soman, S. C. Pradhan, K. N. N. Unni, A. A. P. Mohamed, B. N. Nair and H. U. N. Saraswathy, *New J. Chem.*, 2017, **41**, 1007-1016.
7. K. D. Han, W. Mariah, L. Kyoungmi and P. G. N., *ChemSusChem*, 2013, **6**, 1014-1020.
8. S.-W. Lee, K.-S. Ahn, K. Zhu, N. R. Neale and A. J. Frank, *J. Phys. Chem. C*, 2012, **116**, 21285-21290.
9. N. Fuke, R. Katoh, A. Islam, M. Kasuya, A. Furube, A. Fukui, Y. Chiba, R. Komiya, R. Yamanaka, L. Han and H. Harima, *Energy Environ. Sci.*, 2009, **2**, 1205-1209.
10. Q. Zhang, D. Myers, J. Lan, S. A. Jenekhe and G. Cao, *Phys. Chem. Chem. Phys.*, 2012, **14**, 14982-14998.
11. T. G. Deepak, G. S. Anjusree, S. Thomas, T. A. Arun, S. V. Nair and A. Sreekumaran Nair, *RSC Adv.*, 2014, **4**, 17615-17638.
12. S. Hore, C. Vetter, R. Kern, H. Smit and A. Hinsch, *Sol. Energy Mater. Sol. Cell*, 2006, **90**, 1176-1188.
13. D. Guo, S. Xiao, K. Fan and J. Yu, *ACS Sustainable Chem. Eng.*, 2017, **5**, 1315-1321.
14. Y. Li, Z. Che, X. Sun, J. Dou and M. Wei, *Chem. Comm.*, 2014, **50**, 9769-9772.
15. P. Zhao, L. Wang, Z. Yu, F. Liu, P. Sun, Y. Gao and G. Lu, *RSC Adv.*, 2016, **6**, 17280-17287.
16. H. Fuzhi, C. Dehong, Z. X. Li, C. R. A. and C. Yi-Bing, *Adv. Funct. Mater.*, 2010, **20**, 1301-1305.

17. W.-Q. Wu, H.-L. Feng, H.-S. Rao, Y.-F. Xu, D.-B. Kuang and C.-Y. Su, *Nat. Commun.*, 2014, **5**, 3968.
18. S. Hore, P. Nitz, C. Vetter, C. Prah, M. Niggemann and R. Kern, *Chem. Comm.*, 2005, 2011-2013.
19. H. Se-Hoon, L. Sangwook, S. Hyunjung and S. J. Hyun, *Adv. Funct. Mater.*, 2011, **1**, 546-550.
20. M.-Y. Pu and J. Z. Chen, *Mater. Lett.*, 2012, **66**, 162-164.
21. A. Resmini, I. G. Tredici, C. Cantalini, L. Giancaterini, F. De Angelis, E. Rondanina, M. Patrini, D. Bajoni and U. Anselmi-Tamburini, *J. Mater. Chem. A*, 2015, **3**, 4568-4577.
22. J. Qiu, F. Zhuge, X. Li, X. Gao, X. Gan, L. Li, B. Weng, Z. Shi and Y.-H. Hwang, *J. Mater. Chem*, 2012, **22**, 3549-3554.
23. Manikkedath V. Vinayak, M. Yoosuf, S. C. Pradhan, T. M. Lakshmykanth, S. Soman and K. R. Gopidas, *Sustainable Energy Fuels*, 2018, **2**, 303-314.
24. S. Soman, S. C. Pradhan, M. Yoosuf, M. V. Vinayak, S. Lingamoorthy and K. R. Gopidas, *J. Phys. Chem. C*, 2018, **122**, 14113-14127.
25. J. R. Jennings, A. Ghicov, L. M. Peter, P. Schmuki and A. B. Walker, *J. Am. Chem. Soc.*, 2008, **130**, 13364-13372.
26. Q. Wang, S. Ito, M. Grätzel, F. Fabregat-Santiago, I. Mora-Seró, J. Bisquert, T. Bessho and H. Imai, *J. Phys. Chem. B*, 2006, **110**, 25210-25221.
27. S. C. Pradhan, A. Hagfeldt and S. Soman, *J. Mater. Chem. A*, 2018, **6**, 22204-22214.
28. F. Fabregat-Santiago, G. Garcia-Belmonte, I. Mora-Sero and J. Bisquert, *Phys. Chem. Chem. Phys.*, 2011, **13**, 9083-9118.
29. K. Zhu, S.-R. Jang and A. J. Frank, *J. Phys. Chem. Lett.*, 2011, **2**, 1070-1076.
30. P. Santhini, V. Jayadev, S. C. Pradhan, S. Lingamoorthy, P. Nitha, M. Chaithanya, R. K. Mishra, N. U. KN, J. John and S. Soman, *New J. Chem.*, 2019, **43**, 862-873.
31. B. Hemavathi, V. Jayadev, S. C. Pradhan, G. Gokul, K. Jagadish, G. Chandrashekar, P. C. Ramamurthy, R. K. Pai, K. N. Unni and T. Ahipa, *Solar Energy*, 2018, **174**, 1085-1096.
32. J. Bisquert, A. Zaban, M. Greenshtein and I. Mora-Seró, *J. Am. Chem. Soc.*, 2004, **126**, 13550-13559.

Chapter 3

ZnO hierarchical structures as sacrificial inclusions for enhanced light scattering in TiO₂ photoanodes of dye-sensitised solar cell



Herein, ZnO hierarchical structures of fibrous and sheet like morphologies were utilised as sacrificial inclusions to study the effect of surface roughness and light scattering in TiO₂ photoanode films on DSSC. The ZnO structures coated over TiO₂ were selectively etched by TiCl₄ treatment. The performance of devices was evaluated under one sun and ambient light conditions, in both cases the PCE was found to be increased. An enhancement of 15.56% and 18.64% in PCE was obtained for TiO₂-Zfb and TiO₂-Zsh devices respectively relative to the bare TiO₂ device under one sun conditions. Under low light, an improvement of 39.63% and 6.30% was observed for the same devices aforementioned. The effect of light scattering inside a bilayer structured TiO₂ photoanode is discussed in the later part of this chapter. A porous scattering layer was fabricated by employing a mixture of TiO₂ and micron sized ZnO sheet aggregates as fugitive inclusions. The voids created in the photoanode imparted strong light scattering

effects. The best device offered an improvement of 49.20% in PCE when compared with single layered standard TiO₂ device under one sun illumination and 44.76% under low light conditions.

3.1 Introduction

Dye-sensitised solar cells (DSSCs) are identified as promising alternatives to conventional silicon solar cells due to their appealing characteristics like facile fabrication, colourfulness, low production cost and relatively high power conversion efficiencies at indoor as well as outdoor light conditions. DSSC demonstrates phenomenal performance under various indoor lighting sources such as fluorescent lamps and light-emitting diodes (LEDs) compared to the other solar cell technologies enabling them to be capable of powering wireless sensors and consumer electronics.^{1,2} Diverse strategies are being explored for the improvement of power conversion efficiency in DSSCs by developing photoanode materials with superior features. The widely pursued ones are the use of semiconductors with high surface area for enhanced dye loading,³ exploring 1D materials for fast electron transport,⁴ incorporating submicron particles for internal light scattering⁵ as well as deposition of nano-material films on conductive glass as blocking layer to reduce electron recombination.⁶⁻⁹

Light scattering strategies are applied to DSSCs to improve the optical absorption of the photo anode film. According to Mie Theory, particles with sizes comparable to the wavelength of incident light can effectively scatter incident light.¹⁰ Methods usually adopted for generating light scattering in photo anodes of DSSCs include fabricating bi-layer structured and mixed structured films.^{5,11-13} In the bi-layer structure, a film composing of submicron sized particles are coated over the nanocrystalline semiconductor layer whereas in mixed structure configuration larger particles are incorporated into the nanocrystalline semiconductor layer. In both instances, larger particles promote multiple light scattering so that the average path length of the light within the photo electrode increases which results in enhanced optical absorption by the dye molecules. Even though these methods are recognised to be effective, they do possess certain drawbacks. As the nanocrystalline films are meant to deliver increased surface area for the adsorption of dye molecules, the larger particles embedded in the mixed structure may end up reducing the internal surface area which in turn reduces the dye loading in the film resulting in low optical absorption. In the case of bi-layer

structured photoanode the internal resistance of the solar cell increases which could further obstruct the charge transport inside the solar cell.⁵

A facile strategy to create surface roughness and voids in the TiO₂ photoelectrode to impart light scattering in the solar cell is presented in this chapter. A few studies have been conducted so far to investigate the effect of voids/roughness in active layer as scattering centers to enhance the performance of DSSC and some of the reports based on the same is discussed in chapter 2 introduction section 2.1.¹⁴⁻¹⁷

The commercially available TiO₂ scattering layer paste utilises 400 nm sized particles and the scattering layer fabricated out of it in micro meter thickness is opaque. Such films are not suitable for building integrated photovoltaic (BIPV) applications as light need to be harvested from both sides of solar cell. In order to overcome this issue, a facile method to generate surface roughness/voids over TiO₂ photoanodes for enhanced light scattering without much loss in transparency of the photoanode is demonstrated. Two ZnO hierarchical structures were utilised to act as sacrificial inclusions to serve the purpose owing to its three-dimensional structure, facile synthetic strategy and fast etching rate. As discussed in the previous chapter, TiCl₄ treatment serves the dual purposes of blocking layer deposition as well as etching of ZnO particles to construct surface roughness/voids on TiO₂ nanocrystalline film.

The present chapter discuss the characteristics and properties of two distinct architectures of DSSC. First few sections of this chapter discusses the effect of two different ZnO hierarchical structures on creating surface roughness, light scattering in TiO₂ photoanode films and the performance of DSSC under one sun and low light conditions. In In the second part of the chapter (**Section 3.7** onwards), a bilayer photoanode DSSC with bottom mesoporous TiO₂ layer and top macro porous TiO₂ scattering layer is fabricated. The macro porous scattering layer is fabricated by utilising a mixture of TiO₂ and ZnO as fugitive inclusion. The effect of this porous scattering layer on the photovoltaic characteristics of DSSCs with and without modification of photoanode at 1 sun intensity and low light conditions are studied.

3.2 Experimental

3.2.1 Synthesis of zinc oxide hierarchical structures

Three ZnO hierarchical structures were synthesised through wet chemical processes by changing urea weight percentage (22.5 wt.%, 50 wt.% and 75.0 wt.%) with respect to Zinc nitrate hexahydrate. In a typical synthesis, 100 ml of 0.25 M Zinc nitrate hexahydrate [$\text{Zn}(\text{NO}_3)_2 \cdot 6\text{H}_2\text{O}$, Sigma Aldrich] was added drop wise into 100 ml solution of urea with a specific wt.% (NH_2CONH_2 , Merck) and 200 ml of distilled water under continuous stirring. The reaction mixture was then placed in an oven at 90 °C for 24 hours. The obtained product was washed with distilled water thoroughly and dried at 60 °C.

3.2.2 ZnO paste preparation

About 0.19 g of “as-synthesised powder” prepared via the above-mentioned method was ground thoroughly with 0.05 g of ethylcellulose (TCI) and terpeniol (TCI) in an agate mortar to obtain the ZnO paste.

3.2.3 Etching of ZnO hierarchical structures

In order to etch the ZnO hierarchical structures deposited on the TiO_2 film, the photoanodes were dipped in 40 mM TiCl_4 solution for 30 minutes at 70 °C and successively subjected to programmed annealing processes up to 500 °C.

3.2.4 Material characterisation

X-ray diffraction (XRD) analysis was performed to confirm the crystallinity and phase purity of fabricated ZnO hierarchical structures as well as the films (PANalytical X'Pert PRO operated with $\text{Cu K}\alpha$ radiation (X-ray wavelength $\lambda = 1.5406 \text{ \AA}$)). The morphology and the size of the materials synthesised were confirmed by SEM and TEM analysis. SEM analysis and energy dispersive X-ray spectroscopy (EDX) was done in scanning electron microscope (SEM) Carl Zeiss, Germany. X-ray photoelectron spectroscopy was done using (XPS) PHI 5000 Versa Probe II, ULVAC-PHI Inc., USA, equipped with micro focused (200 μm , 15 KV) monochromatic $\text{Al-K}\alpha$ X-Ray source ($h\nu = 1486.6 \text{ eV}$). Survey

scans were recorded with an X-ray source power of 50W and pass energy of 187.85 eV. TEM analysis was carried out in transmission electron microscope (HRTEM, FEI Tecnai 30 G2S-TWIN) operated at an accelerating voltage of 300 kV. Atomic force microscopy (AFM) images (Tapping-mode) were recorded using Bruker multimode 8-AFM. The thickness of photoanode was measured using a Bruker Dektak XT profilometer. Diffuse reflectance spectra (DRS) of the photoanode films were recorded in UV/VIS/NIR spectrometer (Perkin Elmer Lambda 950).

3.2.5 Fabrication and characterisation of DSSC

The FTO substrates were cleaned using detergent solution, distilled water, acetone and isopropanol respectively and further annealed at 500 °C. The pre-blocking layers were deposited by immersing cleaned FTO substrates in aqueous 40 mM TiCl_4 solution for 30 minutes at 70 °C. The deposited films were subjected to a programmed heating for 15 mins each at 325 °C, 375 °C, 450 °C and 30 min at 500 °C before cooling to room temperature. Subsequently nanocrystalline TiO_2 layer and ZnO layer was deposited by doctor-blading process. The films were then annealed using the same programme as mentioned above. Etching of ZnO layer as well as the deposition of post blocking layer on the annealed electrodes were done simultaneously by immersing the electrode in aqueous 40 mM TiCl_4 solution for 30 minutes at 70 °C. These electrodes were then annealed using the same programme used for pre-blocking layer deposition. Electrodes were then immersed into N719 dye solutions (0.3 mM) with chenodeoxycholic acid (CDCA) as co-adsorbent (10 mM) and kept at room temperature for 15 h. Counter electrodes were prepared by coating platinum sol (Dyesol) on FTO plates having pre-drilled holes followed by annealing at 380 °C for 20 min. The electrodes were then assembled with hot press using 25 μm surlyn spacer. The space in-between the electrodes were filled with liquid I^-/I_3^- electrolyte composed of the standard compositions of 1-butyl-3-methylimidazolium iodide, lithium iodide, iodine, guanidinium thiocyanate and 4-tert-butyl pyridine in acetonitrile. The drilled holes were sealed with microscopic cover slide and surlyn to avoid electrolyte leakage. The photovoltaic performance of the fabricated DSSCs was measured using an AM 1.5 solar simulator (Newport Instruments, USA) equipped with a source meter (Keithley 2400) at room

temperature. The IPCE measurement of the devices was performed under DC mode using a 250W xenon lamp coupled with Newport monochromator. The J-V properties of the cells under one sun and under indoor light conditions were measured using circle shape mask with an active area of 0.1256 cm² and 0.049 cm² respectively (without mask, active area of the cell is 0.317 cm²). The thickness of the photoanodes were measured to be 6-7 μm. The power of the simulated sunlight was calibrated using a reference cell supplied by Newport instruments. The electrochemical impedance spectroscopy measurements of the devices were carried out using an Autolab PGSTAT302N equipped with FRA mode under forward bias in dark. The measurements were performed in the frequency range of 100 kHz to 0.1 Hz with logarithmically increasing order at an AC amplitude of 10 mV. Intensity modulated photovoltage spectroscopy (IMVS) measurements were conducted using the same electrochemical workstation (Autolab PGSTAT302N) equipped with FRA and LED drivers to drive the red LED (627 nm). Photovoltage response of the cells was analysed in the frequency range of 1 Hz to 1 kHz. The amplitude of the sinusoidal modulation for IMVS measurements was 10% of the DC light. Scheme used for the fabrication of the DSSC is given in **Figure 3.1**.

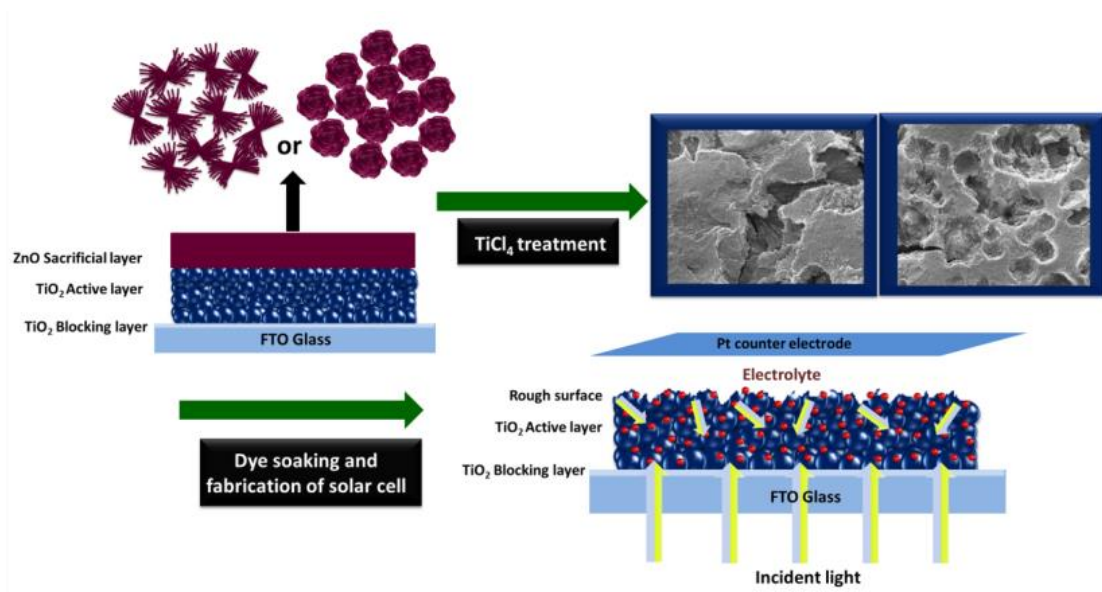


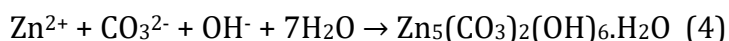
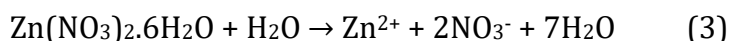
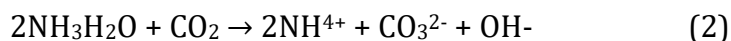
Figure 3.1 Schematic illustration of the fabrication of DSSC utilising ZnO fibril aggregates and ZnO sheet aggregates structure as sacrificial layer to introduce surface roughness over nanocrystalline TiO₂ active layer photoanodes.

3.3 Results and Discussion

3.3.1 Synthesis of ZnO hierarchical structures

In the present study, ZnO hierarchical structures were synthesised from layered zinc hydroxides (LZHs) compounds through a facile solution processing method. LZHs are complex compounds with lamellar structure made up of brucite type positively charged hydroxyl layers, where zinc hydroxyl layers, with zinc atoms positioned in the center of both octahedra and tetrahedra, are coordinated through OH⁻ via edge-sharing and corner sharing. The intercalated anion (eg; CO₃²⁻, NO₃⁻, Cl⁻, CH₃COO⁻ etc.) balance the whole charge as well as governs the interlayer spacing.¹⁸ Here, layered hydroxide zinc carbonates (LHZC) were synthesised, which consists of zinc hydroxide layers combined with water molecules and carbonate ions. These compounds are then annealed to produce the porous three dimensional (3D) hierarchical ZnO structures with high surface area which is not commonly obtained through classical crystal growth of wurtzite type ZnO.¹⁸

The present synthesis utilises a reaction mixture comprising of Zinc nitrate hexahydrate (Zn(NO₃)₂·6H₂O) and urea (CON₂H₄) to obtain the ZnO structures. Urea when heated, liberates ammonia (NH₃) and carbonate anion (CO₃²⁻). This in turn generate ammonium ion (NH₄⁺) from NH₃, eventually increasing the pH of the solution. At this high pH condition, Zn²⁺ ions provided by Zn(NO₃)₂·6H₂O in the solution reacts with CO₃²⁻ ion to form layered hydroxide zinc carbonates LHZC, with chemical formula Zn₅(CO₃)₂(OH)₆·H₂O, which upon annealing will give pure ZnO. Reaction mechanism involved in the synthesis of ZnO in the presence of urea is described as below.¹⁹⁻²¹



In the present study three types of ZnO hierarchical structures were synthesised by changing urea weight% (22.5 wt.%, 50 wt.% and 75 wt.%).

3.3.2 X-ray diffraction analysis

To verify the phase purity and structure of the synthesised products, XRD analysis was performed. **Figure 3.2** shows the XRD patterns of the as-synthesised powders (designated as 22.5 as, 50 as, 75 as) and the same annealed at 300 °C (designated as 22.5 300, 50 300, 75 300). It indicates that the as-synthesised powders corresponding to the LHZC compound with chemical formula $Zn_5(CO_3)_2(OH)_6$ having characteristic XRD peaks matching with the Joint Committee on Powder Diffraction Standards (JCPDS) File No. 01-072-1100. The diffraction peak at the 2θ angle of 13.0° corresponds to (200) crystal plane and indicates that the samples prepared at different zinc nitrate hexahydrate: urea ratio possess a layered structure with the d spacing of 6.77\AA (**Figures 3.2 a, b and c**). After annealing these powders at 300 °C, the samples no longer retained their LHZC

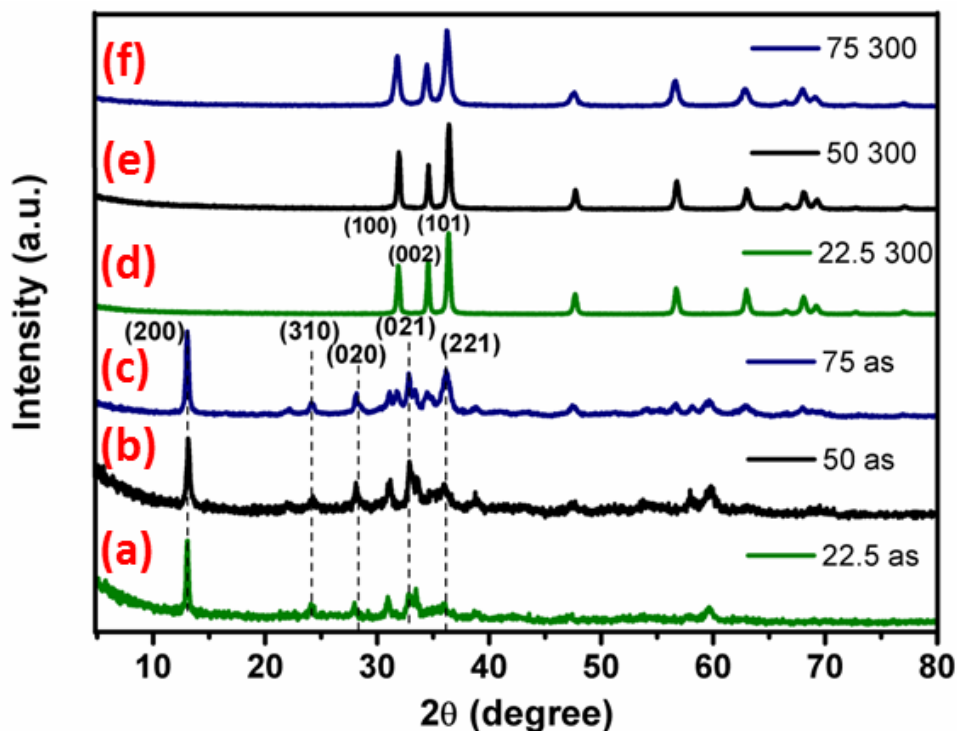


Figure 3.2 XRD patterns of “as-synthesised” and respective samples annealed at 300 °C.

structure and were transformed into phase pure ZnO hexagonal wurtzite structure with characteristic peaks at 31.7°, 34.4° and 36.2° corresponding to the crystal planes of (100), (002) and (101) respectively and matching with JCPDS file no. 76-0704 (**Figures 3.2 d, e and f**). The “as-synthesised” LHZC powder was used for the paste preparation for photoanode modifications as it will directly convert to ZnO during annealing.

3.3.3 Thermogravimetric analysis

The thermal degradation profile of LHZC is studied using TGA analysis. As presented in **Figure 3.3**, the initial weight loss at 220 °C is attributed to the dehydration of zinc hydroxide layers. A second sharp weight loss around 245 °C is due to the release of carbonate ions in LHZC. After annealing at 300 °C LHZC are converted to phase pure ZnO as already evidenced by XRD analysis.¹⁸

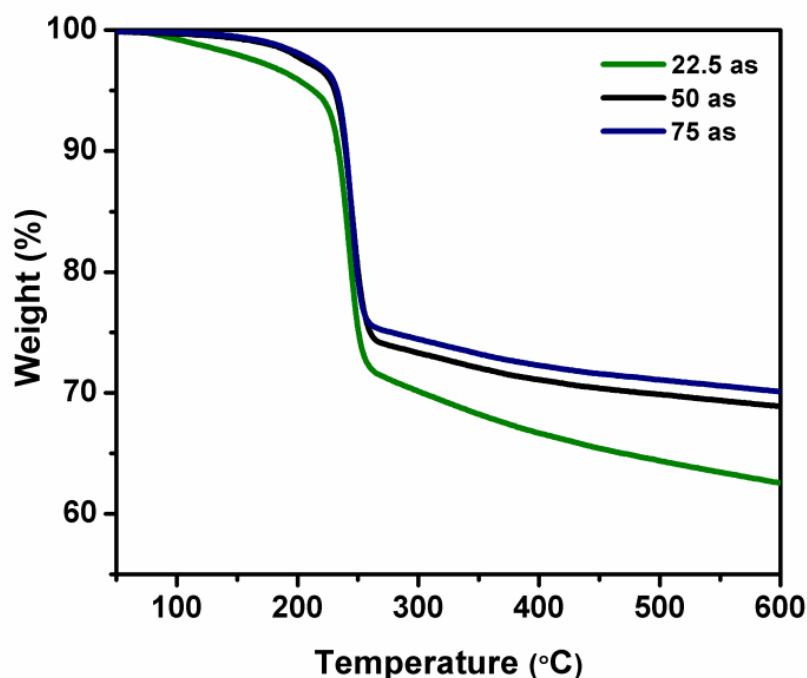


Figure 3.3 TGA curves of LHZCs.

3.3.4 Scanning electron microscopy

The morphology of as-synthesised powder with different wt.% of urea was examined by SEM analysis and the micrographs are provided in **Figure 3.4**. 22.5 wt.% sample offered

bundles of fibrils while samples derived from 50 wt.% and 75 wt.% were found to be aggregates of sheets. The fibrils are of $\sim 10\ \mu\text{m}$ size in length and of $\sim 100\ \text{nm}$ thick (Figures 3.4 a and b). 50 wt.% and 75 wt.% samples delivered aggregates of sheet like structures with various sizes ranging from 5-16 μm (Figures 3.4 c and e). The high magnification images of the same are provided in Figures 3.4 d and f clearly indicate the aggregates of sheets in large numbers.

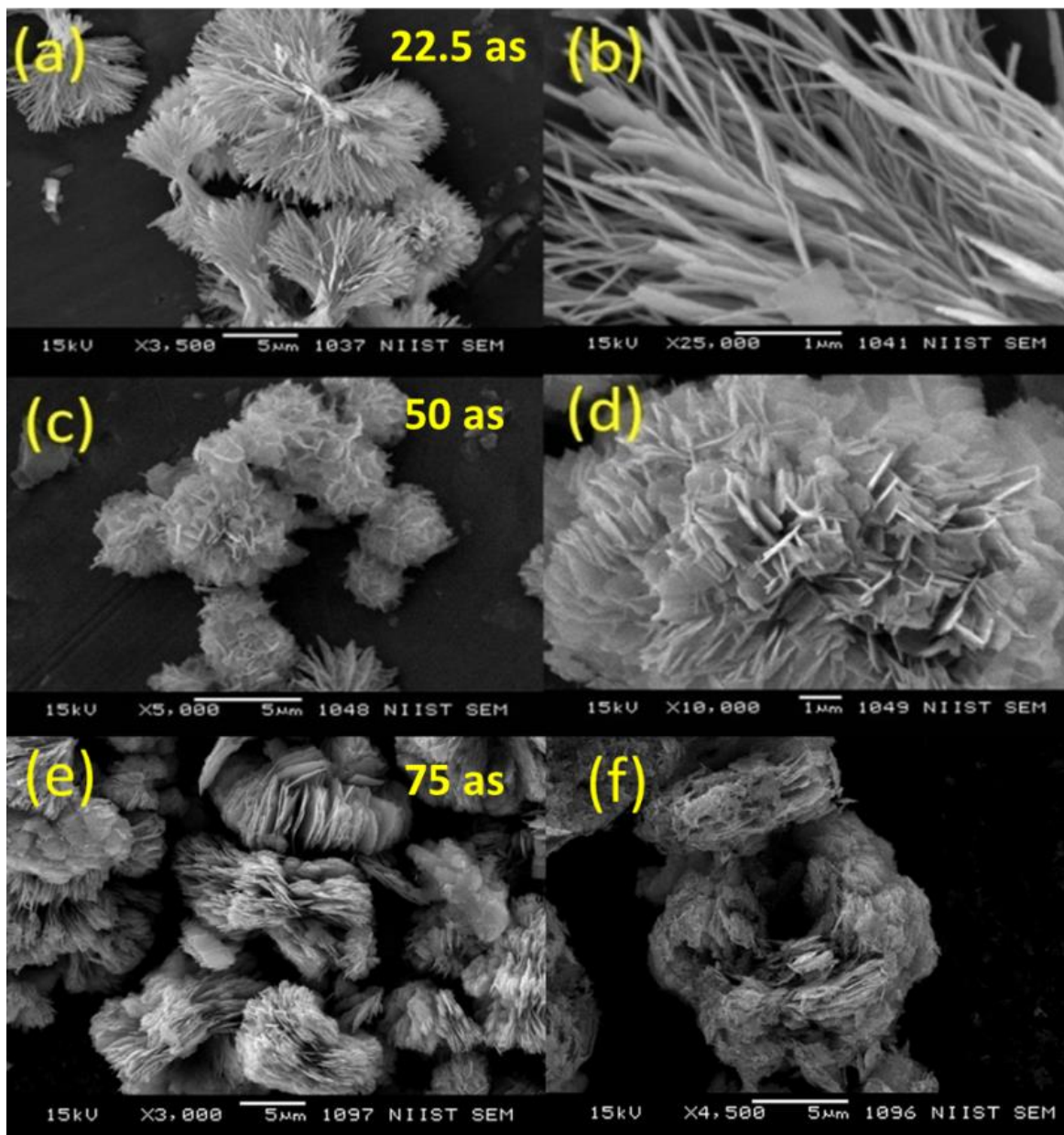


Figure 3.4 SEM images of LHZCs

3.3.5 Surface area and pore size analysis

The specific surface area and pore size distribution of the ZnO derived from annealed (300 °C) LZHCs have been measured using N₂ adsorption/desorption analysis. All ZnO samples showed Type II b isotherm with H3 hysteresis loop as shown in **Figure 3.5a**, indicating that the particles are aggregates with slit shaped pores. The N₂ adsorption/desorption isotherms and Barrett–Joyner–Halenda (BJH) pore size distribution of the same are provided in **Figure 3.5b**. The pore size distribution graphs for all samples indicate that ZnO powders possess both meso and macro pores. The Brunauer–Emmet–Teller (BET) surface area and pore sizes obtained for the samples are summarised in **Table 3.1**.

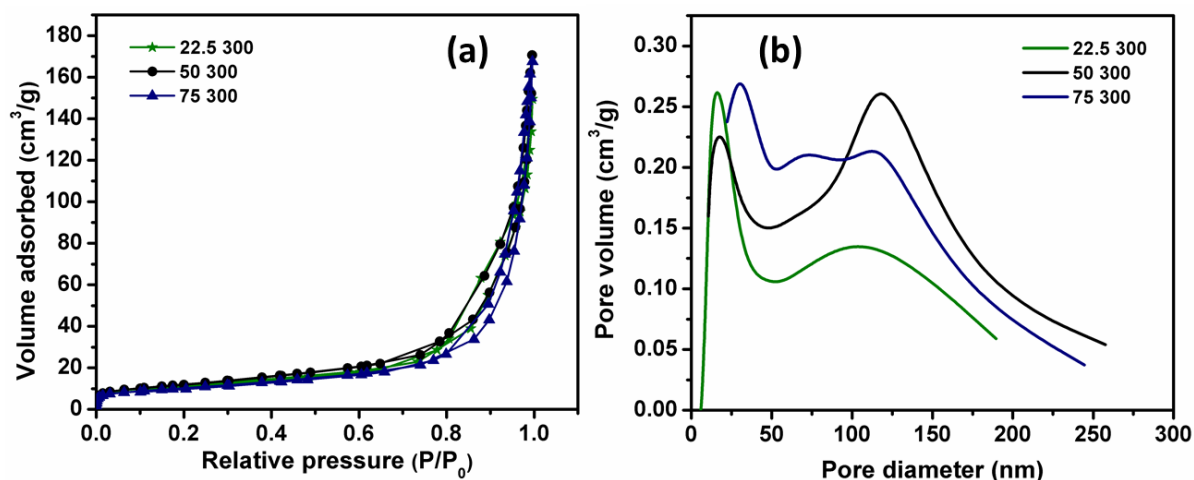


Figure 3.5 (a) N₂ adsorption/desorption isotherms of ZnO derived by annealing LZHCs at 300 °C and (b) corresponding BJH pore size distribution curve.

Irrespective of different morphologies, no significant difference in the surface area as well as the pore size was observed. Generally, ZnO structures are recognised with low surface area but, it is interesting to note that, micron sized exotic ZnO hierarchical structure obtained through the present synthetic method offered considerable surface area. This high surface area values can be attributed to the unique morphology of the ZnO porous structures which are formed by the aggregation of nano sized (thickness) fibrils and sheets.

Table 3.1 Surface area and average pore size of the samples

Sample	BET surface area (m ² /g)	Average pore size (nm)
22.5 300	40	20
50 300	42	22
75 300	36	26

3.3.6 Infrared spectroscopy

The formation of LZHC structure as well as its conversion to ZnO is also evidenced by attenuated total reflectance infrared (ATR) spectroscopy. **Figure 3.6** shows IR spectra of the LZHC structures and the films cast from it for photoanode modifications.

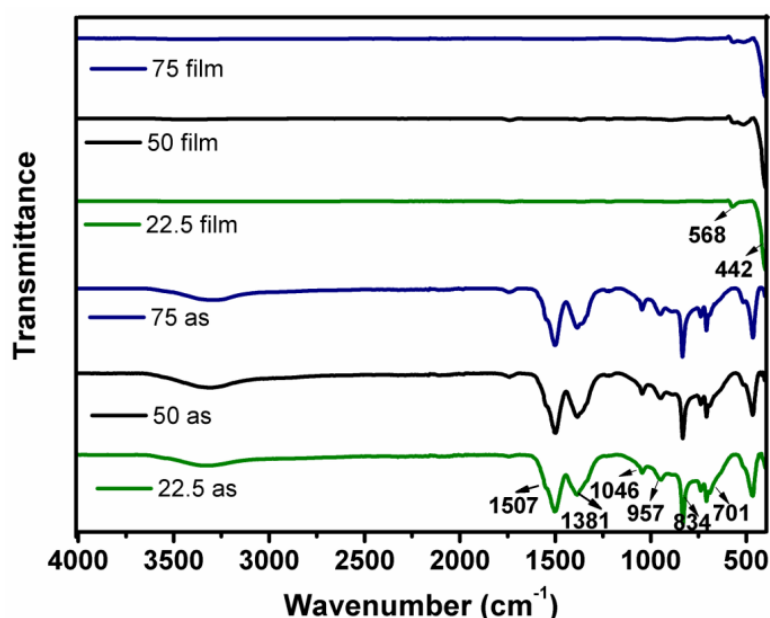


Figure 3.6 IR spectra of LZHCs and corresponding annealed films; samples collected by scraping from the FTO glass.

The as prepared powder samples (LZHCs) have shown the following IR absorption bands of carbonate: (i) two large absorption bands around 1507 and 1381 cm⁻¹ corresponding to the asymmetric stretching ν_3 mode, (ii) absorption band around 1046 cm⁻¹ is assigned to the symmetric stretching ν_1 mode, (iii) a sharp absorption band located at 834 cm⁻¹

attributed to the out-of-plane deformation of ν_2 mode, (iv) the absorption band at 701 cm^{-1} is assigned to the asymmetric stretching ν_2 mode. Apart from these, the presence of Zn–OH bonding is also verified through the absorption bands appearing at 957 cm^{-1} . The IR spectrum of the films derived from the as-prepared samples after annealing up to $500\text{ }^\circ\text{C}$ suggests that the LHZC structure has completely transformed into ZnO.²⁰ The absorption bands of carbonate ion disappeared completely and the absorption bands attributed to the stretching vibrations of Zn–O bond around 442 and 568 cm^{-1} has emerged.^{22, 23}

3.3.7 Transmission electron microscopy

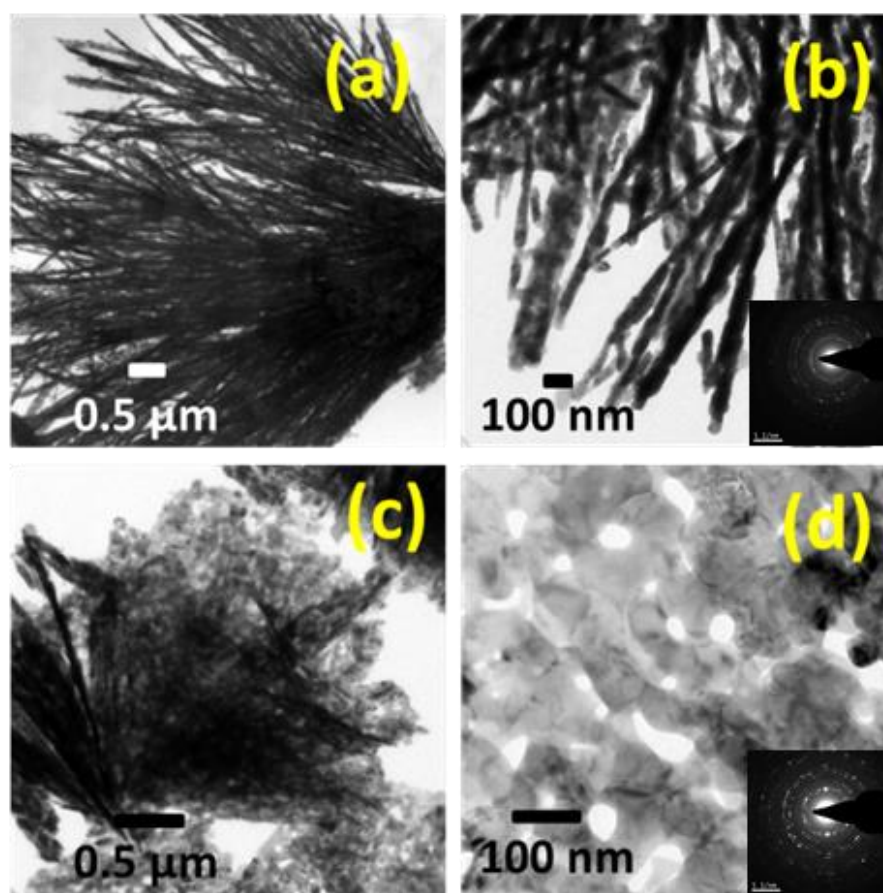


Figure 3.7 TEM images of annealed Zfb film (a and b) and Zsh film (c and d)

TEM analysis was done in order to closely view the morphological features of annealed ZnO paste (**Figure 3.7**). The sample was coated over a bare FTO glass and annealed; it

was then scratched from the glass. Out of the three compositions tried for ZnO, only two were utilised for photoanode modification, fibril bundles derived from 22.5 wt.% (zfb) and sheet like aggregates derived from 75 wt.% (zsh) as 50 wt.% offered similar kind of sheet like aggregate morphology. It was observed that the fibrils as well as sheet aggregates were composed of nanoparticles with less than 100 nm diameter (**Figures 3.7 a and b**). It is also seen that the sheet like structures possess a lot of irregular pores which is due to the release of intercalated species; CO₂ and H₂O formed by the decomposition of LHZCs (**Figures 3.7 a and b**).¹⁸

3.4 Characterisation of photoanode films

3.4.1 X-ray diffraction analysis

The photoanode films employed for fabrication of DSSC are designated as follows. TiCl₄ treated TiO₂ layer as 'TiO₂'; bilayer film without TiCl₄ treatment as TiO₂-ZnO fibril or TiO₂-ZnO sheet; and TiCl₄ treated TiO₂-ZnO bilayer film corresponding to two different morphology as 'TiO₂-Zfb' and 'TiO₂-Zsh'. **Figure 3.8** compares XRD patterns of annealed films scratched from the FTO glass. The diffraction peaks of TiCl₄ treated pure TiO₂ film

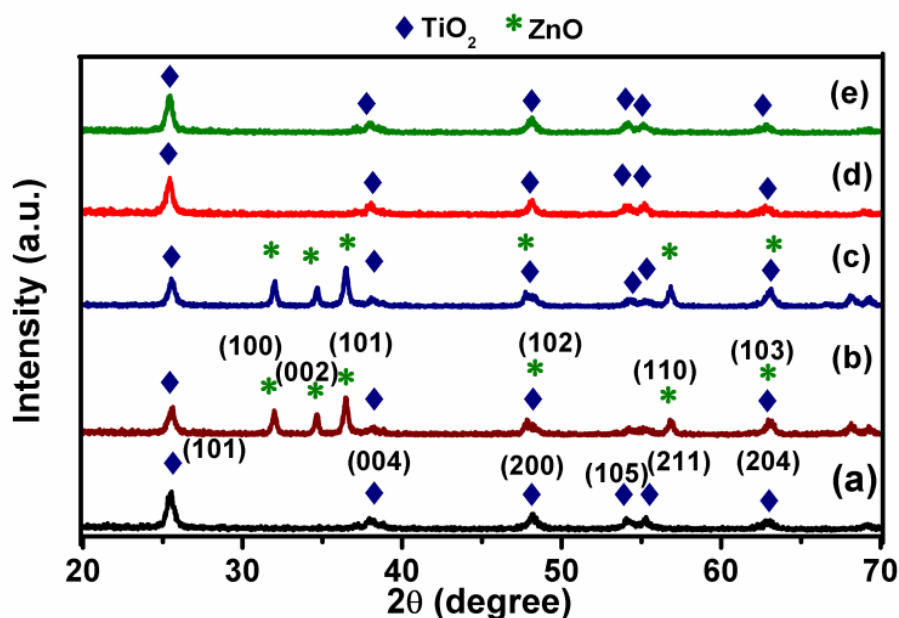


Figure 3.8 XRD patterns of annealed photoanode films: (a) TiO₂, (b and c) TiO₂-ZnO (fibril and sheet), (d) TiO₂-Zfb and (e) TiO₂-Zsh.

provided in **Figure 3.8a** are assigned to anatase crystal of TiO_2 (JCPDS file no 01-075-1537). **Figures 3.8 b and c** correspond to the bilayer films, indicating diffraction peaks of both anatase TiO_2 and wurtzite ZnO . After the TiCl_4 treatment of the bi layered films, the patterns displayed only diffraction peaks corresponding to anatase TiO_2 and indicating that the ZnO may not be present anymore in detectable limits. (**Figures 3.8 d and e**).

3.4.2 Scanning electron microscopy

The surface features of the photoanode films are studied using SEM analysis. **Figures 3.9 a and b** depict SEM images of TiCl_4 treated TiO_2 . It is clearly observed that the film is homogenous in nature and is composed of nanoparticles with sizes less than 50 nm. **Figures 3.9 c and e** presents the morphology of the bilayer films TiO_2 - ZnO fibril and TiO_2 - ZnO sheet respectively. The morphology of particles was found to be slightly deformed when it is cast as films over TiO_2 layer which could be attributed to the vigorous grinding process during paste preparation. The high-resolution images of the same are shown in **Figure 3.9 e and f**. These bilayers are then subjected to TiCl_4 treatment and due to the instability of the basic ZnO in TiCl_4 solution, these ZnO particles should have been completely etched off from the TiO_2 layer leaving behind the imprints of the ZnO structures (**Figure 3.9 g and h**).²⁴ It is believed that while doctor blading the sacrificial ZnO layer over TiO_2 layer, the ZnO aggregates would have partially submerged into the bottom layer leaving their impressions. The same is highlighted in the SEM image provided in the **Figures 3.9 g and h**. It is evident from the SEM images that the methodology adapted is capable of inducing surface roughness throughout the film compared to the TiCl_4 treated bare TiO_2 film.

3.4.3 Energy dispersive X-ray analysis

To scrutinize the distribution of elements Ti, O and Zn over the surface of photoanode films, EDX analysis was performed and the results are shown in **Figure 3.10**. **Figures 3.10 a and b** show the EDX spectra of the bilayer photoanodes TiO_2 - ZnO fibril and TiO_2 - ZnO sheet respectively. The relative percentage of Zn element with respect to Ti and O was detected to be 27.06% and 34.79% TiO_2 - ZnO fibril and TiO_2 - ZnO sheet respectively. After TiCl_4 treatment, only 0.09 % of Zn is present in TiO_2 -Zfb sample and no trace of Zn

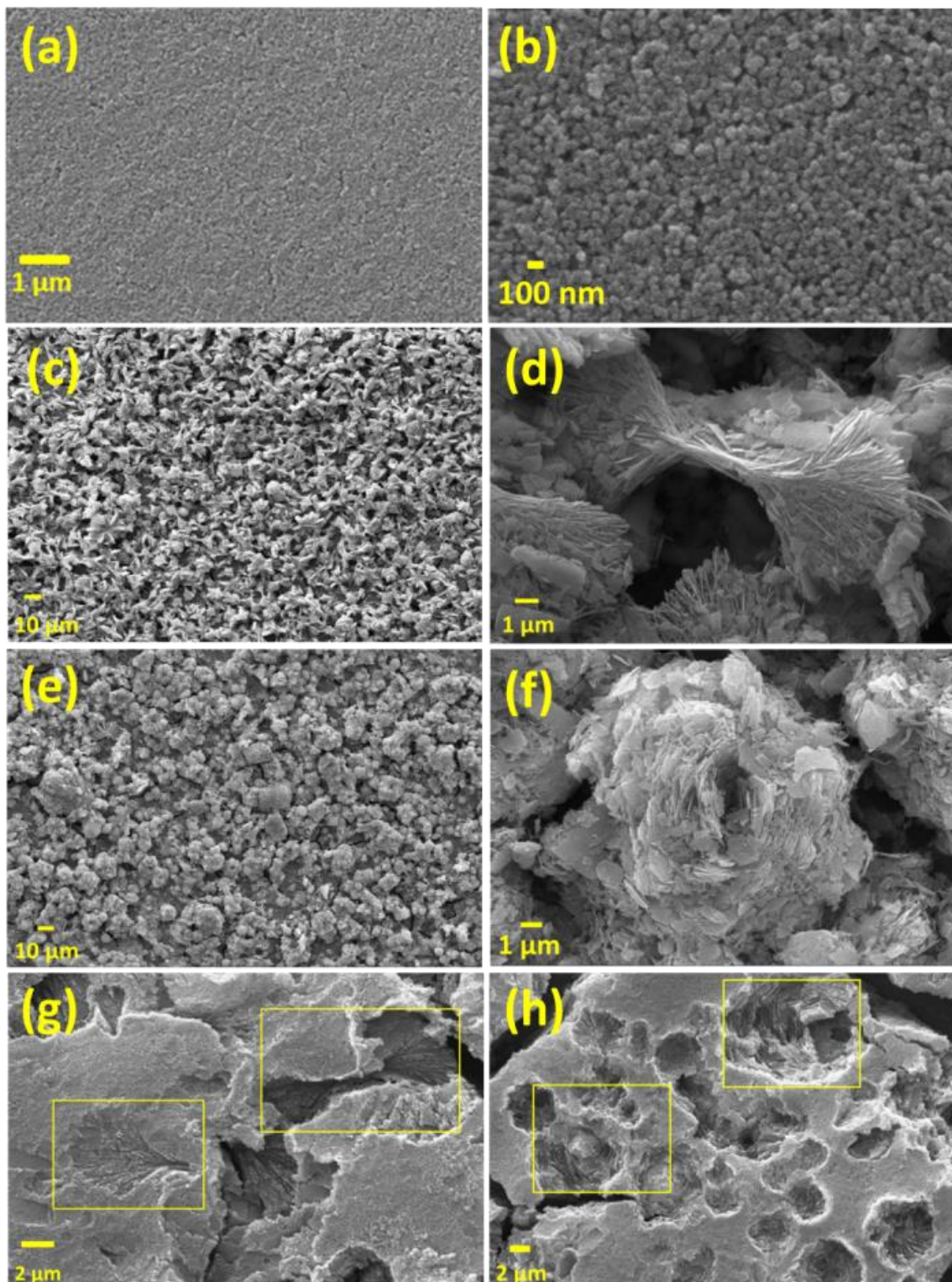


Figure 3.9 SEM images of TiO₂ (a and b), TiO₂-ZnO fibril bilayer film (c and d), TiO₂-ZnO sheet bilayer film (e and f), TiO₂-Zfb film (g) and TiO₂-Zsh film (h).

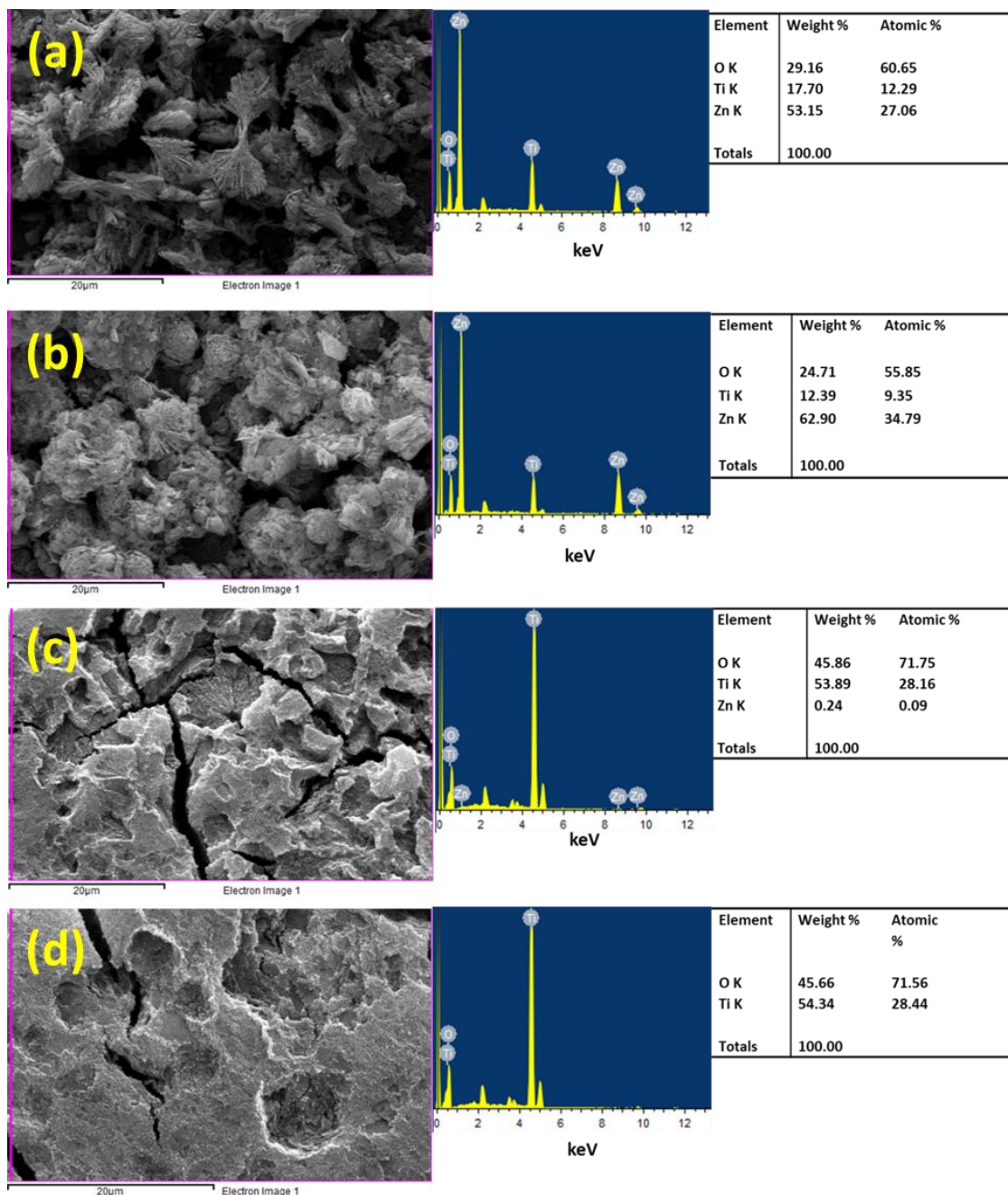


Figure 3.10 EDX of (a) $\text{TiO}_2\text{-ZnO}$ fibril bilayer film, (b) $\text{TiO}_2\text{-ZnO}$ sheet bilayer film, (c) $\text{TiO}_2\text{-Zfb}$ film and (d) $\text{TiO}_2\text{-Zsh}$ film.

was detected in $\text{TiO}_2\text{-Zsh}$ (**Figures 3.10 c and d**) samples. These results confirm that the TiCl_4 treatment had helped to etch ZnO more or less fully. It may be recalled that the EDX of TiCl_4 treated bare TiO_2 is provided in chapter2 **Figure 2.10a**. The results of ZnO

etching discussed here and the results in **Figure 2.10a** clearly evidence that TiCl_4 etching was effective in removing ZnO selectively without damaging the TiO_2 structure.

3.4.4 X-ray photoelectron spectroscopy

X-ray photoelectron spectroscopy was done to corroborate the elements present in the photoanode film. **Figure 3.11** provides the survey spectra of the TiCl_4 treated ZnO modified photoanode films. The peaks of Ti $2p_{3/2}$, O 1s, C 1s are clearly seen in the spectra at 458.5 eV, 529.7 eV and 284.8 eV respectively. A negligible intensity peak for Zn $2p_{3/2}$ is detected at 1021.9 eV. The atomic percentage of each element is tabulated in the **Table 3.2**. 0.1% of Zn was detected in both TiO_2 -Zfb film and TiO_2 -Zsh film.

Table 3.2 Atomic% of elements present in photoanode layer

Element	TiO_2 -Zfb film (atomic%)	TiO_2 -Zsh film (atomic%)
Oxygen	56.0	56.7
Titanium	22.7	23.1
Carbon	21.2	20.1
Zinc	0.1	0.1

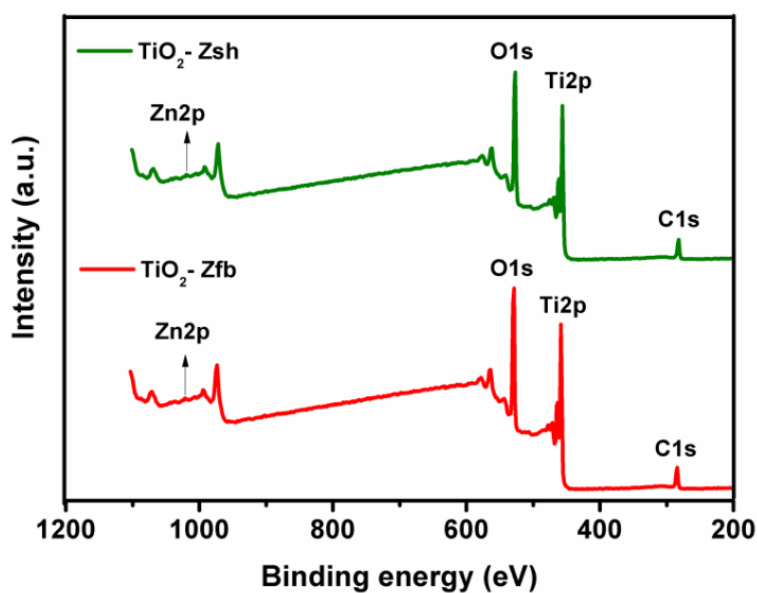


Figure 3.11 XPS survey spectra of photoanode films: TiO_2 -Zfb film and TiO_2 -Zsh film.

3.4.5 Diffuse reflectance spectroscopy

To validate the scattering ability of the fabricated photoanodes diffuse reflectance spectra (DRS) was analysed. **Figure 3.12** compares the DRS spectra of TiCl_4 treated pure TiO_2 , TiO_2 -Zfb and TiO_2 -Zsh. About 2 to 5% of reflectance is found to be higher for the modified TiO_2 layers than that of the TiCl_4 treated pure TiO_2 film in the wavelength range of 450- 680 nm. Thus, it is clarified that the voids/surface roughness created can clearly act as light scattering centres. It is also noted that there is not much difference in the percentage of reflectance between TiO_2 -Zfb and TiO_2 -Zsh. Results of the photoanodes TiO_2 , TiO_2 -Zno fibril and TiO_2 -Zno sheet before and after TiCl_4 treatment are presented in **Figure 3.13**. Before TiCl_4 treatment bare TiO_2 film is observed to be transparent (**Figure 3.13a**) whereas TiO_2 -ZnO fibril and TiO_2 - ZnO sheet appeared opaque due to the larger particle size of the ZnO (**Figures 3.13 b and c**). After TiCl_4 treatment the transparency of the bare TiO_2 remains unaltered but at the same time due to the etching of ZnO particles, voids were created over the bottom TiO_2 layer and the transparency got reduced compared to TiCl_4 treated TiO_2 (**Figures 3.13 d, e and f**).

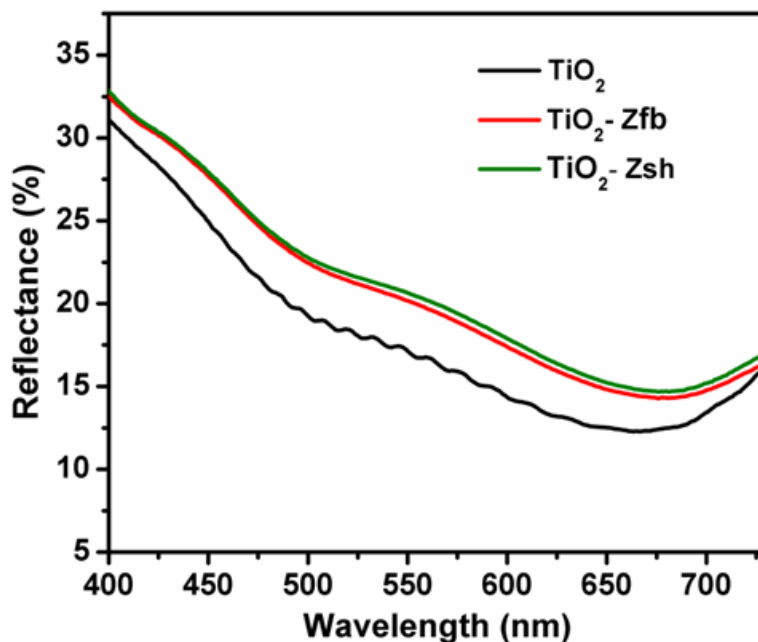


Figure 3.12 UV-vis diffuse reflectance spectra of photoanode films before dye loading.

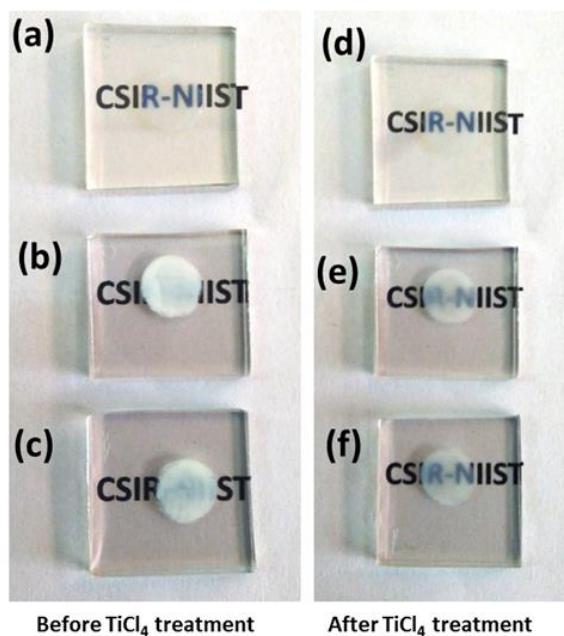


Figure 3.13 Photoanodes before TiCl₄ treatment (a) bare TiO₂ film, (b) TiO₂-ZnO fb film, (c) TiO₂-ZnO sh film and corresponding films after TiCl₄ treatment (d, e and f) respectively.

3.4.6 Atomic force microscopy

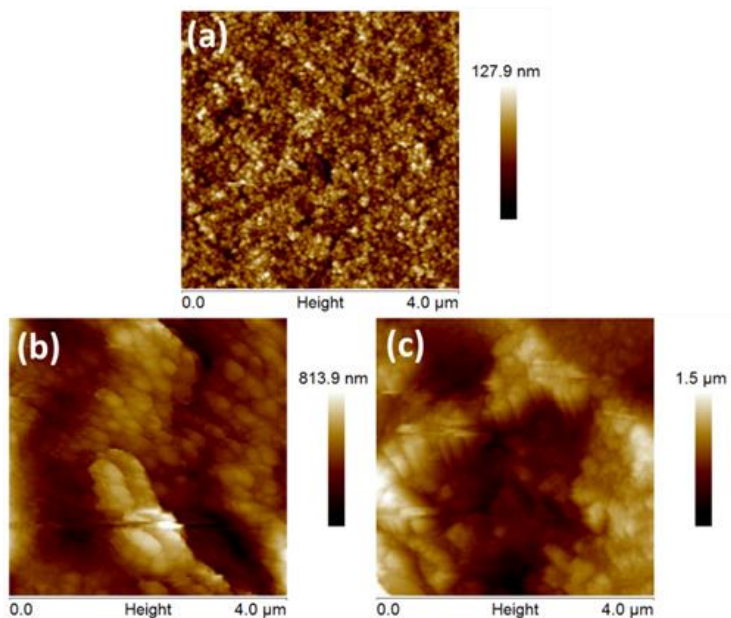


Figure 3.14 AFM spectra of (a) TiO₂ and (b) TiO₂-Zfb and (c) TiO₂-Zsh photoanodes.

Surface roughness of the TiCl_4 treated photoanodes were characterised by AFM analysis (**Figure 3.14**). TiCl_4 treated pure TiO_2 possess root mean square (R_q) value of 18 nm whereas TiO_2 -Zfb and TiO_2 -Zsh have R_q values of 116 nm and 251 nm respectively. Such 10 times increment of the surface roughness of ZnO modified photoanode films should be attributed to the presence of surface voids over the TiO_2 film (**Figures 3.14 b and c**).

3.4.7 Dye loading studies

The quantity of dye adsorbed on to the TiO_2 film was analysed using dye adsorption-desorption procedure. Desorption of the adsorbed dye is carried out by soaking the electrodes in 0.1 N NaOH solution in water. After the complete desorption of dye, the absorbance spectra of the desorbed dye were recorded (**Figure 3.15**). The concentration of the dye is calculated using the equation provided below.

$$\text{Dye loading} = AV/\epsilon Sb \quad (6)$$

Where A is the absorbance of the dye, V is the volume of NaOH used to desorb the dye (5 ml), ϵ is the molar extinction coefficient of the dye N719 ($13500 \text{ mol cm}^{-1}$), S is the area of the electrode (0.317 cm^2) and b is the path length (1 cm).

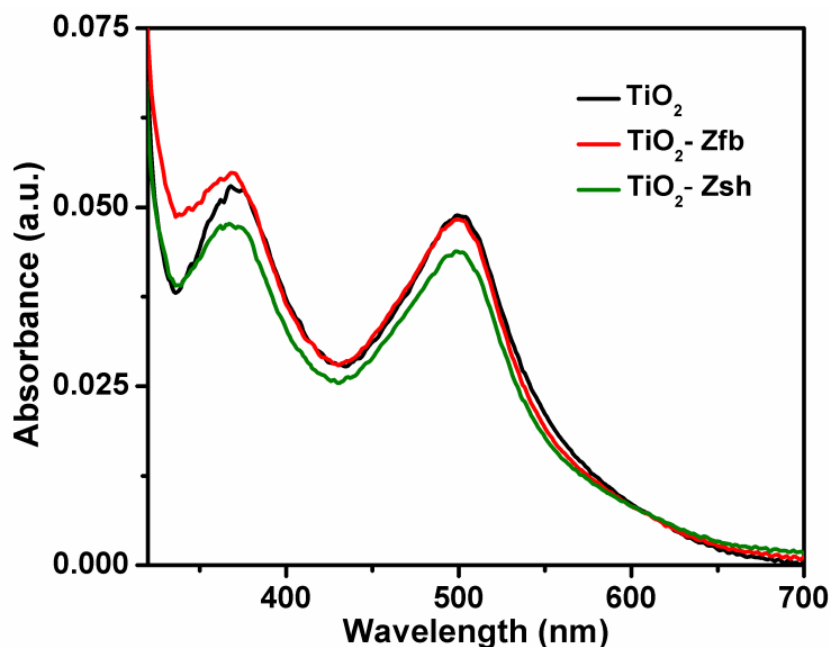


Figure 3.15 Absorption spectra of the desorbed dyes from the photoanodes.

Bare TiO₂ have shown a dye loading of 5.75×10^{-8} mol cm⁻² and TiO₂-Zfb has also displayed almost similar dye loading of 5.68×10^{-8} mol cm⁻² the dye loading for TiO₂-Zsh negligibly decreased to 5.17×10^{-8} mol cm⁻². Hence it can be concluded that the surface roughness created over the TiO₂ layer does not contribute much as far dye loading is concerned. Huang *et al.* reported that the presence of Zn element can enhance the dye adsorption due to its higher basicity, which encourage the dye adsorption through the carboxylic acid group of the N719 dye.²⁵ Here, it is noteworthy that the 0.1% Zn element detected in the photoanode films has also not proven to contribute much in dye loading.

3.5 Photovoltaic Characterisations

3.5.1 Current voltage characteristics and IPCE measurements

Under one sun conditions (100mW/cm², Air Mass 1.5 G), the photovoltaic performance of the cells namely TiO₂-Zfb as well as TiO₂-Zsh were better compared to bare TiO₂ device. **Figure 3.15** shows the current density versus voltage (*J-V*) curve for the three kinds of DSSCs, with illumination from the front side. The short-circuited current density (*J_{sc}*) for the TiO₂, TiO₂-Zfb and TiO₂-Zsh devices were 12.99 ± 2.38 mAcm⁻², 14.56 ± 0.71 mAcm⁻² and 14.71 ± 0.66 mAcm⁻² respectively, giving rise to an overall PCE up to $6.17 \pm 0.89\%$, $7.13 \pm 0.19\%$ and $7.32 \pm 0.48\%$ respectively. The TiO₂-Zfb device exhibited an improvement of 12.09% in *J_{sc}* whereas the TiO₂-Zsh device showed an increment of 13.24% in *J_{sc}* when compared to the bare TiO₂ device. This resulted in an enhancement of 15.56% and 18.64% in power conversion efficiency for the TiO₂-Zfb and TiO₂-Zsh devices, respectively, relative to the TiO₂ device. The corresponding parameter values are being listed in **Table 3.3**. The enhancement in PCE of the ZnO-modified devices is ascertained to the following reasons. The absorption peak of N719 dye lie within the wavelength range of 430 to 580 nm and the scattering effect displayed by the ZnO modified photoanodes are also within similar wavelength range. Hence it results in a perfect synchronisation of scattering effect and dye absorption leading to further improvements in *J_{sc}* and thereby PCE.

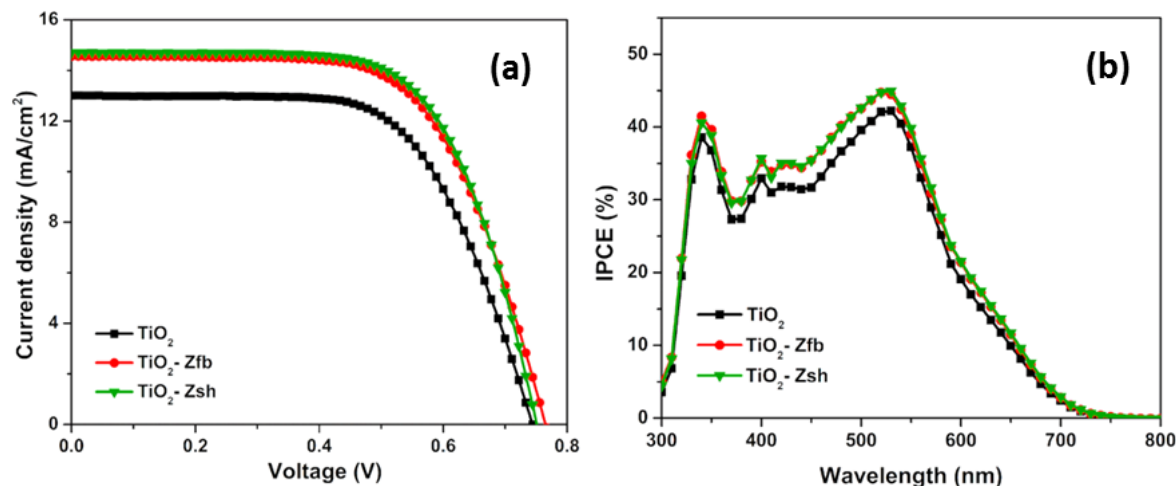


Figure 3.16 (a) J - V characteristics under one sun condition and (b) IPCE spectra of the devices with front side illumination.

Incident photon to current conversion efficiency ($IPCE$) can be defined as the ratio of number of photo-generated electrons to the number of photons incident on the solar cell.²⁶ The $IPCE$ spectra of the devices illuminated from front side, as shown in **Figure 3.16**, were in accordance with the observed values of the devices. $IPCE$ can be expressed in terms of light harvesting efficiency (LHE), electron injection efficiency (η_{inj}), dye regeneration efficiency (η_{reg}), and the charge collection efficiency (η_{cc}) as,

$$IPCE = LHE \times \eta_{inj} \times \eta_{reg} \times \eta_{cc} \quad (7)$$

LHE depends on the light scattering effect (which is linearly related to the optical thickness) of the photo-anode, dye concentration in the photo-anode, molar extinction coefficient of the dye, and thickness of the absorbing layer.²⁷⁻²⁹ Since we have used the same dye and electrolyte in all the devices η_{reg} can be ignored for the enhancement in $IPCE$ of TiO₂-Zfb and TiO₂-Zsh devices. The roughness over semiconductor enhanced the light scattering effect leading to increased LHE and $IPCE$ of TiO₂-Zfb and TiO₂-Zsh devices.^{14, 30} The contribution of injection and charge collection towards the better $IPCE$ for the devices with surface modified photoanodes were addressed using the advanced characterisation techniques.

Table 3.3 J - V parameters for TiO_2 , TiO_2 -Zfb and TiO_2 -Zsh devices with front side illumination under one sun conditions.

Device	V_{oc} (mV)	J_{sc} (mAcm^{-2})	FF (%)	η (%)
TiO_2	744 ± 14	12.99 ± 2.38	63.80 ± 3.15	6.17 ± 0.89
TiO_2 -Zfb	765 ± 80	14.56 ± 0.71	63.99 ± 2.76	7.13 ± 0.19
TiO_2 -Zsh	751 ± 60	14.71 ± 0.66	66.23 ± 1.83	7.32 ± 0.48

With back illumination, the standard TiO_2 device gave, J_{sc} of $9.12 \pm 0.66 \text{ mAcm}^{-2}$ yielding η of $4.79 \pm 0.37\%$ and TiO_2 -Zfb offered a J_{sc} of $9.55 \pm 1.48 \text{ mAcm}^{-2}$ and η of $5.03 \pm 0.78\%$. For TiO_2 -Zsh, J_{sc} of $9.63 \pm 0.39 \text{ mAcm}^{-2}$ and η of $4.96 \pm 0.17\%$, was measured.

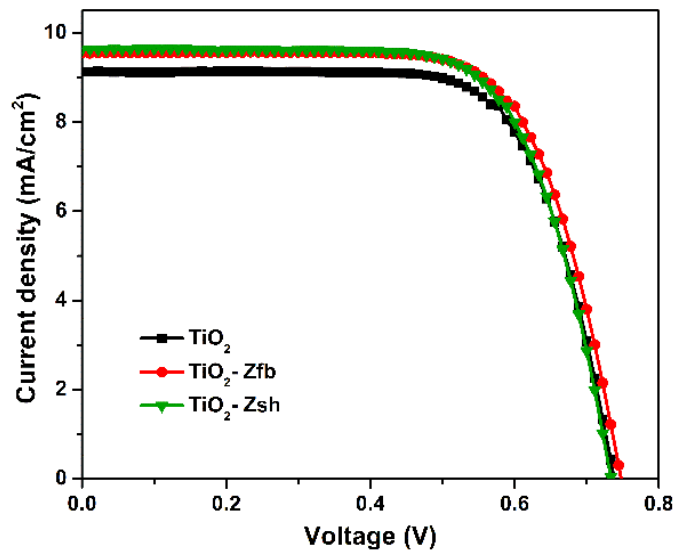


Figure 3.17 J - V characteristics under one sun conditions of the devices with back side illumination.

Table 3.4 Photovoltaic parameters of the devices with back side illumination under one sun conditions.

Device	V_{oc} (mV)	J_{sc} (mAcm ⁻²)	FF (%)	η (%)
TiO ₂	738 ± 9	9.12 ± 0.66	71.16 ± 0.36	4.79 ± 0.37
TiO ₂ -Zfb	749 ± 12	9.55 ± 1.48	70.48 ± 1.46	5.03 ± 0.78
TiO ₂ -Zsh	733 ± 5	9.63 ± 0.39	70.14 ± 0.93	4.96 ± 0.17

There was 4.71% increase in J_{sc} resulting in 5.01% increment in η for TiO₂-Zfb, meanwhile, an elevation of 5.59% in J_{sc} , gave rise to 3.55% improvement in η for TiO₂-Zsh than the TiO₂ device. Since the light encounters the back sealing (surlyn), the platinum layer and the electrolyte, before reaching the photoanode, the PV performance of DSSC with back illumination is less compared to front illumination.³¹ The higher FF values under illumination from the rear side can be attributed to the decreased recombination rate arising from the lower illumination intensity.³² The corresponding J - V plots and photovoltaic parameters are given in **Figure 3.17** and **Table 3.4** respectively.

3.5.2 Electrochemical impedance spectroscopy

Electrochemical impedance spectroscopy (EIS) was done under dark to study the charge transfer dynamics at the TiO₂-electrolyte interface. **Figure 3.18** shows Nyquist and Bode plot. Nyquist plot displayed two distinct semicircles. The first semicircle corresponds to charge transfer at the Pt/electrolyte interface and the second semicircle is due to the charge recombination at TiO₂/electrolyte interface. The plot was fitted using equivalent circuit with transmission line model (**Chapter 2 Figure 2.18**). The equivalent-circuit model consists of R_s (resistance due to the FTO and contact resistance), R_{Pt} , C_{Pt} (resistance and capacitance at Pt/electrolyte interface), C_{TCO} (capacitance at

FTO/electrolyte interface) and $B2$ (transmission line model used to explain charge transfer at dye/TiO₂/electrolyte interface). $B2$ includes R_t (transport resistance for TiO₂), R_{rec} (recombination resistance at dye/TiO₂/electrolyte interface) and C_{μ} (Chemical capacitance of TiO₂ in contact with electrolyte and is used to find out the position of conduction band (CB) of TiO₂).

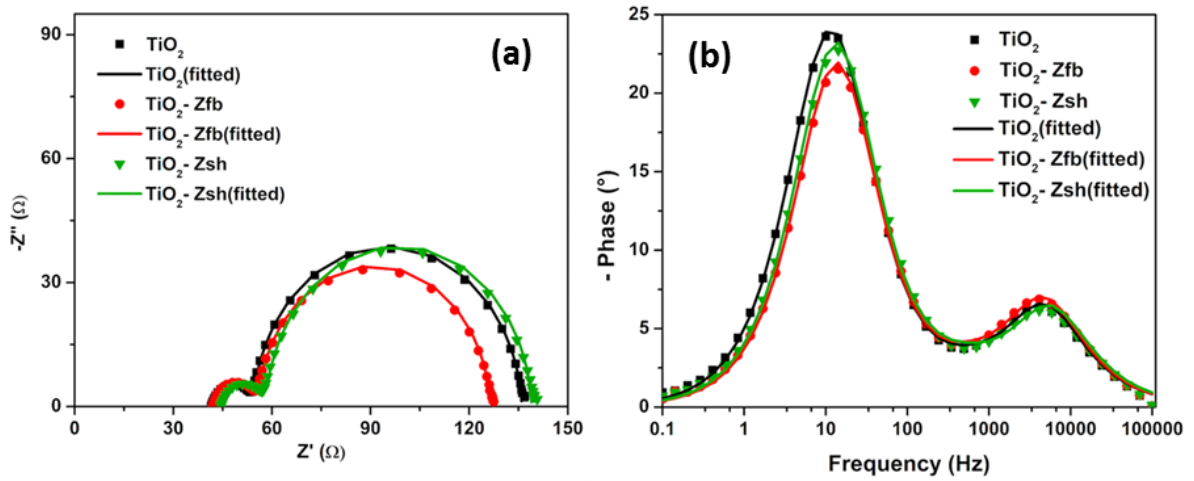


Figure 3.18 (a) Nyquist Plot and (b) Bode Plot obtained from EIS measurement.

Electron lifetime is calculated from Bode plot using the relation

$$\tau_n = \frac{1}{2\pi f_m} \quad (8)$$

where f_m is the frequency corresponding to the highest phase (ϕ) value in the Bode plot.

Fermi voltage (V_F) is calculated by the following equation given below

$$V_F = V_{app} - V_{series} \quad (9)$$

$$V_{series} = I \times R_{series} \quad (10)$$

$$R_{series} = R_S + R_{Pt} + R_d \quad (11)$$

Where V_{app} is the applied DC voltage and V_{series} is the voltage drop due to the series resistance. I is the DC current derived from EIS. R_{series} is the total series resistance and R_d is the diffusion resistance of electrolyte. **Figure 3.19a** shows C_{μ} as a function of Fermi voltage (V_F), a negative shift of about 30mV for TiO₂-Zfb and 19 mV for TiO₂-Zsh with

respect to the standard TiO₂ device was observed. Owing to this reason the lifetime of TiO₂-Zfb and TiO₂-Zsh was found decreased compared to standard TiO₂ (**Figure 3.19b**).

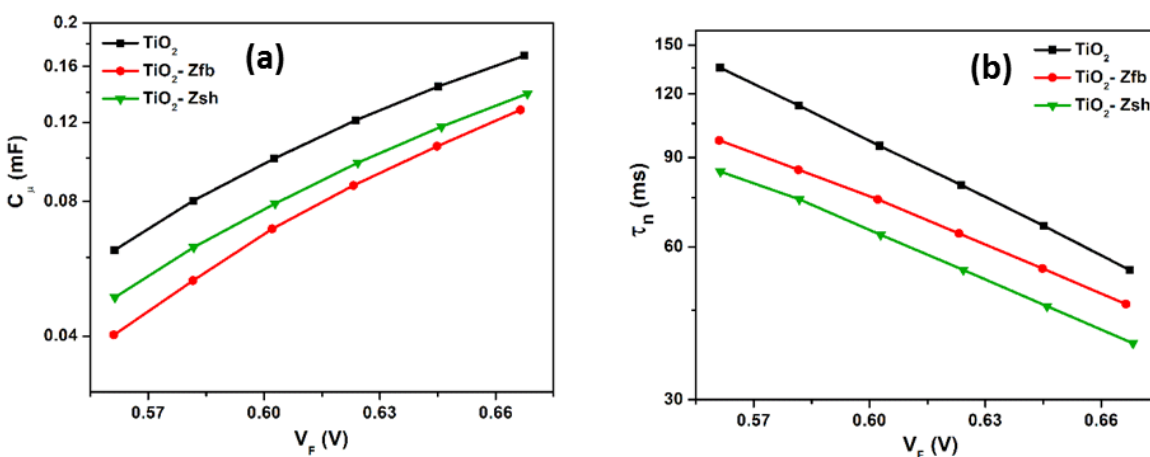


Figure 3.19 (a) Capacitance plot and (b) Lifetime plot from EIS in dark.

3.5.3 Intensity-modulated photovoltage spectroscopy and Intensity-modulated photocurrent spectroscopy

IMPS and IMVS are optical perturbation techniques which give the information of charge recombination and diffusion at TiO₂ electrolyte interface. IMPS is carried out in short circuit condition whereas IMVS is carried out at open circuit condition. For both measurements a constant illumination was given using LED light. Charge transport in mesoporous TiO₂ occurs via diffusion process and the electrons get trapped in energy state in band gap and detrapp back to transport state in CB. Only the detrapped electrons i.e. free electrons contribute to the current as well as recombination and this process of electron transport is well explained by multiple trapping and detrapping model.^{33, 34}

Figure 3.20 shows lifetime and transport time plot obtained from IMVS and IMPS measurement respectively. It is clear from the plots (**Figures 3.20 a and b**) that TiO₂-Zfb and TiO₂-Zsh devices showed lower lifetime and faster charge transport than the standard TiO₂ devices. This is due to the scattering property of TiO₂-Zfb and TiO₂-Zsh which helped to create higher concentration gradient of electrons in semiconductor leading to faster diffusion than TiO₂ devices.

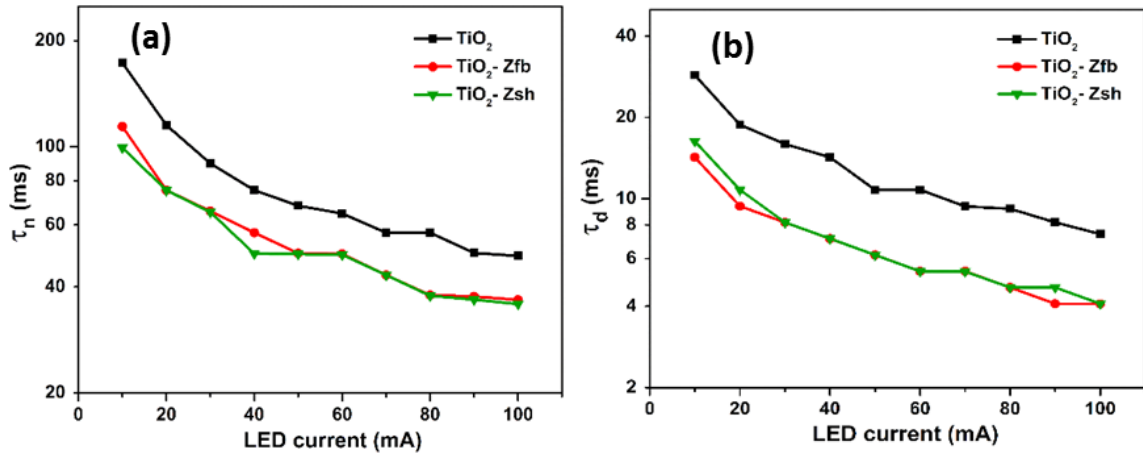


Figure 3.20 (a) Life time plot and (b) Transport time plot obtained from IMVS and IMPS data respectively.

Diffusion coefficient (D_n) and Charge collection efficiency (η_{cc}) are calculated using the equation given below

$$D_n = \frac{d^2}{\tau_d} \quad (12)$$

$$\eta_{cc} = \left(1 - \frac{\tau_d}{\tau_n}\right) \times 100 \quad (13)$$

Where 'd' is the thickness of the photoanode, τ_d is the transport time/diffusion time and τ_n is the life time.

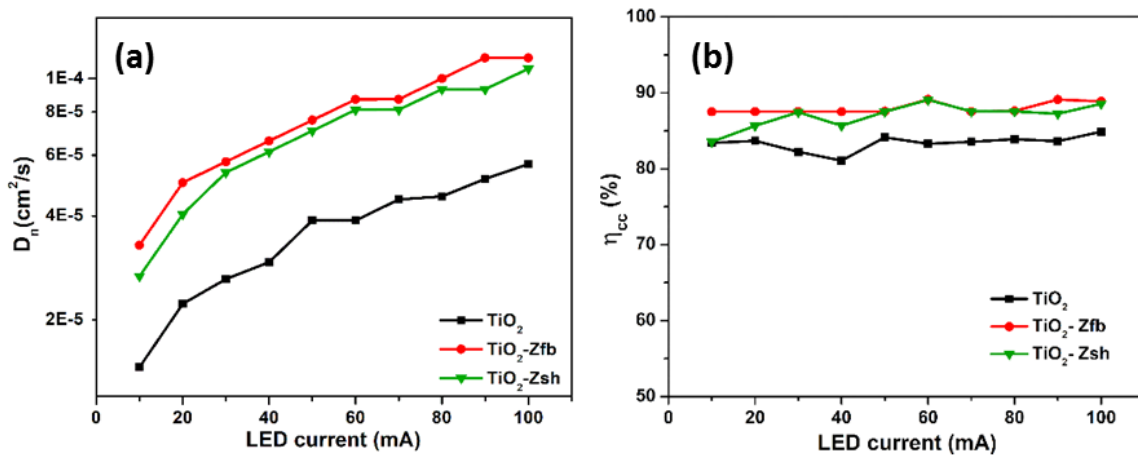


Figure 3.21 (a) Diffusion coefficient plot obtained from IMPS and (b) Charge collection efficiency plot obtained from IMPS and IMVS data.

Due to the faster diffusion of electrons in the TiO₂-Zfb and TiO₂-Zsh devices, they showed larger diffusion coefficient (**Figure 3.21a**), than the standard device. This paved the way for the higher charge collection efficiency (η_{cc}) (**Figure 3.21b**) in TiO₂-Zfb and TiO₂-Zsh devices. It is to be noted that higher η_{cc} significantly contributes in the achievement of higher IPCE.

3.5.4 Photovoltaic performance under indoor light conditions

The photovoltaic performance of the devices was studied with illumination from front side as well as from back side. The indoor light measurements were done by the illumination of 1000 lux daylight CFL. The J - V characteristics is plotted in **Figure 3.22** and the corresponding photovoltaic parameters are summarised in **Table 3.4**. With illumination from the front side, the standard TiO₂ device showed J_{sc} of $81 \pm 4 \mu\text{Acm}^{-2}$ and η of $11.1 \pm 0.4\%$, while TiO₂-Zfb and TiO₂-Zsh cells outperformed it. TiO₂-Zfb achieved a J_{sc} of $94 \pm 3 \mu\text{Acm}^{-2}$ leading to η of $15.5 \pm 1.9\%$, whereas TiO₂-Zsh attained a J_{sc} of $86 \pm 11 \mu\text{Acm}^{-2}$ and η of $11.8 \pm 3\%$. When the light was incident from back side, the standard TiO₂ device displayed a J_{sc} of $57 \pm 1 \mu\text{Acm}^{-2}$ giving η of $5.9 \pm 1.4\%$, while TiO₂-Zfb and TiO₂-Zsh devices showed improved performance with TiO₂-Zfb displaying J_{sc} of $64 \pm 2 \mu\text{Acm}^{-2}$ and η of $8.5 \pm 0.8\%$, at the same time TiO₂-Zsh devices exhibiting J_{sc} of $59 \pm 6 \mu\text{Acm}^{-2}$ and η of $8.5 \pm 0.8\%$. The increment in current in ZnO modified device should be due to the light scattering effect leading to better PCE.

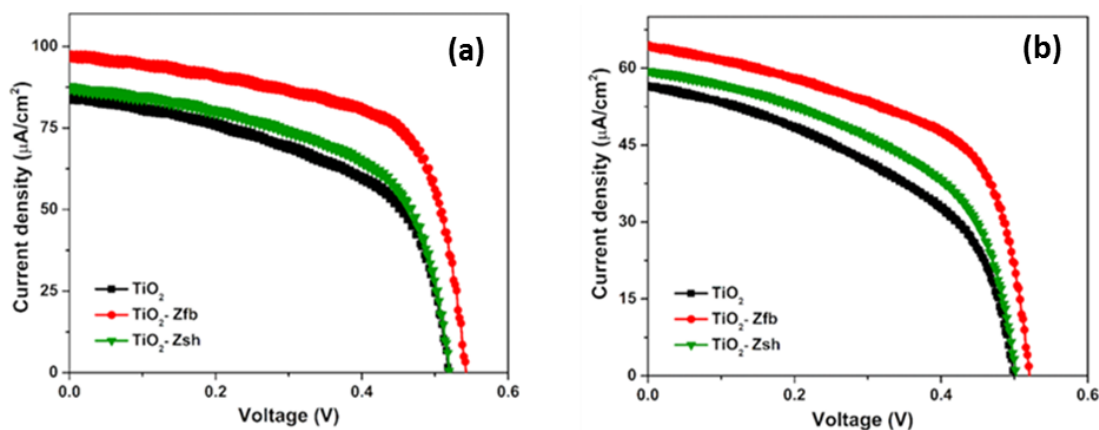


Figure 3.22 J - V characteristics of the devices, when illuminated with 1000 lux day-light CFL from (a) front side and (b) back side

Table 3.5 Photovoltaic parameters of the devices under 1000 lux illumination.

Light incident on	Device	V_{oc} (mV)	J_{sc} (μAcm^{-2})	FF (%)	η (%)
Front side of the device	TiO ₂	518 ± 11	81 ± 04	61 ± 01	11.1 ± 0.4
	TiO ₂ -Zfb	543 ± 01	94 ± 03	69 ± 07	15.5 ± 1.9
	TiO ₂ -Zsh	521 ± 21	85 ± 11	61 ± 04	11.8 ± 3.0
Back side of the device	TiO ₂	498 ± 17	57 ± 01	48 ± 09	5.9 ± 1.4
	TiO ₂ -Zfb	519 ± 05	64 ± 02	59 ± 02	8.5 ± 0.8
	TiO ₂ -Zsh	502 ± 23	59 ± 06	53 ± 08	6.8 ± 2.2

3.6 Conclusions

Light scattering in the photoanode of the DSSC was enhanced by employing sacrificial inclusions of ZnO hierarchical structures. The roughness of the ZnO modified TiO₂ photoanode was found to increase by 10 times that of standard photoanode. The voids/roughness created by the selectively etched ZnO hierarchical structures on the TiO₂ layer effectively functioned as scattering centers to improve the current density of DSSC at one sun and indoor light conditions. As the dye loading was found to be almost same for all devices, it can be concluded that the increase in current density, is due to enhanced light scattering. An enhancement of 15.56% and 18.64% in PCE was obtained for TiO₂-Zfb and TiO₂-Zsh devices respectively relative to the standard TiO₂ device in one sun conditions. Under low light, an improvement of 39.63% and 6.30% was observed for the same devices. As the photoanodes described in this study are transparent, they can be utilised for BIPV applications.

3.7 Macro porous titania scattering layers from TiO₂-ZnO mixed compositions

In this section, the effect of voids inside the TiO₂ photoanodes was studied. A bilayer photoanode comprising of a TiO₂ bottom layer and a porous TiO₂ top layer were fabricated for this purpose. Three different weight percentage of TiO₂-ZnO sheet aggregates were utilised to create porous TiO₂ scattering layer. It was observed that the top porous layer imparted strong light scattering inside the device. The designed architecture allowed the development of DSSC which could effectively function at both indoor and one sun conditions.

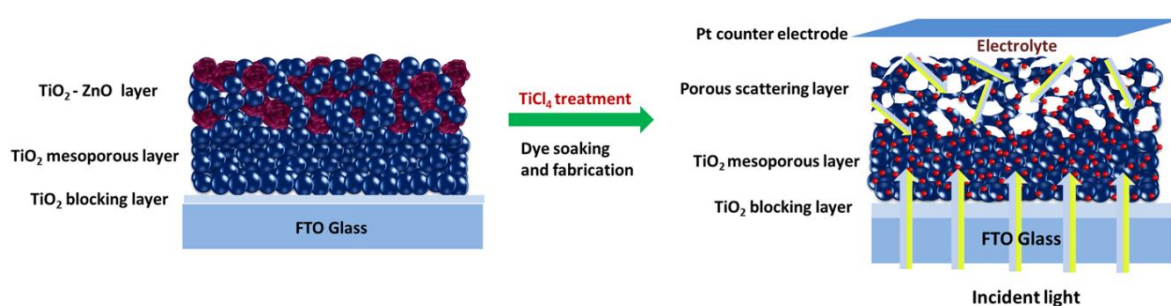


Figure 3.23 Schematic illustration of the fabrication of porous TiO₂ scattering layer for DSSC utilising ZnO sheet aggregates structure as sacrificial inclusions.

3.7.1 Synthesis of TiO₂ - ZnO Paste

Three different TiO₂-ZnO pastes with varying ZnO wt.% (10, 20, 40) with respect to TiO₂ were prepared. ZnO sheet like aggregates synthesised via wet chemical method described in the section 3.2.1, was mixed with TiO₂ paste and doctor bladed over pure TiO₂ layer and annealed up to 500 °C. The photoanodes thus formed were then subjected to TiCl₄ treatment (40 mM) at 70 °C for 45 minutes. As mentioned in the previous sections, due to the instability of ZnO in acidic TiCl₄, macro pores are created inside the TiO₂ layer. The structure of the photoanode therefore depends on the amount of ZnO removed by TiCl₄. The photoanodes were designated as T (control sample, one layer TiO₂), T Z10, T Z20 and T Z40 according to the wt.% of ZnO in the TiO₂-ZnO paste. The thickness of the standard device T was measured as ~ 6 μm and the corresponding value for T Z10, T Z20, T Z40 was ~ 14, 15 and 10 μm respectively.

3.8 Results and Discussion

3.8.1 X-ray diffraction analysis

XRD patterns of the bilayer photoanodes after TiCl_4 treatment is provided in **Figure 3.24**. It is clear that all peaks are assigned to anatase phase of TiO_2 (JCPDS file no 01-075-1537) and that no diffraction peaks from ZnO is visible in the patterns.

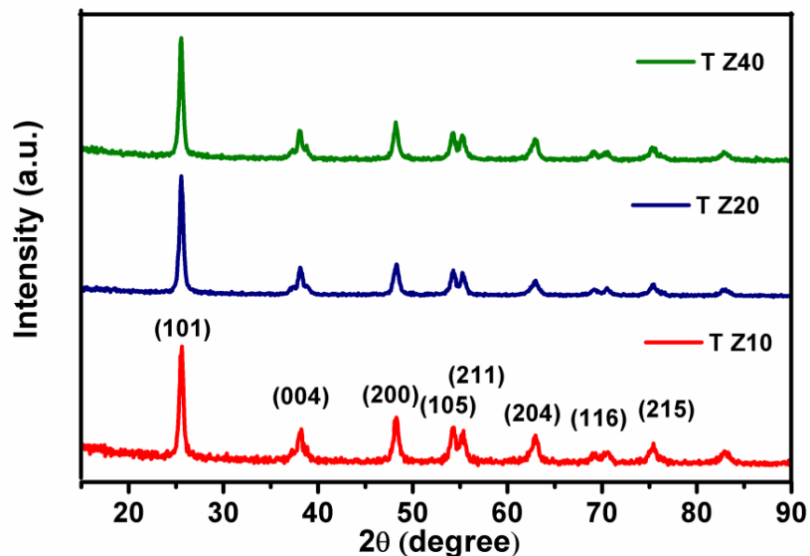


Figure 3.24 XRD patterns of TiCl_4 treated films.

3.8.2 Scanning electron microscopy and Energy dispersive X-ray analysis

The surface morphology of the bilayer photoanode after etching are presented in **Figure 3.25**. The incorporation of ZnO sheet aggregates in the paste and its annealing followed by TiCl_4 treatment has resulted in the formation of TiO_2 layers with macropores and cracks. It is clearly evident from the SEM images that, as the wt.% of ZnO increases the number of cavities as well as the crack throughout the film is also increased (T Z10 < T Z20 < T Z40). High magnification SEM images clearly suggest that the cavities and cracks were formed by the removal of ZnO aggregates. EDX analysis provided in **Figure 3.26** shows the presence of Zn is negligible in all samples (0.08 atomic% of Zn is in sample T Z10, and 0.11 atomic% in T Z20 and 0% in T Z40). As ZnO is incorporated into the TiO_2

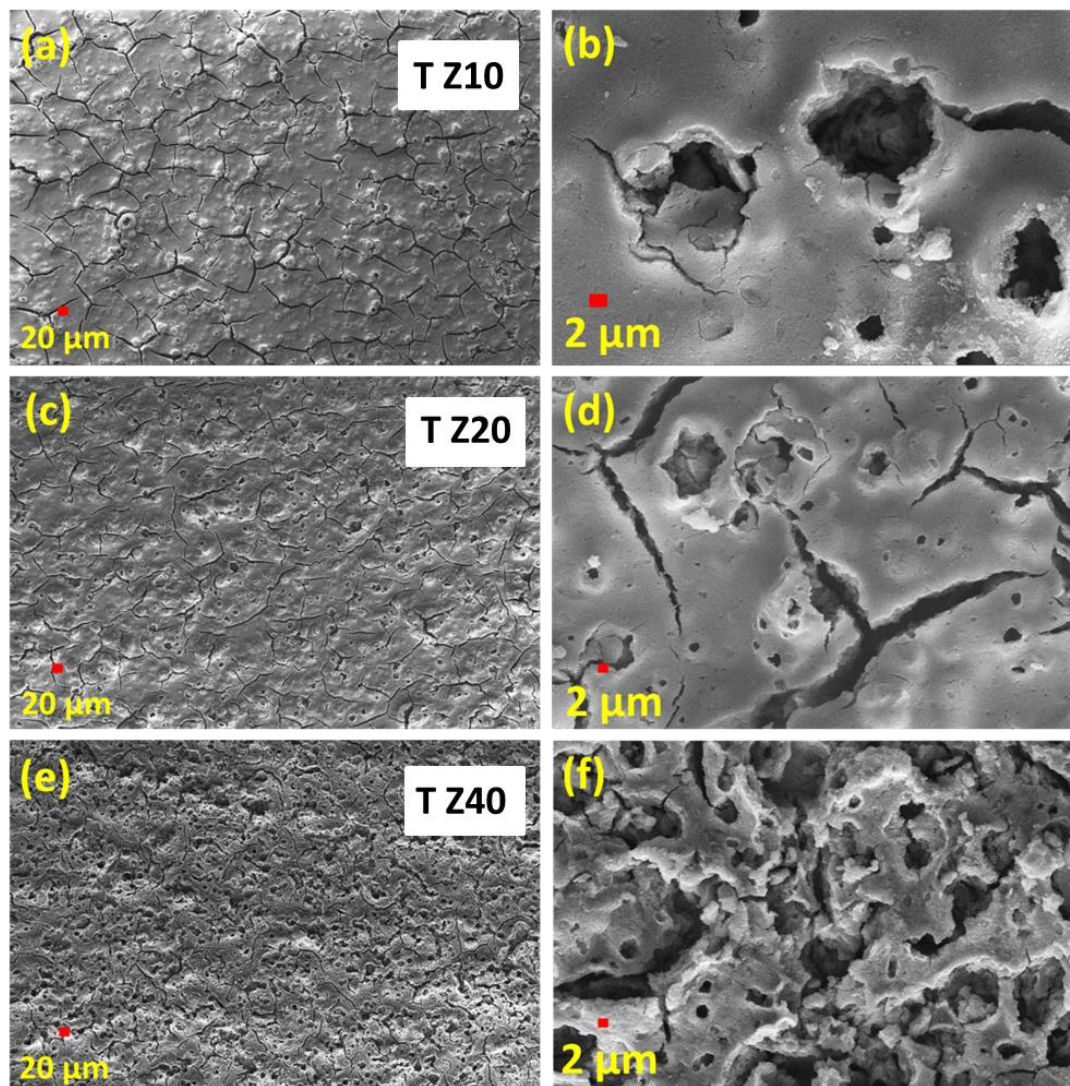


Figure 3.25 SEM images of TiCl_4 treated bilayer films: T Z10 (a and b), T Z20 (c and d) and T Z40 (e and f).

matrix the cross-sectional image of the coating and EDX analysis was performed. **Figure 3.27** shows the cross sectional image of sample T Z20 (best device) and ZnO is found to be absent inside the TiO_2 layer. Results suggests that, even if, any trace amount of Zn ions are present in the structure, the amount is too negligible to have any significant influence in the properties.

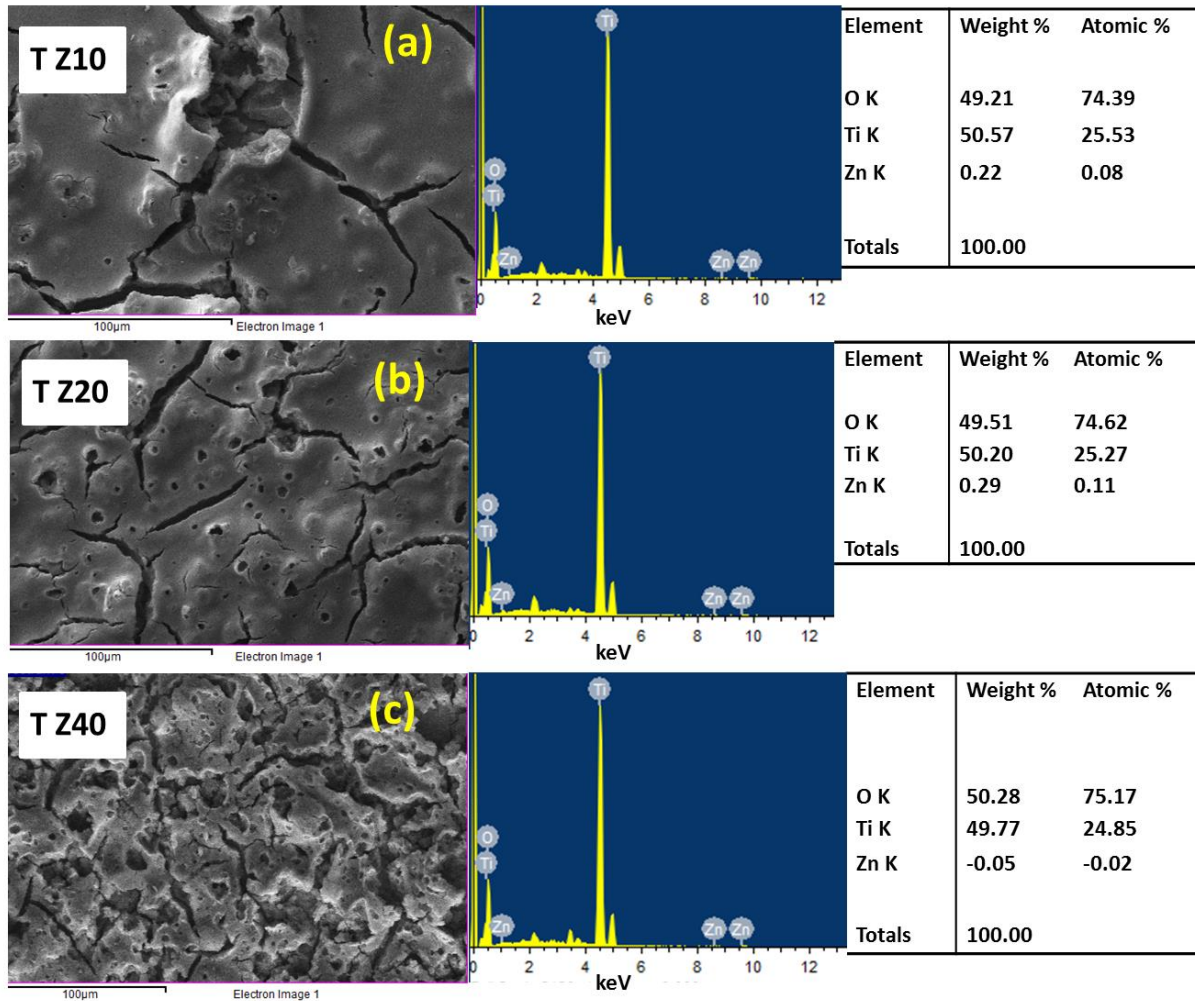


Figure 3.26 EDX of TiCl_4 treated bilayer films: (a) T Z10, (b) T Z20 and (c) T Z40.

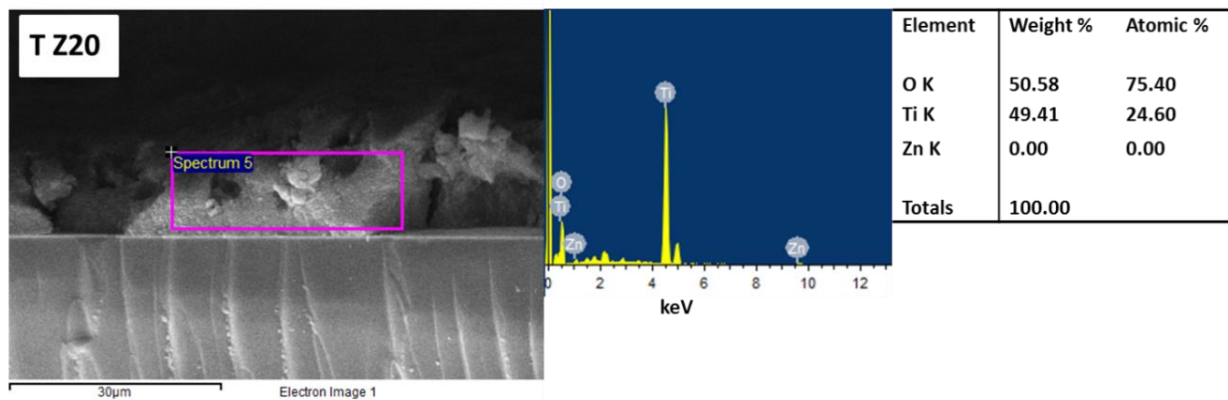


Figure 3.27 EDX of TiCl_4 treated film cross section of the best device T Z20.

3.8.3 Diffuse reflectance spectroscopy

The photographs of the photoanodes before and after TiCl_4 treatment is presented in **Figure 3.28**. The single layer pure TiO_2 retains its transparency after TiCl_4 treatment. The transparency goes on decreasing for all the bilayered structured anodes. It is observed that before TiCl_4 treatment T Z10 is slightly transparent than T Z20 and T Z40 which are opaque due to the presence of higher amounts of ZnO in it. After TiCl_4

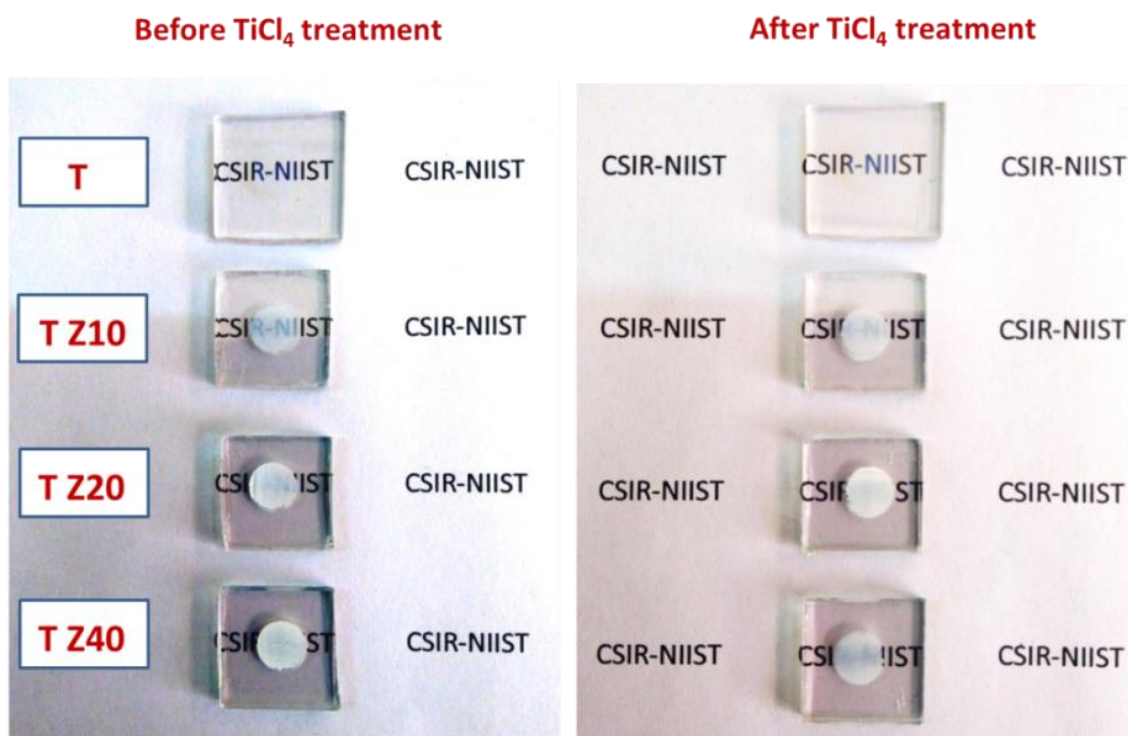


Figure 3.28 Photographs of photoanodes before and after TiCl_4 treatment

treatment, single layer TiO_2 (T) retained its transparency, T Z10 and T Z40 have remained slightly transparent, whereas T Z20 became more or less opaque. It is expected that in the case of T Z10 the amount of ZnO is less so that the voids created will be less in the sample, thus retaining slight transparency as in the case of sample “T”. In the case of T Z40 with the highest amount of ZnO, TiCl_4 treatment should have removed all the ZnO, and the comparatively low amount of TiO_2 remaining should have helped it to retain its transparency. But in the case of T Z20 the quantity of ZnO is optimum to create enough

amounts of voids inside the TiO₂ top layer matrix on etching with TiCl₄ leading to enhanced light scattering and loss of transparency.

In order to confirm the scattering property of the fabricated films, diffuse reflectance spectra were taken. **Figure 3.29a** shows the diffuse reflectance spectra of photoanodes after TiCl₄ treatment. Around 15% of reflectance is increased for samples T Z10, T Z40 whereas T Z20 exhibited the highest scattering ability offering around 25% increment in reflectance. The absorbance spectra of the electrodes after dye loading was also measured (**Figure 3.29b**). Here, it is clearly observed that due to scattering, the absorbance of the all bilayer porous electrodes have increased than that of standard photoanode. The peaks at 500-600 nm are due to the absorbance of the N719 dye. The absorbance spectra followed the same trend as that of reflectance spectra of the photoanodes before dye loading. The photographs samples after dye loading are provided in **Figure 3.30**.

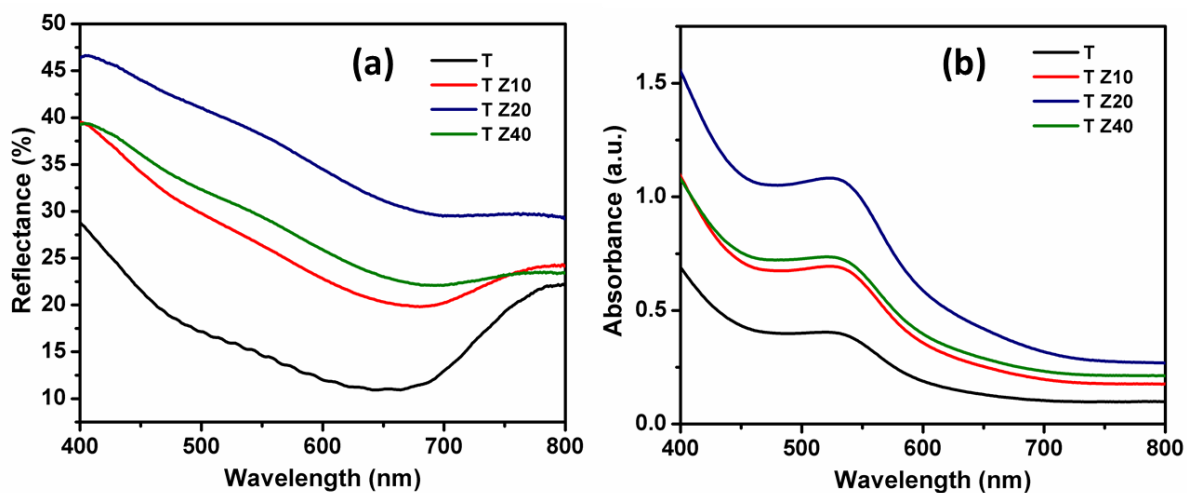


Figure 3.29 UV-vis diffuse reflectance spectra of TiCl₄ treated photoanodes (a) without dye and (b) absorption spectra after dyeloading.

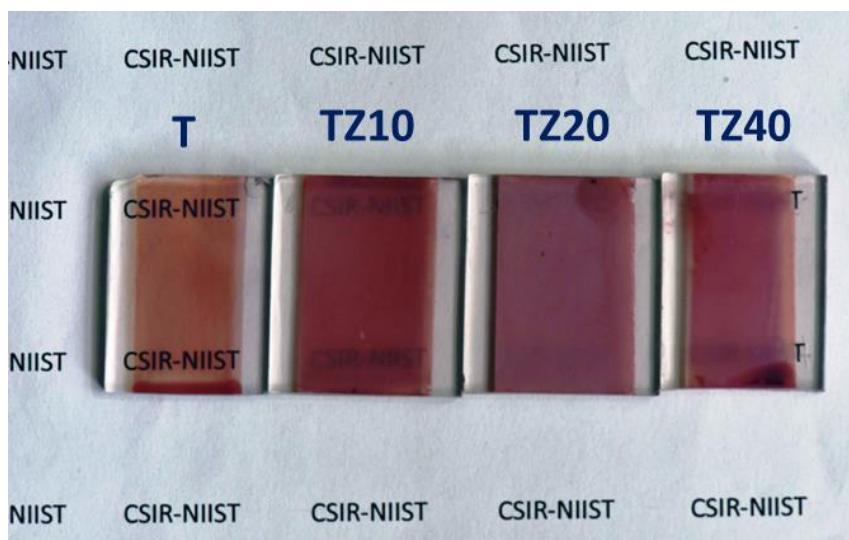


Figure 3.30 Photographs of substrates used to analyse absorbance spectra after dye loading.

3.8.4 Dye loading studies

The quantity of dye adsorbed on to the photoanodes was examined using dye adsorption-desorption procedure (see section 3.4.7).

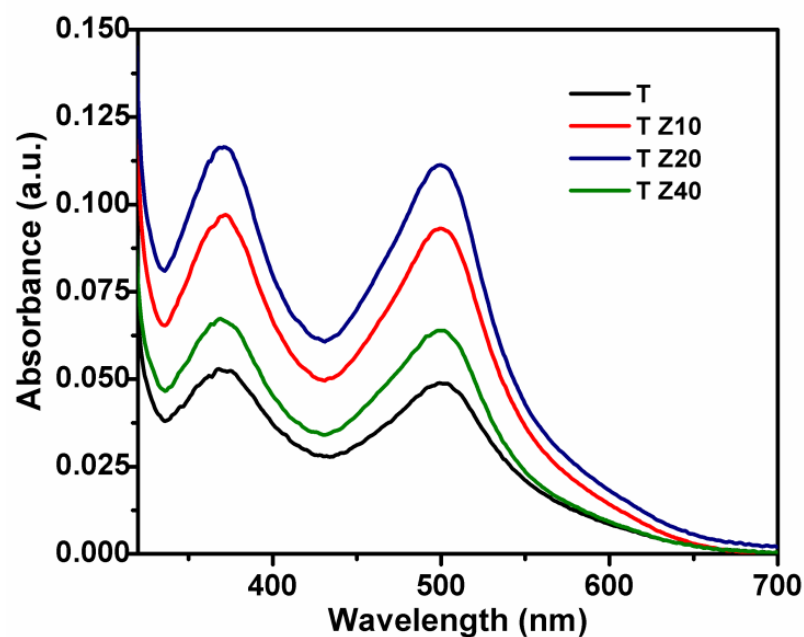


Figure 3.31 Absorption spectra of the desorbed dyes from the photoanodes.

Dye loading was found higher for all the bilayer structured than single layer structured anodes due to higher number of TiO₂ particles in the bilayered ones. Single layer TiO₂ sample showed a dye loading value of 5.75×10^{-8} mol cm⁻² as in **Table 3.6**. The bilayered photoanodes displayed dye loading values of 10.84×10^{-8} mol cm⁻² for TZ 10, 12.95×10^{-8} mol cm⁻² for TZ 20 and 7.52×10^{-8} mol cm⁻² for TZ 40. The quantity of dye adsorbed for TZ 20 is 2.25 times higher than that of single layer TiO₂ and 1.88 times and 1.30 higher than that of TZ 10 and TZ 40 respectively. The better dye adsorption capability of TZ 20 is associated with its optimum porous structure which is also supported by SEM image (**Figures 3.25 c and d**). Even though T Z40 was found to be more porous among the three, it offered the lowest dye loading, which could be ascribed to the lesser amount of TiO₂ particles in the film.

Table 3.6 Dye loading studies.

Sample	Dye loaded (mol/cm ²)
T	5.75×10^{-8}
T Z10	10.84×10^{-8}
T Z20	12.95×10^{-8}
T Z40	7.52×10^{-8}

3.9 Photovoltaic characterisation of dye-sensitised solar cells

3.9.1 Current voltage characteristics and IPCE measurements

J-V characteristics of the fabricated devices under one sun condition are shown in **Figure 3.32a** and the corresponding photovoltaic parameters measured are summarised in **Table 3.7**. From the J-V data, it is obvious that the devices with ZnO modified-TiO₂ layers outperformed the standard device with single layer of TiO₂. In all devices J_{sc} was found to increase remarkably owing to the enhancements in the light scattering and dye loading introduced by the porous layer which in turn contributed to the high PCE. The PCE of the

devices followed the trend T Z20>T Z10>T Z40>T. Owing to the optimum porous structure device T Z20 exhibited the highest PCE of 9.40% with FF of 73%, J_{sc} of 17.93 mAcm^{-2} and V_{oc} of 0.72V. The PCE increased by 49.20% compared to the standard device having pure TiO_2 layers. Though the SEM images (**Figures 3.25 e and f**) revealed that the most porous photoanode was T Z40; due to its low TiO_2 content, low dye loading and lesser light scattering, its measured PCE was found lower than that of T Z20 sample.

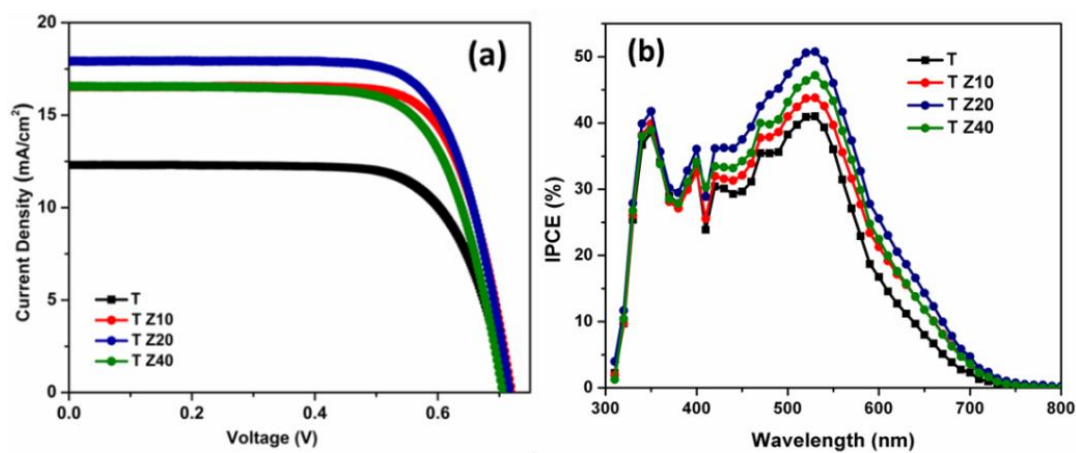


Figure 3.32 (a) J - V characteristics of the devices with front illumination and (b) IPCE of the devices with front illumination.

Table 3.7 Photovoltaic parameters of the devices with front side illumination under one sun conditions.

Device	V_{oc} (V)	J_{sc} (mAcm^{-2})	Fill factor (%)	Efficiency (%)
T	0.71	12.31	71.6	6.30
T Z10	0.72	16.52	74.19	8.83
T Z20	0.72	17.93	73.00	9.40
T Z40	0.71	16.57	71.62	8.38

The IPCE values for all the ZnO modified devices were found to have increased with respect to the standard device (**Figure 3.32b**). The IPCE spectra of the four devices are in accordance with their corresponding J_{sc} values.

3.9.2 Photovoltaic performance under indoor light

Figure 3.33 shows the J-V characteristics recorded under indoor light (Daylight CFL) with 1000 lux intensity. The highest PCE was obtained for the device T Z20 (PCE of 17.85%) which was 44.76% higher than that of the standard device. PCE of the DSSCs follows the same trend as obtained under one sun conditions; T Z20>T Z10>T Z40>T. Even though measured PCE was higher, the device T Z20 is opaque and therefore might not be the best candidate for BIPV applications.

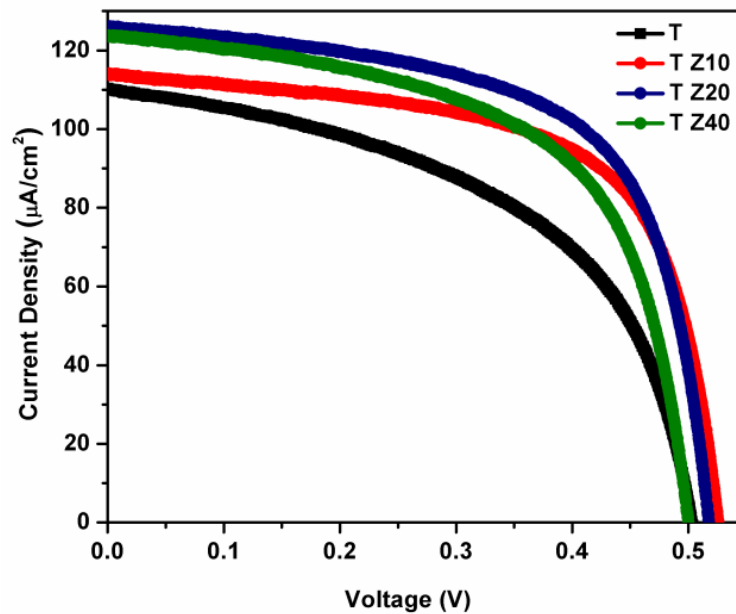


Figure 3.33 J-V characteristics of devices with front illumination under 1000 lux.

The second-best performance was exhibited by T Z10 (PCE of 16.66%), which was 35.11% higher than the standard device. As this device offers transparency, it could find applications in BIPV sector. The photovoltaic parameters obtained are summarised in **Table 3.8**.

Table 3.8 Photovoltaic parameters of the devices with front side illumination under 1000 lux conditions

Device	V_{oc} (V)	J_{sc} (μAcm^{-2})	FF (%)	η (%)
T	0.50	110	51.10	12.33
T Z10	0.53	114	63.80	16.66
T Z20	0.52	126	62.90	17.85
T Z40	0.50	124	59.20	15.92

3.10 Conclusions

In this section, a strategy to fabricate photoanode layer with improved light scattering is demonstrated by utilising $\sim 5\text{-}16\ \mu\text{m}$ sized ZnO sheet like aggregates and its effect on the performance of the DSSC is demonstrated. Three different wt.% of TiO₂-ZnO pastes were prepared and deposited over single layer TiO₂. The fabricated bilayer photoanodes displayed superior light scattering and dye loading as evidenced by diffuse reflectance and dye loading studies. Owing to these attributes, the DSSCs fabricated showed excellent photovoltaic performances. The device T Z20 fabricated with 20 wt.% ZnO has offered the best performance under one sun and 1000 lux light intensity. The best device offered an improvement of 49.20% in PCE when compared with single layered standard TiO₂ device under one sun illumination and 44.76% under low light conditions.

References

1. C.-Y. Chen, Z.-H. Jian, S.-H. Huang, K.-M. Lee, M.-H. Kao, C.-H. Shen, J.-M. Shieh, C.-L. Wang, C.-W. Chang, B.-Z. Lin, C.-Y. Lin, T.-K. Chang, Y. Chi, C.-Y. Chi, W.-T. Wang, Y. Tai, M.-D. Lu, Y.-L. Tung, P.-T. Chou, W.-T. Wu, T. J. Chow, P. Chen, X.-H. Luo, Y.-L. Lee, C.-C. Wu, C.-M. Chen, C.-Y. Yeh, M.-S. Fan, J.-D. Peng, K.-C. Ho, Y.-N. Liu, H.-Y.

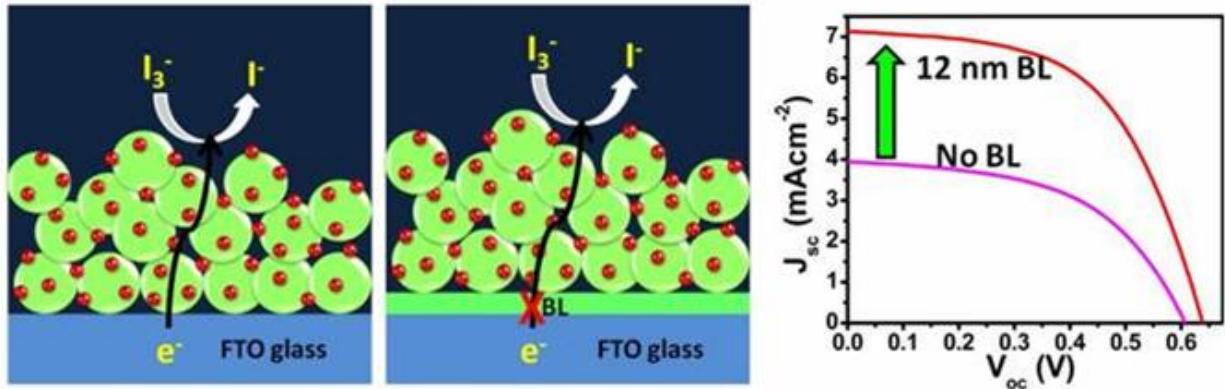
- Lee, C.-Y. Chen, H.-W. Lin, C.-T. Yen, Y.-C. Huang, C.-S. Tsao, Y.-C. Ting, T.-C. Wei and C.-G. Wu, *J. Phys. Chem. Lett.*, 2017, **8**, 1824-1830.
2. M. Freitag, J. Teuscher, Y. Saygili, X. Zhang, F. Giordano, P. Liska, J. Hua, S. M. Zakeeruddin, J.-E. Moser, M. Grätzel and A. Hagfeldt, *Nat. Photonics*, 2017, **11**, 372-378.
 3. D. Yong, Z. Li, M. Li'e, J. Ling, H. Linhua, L. Zhaoqian, C. Shuanghong and D. Songyuan, *Adv. Funct. Mater.*, 2015, **25**, 5946-5953.
 4. B. Liu and E. S. Aydil, *J. Am. Chem. Soc.*, 2009, **131**, 3985-3990.
 5. Q. Zhang, D. Myers, J. Lan, S. A. Jenekhe and G. Cao, *Phys. Chem. Chem. Phys.*, 2012, **14**, 14982-14998.
 6. S. Sasidharan, S. Soman, S. C. Pradhan, K. N. N. Unni, A. A. P. Mohamed, B. N. Nair and H. U. N. Saraswathy, *New J. Chem.*, 2017, **41**, 1007-1016.
 7. K. D. Han, W. Mariah, L. Kyoungmi and P. G. N., *ChemSusChem*, 2013, **6**, 1014-1020.
 8. S.-W. Lee, K.-S. Ahn, K. Zhu, N. R. Neale and A. J. Frank, *J. Phys. Chem. C*, 2012, **116**, 21285-21290.
 9. N. Fuke, R. Katoh, A. Islam, M. Kasuya, A. Furube, A. Fukui, Y. Chiba, R. Komiya, R. Yamanaka, L. Han and H. Harima, *Energy Environ. Sci.*, 2009, **2**, 1205-1209.
 10. T. G. Deepak, G. S. Anjusree, S. Thomas, T. A. Arun, S. V. Nair and A. Sreekumaran Nair, *RSC Adv.*, 2014, **4**, 17615-17638.
 11. D. Guo, S. Xiao, K. Fan and J. Yu, *ACS Sustainable Chem. Eng.*, 2017, **5**, 1315-1321.
 12. S. Hore, C. Vetter, R. Kern, H. Smit and A. Hinsch, *Sol. Energy Mater. Sol. Cell*, 2006, **90**, 1176-1188.
 13. Y. Li, Z. Che, X. Sun, J. Dou and M. Wei, *Chem. Commun.*, 2014, **50**, 9769-9772.
 14. S. Hore, P. Nitz, C. Vetter, C. Prah, M. Niggemann and R. Kern, *Chem. Commun.*, 2005, 2011-2013.
 15. M.-Y. Pu and J. Z. Chen, *Mater. Lett.*, 2012, **66**, 162-164.
 16. G. Yang, J. Zhang, P. Wang, Q. Sun, J. Zheng and Y. Zhu, *Curr. Appl. Phys.*, 2011, **11**, 376-381.
 17. H. Se-Hoon, L. Sangwook, S. Hyunjung and S. J. Hyun, *Adv. Energy Mater.*, 2011, **1**, 546-550.

18. B. Song, Y. Wang, X. Cui, Z. Kou, L. Si, W. Tian, C. Yi, T. Wei and Y. Sun, *Cryst. Growth Des.*, 2016, **16**, 887-894.
19. T. Alhawi, M. Rehan, D. York and X. Lai, *Procedia Eng.*, 2015, **102**, 356-361.
20. C.-Y. Lin, Y.-H. Lai, H.-W. Chen, J.-G. Chen, C.-W. Kung, R. Vittal and K.-C. Ho, *Energy Environ. Sci.*, 2011, **4**, 3448-3455.
21. E. Hosono, S. Fujihara, I. Honma and H. Zhou, *Adv. Mater.*, 2005, **17**, 2091-2094.
22. Y. Zhu, A. Apostoluk, P. Gautier, A. Valette, L. Omar, T. Cornier, J. M. Bluet, K. Masenelli-Varlot, S. Daniele and B. Masenelli, *Sci. Rep.*, 2016, **6**, 23557.
23. M. Kooti and A. Naghdi Sedeh, *Journal of Chemistry*, 2013, **2013**, 4.
24. J. Qiu, F. Zhuge, X. Li, X. Gao, X. Gan, L. Li, B. Weng, Z. Shi and Y.-H. Hwang, *J. Mater. Chem.*, 2012, **22**, 3549-3554.
25. N. Huang, Y. Liu, T. Peng, X. Sun, B. Sebo, Q. Tai, H. Hu, B. Chen, S.-s. Guo and X. Zhao, *J. Power Sources*, 2012, **204**, 257-264.
26. N.-G. Park, *Korean J. Chem. Eng.*, 2010, **27**, 375-384.
27. M.-K. Son, H. Seo, S.-K. Kim, N.-Y. Hong, B.-M. Kim, S. Park, K. Prabakar and H.-J. Kim, *Int. J. photoenergy*, 2012, **2012**.
28. Y. Tachibana, K. Hara, K. Sayama and H. Arakawa, *Chem. Mater.*, 2002, **14**, 2527-2535.
29. A. Mihi, F. J. López-Alcaraz and H. Míguez, *Appl. Phys. Lett.*, 2006, **88**, 193110.
30. X. Chen, Q. Du, W. Yang, W. Liu, Z. Miao and P. Yang, *J. Solid State Chem.*, 2018, **22**, 685-691.
31. S. Ito, S. M. Zakeeruddin, P. Comte, P. Liska, D. Kuang and M. Grätzel, *Nat. Photonics*, 2008, **2**, 693.
32. H. Li, Y. Xiao, G. Han and Y. Zhang, *Organic Electronics*, 2017, **50**, 161-169.
33. J. Van de Lagemaat, N.-G. Park and A. Frank, *J. Phys. Chem. B*, 2000, **104**, 2044-2052.
34. T. Pauporté and C. Magne, *Thin Solid Films*, 2014, **560**, 20-26.

Chapter 4

Fine tuning ZnO blocking layers for enhanced photovoltaic performance in ZnO based dye-sensitised solar cells

Abstract



The electron-hole recombination and back electron flow at the FTO-electrolyte interface in Dye-Sensitised Solar Cells (DSSCs) is generally tackled by the use of pre-blocking layers. In this chapter, the effect of zinc oxide (ZnO) blocking layers (BLs) with varying thickness, on the photovoltaic parameters of ZnO based DSSC are studied in detail. BLs deposited by a low temperature solution process provided uniform surface coverage of nanosized ZnO particles over FTO. Devices with ZnO blocking layer thickness (12 nm) displayed better performance (PCE 2.57%) in comparison to the devices fabricated without blocking layer (1.27%) by reducing the interfacial recombination at the FTO-electrolyte interface and improving life time.

4.1 Introduction

Dye-sensitised solar cells (DSSCs) are accepted as efficient and economic photovoltaic devices since 1991.¹ Much research have been conducted in the area of DSSC for the development of photoelectrodes employing different functional materials.^{2,3} The interface between fluorine doped tin oxide (FTO)/indium doped tin oxide (ITO) conductive glass and the mesoporous active layer plays an essential role in influencing the charge dynamics of DSSCs. Such effects are more significant in low light conditions and hence is a critical characteristic for efficiency improvements.^{4,5} Anatase titanium dioxide (TiO₂) is the most widely used photoanode material in DSSCs, and power conversion efficiencies (PCEs) up to 14% are realised with such devices.⁶ In addition to TiO₂, zinc oxide (ZnO) is employed as a feasible alternative due to its favourable attributes like wide band gap (3.37 eV), high bulk electron mobility (10 times higher than anatase TiO₂), and large exciton binding energy (60 meV).² Additionally, the easiness in synthesising ZnO in diverse morphologies (ie; nanorods,⁷ nanowires,⁸ nanosheets,⁹ nanotubes,¹⁰ nanotetrapods,¹¹ nanotrees,¹² hierarchical aggregates¹³ etc.) compared to TiO₂ encourages the idea of replacement of TiO₂ by ZnO.^{2,14,15}

ZnO is found to be the first semiconductor electrode to perform ideally in combination with a liquid electrolyte interface owing to its low density of defects and potential distribution across the metal oxide/electrolyte interface.^{16,17} However the low injection and electron transfer (ET) rate in ZnO based DSSC stimulates the recombination (backward electron transfer processes), adversely affecting the PCE of devices.¹⁸ Recombination of photoinjected electrons in DSSCs occur majorly in two ways, either through recombination from FTO with the oxidised dye molecules or with the electrolyte at the FTO/electrolyte interface. It can also happen from the bulk semiconductor material to the HOMO of the dye and also to the electrolyte.¹⁹⁻²² This obviously suggests the necessity to investigate the recombination processes occurring in devices comprehensively along with altering the surfaces in a meticulous manner to accomplish higher efficiencies in devices.

DSSCs find potential application in devices that works in ambient light conditions like sensors and decorations. Moreover Internet of Thing (IoT) supported applications are an emerging area for DSSC where it outperforms the counterparts like c-Si and a-Si solar cells.²³⁻²⁶ In DSSCs, since the recombination at FTO/electrolyte interface is more pronounced at the low light conditions as the short circuit current is small, the presence of compact interlayers are important. The change in open circuit voltage with light intensity is also found to be sharp at low light conditions, due to the recombination at FTO/electrolyte interface.²⁷⁻³⁰

The widely pursued strategy to overcome the mentioned problem is to deposit blocking layers (BLs) over FTO/active layer interface. Previous studies revealed that insertion of a blocking or barrier layer between FTO and mesoporous semiconductor nanoparticle film can significantly reduce the back electron transfer thereby enhancing the PCE. The better physical contact of semiconductor nanoparticles on the FTO surface reduce the direct contact of FTO electrode with electrolyte thus preventing the recombination.³¹⁻³³ Enormous methods are reported for the deposition of the BLs, which include spray pyrolysis,^{4,33} spin coating,³⁴ sputtering,^{30,31,35} atomic layer deposition,³⁶ electrochemical deposition,³⁷ thermal oxidation³⁷, sol-gel method^{34,38} etc.

A few reports deal with the study of ZnO blocking layers in ZnO based DSSC. Herná'ndez *et al.* investigated the effect of compact ZnO layer between the FTO and ZnO mesoporous layer. The layer was deposited by rf magnetron sputtering method. The insertion of the layer found to reduce the electron recombination from the FTO substrate and it has increased the overall performance of the device particularly increasing the open-circuit voltage of the device under low light. With 194 nm thick compact ZnO layer a PCE of 2.73% was observed whereas, without the interlayer it was 2.71% under one sun conditions.³⁰ The highest efficiency obtained for nonoptimised device at one sun was 4.0%.³⁰ Gurupreet sikh *et al.* investigated the photovoltaic properties of DSSCs as a function of the thickness of BL in two morphologically different ZnO active layer; hierarchically self-assembled nanoparticles and microcubes. The BLs were generated through spray pyrolysis method. Their studies revealed that regardless of the morphology of the active layer, deposition of the BL leads to drastic increase in the

current density (J_{sc}). They were able to fabricate solar cells with PCE 5.6%, with a BL thickness of 800 nm in ZnO nanoparticle based DSSC. A PCE of 2.6% was found for such devices without BL. In the case of ZnO microcube based DSSC the efficiency was found to be increased from 2.7% to 3.8% with the deposition of BL.³²

Jie *et al* prepared ZnO compact layer by spin coating zinc acetate sol prepared via sol-gel method and studied the effect of compact layer as a function of sol concentration in ZnO based DSSC. The J_{sc} and V_{oc} were significantly improved and the highest efficiency of 3.34% was obtained when 0.1 M zinc acetate solution was used for generating BL. Device with bare FTO delivered an efficiency of 2.76%. However a direct correlation between the compact layer thickness and the performances of solar cell was not discussed in their study.³⁸ Jaing *et al.* reported the influence of ZnO BL on TiO₂ based DSSCs. In the mentioned work, anatase-rutile mixture of titania nanofibers were employed as active layer and ultrathin ZnO was deposited by ALD method as blocking layers. The thickness of BL was varied from 4-20 nm and a 15 nm thick BL offered highest improvements in current density and PCE (8.01%) in the device. However, the use of ALD for large area fabrication is expensive and is therefore not a favourable option for the mass development of solar cells.³⁶ Yeoh *et al.* had studied the influence of ZnO and TiO₂ blocking layers in TiO₂ based DSSCs. ZnO and TiO₂ were synthesised via sol gel method and deposited by spin coating technique over the FTO glass. By the deposition of 120 nm thick ZnO blocking layer, the PCE was found to be improved from 3.86% to 4.34% and this was even enhanced to 4.36% by the replacement with TiO₂ blocking layers.³⁴

This chapter demonstrates the effect of ZnO BLs, on the recombination mechanism of ZnO based dye-sensitised solar cells (**Figure 4.1**). The thicknesses of the BLs deposited by a simple low-temperature solution processing route, were varied by using different concentrations of ZnO dispersions. The objective of the present work is to study the effect of back electron transfer at FTO/electrolyte interface with and without the ZnO blocking layers. Methods like electrochemical impedance spectroscopy (EIS), intensity modulated photovoltage spectroscopy (IMVS) and open circuit voltage decay (OCVD) were employed to evaluate the cell properties. It is already reported by Bisquert *et al.* that lifetime is a kinetic quantity that contains information not only on the rate constants

of charge transfer taking place at the interface but also on the distribution of electronic states and electronic transition that intercede in the operation of DSSC.^{39,40} With the right ZnO blocking layer with optimum thickness (12 nm), we have achieved longer lifetime and improved electron collection efficiency leading to higher J_{sc} and V_{oc} for enhanced power conversion efficiencies.

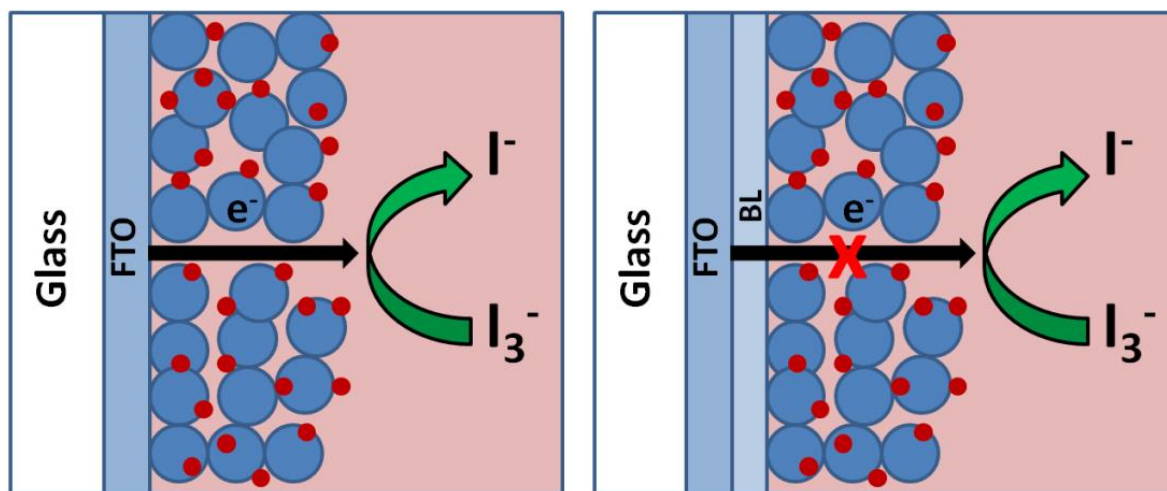


Figure 4.1 Schematic representation of blocking layer effect

4.2 Experimental

4.2.1 Deposition of blocking layer

ZnO nanoparticles were synthesised according to literature procedures.⁴¹⁻⁴³ About 2.95 g zinc acetate dihydrate (Merck) was dissolved in 125 ml methanol under stirring at 65 °C. A solution of 1.48 g of potassium hydroxide (HPLC pvt. Ltd.) in 65 ml of methanol was then introduced drop wise to the above solution at 60-65 °C with continuous stirring. This reaction mixture was then stirred for 2.5 h at the same temperature. The ZnO nanoparticles obtained were then allowed to precipitate for an additional 2 h at room temperature. These ZnO nanoparticles were then collected and rinsed with methanol. A dispersion of ZnO nanoparticles is then made in a solvent mixture containing 70 ml n-butanol, 5ml methanol, and 5ml chloroform to obtain a concentration of about 10 mg/ml. The thickness of the blocking layers was then tuned by further dilution of the stock solution in n-butanol to obtain concentrations of 1, 2, 5 and 10 mg/ml of ZnO content

solutions. These solutions were ultra sonicated and dip coated over cleaned FTO glass (Dyesol) to generate the blocking layers. These films were annealed at 180 °C for 1 h in a laboratory oven prior to the deposition of the ZnO active layer. Blocking layers fabricated from the ZnO contents of 1, 2, 5 and 10 mg/ml are coded as BL1, BL2, BL3 and BL4 respectively.

4.2.2 ZnO paste preparation for porous active layer

About 1.12 g of ZnO nanoparticles synthesised by the previously mentioned method is made into a paste by grinding with 0.23 g of ethylcellulose (TCI) and terpeniol (TCI) in an agate.

4.2.3 ZnO characterisation

The phase purity and crystal structure analysis were done using X-ray diffractometer PANalytical X'Pert PRO, operating with Cu K α radiation (X-ray wavelength $\lambda = 1.5406 \text{ \AA}$). X-ray diffraction patterns (XRD) were collected in the 2θ range of 5 to 80°. Additionally, the size and crystallinity of ZnO nanoparticles were investigated by high resolution transmission electron microscope (HRTEM, FEI Tecnai 30 G2S-TWIN) operated at an accelerating voltage of 300 kV. The morphology of the ZnO films was observed by scanning electron microscope (SEM) JEOL JSM-5600LV. Tapping-mode AFM images were recorded by using Bruker multimode 8 – AFM. The thickness measurements of blocking layers were done in Bruker Dektak XT profilometer. The surface area and pore size distribution of the ZnO particles and film were analysed from the adsorption/desorption isotherms of N₂ at 77 K by BET and BJH method using a Tristar II surface area and porosity analyser (Micromeritics instrument ,USA).

4.3 Fabrication and Characterisation of DSSC

The FTO substrates used for ZnO deposition were systematically cleaned using soap solution, distilled water, acetone and isopropanol. Deposition of blocking layers was done by dip coating technique. These films were annealed at 180 °C for 1 h followed by the deposition of active ZnO layer by doctor-blading. The electrodes were then subjected to programmed heating at 325 °C for 15 min, 375 °C for 15 min, 450 °C for 15 min, and

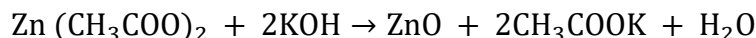
500 °C for 30 min and slowly cooled down to room temperature. Electrodes were then soaked in N719 dye solutions (0.3 mM) with CDCA as co adsorbent (10 mM) and kept at room temperature for 15 h. Counter electrodes were fabricated by coating Pt paste (Dyesol) on FTO plates with pre-drilled holes and annealing at 380 °C for 20 min. The electrodes were then assembled with hot press using 25 µm surlyn spacer. Liquid iodide/triiodide (I^-/I_3^-) electrolyte containing standard compositions of 1-butyl-3-methylimidazolium iodide, lithium iodide, iodine, guanidinium thiocyanate and 4-*tert*-butyl pyridine in acetonitrile was injected into the sandwiched electrodes. The holes over the cells were sealed with microscopic cover slide and surlyn to avoid electrolyte leakage.

The photovoltaic parameters of the fabricated DSSCs was measured using an AM 1.5 solar simulator (Newport Instruments, USA) equipped with a source meter (Keithley 2400) at room temperature. The IPCE measurement of the devices was carried out under DC mode using a 250W xenon lamp coupled with Newport monochromator. The J-V characteristics of the cells were analysed using square shaped mask with an active area of 0.25 cm² (without mask active area is 0.36 cm²). Open circuit voltage decay (OCVD) measurements are done at open circuit. The cell was in the dark at the beginning of the measurement, and then the lights were switched on until the voltage got stabilised, followed by turning the light off and recording the decay of photovoltage. Lifetime data was analysed through previously reported methods.^{44, 45} The electrochemical impedance spectroscopy measurements of the devices were performed using an Autolab PGSTAT302N equipped with FRA (frequency response analyser) mode under forward bias in dark. The measurements were performed in a frequency range from 100 kHz to 0.1 Hz with logarithmically increasing order at an ac amplitude of 10 mV.⁴⁶ Intensity modulated photovoltage spectroscopy (IMVS) measurements were conducted using the same electrochemical workstation (Autolab PGSTAT302N) equipped with FRA and LED driver to drive the red LED (627 nm). Photovoltage response of the cells was measured in the frequency range of 1 Hz to 1 kHz. The amplitude of the sinusoidal modulation for IMVS measurements was 10% of the dc light.

4.4 Results and Discussion

4.4.1 Synthesis and characterisation of ZnO nanoparticles and films

The ZnO nanoparticles for the deposition of both blocking layers and active layer were synthesised from zinc acetate dihydrate and potassium hydroxide in methanol at 60-65 °C by hydrolysis and condensation, according to the following equation.



A stable dispersion of the synthesised nanoparticles were prepared in a mixture of butanol, methanol and chloroform. Thin blocking layers were then uniformly deposited over FTO glass using this stock dispersion. Mesoporous ZnO active layer was fabricated by preparing ZnO nanoparticle paste and coated on BL deposited FTO glass by doctor blading technique. The thickness of the active layer was preserved constant and the effect of back electron transfer at FTO/electrolyte interface was studied using ZnO blocking layers of different thicknesses.

4.4.2 X-ray diffraction analysis

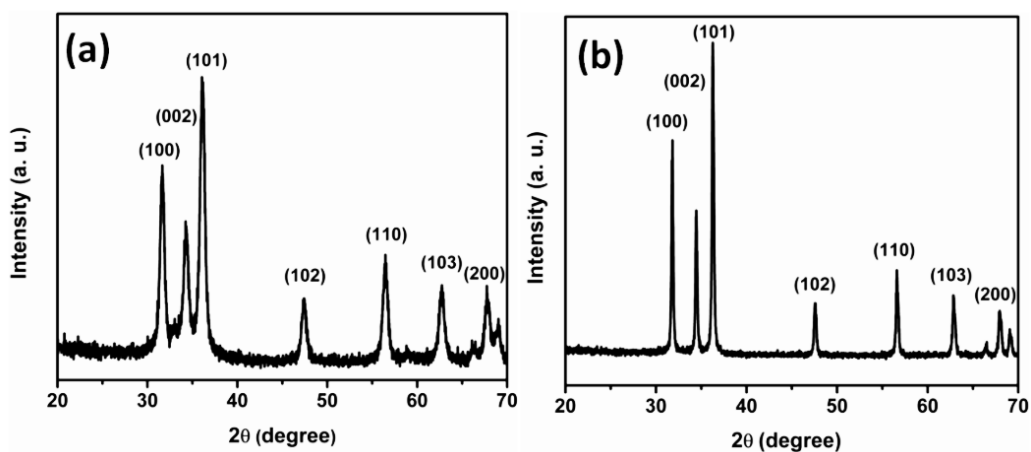


Figure 4.2 (a) XRD pattern of as-synthesised ZnO nanoparticle and (b) XRD of ZnO film annealed at 500°C.

The XRD patterns of the as-synthesised ZnO nanoparticles employed for the fabrication of BL and the ZnO paste annealed at 500°C are presented in **Figure 4.2** (a and b)

respectively. In both cases, diffraction peaks can be ascribed to ZnO of wurtzite structure matching with the Joint committee on powder diffraction standards (JCPDS) file no. 76-0704. The narrowing of the peaks after annealing is due to the increase in particle sizes.

4.4.3 Transmission electron microscopy

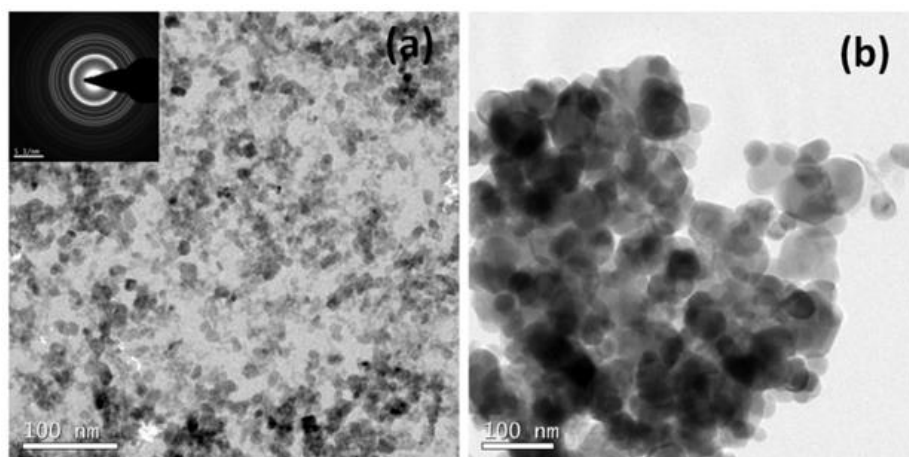


Figure 4.3 TEM images of (a) as-synthesised ZnO nanoparticles and (b) its paste annealed at 500 °C.

Figure 4.3 (a and b) provides the TEM images of the dispersion of ZnO nanoparticle utilised for blocking layer deposition and paste preparation respectively. **Figure 4.3a** suggests that the particles possess an average diameter of 5 nm and SAED given in inset indicates high crystallinity of the ZnO nanoparticles. The average particle size annealed ZnO paste used for active layer preparation was found to be increased to ~ 40 nm (**Figure 4.3b**).

4.4.4 Bandgap analysis

Band gap of the ZnO nanoparticle is calculated by Tauc relation for direct bandgap semiconductor material

$$(\alpha h\nu)^2 = A(h\nu - E_g) \quad (1)$$

Where 'h' is Planck's constant, 'ν' is the frequency of the incident photon, A is the proportionality constant, E_g is the band gap energy of the material. The band gap of ZnO

is obtained by plotting $(\alpha h\nu)^2$ vs $h\nu$ and extrapolating the linear absorption edge of the graph to intersect the energy axis (**Figure 4.4**). The calculated band gap value is 3.22 eV.

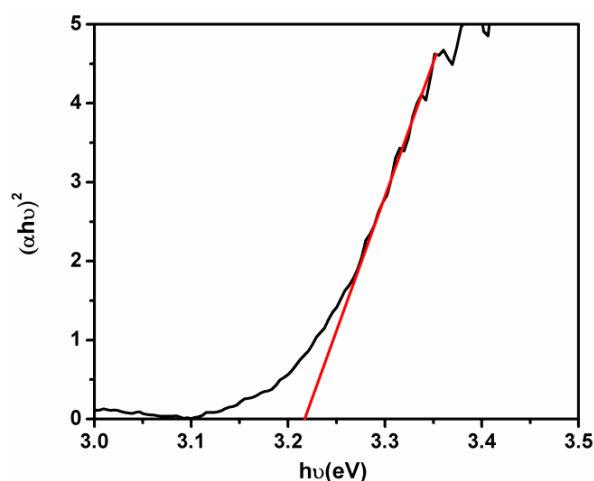


Figure 4.4 Band gap plot of as-synthesised ZnO nanoparticles

4.4.5 Thermogravimetric analysis (TGA)

The thermal decomposition characteristics of the ZnO paste are presented in the TGA data shown in **Figure 4.5**. The data shows a three stage weight loss for the paste with an initial weight loss of terpeneol solvent in the temperature range 95-240 °C. The second weight loss (24%) at 240-350 °C is due to the combustion of ethyl cellulose to CO₂ (g) and H₂O (g). The smallest and the final weight loss around 2% at 350-400 °C is attributed to the combustion of residual carbonaceous material from ethyl cellulose.

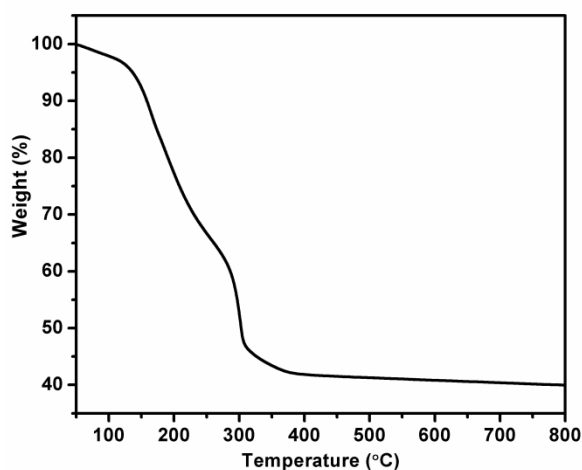


Figure 4.5 TGA curve of ZnO paste used for active layer

4.4.6 Scanning electron microscopy

The morphology of the ZnO active layer deposited over FTO glass is shown in **Figure 4.6**. The mesoporous nature of the film is clearly visible from the SEM image and such films with high meso porosity are desirable for the adsorption of dye molecules.

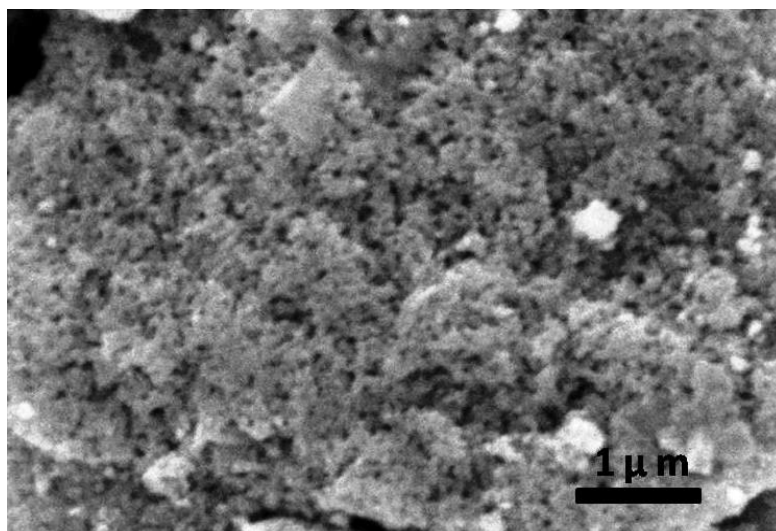


Figure 4.6 SEM image of ZnO active layer

4.4.7 BET surface area analysis

Surface area and pore size distribution of the as synthesised ZnO nanoparticle and film was measured using N_2 adsorption/desorption analysis at liquid N_2 temperature. ZnO nanoparticles showed Type II b isotherm with H3 hysteresis loop (**Figure 4.6a**), which conveys that the particles form aggregates having non rigid slit shaped pores. The surface area was measured to be $37 \text{ m}^2/\text{g}$ and its nitrogen adsorption-desorption isotherm is shown in **Figure 4.7a**. BJH (Barrett–Joyner–Halenda) pore size analysis of the sample provided in **Figure 4.7b** revealed an average size of $\sim 8 \text{ nm}$. We have also analysed the surface area and pore size distribution of the annealed films using the same technique. ZnO film displayed type II b isotherm with H3 hysteresis loop with a surface area of $6 \text{ m}^2/\text{g}$. The reduction in surface area is due to the increase in the particle size after annealing (**Figure 4.7c**). The BJH pore size distribution of the ZnO active layer (**Figure 4.7d**) showed an average pore size of 53 nm .

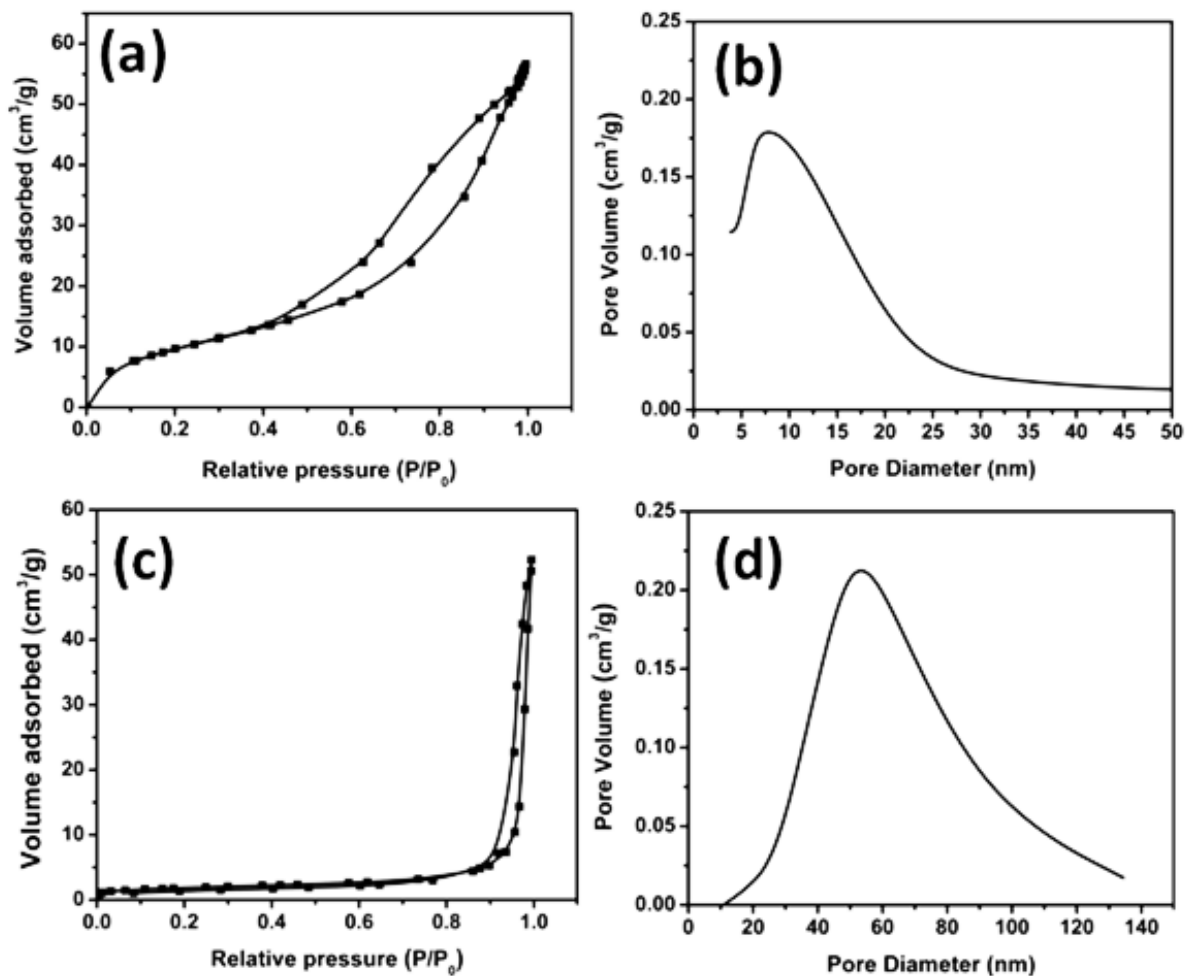


Figure 4.7 N₂ adsorption/desorption isotherms (a and c) and BJH pore size distribution curve (b and d) for as-synthesised ZnO nanoparticles and ZnO nanoparticles scraped from the annealed active layer.

4.4.8 Atomic force microscopy

Surface topography of blocking layers is evaluated through AFM analysis. AFM images presented in **Figure 4.8 (a-d)** provide the surface morphology of the BLs. The images suggest that the deposited ZnO layer offers much smoother surfaces as the ZnO concentration is increased. AFM image of the bare FTO substrate is shown in **Figure 4.8e**. The average thickness of the BLs were measured using profilometer and it was obtained to be 5 ± 1 nm, 7 ± 1 nm, 12 ± 2 nm and 15 ± 2 nm for BL1, BL2, BL3 and BL4 respectively (**Table 4.1**).

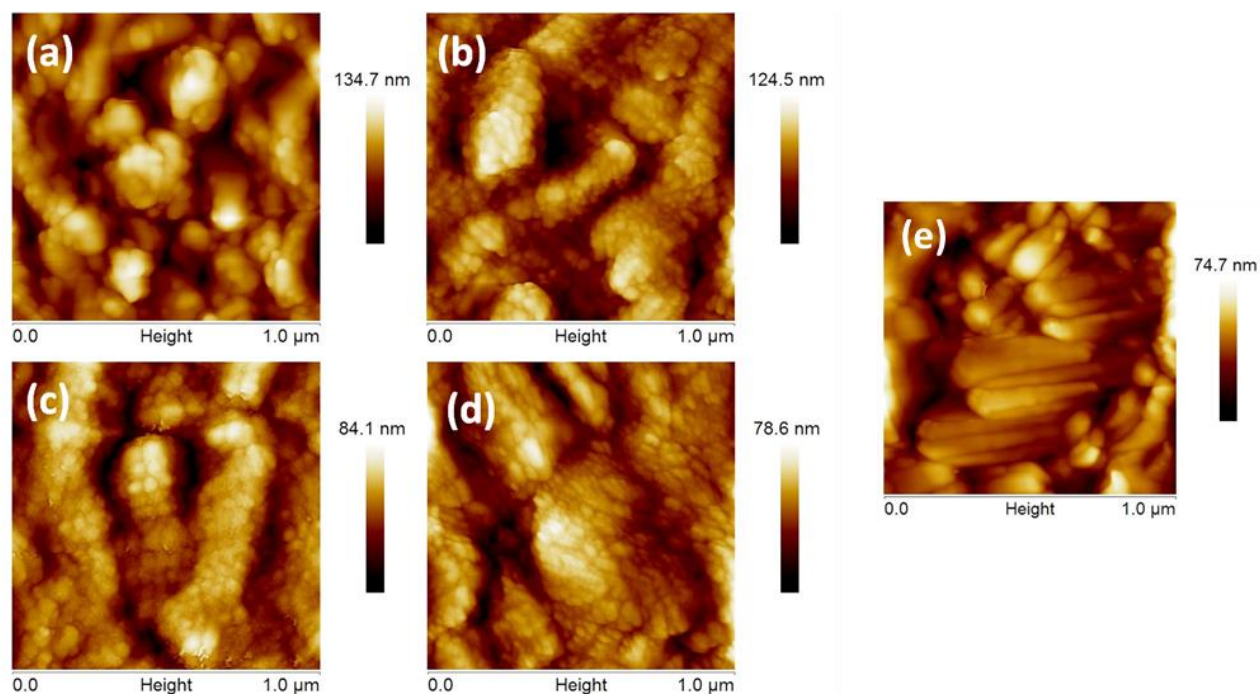


Figure 4.8 AFM images (a) BL1, (b) BL2, (c) BL3 (d) BL4 and (e) bare FTO coated glass.

Table 4.1 Concentration of ZnO solution and thickness of the blocking layers deposited.

Sample code	ZnO Concentration (mg/ml)	Thickness approx. (nm)
BL1	1	5 \pm 1
BL2	2	7 \pm 1
BL3	5	12 \pm 2
BL4	10	15 \pm 2

4.4.9 Photovoltaic characterisation of dye-sensitised solar cells

4.4.9.1 Current-voltage characteristics

The performance of all devices fabricated on bare FTO and FTO with ZnO pre-blocking layers of varying thickness is analysed under AM 1.5G irradiation (100 mW/cm^2). **Figure 4.9a** presents the photocurrent density-voltage characterisation curves (J - V) for all the devices. Detailed photovoltaic parameters are listed in **Table 4.2**. The thickness of active ZnO layer was retained as $\sim 20 \text{ }\mu\text{m}$ in all cases in order to ensure the proper comparison of effect of blocking layers in all the devices. Devices fabricated on bare FTO showed short-circuit current density of (J_{sc}) of 3.95 mAcm^{-2} , open-circuit voltage (V_{oc}) of 0.61 V and fill factor (FF) of 0.53 leading to a PCE of 1.27% . Further attempts were not made to achieve higher efficiencies as the prime objective of the work was to reveal the effects of ZnO blocking layers on the interfacial charge transfer properties.

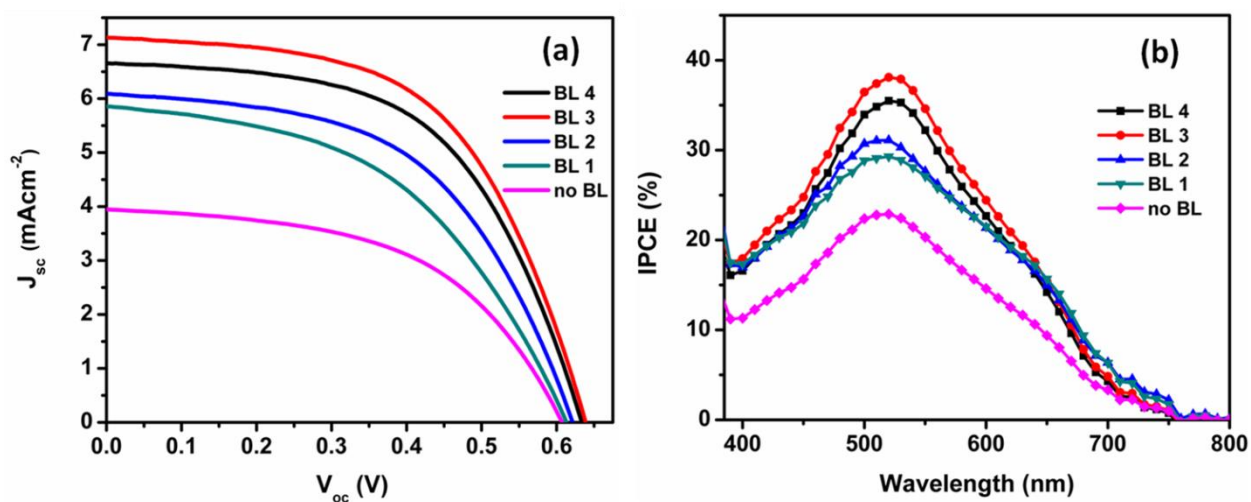


Figure 4.9 (a) J - V and (b) IPCE characteristics without ZnO blocking layers and with blocking layers.

There is a systematic improvement in performance of DSSC devices by the application of ZnO blocking layers deposited on FTO. DSSC devices with a 12 nm thick ZnO layer delivered the best performance, with a short-circuit current density (J_{sc}) of 7.13 mA/cm^2 , an open-circuit voltage (V_{oc}) of 0.64 V , fill factor (FF) of 0.56 and a resultant efficiency of 2.57% which is more than double the performance of devices without blocking layers.

With a further increase in the ZnO BL thickness to 15 nm, the efficiency decreased to 2.37% which is mainly due to the decrease in current density and voltage. The enhanced performance with the application of blocking layers is mainly credited to the increase in current density. With the increase of thickness from 0 nm to 12 nm the photocurrent density improved from 3.95 mAcm⁻² to 7.13 mAcm⁻². It is to be noted that the improvement in current compared to the increment in voltage and fill factor is negligible. Hamann *et al.* reported that for DSSCs the current density (J_{sc}) is determined by light harvesting efficiency (LHE), charge injection efficiency (η_{inj}), dye regeneration efficiency (η_{reg}) and charge collection efficiency (η_{cc}).^{47,48} In the present work, we used the same dye (N719), electrolyte (I⁻/I₃⁻) and semiconductor active layer (ZnO) with similar thickness for the fabrication of all devices.

Table 4.2 Characteristic photovoltaic parameters obtained from DSSCs prepared with different ZnO compact blocking layers.

Sample Code	J_{sc} (mAcm ⁻²)	V_{oc} (V)	FF	η (%)	R_s
no BL	3.95	0.61	0.53	1.27	52
BL 1	5.86	0.61	0.49	1.75	41
BL 2	6.09	0.62	0.53	2.02	34
BL 3	7.13	0.64	0.56	2.57	30
BL 4	6.66	0.63	0.56	2.37	28

It is rational to assume that all the devices possessed similar LHE , η_{inj} and η_{reg} . This clearly indicates that the enhancement in current density is majorly due to the improvement in charge collection efficiency which is directly influenced by the interfacial recombinations at FTO/electrolyte and ZnO/electrolyte interfaces. By employing blocking layers of ZnO on FTO, we were able to reduce the recombination taking place at the FTO/electrolyte interface. This results in more population of electrons in the conduction band of ZnO leading to a negative shift in quasi-Fermi level which impedes recombination enhancing current and voltage. Since both the blocking and

active layers are composed of ZnO nanoparticle, the charge created at the conduction band is collected efficiently leading to an increased photocurrent density.

4.4.9.2 IPCE measurements

Figure 4.9b demonstrates the monochromatic incident photon-to-current conversion efficiency (IPCE) spectra of the fabricated DSSCs. The difference in short-circuit current density is entirely consistent with the trend obtained in IPCE measurements concerning equation 2 where 'e' is the elementary charge, and $I_0(\lambda)$ is the solar irradiance spectra under AM1.5G condition.

$$J_{sc} = e \int I_0(\lambda) \times IPCE(\lambda) d\lambda \quad (2)$$

Device fabricated on bare FTO gave an IPCE maximum of 22% while with the application of blocking layers with increased thickness the IPCE values increased in the order of BL3 > BL4 > BL2 > BL1 > no BL. The peak IPCE peak value of 38% was obtained for device with ZnO BL thickness of 12 nm (**Figure 4.9b**). With further increase in thickness, the maximum value got decreased to 36%. The IPCE results are in good agreement with that of the J-V characteristics. Like current density, IPCE is also related to light harvesting efficiency, injection efficiency, regeneration efficiency and charge collection efficiency by the equation given below,

$$IPCE(\lambda) = LHE \times \eta_{inj} \times \eta_{reg} \times \eta_{cc} \quad (3)$$

Considering the use of same dye, electrolyte and ZnO paste with same active layer thickness, the net increase in the IPCE characteristic in the visible region can be ascribed to better charge collection efficiency which was tuned in a meticulous way by the application of ZnO blocking layers. In the case of TiO₂ based DSSCs the deposition of blocking layers leads to high series resistance in the cell. Thus TiO₂ BLs will reduce the back electron transfer from FTO to tri-iodide ions in the electrolyte under short circuit conditions but in open circuit conditions electrons get accumulate at the surface of BLs resulting in high sheet resistance.^{4,5,19} The effect of BLs in ZnO-based DSSC are completely different where the presence of BLs results in lowering of series resistance.

4.4.9.3 EIS measurements

Electrochemical impedance spectroscopy (EIS) was done under different bias conditions in dark to study the internal charge dynamics involving transfer and transport of electrons in the fabricated cells. The impedance spectra were recorded at direct applied potentials from 0.3 V to -0.8 V, stepped in 0.1 V increments, with a 10 mV alternating potential superimposed on the direct bias. The ac modulation frequency was from 100 MHz to 100 kHz in logarithmically increasing order. Detailed fitting and interpretation of the acquired data was carried out based on the reported literature available in this area.^{51,49}

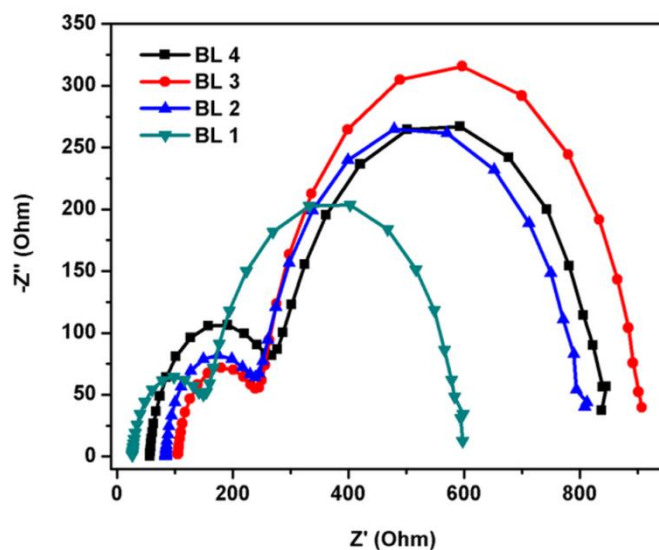


Figure 4.10 Nyquist plots of ZnO DSSCs with various blocking layer thickness.

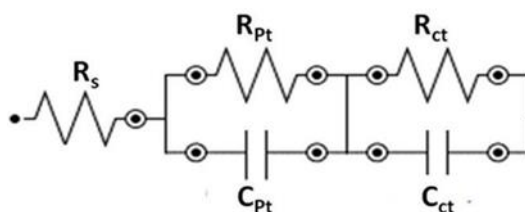


Figure 4.11 Randles circuit used for fitting the impedance data.

It is important to note that the transmission-line features commonly seen due to the electron transport in TiO_2 semiconductor oxides were not observed in the Nyquist plots

of the ZnO devices (**Figure 4.10**) as recognised previously by L. M. Peter *et al.*⁵⁰ The transport part was not seen in any of the Nyquist plots (**Figure 4.10**) which is a characteristic feature of ZnO based DSSC. Higher charge transfer and transport leading to improved charge collection efficiencies in comparison to TiO₂. Fitting of the data with transmission line model proposed by Bisquert *et al.*,⁵¹ is therefore difficult to be applied here and the Nyquist plots were fitted with R-RC-RC circuit (Randle's circuit, **Figure 4.11**) in the present case. The absence of transport feature accounts the higher mobility of electrons in ZnO compared to TiO₂. The interfacial charge recombination resistance (R_{ct}) and recombination lifetimes (τ_n) were obtained by fitting the experimental data and were plotted as a logarithmic function of the applied bias as represented in **Figure 4.12a** and **4.12b**. Both R_{ct} and τ_n are important factors that provide better insight into the recombination pathways happening at the FTO/electrolyte interface at short circuit conditions in DSSC.⁵²

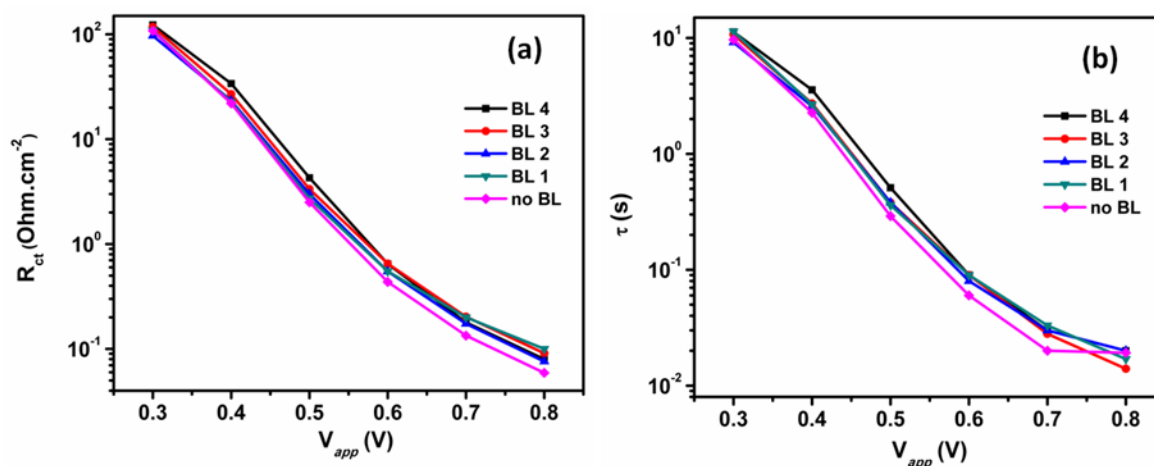


Figure 4.12 (a) The variation of recombination resistance as a function of applied potential and (b) variation of lifetime as a function of applied potential.

Figure 4.12a shows the variation of recombination resistance as a function of applied potential. It is quite clear from the graph that insertion of blocking layers resulted in improving the charge transfer resistance values compared to the bare FTO which forbids the back electron transfer leading to better lifetime for the devices employing blocking layers as given in **Figure 4.12b**. The electron lifetime (τ_n) was calculated based on the equation 4.⁵⁰

$$\tau_n = R_{ct} \times C_{\mu} \quad (4)$$

Vomiero *et al.* reported that the variation of the trend in between the compact blocking layers on R_{ct} and τ_n are less prominent for the data obtained from EIS measurements at short circuit conditions.³² To achieve a deeper understanding of the dynamics of electron transport at the FTO/electrolyte interface we did detailed open circuit voltage decay measurements (OCVD) and intensity modulated photovoltage spectroscopic measurements (IMVS).

4.4.9.4 OCVD measurements

Open-circuit voltage decay (OCVD) is an excellent tool to study the recombination kinetics of photogenerated electrons with oxidised species in the electrolyte that provide information on the origin of decrease in electron lifetimes.^{40,45} OCVD technique involves switching off the illumination in a steady state condition and then monitoring the subsequent decay of photovoltage (V_{oc}). The lifetime/response time of the electron accumulated in conduction band and sub-band gap trap states are obtained by taking the reciprocal of the derivative of decay curve normalised by the thermal voltage as given by equation 5.

$$\tau_n = -\frac{k_B T}{e} \left(\frac{dV_{oc}}{dt} \right)^{-1} \quad (5)$$

This method has an advantage over the small perturbation techniques in both frequency and time domain (EIS, IMPS and IMVS) as OCVD gives a far better resolution along the Fermi level in one single and fast measurement. The trend in lifetime decay plots obtained by OCVD presented in **Figure 4.13a** gives direct insight into the recombination taking place at the FTO/electrolyte interface. It is evident from the lifetime plot that with the application of ZnO BLs, lifetime is improved and the maximum life time is obtained for the device with a BL thickness of 12 nm (BL3). When the thickness is further increased the lifetime is found to be decreased which could be due to the fact that with higher thickness the injection of electrons is blocked resulting in more recombination and reduction in lifetime. The lifetime was observed to decrease in the order of BL3 > BL4 > BL2 > BL1 > no BL. The results convey the significance of studying recombination

at the FTO/electrolyte interface which plays a substantial role in determining the performance of the devices. The effect of BLs on solar cell performances is more prominent at low light conditions. It is reported that at lower intensities devices employing BLs give an improved open circuit voltage than that of the devices on bare FTO which is finally converted to higher efficiencies.³⁰

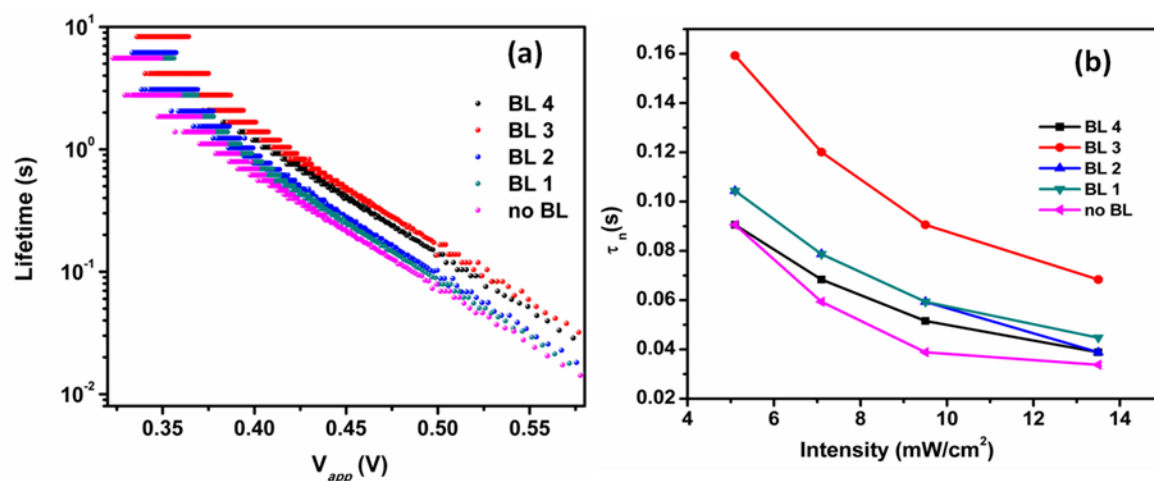


Figure 4.13 (a) The variation of lifetime as a function of applied potential obtained from OCVD measurements and (b) variation of lifetime as a function of light intensity obtained from IMVS measurement.

4. 4.9.5 IMVS measurements

Charge transfer characteristics of DSSCs were analysed using intensity-modulated photovoltage spectroscopy (IMVS) at various illumination intensities. A monochromatic red colour LED having a wavelength of 627 nm was used as the light source for illumination. The amplitude of the sinusoidal modulation for IMVS measurements was 10% of the dc light at a frequency range of 1 Hz to 1 kHz. The applied frequency was in logarithmically increasing order. In DSSC the recombination can happen not only from the conduction band of ZnO but also from the sub-band gap trap states of both active layers and blocking layers.⁵³ The lifetime of electrons at different steady state can be calculated more accurately by intensity modulated photovoltage spectroscopy (IMVS).^{54,55} IMVS measurements at open circuit were carried out at a given steady state in a way to examine the recombination taking place from the conduction band. Since the

switching frequency of the LED light (627 nm) is high the lifetime response involves both recombination to the electrolyte as well as to the dye ground state from ZnO conduction band. The electron lifetime (τ_n) is determined from the IMVS measurement using equation 6,

$$\tau_n = \frac{1}{2\pi f_{IMVS}} \quad (6)$$

where f_{IMVS} is the frequency at the top of the semicircle in the Nyquist plots. **Figure 4.13b** shows the variation in lifetime as a function of LED light intensity measured using IMVS technique. It is quite evident from the graph that application of ZnO BLs resulted in enhancing the lifetime to a greater extent following the trend $\tau_{no\ BL} < \tau_{BL1} < \tau_{BL2} < \tau_{BL4} < \tau_{BL3}$ clearly this indicated that the improvement in electron lifetime by the application of BLs resulting from a reduction in charge recombination. However, it is to be noticed that when the thickness increases above 12 nm, there is a decrease in lifetime due to more recombination, as a result of limited injection by the formation of a potential barrier blocking effect.

In this chapter, by employing ZnO BLs, due to the inherent properties of better charge collection and transport of ZnO nanoparticle reduces the accumulation of charges in the ZnO BLs were reduced which helped in successfully reducing the recombination resulting in improved lifetime and enhanced charge collection efficiency. This further leads to lower series resistance and better PCE.

4.5 Conclusions

The present chapter demonstrated that ultrathin ZnO blocking layers (BLs) can successfully reduce the back electron transfer from FTO to the electrolyte in ZnO based DSSC. The blocking layers offer efficient collection of photoinjected electrons and improved life time resulting in better device performance. A 12 nm thick ZnO layer deposited by a simple solution based deposition technique is proved to have the highest lifetime by successfully reducing the recombination as evident from EIS, OCVD and IMVS measurements. This effect is found to be more pronounced in low light conditions. Device without BL delivered a PCE of 1.27% which is enhanced up to 2.57% with the

presence of 12 nm BL. It is therefore very important to choose the right thickness of BLs, as increased thickness can impede electron injection leading to reduced performance.

References

1. B. O'Regan and M. Gratzel, *Nature*, 1991, **353**, 737-740.
2. J. A. Anta, E. Guillén and R. Tena-Zaera, *J. Phys. Chem. C*, 2012, **116**, 11413-11425.
3. L. Peter, *Acc. Chem. Res.*, 2009, **42**, 1839-1847.
4. P. J. Cameron and L. M. Peter, *J. Phys. Chem. B*, 2003, **107**, 14394-14400.
5. P. J. Cameron and L. M. Peter, *J. Phys. Chem. B*, 2005, **109**, 7392-7398.
6. K. Kakiage, Y. Aoyama, T. Yano, K. Oya, J.-i. Fujisawa and M. Hanaya, *Chem Comm*, 2015, **51**, 15894-15897.
7. R. Gao, Z. Liang, J. Tian, Q. Zhang, L. Wang and G. Cao, *RSC Adv.*, 2013, **3**, 18537-18543.
8. M. Law, L. E. Greene, J. C. Johnson, R. Saykally and P. Yang, *Nat. Mater.*, 2005, **4**, 455-459.
9. C.Y. Lin, Y.H. Lai, H.W. Chen, J. G. Chen, C.W. Kung, R. Vittal and K.-C. Ho, *Energy Environ. Sci*, 2011, **4**, 3448-3455.
10. A. B. F. Martinson, J. W. Elam, J. T. Hupp and M. J. Pellin, *Nano Lett.*, 2007, **7**, 2183-2187.
11. W. Chen, H. Zhang, I. M. Hsing and S. Yang, *Electrochem. commun.*, 2009, **11**, 1057-1060.
12. S. H. Ko, D. Lee, H. W. Kang, K. H. Nam, J. Y. Yeo, S. J. Hong, C. P. Grigoropoulos and H. J. Sung, *Nano Lett.*, 2011, **11**, 666-671.
13. N. Memarian, I. Concina, A. Braga, S. M. Rozati, A. Vomiero and G. Sberveglieri, *Angew. Chem., Int. Ed.*, 2011, **50**, 12321-12325.
14. W. Chen, Y. Qiu and S. Yang, *Phys Chem Chem Phys*, 2012, **14**, 10872-10881.
15. Y. He, J. Hu and Y. Xie, *Chem. Commun.*, 2015, **51**, 16229-16232.
16. A. Walker, H. J. Snaith, F. D. Angelis, E. D. Como, *Unconventional Thin Film Photovoltaics*, Royal Society of Chemistry, Cambridge, 2016.
17. J. F. Dewald, *J. Phys. Chem. Solids*, 1960, **14**, 155-161.
18. H. Wei, J.-W. Luo, S.-S. Li and L.-W. Wang, *J. Am. Chem. Soc.*, 2016, **138**, 8165-8174.

19. T. Oekermann, T. Yoshida, H. Minoura, K. G. U. Wijayantha and L. M. Peter, *J. Phys. Chem. B*, 2004, **108**, 8364-8370.
20. T. Oekermann, T. Yoshida, C. Boeckler, J. Caro and H. Minoura, *J. Phys. Chem. B*, 2005, **109**, 12560-12566.
21. E. Galoppini, J. Rochford, H. Chen, G. Saraf, Y. Lu, A. Hagfeldt and G. Boschloo, *J. Phys. Chem. B*, 2006, **110**, 16159-16161.
22. M. V. Vinayak, T. M. Lakshmykanth, M. Yoosuf, S. Soman and K. R. Gopidas, *Solar Energy*, 2016, **124**, 227-241.
23. T. Toyoda, T. Sano, J. Nakajima, S. Doi, S. Fukumoto, A. Ito, T. Tohyama, M. Yoshida, T. Kanagawa, T. Motohiro, T. Shiga, K. Higuchi, H. Tanaka, Y. Takeda, T. Fukano, N. Katoh, A. Takeichi, K. Takechi and M. Shiozawa, *J. Photochem. Photobiol. A*, 2004, **164**, 203-207.
24. C. L. Wang, P. T. Lin, Y. F. Wang, C. W. Chang, B.-Z. Lin, H. H. Kuo, C. W. Hsu, S.-H. Tu and C.-Y. Lin, *J. Phys. Chem. C*, 2015, **119**, 24282-24289.
25. Renewable energy focus.com, <http://www.Renewableenergyfocus.com/view/3304/can-dye-sensitised-solar-cells-deliver-low-cost-pv/>, October 2008.
26. J. Eliasson , J. Delsing , S. J. Thompson , Y. -B. Cheng , and P. Chen, *Int. J. Ad. Syst. Meas.*, 2012, **5**(1&2), 45-54.
27. P. J. Cameron, L. M. Peter and S. Hore, *J. Phys. Chem. B*, 2005, **109**, 930-936.
28. S. Hore and R. Kern, *Appl. Phys. Lett.*, 2005, **87**, 263504.
29. A. Ofir, L. Grinis and A. Zaban, *J. Phys. Chem. C*, 2008, **112**, 2779-2783.
30. G. Pérez-Hernández, A. Vega-Poot, I. Pérez-Juárez, J. M. Camacho, O. Arés, V. Rejón, J. L. Peña and G. Oskam, *Sol. Energ. Mat. Sol. Cells*, 2012, **100**, 21-26.
31. M. S. Góes, E. Joanni, E. C. Muniz, R. Savu, T. R. Habeck, P. R. Bueno and F. Fabregat-Santiago, *J. Phys. Chem. C*, 2012, **116**, 12415-12421.
32. G. S. Selopal, N. Memarian, R. Milan, I. Concina, G. Sberveglieri and A. Vomiero, *ACS Appl. Mater. Interfaces*, 2014, **6**, 11236-11244.
33. L. Kavan and M. Grätzel, *Electrochim. Acta*, 1995, **40**, 643-652.
34. M.-E. Yeoh and K.-Y. Chan, *J. Electron. Mater.*, 2019, **48**, 4342-4350.

35. A. Alberti, G. Pellegrino, G. G. Condorelli, C. Bongiorno, S. Morita, A. La Magna and T. Miyasaka, *J. Phys. Chem. C*, 2014, **118**, 6576-6585.
36. Ding, Y. Li, H. Hu, L. Bai, S. Zhang and N. Yuan, *Nanoscale Res. Lett.*, 2013, **8**, 1-9.
37. L. Kavan, N. Tétreault, T. Moehl and M. Grätzel, *J. Phys. Chem. C*, 2014, **118**, 16408-16418.
38. J. Guan, J. Zhang, T. Yu, G. Xue, X. Yu, Z. Tang, Y. Wei, J. Yang, Z. Li and Z. Zou, *RSC Adv.*, 2012, **2**, 7708-7713.
39. J. Bisquert and V. S. Vikhrenko, *J. Phys. Chem. B*, 2004, **108**, 2313-2322.
40. J. Bisquert, A. Zaban, M. Greenshtein and I. Mora-Seró, *J. Am. Chem. Soc.*, 2004, **126**, 13550-13559.
41. C. Pacholski, A. Kornowski and H. Weller, *Angew. Chem. Int. Ed.*, 2002, **41**, 1188-1191.
42. W. J. E. Beek, M. M. Wienk, M. Kemerink, X. Yang and R. A. J. Janssen, *The J. Phys. Chem. B*, 2005, **109**, 9505-9516.
43. D. Liu and T. L. Kelly, *Nat. Photon.*, 2014, **8**, 133-138.
44. S. Soman, Y. Xie and T. W. Hamann, *Polyhedron*, 2014, **82**, 139-147.
45. A. Zaban, M. Greenshtein and J. Bisquert, *ChemPhysChem*, 2003, **4**, 859-864.
46. S. Soman, M. A. Rahim, S. Lingamoorthy, C. H. Suresh and S. Das, *Phys Chem Chem Phys*, 2015, **17**, 23095-23103.
47. T. W. Hamann, R. A. Jensen, A. B. F. Martinson, H. Van Ryswyk and J. T. Hupp, *Energy Environ. Sci.*, 2008, **1**, 66-78.
48. J. W. Ondersma and T. W. Hamann, *Coord. Chem. Rev.*, 2013, **257**, 1533-1543.
49. J. Bisquert, D. Cahen, G. Hodes, S. Rühle and A. Zaban, *J. Phys. Chem. B*, 2004, **108**, 8106-8118.
50. E. Guillén, L. M. Peter and J. A. Anta, *J. Phys. Chem. C*, 2011, **115**, 22622-22632.
51. J. Bisquert, I. Mora-Sero and F. Fabregat-Santiago, *ChemElectroChem*, 2014, **1**, 289-296.
52. J. P. Gonzalez-Vazquez, G. Oskam and J. A. Anta, *J. Phys. Chem. C*, 2012, **116**, 22687-22697.
53. J. Bisquert, A. Zaban and P. Salvador, *J. Phys. Chem. B*, 2002, **106**, 8774-8782.

54. G. Schlichthörl, S. Y. Huang, J. Sprague and A. J. Frank, *J. Phys. Chem. B*, 1997, **101**, 8141-8155.
55. A. C. Fisher, L. M. Peter, E. A. Ponomarev, A. B. Walker and K. G. U. Wijayantha, *J. Phys. Chem. B*, 2000, **104**, 949-958.
56. B. E. Hardin, H. J. Snaith and M. D. McGehee, *Nat Photon*, 2012, **6**, 162-169.
57. I. S. Kim, R. T. Haasch, D. H. Cao, O. K. Farha, J. T. Hupp, M. G. Kanatzidis and A. B. F. Martinson, *ACS Appl. Mater. Interfaces*, 2016, **8**, 24310-24314.

Chapter 5

Summary and future scope of the work

Dye-sensitised solar cells (DSSCs) have been vigorously pursued for the last two decades as promising alternatives to conventional silicon and thin film technologies owing to its low production cost, ease of fabrication and relatively high power conversion efficiency (PCE). Recent reports testify the incredible performance of DSSC under indoor lighting sources such as fluorescent lamps and light-emitting diodes (LEDs). This has opened up the possibility of employing dye-sensitised cells (DSCs) for powering wireless sensors and consumer electronics. However, the efficiency of DSSC/DSC is still lagging behind the conventional photovoltaic technologies and concerted efforts are made to tune the functional layers of DSSC/DSC to improve the performances. The thesis is thus focused on the modification of the semiconductor photoanode layer to improve the device performance. The photoanode of DSSC/DSC comprising of an active layer, blocking layer and scattering layer is tuned to enhance the PCE. Insertion of scattering layers and blocking layer in the photoanode architecture increases the light harvesting characteristics and reduces electron–hole recombination thereby improving efficiency of DSSC/DSCs.

DSSC/DSCs generally utilise submicron sized particles to fabricate scattering layers and the photoanodes thus obtained are found to be opaque. Such cells are therefore unsuitable for building integrated photovoltaic applications (BIPV). In the present work, ZnO microstructures are employed as a sacrificial layer over TiO₂ photoanode and surface roughness/voids are created by the selective etching of it through TiCl₄ treatment. TiCl₄ treatment is an inevitable step to deposit tiny TiO₂ particles as a blocking layer over TiO₂ in the fabrication of DSSC/DSC. The advantage of the proposed work is that without losing the transparency and without any secondary treatments, it was possible to create light scattering effects inside the photoanode.

The first chapter depicts the effect of creating surface roughness/voids on the light scattering characteristics of a DSSC. Micron sized (2-4 μm) ZnO flowers synthesised via

wet chemical route is employed as a sacrificial template to impart surface roughness/voids in TiO₂ active layer. ZnO flowers are coated over TiO₂ layer by doctor blade method and selectively etched by TiCl₄ treatment. After TiCl₄ treatment, the roughness of ZnO modified TiO₂ film increased 10 times that of bare TiO₂. The TiCl₄ treatment serves the dual purpose of blocking layer deposition as well as etching of ZnO particles to induce surface roughness/voids on TiO₂ nanocrystalline film. Current density of the device is improved owing to the improved light scattering effects. Under one sun conditions, an improvement in power conversion efficiency of 12.9% with front illumination and 17.5% from back illumination is obtained. The interfacial charge transfer analysis of the DSSCs were done using EIS, light perturbation techniques such as IMVS, IMPS and OCVD. With the surface engineered DSC an enhancement in PCE up to 84.7% was achieved in ambient light (1000 lux, CFL) conditions. It is demonstrated that the photoanode modifications, using ZnO hierarchical structures as sacrificial inclusions, is an effective approach to improve the performance of DSSCs under one sun and ambient light conditions for bifacial building integrated photovoltaic (BIPV) applications.

In the third chapter, diverse morphologies of ZnO structures namely ZnO fibrils (~10 μm size) and sheet like aggregates (5-16 μm size) were utilised to create voids in functional layer. These structures were synthesised from zinc nitrate hexahydrate and urea by changing the urea loading through precipitation. The as-synthesised products were layered hydroxide zinc carbonate which upon annealing at 300 °C resulted in pure ZnO. Surface roughness was created by depositing a layer of ZnO over TiO₂ layer, followed by TiCl₄ treatment. The transparent and porous photoanodes thus obtained, displayed enhanced current density at one sun and indoor light conditions. As the dye loading is found to be almost same for all devices, it can be concluded that the increase in current density, is due to enhanced light scattering effects. An enhancement of 15.56% and 18.64% in PCE was obtained for TiO₂-Zfb and TiO₂-Zsh devices respectively, relative to the standard TiO₂ device in one sun conditions. The interfacial charge transfer analysis of the DSSCs were done using EIS, light perturbation techniques such as IMVS and IMPS. Under low light conditions, improvement of 39.63% and 6.30% are observed for the same devices.

The chapter also presents the fabrication of a bilayer photoanode comprising of a TiO₂ bottom layer and a macroporous TiO₂ top layer. Three different weight percentages of TiO₂-ZnO sheet aggregates (10, 20, 40 wt.%) were utilised to create layers with different porosity. It was observed that the top porous layer imparted strong light scattering which was confirmed by DRS spectra. Owing to these porous features introduced, the DSSC/DSCs fabricated showed excellent photovoltaic performances. The device T Z20 fabricated with 20 wt.% ZnO has offered the best performance under one sun and 1000 lux light intensity. The best device offered an improvement of 49.20% in PCE when compared with single layered standard TiO₂ device under one sun illumination and 44.76% under low light conditions.

The electron-hole recombination and back electron transfer at the FTO-electrolyte interface in DSSC is generally addressed by the use of pre-blocking layers. The effect of ZnO blocking layers (BLs) with varying thickness, on the photovoltaic parameters of ZnO based DSSC are studied in detail in the final chapter. BLs deposited by a low temperature solution process provided uniform surface coverage of nanosized ZnO particles over FTO. The interfacial charge transfer analysis is done using EIS, IMPS and OCVD measurements. Devices with ZnO blocking layer thickness (12 nm) displayed better performance (PCE 2.57%) in comparison to the devices fabricated without blocking layer (1.27%) by reducing the interfacial recombination at the FTO-electrolyte interface and improving life time. It is therefore very essential to choose the right thickness of BLs, as increased thickness can reduce electron injection leading to less performance of the device.

The thesis thus demonstrates the use of ZnO hierarchical structures as fugitive inclusions for improving the light scattering effects in the functional layer of DSSC/DSCs. Significant improvements in PCE was obtained both under 1 sun and 1000 lux conditions without adversely affecting the transparency thereby enabling possible applications in building integrated photovoltaics.

Suggestion for the future work

1. Fabrication of transparent photoanode modules for BIPV applications
2. Study the effect of blocking layer thickness in perovskite based solar cells
3. Utilisation of high surface area ZnO fibrils and sheet aggregates for super capacitor application.

LIST OF PUBLICATIONS

1. Fine tuning compact ZnO blocking layers for enhanced photovoltaic performance in ZnO based DSSC: a detailed insight using β recombination, EIS, OCVD and IMVS techniques. **Sasidharan Swetha**, Suraj Soman,* Sourava Chandra Pradhan, Narayanan Unni K. N, * Abdul Azeez Peer Mohamed, Balagopal Narayanan Nair, and Unnikrishnan Nair Saraswathy Hareesh* *New J. Chem.*, **2017**,41, 1007-1016.
2. Bifacial dye-sensitised photovoltaic devices with enhanced light scattering and improved power conversion efficiency in full sun and low light. **Swetha S.**, Sourava Chandra Pradhan, Anooja Jagadeesh, Suraj Soman,* Narayanan Unni K. N,* Abdul Azeez Peer Mohamed, Balagopal Narayanan Nair, and Unnikrishnan Nair Saraswathy Hareesh* (to be communicated)
3. Effect of morphologically diverse ZnO micro structures as sacrificial layers over TiO₂ photoanode for enhanced light scattering effects in dye-sensitised solar cell. **Swetha S.**, Anooja Jagadeesh, Sourava Chandra Pradhan, Suraj Soman* Narayanan Unni K. N* Abdul Azeez Peer Mohamed, Balagopal Narayanan Nair, and Unnikrishnan Nair Saraswathy Hareesh* (to be communicated)
4. TiO₂-ZnO hybrid compositions for macro porous inclusions as light scattering centers in TiO₂ based DSSCs. **Swetha S.**, Anooja Jagadeesh, Sourava Chandra Pradhan, Suraj Soman,* Narayanan Unni K. N,* Abdul Azeez Peer Mohamed, Balagopal Narayanan Nair, and Unnikrishnan Nair Saraswathy Hareesh* (manuscript under preparation)
5. Aminoacid Inspired Tunable Superparamagnetic Iron oxide (SPION) Nanostructures with High Magnetic Hyperthermia Potential as Biofunctional Magnetic Probes. K. Ananjana, **S. Swetha**, Prakash Prabha, K. V. Nishad, Komath Manoj, Balagopal N. Nair, G. S. Sailaja* (Just accepted manuscript, *New J. Chem.*)

LIST OF CONFERENCES

1. MCM-41 Silica as Scaffold Layer for Perovskite Solar Cell Swetha S, Priyesh P , Balagopal N Nair, U S Hareesh*. **NCMST -2015**, IIST Thiruvananthapuram. (Poster presentation)
2. Optimized paste formulations for the development of Zinc oxide based Dye-sensitized Solar Cell. Swetha S, Suraj Soman, A Peer Mohammed , Balagopal N Nair, U S Hareesh* **CAMEE- 2015**, Christ University Bangalore. (Poster presentation)
3. Zinc oxide-Titania hybrid architectures as active layer in Dye-sensitized solar cell Swetha S, Suraj Soman, Sourava C Pradhan , A Peer Mohammed , Narayanan Unni K N and U S Hareesh*. **IUMRS – 2016** IISc. Bangalore. (Poster presentation)
4. Titania -Zinc Oxide Micro Flower Hybrid Dye-Sensitized Solar Cell For Efficient Power Generation Under Indoor Light. Swetha S, Suraj Soman, Sourava C Pradhan, Vidhu S Nair, Balagopal N Nair, A Peer Mohammed, Narayanan Unni K N* and U S Hareesh* **EAS8-2017**, CSIR-NIIST, Thiruvananthapuram. (Poster presentation)
5. Morphologically variant ZnO nano/micro structures for Dye sensitized Solar cells. Swetha S, Sourava C Pradhan, Anooja Jagadeesh, Balagopal N Nair, A Peer Mohammed, Suraj Soman, * Narayanan Unni K N and U S Hareesh* **MRSI, Annual Technical Meeting - 2018**, IISER, Vithura, Thiruvananthapuram. (Oral presentation)
6. ZnO hierarchical structures as fugitive inclusions for enhanced light scattering in TiO₂ photoanode of dye-sensitized solar cell. Swetha S, Sourava C Pradhan , Anooja Jagadeesh, Suraj Soman,* Balagopal N Nair, A Peer Mohammed, Narayanan Unni K N* and U S Hareesh*, **STAEM-2018** and 5th Annual Meeting of the Academy of Microscope Science & Technology (AMST), India, CSIR-NIIST. Thiruvananthapuram. (Oral presentation, **Best Oral presentation award**)

